

# Cryogenic Memory Elements using Rare Earth Nitrides

by

Samuel Thomas Devese

A thesis  
submitted to the Victoria University of Wellington  
in fulfilment of the requirements  
for the degree of Doctor of Philosophy

Victoria University of Wellington  
2023

# Abstract

The rare earth nitrides (RENs) are a series of intrinsically ferromagnetic semiconductors with a range of contrasting magnetic properties across the series due to the filling of their  $4f$  electron orbitals. The electrical conductivity of the RENs can be tuned via nitrogen vacancy doping to achieve conductivities ranging from insulating to metallic-like. It is these properties that have prompted their use in memory device structures in recent years, with the potential for integration with superconducting computing in the future. We report on the potential use of the RENs as ferromagnetic (FM) layers in tunnelling magnetoresistance (TMR) and giant magnetoresistance (GMR) device structures for non-volatile memory storage devices.

In this thesis, we present a study on the use of gadolinium nitride and dysprosium nitride as the ferromagnetic layers in a range of device structures including magnetic tunnel junctions (MTJs) and in-plane conduction devices based on the giant magnetoresistance effect. First, we have fabricated and characterised GdN/AlN/GdN/Gd and GdN/GaN/GdN/Gd MTJ structures with a maximum TMR of 135% at 5 K for magnetic fields of  $\pm 8$  T. The maximum difference in resistance between the high- and low-resistance states – corresponding to the anti-aligned and aligned magnetisation states – at 0 T was  $\sim 0.53\%$ .

Following this, magnetic tunnel junctions and GMR-style devices have been fabricated using gadolinium nitride and dysprosium nitride as the two FM layers. In the MTJ, lutetium nitride was used as the tunnel barrier material (GdN/LuN/DyN), while in the GMR-style devices, Lu and Al were separately used as the conductive exchange blocking layers (GdN/Lu/DyN and GdN/Al/DyN). A maximum difference in resistance states of  $\sim 1.2\%$  and  $\sim 0.04\%$  at 0 T was observed at 5 K for the MTJ and GMR-style devices respectively. This is the first time that a difference in resistance between the aligned and anti-aligned configuration has been observed for these device structures in the absence of an external magnetic field, demonstrating the use of GdN and DyN in such non-volatile memory elements.

We also report electrical transport and optical spectroscopy measurements on a series of lutetium nitride thin films variously doped with nitrogen vacancies, along with the computed band structures of stoichiometric and nitrogen vacancy doped LuN. Here, we bridge the void between computation and experiment with a combined study of LuN focusing on its electronic properties. We find that stoichiometric LuN is a semiconductor with an optical bandgap of  $\sim 1.7$  eV. Its conductivity can be controlled by doping with nitrogen vacancies, which results in defect states at the conduction band minimum and valence band maximum. These results not only provide information on LuN but also help underpin understanding of the electronic properties of the entire rare earth nitride series.

## Acknowledgments

First and foremost, thank you to my supervisor, Franck Natali. Know that I have truly appreciated every minute you have spent on this project with me. You have been much more than just a wealth of knowledge, you have been a balanced combination of patience and impatience to guide me through this project; patience to facilitate my learning and understanding, and impatience to push me to achieve far more than I would have by myself. If even one tenth of your work ethic has rubbed off on me over the past three and a half years, I will be a very productive man.

Thank you to the rest of the REN group that have been so impressive and inspiring to work alongside: Ben, Joe, Eva, Bob, James, and Denis. Thank you, Will, for your perpetual assistance and ideas throughout, from REN physics to devices to computations. Jackson, thank you for many enlightening office discussions and for always asking pertinent questions, of myself and of others; the ensuing answers and discussions I always find myself learning from. Thanks to Simon, for providing so much value to device meetings and my project with your analysis and insight. And of course, for being our point-of-call out at Robinson. Thank you, Catherine, for all the time spent in the various labs working together and for continuing the work on devices. Thank you to all other REN group members, Ali, Jay, Tane, Kira, Martin, Kiri, and Ted. And past members too, Felicia and Harry, for pioneering the REN device project that I was so fortunate to have been a part of.

Thank you to Natalie and the members of the cleanroom group, Mohsen, Erica H, Erica C, Jenna, and Ned, for allowing me to share your space and resources in the lab next door. It has been an amazing environment full of camaraderie towards helping each other with even the small tasks such as evaporator runs or glove refills.

To those at Robinson: Shen, Guy, and Yao, (Simon and Tane included), thank you for assisting with equipment maintenance and measurements, especially early on in my project.

Thank you to my friends who have been by my side in spirit and in person along the way, sharing in the adventure: Chloe, Seth, Danny, Sam, Nick, and Madi. Your company in this journey has kept my cup full always.

And of course, my last thank you goes to those who have been there from the start. Mum, Dad, Ben, and Lucy, I think half the reason I thought I could do this at all was because you all somehow knew that I could.



# Contents

<b>1</b>	<b>Introduction .....</b>	<b>1</b>
1.1	Motivation.....	1
1.2	Thesis Outline .....	2
<b>2</b>	<b>Motivation and the Rare Earth Nitrides .....</b>	<b>4</b>
2.1	Introduction.....	4
2.2	Memory Storage.....	6
2.2.1	Moore's Law .....	6
2.2.2	More than Moore .....	7
2.2.3	Superconducting Computing .....	8
2.2.4	Memory Elements.....	8
2.3	Rare Earth Nitrides .....	12
2.3.1	Overview .....	12
2.3.2	Electronic Properties .....	14
2.3.3	Magnetic Properties .....	16
2.3.4	Relevant Rare Earth Nitrides .....	18
<b>3</b>	<b>Device Fabrication and Experimental Techniques .....</b>	<b>21</b>
3.1	Introduction.....	21
3.2	Thin Film Deposition.....	21
3.2.1	Ultra-High Vacuum System.....	21
3.2.2	Substrates and Growth Parameters .....	23
3.2.3	Capping Layer.....	24
3.2.4	Other Systems .....	25
3.3	Fabrication of Magnetic Tunnel Junctions .....	25
3.3.1	Photolithography.....	25

3.4	Structural Characterisation.....	34
3.4.1	Dektak Profilometry.....	34
3.4.2	Optical Microscope.....	35
3.4.3	X-Ray Diffraction .....	36
3.5	Electrical Transport Measurements .....	39
3.5.1	Closed Cycle Cryostat.....	39
3.6	Magnetic Measurements .....	41
3.6.1	Physical Property Measurement System.....	41
3.6.2	Magnetic Property Measurement System .....	43
<b>4</b>	<b>Rare Earth Nitrides in Magnetic Tunnel Junctions .....</b>	<b>44</b>
4.1	Introduction.....	44
4.2	Previous REN Group Work on Magnetic Tunnel Junctions.....	45
4.2.1	GdN-based Magnetic Tunnel Junctions.....	46
4.3	Tunnel Barrier Theory .....	52
4.4	Voltage Drop.....	55
4.4.1	Background .....	55
4.4.2	Physical and Geometrical Parameters of the Structure.....	57
4.4.3	Modelling a Simple Case: Gold/REN layer/Aluminium .....	57
4.4.4	Current and Potential Drop in the Region $0 < x < L$ .....	60
4.4.5	Temperature Effects.....	68
4.4.6	Resistance of the Device Active Area .....	69
4.4.7	Closing Thoughts .....	71
4.5	GdN/I/GdN/Gd Devices.....	72
4.5.1	Fabrication, growth, and Experimental Methods.....	72
4.5.2	Results.....	75
4.6	Conclusion .....	94

<b>5</b>	<b>Lutetium Nitride: A Non-Magnetic Semiconducting Rare Earth Nitride</b>	<b>95</b>
5.1	Introduction	95
5.1.1	LuN: A Brief Historical Review	97
5.1.2	LuN Since 2004	97
5.2	LuN Thin Film Growth	99
5.3	Structural Properties	102
5.3.1	X-Ray Diffraction	102
5.3.2	Raman	107
5.4	Magnetic Properties	111
5.5	Electronic Properties	112
5.6	Computational Band Structure	118
5.6.1	Background	118
5.6.2	Computational Details	119
5.6.3	Results	120
5.7	Conclusion	122
<b>6</b>	<b>Gadolinium Nitride and Dysprosium Nitride as Ferromagnetic Materials in Trilayer Structures</b>	<b>123</b>
6.1	Introduction	123
6.2	Device Structure	123
6.2.1	Giant Magnetoresistance	124
6.2.2	Current Perpendicular-to-Plane vs Current-In-Plane	126
6.3	GdN/EB/DyN Devices	130
6.3.1	Fabrication, Growth, and Experimental methods	130
6.3.2	Results	131
6.4	Conclusion	150
<b>7</b>	<b>Summary and Outlook</b>	<b>152</b>

7.1 Conclusions.....	152
7.2 Future Work.....	154
<b>Appendix A .....</b>	<b>156</b>
<b>Bibliography .....</b>	<b>160</b>





# Chapter 1

## Introduction

### 1.1 Motivation

There is an intense research and development effort for novel solid state memory devices that is critical for the future of cloud computing and data storage [1–4]. Much of the power saving that has occurred in these systems over the years has been due to advances in the cooling systems rather than the memory systems themselves [1]. The innovation of new energy-efficient memory storage devices would allow for the continued expansion of technologies such as data centres and supercomputers with minimally increased energy consumption [5]. The quest is to balance speed, power, size, and cost in order to enable a new paradigm of non-volatile random-access memory (RAM) [6–8]. Several architectures and technologies for various types of random-access memory, including spin-transfer torque RAM (STT-RAM), magnetic RAM (MRAM), and ferroelectric RAM (FeRAM) have drawn the most attention and have been studied extensively during the past several years [9–13].

From a material perspective, metallic ferromagnetic materials have been historically by far the most common ferromagnetic (FM) layers in ambient-temperature memory elements, either in a giant magnetoresistance (GMR) structure [14,15] or as magnetic tunnel junctions (MTJs) [11,16]. Such devices typically comprise a trilayer made of two metallic ferromagnetic layers separated by an exchange-blocking (EB) layer, with the resistance of the layered structures dependant on the relative orientation of magnetisation – parallel or anti-parallel magnetic alignment – in the FM layers. Such elements are already commonly applied as both memory structures and read heads for magnetic memories but materials used lack the ability to independently tune the magnetic and electronic properties [6]. In contrast, ferromagnetic semiconductors offer a potential range of new functionalities based on their tuneable carrier concentration and spin polarisation.

Here we present the rare earth nitrides (RENs). The rare earth nitrides form a series of epitaxy-compatible intrinsic ferromagnetic semiconductors (IFS) which display the full range of magnetic and semiconducting properties necessary to exploit for memory elements that function

at cryogenic temperatures [2,5,17–19]. Device structures incorporating RENs that have been fabricated in the past tend to use the REN as the barrier layer, such as for spin filter Josephson junctions and spin filter tunnel junctions [20–24]. More recently, magnetic tunnel junctions using RENs as the ferromagnetic electrodes have been realised [25–28]. To facilitate full establishment of the superconducting computing platform, high-density cryogenic memory storage elements need to be developed that exhibit low-power usage and non-volatility [29]. In this thesis, we focus in particular on non-volatile cryogenic memory elements. GdN and DyN are used as the FM layers in MTJ and GMR-style device structures to serve as a proof-of-concept demonstration of non-volatile memory storage in device structures utilising RENs.

## 1.2 Thesis Outline

The rare earth nitride series is inherently interesting to study from a fundamental sense, but also provides value in the potential material applications of its members. Here we focus on the application of GdN, DyN, and LuN in non-volatile cryogenic memory elements, with an included fundamental study of one of the relatively less-studied members: LuN.

**Chapter 2** provides a more thorough discussion on the specific need for non-volatile memory elements that function at cryogenic temperatures. Here the RENs are introduced with a focus on the magnetic and electronic properties of GdN, SmN, DyN, and LuN.

**Chapter 3** then introduces the fabrication and film growth processes used for sample preparation, including the photolithography process for patterning of the MTJ devices. The main experimental techniques used to characterise these samples are also discussed here.

**Chapter 4** is the first of three experimental chapters. This chapter begins by reviewing the previous work on REN-based magnetic tunnel junctions [25,26]. We have developed a model to understand the current paths and material requirements of the geometry used. Finally, a magnetic tunnel junction is constructed using GdN as the two ferromagnetic electrodes – one pinned with a ferromagnetic Gd layer – and characterised in terms of its electrical and magnetic behaviour.

**Chapter 5** contains a combined experimental and computational study that probes the effect of nitrogen vacancies on the electrical and optical properties of LuN, as well as its band structure.

**Chapter 6** then combines the findings from the previous two chapters to construct a fully REN-based magnetic tunnel junction with LuN as the tunnel barrier and GdN and DyN as the ferromagnetic electrodes. Alongside this, devices based on the giant magnetoresistance effect using a conductive layer to separate the two ferromagnetic layers were also fabricated and characterised to provide a low-resistance alternative device structure.

**Chapter 7** summarises the contributions and findings of this thesis and provides recommendations for expanding on this work in the future.

## Chapter 2

# Motivation and the Rare Earth Nitrides

### 2.1 Introduction

Humans have always been an information-hungry species. With the progressing of society, we are generating increasingly vast amounts of information; data that must be stored somewhere, even temporarily. With the advent of the computer and transistor, data storage capabilities increased exponentially, with the number of transistors on a microchip doubling every two years in accordance with the empirically observed Moore's Law [30]. However, as with any real-world exponential trend, Moore's Law must come to an end eventually, and with silicon technology reaching its physical limit, we must look to alternative technologies to fuel both our desire for information and subsequent necessity for data storage [31–33].

This insatiable demand for information has led to an increasing number of massive memory storage facilities known as data centres, as shown in **Figure 2.1** [1]. Data centres are buildings that contain aisles of memory drives to store data and facilitate fast access to this digital information. Accessing these memories requires electrical current to probe which state the memory element is in and so large data centres require large amounts of power. In 2018, data centres consumed 205 terawatt-hours (TWh) of electricity, which was about 1% of the world's total demand [34]. Much of the power saving that has occurred in these systems over the years was due to advances in the cooling systems rather than the memory systems themselves. The innovation of new energy-efficient memory storage devices would allow for the continued expansion of data centres and shared information with minimally increased energy consumption.

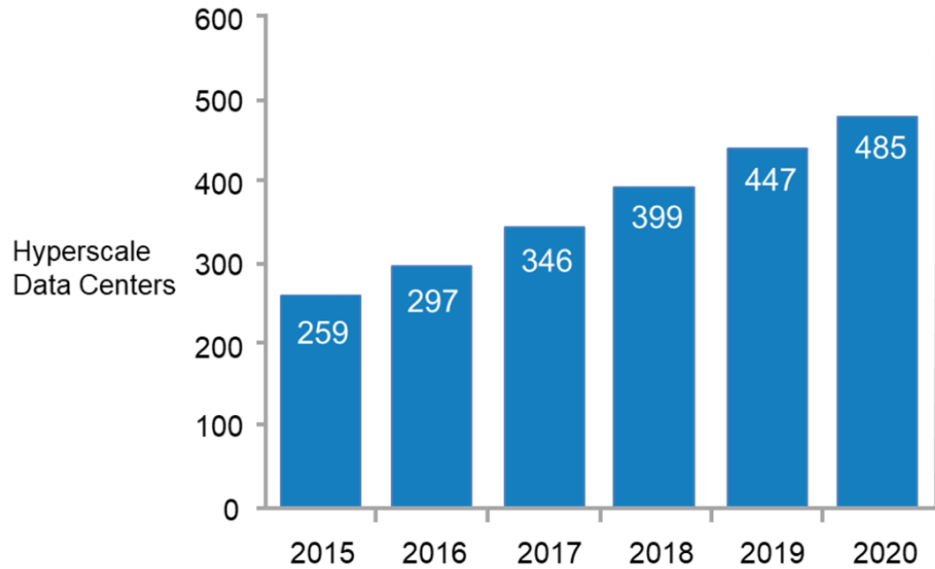


**Figure 2.1:** The number of large – so-called ‘hyperscale’ – data centres has been increasing over the last few years.  
© 2021 IEEE. Reprinted, with permission, from reference [1].

Another big consumer of global energy is the use of supercomputers [2,6,8,35,36]. Supercomputers typically consist of many central processing units (CPUs) that work together to provide large computational power. They are often arbitrarily defined as the highest performance computers at a given time [37] and used to perform computationally intensive calculations such as climate/weather forecasting or molecular modelling. Astronomers also make use of supercomputers to simulate astronomical phenomena such as extremely large-scale many-body simulations. However, Stevens *et al.* found that the use of supercomputers was the largest contribution of individual astronomers in Australia towards carbon emissions, over three times more than the next contribution of air travel [38,39]. While not directly equivalent to energy consumption, carbon emission levels like these suggest a massive usage of energy by these high-performance supercomputers.

One pathway to more energy efficient platforms for both data centres and supercomputers is with superconductors. Superconducting computing is a developing field of technology that offers dramatically lower power consumption and ultra-fast performance compared to current supercomputing technology. Logic circuits, interconnects, and cooling technology have all been established for superconducting computing; the last needed element is high-density memory [6–

8]. To facilitate full establishment of the superconducting computing platform, high-density non-volatile cryogenic memory storage elements need to be developed that exhibit low-power usage and memory retention at zero magnetic field. In this thesis we focus in particular on non-volatile memory elements with potential application in data centres and/or supercomputer settings. Present approaches have been limited by the availability of materials with the range of properties needed to meet the device requirement [6].

In this chapter, we first look at the technology and state of memory storage devices within the field of computing. We then introduce the rare earth nitrides (RENs) and outline their recent experimental history, with a focus on the structural, electrical, and magnetic properties of GdN, SmN, and DyN, as well as LuN, due to their marked use throughout this thesis.

## 2.2 Memory Storage

The basis for any binary memory storage is the availability of two distinct states. One state represents an ‘on’ or ‘1’ configuration, while the other forms the ‘off’ or ‘0’ state, and the combination of numerous binary systems allows for the encoding of information. These two states must be sufficiently distinct as to not be misinterpreted, but not too dissimilar that switching from one state to the other is overly time consuming. This fundamental unit of information is called a bit. For example, the magnetic orientation of a ferromagnet (up/down) or the charge state (charged/uncharged) of a capacitor in complimentary metal-oxide-semiconductor (CMOS) logic [1].

### 2.2.1 Moore’s Law

In 1965, Gordon Moore observed that the number of transistors on a computer chip was doubling every two years, based on the first 5 years of transistor progress. He predicted that this trend would continue, a phenomenon that would famously become known as Moore’s Law [30]. Incredibly, this was the case for over 40 years, with computer chips now able to hold over 10 billion transistors compared to ~10 in 1960, which has resulted in massive progress and improvement to computer memory systems [33,40].

In the pursuit to continually miniaturise transistors, size has become the defining feature. For existing metal-oxide-silicon transistor technology, process nodes are categorised by size markers, with recent sizes of approximately 5 nm (in 2020) and 3 nm (in 2022) [1]. It is difficult to make silicon transistors much smaller than 100 nm because in this size regime, electrons tunnel through the insulating gate that is meant to block current, resulting in non-negligible current leakage and a loss in distinction between the two states. Simultaneously, these small devices heat up considerably and suffer from low heat dissipation, increasing internal resistance and further blurring the difference in distinct states. These effects have proven challenging to overcome and have slowed the typical progress that has been associated with semiconductor technology development for so long [31,33].

The International Technology Roadmap for Semiconductors (ITRS) was established in 1998 [41] and was a shared platform of information and future developments for semiconductor technology but is no longer being updated as of 2017 in response to the departure from Moore's Law. Instead, it has been replaced by the International Roadmap for Devices and Systems (IRDS) [1]. This is a significant acknowledgement by the semiconductor community about the end of Moore's Law, but this is not the first time that the industry has had their doubts. The early 80's saw the challenges of developing transistors at increasingly smaller sizes [42], and in 1995 it was predicted that Moore's Law would come to an end below the 100 nm size, with the industry declaring it a losing battle [40].

## 2.2.2 More than Moore

The so-called "More than Moore" (MtM) methodology refers to the use of elements in memory devices that do not necessarily follow the shrinking transistor size associated with Moore's Law but provide value in different ways [1,43]. In this way, new technologies could be used to help extend the use of silicon-based technology. Current approaches often make use of the scaling capabilities that have been developed from the massive progress by the microelectronics industry to incorporate new functionalities into the systems.

Spintronics is one such example of a MtM system. It builds on the charge-based electronics transistor technology by incorporating elements with spin current to offer an additional degree of



freedom [3,11,16,44–46]. Through the control of the charge transport using magnetisation, a number of phenomena have been discovered including the giant magnetoresistance (GMR) effect in multilayer structures [14,47,48] and spin-transfer torque (STT) effect [11,49]. This has opened up the field to a number of developments, including the advancement of magnetic tunnel junctions (MTJs) which has revolutionised memory storage elements through applications such as read heads and magnetic random-access memory (MRAM) [11,16].

### 2.2.3 Superconducting Computing

Superconducting computers show strong promise as a “More than Moore” computing platform [2,50]. Even with the additional cost of cryogenic cooling, there exists the potential of two orders of magnitude lower power consumption than current CMOS technology [50]. This is largely due to the near-lossless currents in superconducting wires, as well as the extremely low switching energy of Josephson junctions (JJs). Josephson junctions are the building blocks of many applications in superconducting electronics, used in superconducting quantum interference devices (SQUIDs), radio-frequency electronics, and quantum mechanical circuits. JJs consist of two superconducting layers placed in proximity and coupled by a weak link. This weak link is often a thin insulating/oxide layer, so-called barrier. JJ-based memory elements rely on the presence or absence of a persistent electrical current to act as the two distinct memory states, “0” and “1” [50,51]. The energy efficiency of superconducting elements such as these JJs prompts their development as a potential interface to quantum computing systems [52].

Superconducting logic elements have been developed at a rate far exceeding that of complimentary memory elements operable at cryogenic temperatures [7,35,50]. There is of course active development of superconducting memories [29,53,54], however, the largest demonstrated superconducting random-access memory (RAM) is only at the 4 kB level (4096 bits) [55,56] and so cryogenic random-access memory with sufficient density and capacity continues to be the most important area needed to realise the complete superconducting computing platform [57].

## 2.2.4 Memory Elements

CMOS-based memory elements offer the required scalability but tend to suffer from high power consumption at the cryogenic temperatures necessary for superconducting elements [50,58,59]. Focus has instead been directed more towards magnetic memories [49,60] for incorporation as magnetic-superconducting hybrid elements [6,50,58,61]. These devices provide the required low power consumption and non-volatility, along with the important factor of scalability. Semiconductor-based spin valves or magnetic tunnel junctions could be integrated with superconducting circuitry as an attractive pathway towards the development of large-scale cryogenic memory.

The basic structure of a magnetic tunnel junction consists of two ferromagnetic (FM) layers separated by a thin, insulating (I) layer. This structure is typically denoted as FM/I/FM. The purpose of the insulating layer – also called a barrier layer – is twofold: to magnetically separate (uncouple) the two ferromagnetic layers and to induce tunnelling between them. This layer is typically an insulating layer of less than  $\sim 10\text{nm}$ , which forces electrons to tunnel across the barrier potential between the two ferromagnets.

The memory storage aspect of MTJs is due to the two resistance states possible, defined as ‘aligned’ and ‘anti-aligned’. These alignments refer to the relative magnetisation of the ferromagnetic layers. Below the Curie temperature, the conduction bands in a ferromagnet undergo exchange splitting whereby the bands are moved higher/lower in energy depending on the spin of the electrons. When the FM electrodes are magnetised in the same direction – the aligned state – the tunnelling current across the barrier is dominated by majority-majority band transport, highlighted in **Figure 2.2**, and thus is more easily facilitated due to the many available states above the Fermi level, resulting in a (relatively) low resistance state. **Figure 2.2 (right)** shows the alternative case for the high-resistance state, where transport is more restricted as electrons must tunnel to (or from) a minority band with fewer available states. Note that the device resistance is controlled by the majority spin polarisation rather than the magnetisation, though in general the spin polarisation can be controlled via the magnetisation.

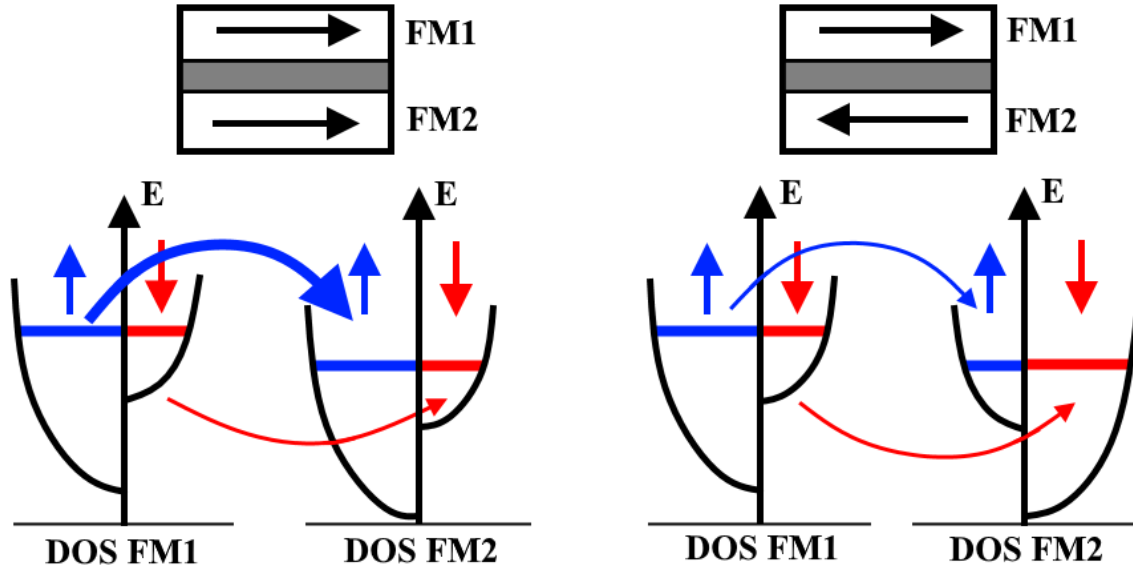


**Figure 2.2:** Schematic example of the density of states (DOS) either side of a tunnel barrier for when the magnetisation of the ferromagnetic layers is aligned (**left**) or anti-aligned (**right**).

The magnetisation direction of the FM layer can be controlled in several ways, such as through external magnetic fields or the use of spin transfer torque via spin-polarised currents. In this thesis, all control of the magnetisation direction in FM layers is through the use of externally applied magnetic fields because this is the easiest and fastest way to implement using a Physical Property Measurement System (PPMS). The setting of the magnetisation direction encodes information in the MTJ, a process known as ‘writing’, and is one of two processes that make up the act of memory storage and use. The counterpart is ‘reading’ and is defined as the act of probing the electrical resistance of the MTJ to determine its state, either aligned (low resistance) or anti-aligned (high resistance). Reading can similarly be achieved in multiple ways, but the method used in this thesis is by applying a known current and measuring the voltage across the device to determine the resistance of the MTJ. The process of writing information to the memory element and having it persist when removed from the external magnetic field is known as ‘retention’ and is an important characteristic of memory elements required for non-volatile memory storage.

Common notation denotes that the FM layer with the relatively lower coercive field is called the ‘soft’ ferromagnetic layer and it is this layer which changes the direction of its magnetisation direction in the writing process. The FM layer with the relatively higher coercive

field is subsequently the ‘hard’ ferromagnetic layer and the magnetisation direction in this layer is fixed, provided the external magnetic field stays at/below the coercive field of the soft FM layer.

MTJs are an important ‘building block’ in the development process of new memory elements. They serve as the prototypical structure to assess the properties and suitability of any new material for a potential device structure. From a material perspective, metallic ferromagnetic materials have been historically by far the most common ferromagnetic layers in ambient-temperature memory elements, either in a giant magnetoresistance structure [14,62,63] or as magnetic tunnel junctions [16,64,65]. Such elements are already commonly applied as both memory structures and read heads for magnetic memories but the materials used lack the ability to independently tune the magnetic and electronic properties [6]. In contrast, ferromagnetic semiconductors offer a potential range of new functionalities based on their independently-tuneable carrier concentration and spin polarisation [17,18,44,66,67].

Dilute magnetic semiconductors (DMS), a class of materials that combine properties of a semiconductor host with magnetic effects due to an impurity dopant, have shown promise in memory and logic applications [66,67]. However, the dependence of the transition temperature on the density of mobile carriers limit their range of applications [44,45,66,68]. In contrast, the separation of electronic and magnetic degrees of freedom in the series of intrinsically ferromagnetic rare earth nitride semiconductors make them ideal candidate materials for non-volatile memory elements at cryogenic temperatures [17,18,69–71].

The rare earth nitrides form a series of epitaxy-compatible intrinsic ferromagnetic semiconductors (IFS) which display the full range of magnetic and semiconducting properties that can be exploited to make memory elements which function at cryogenic temperatures and are fully compatible with superconducting electronics [17–19]. In this thesis, rare earth nitrides are incorporated into various heterostructures, such as magnetic tunnel junctions and giant magnetoresistance devices, to serve as a proof-of-concept for the viability of REN-based memory storage devices, as well as to further explore their electrical and magnetic behaviour.

In this regard, it is worth noting that heterostructures incorporating RENs have already been realised [19,22,24–28], though there has been no demonstration of the non-volatility required for a suitable cryogenic memory element.

## 2.3 Rare Earth Nitrides

Rare earth nitrides could serve as a MtM-esque technology as they incorporate magnetism intrinsically with semiconducting characteristics. This means that we can leverage the mature field of semiconductor processing and fabrication to create high-density memory storage devices that benefit from the additional value of magnetism.

In this section, we discuss the rare earth nitrides and their interesting ferromagnetic and semiconducting properties. We introduce GdN as the prototypical rare earth nitride and SmN and DyN as comparative and relevant examples. LuN is described briefly here but in much greater detail later in this thesis, in **Chapter 5**.

### 2.3.1 Overview

The rare earth elements span the atomic numbers of 57-71, from lanthanum to lutetium (Note that scandium and yttrium are also considered as rare earths). This series contains the elements where electrons begin to occupy and eventually fill the  $f$ -orbitals. The majority of the rare earths have a  $3+$  charge state and readily react with nitrogen to form a rare earth nitride comprised largely of  $L^{3+}$  and  $N^{3-}$  ions in a rock salt crystal structure [17,72]. When bonding with nitrogen, the rare earth atom first loses its  $5d$  electrons, leaving the  $4f$  electrons as the valence orbital. The  $f$ -orbitals are strongly localised which introduces contrasting magnetic properties across the series [17,73]. Importantly, they are ferromagnetic at cryogenic temperatures.

In the stoichiometric form, as shown in **Figure 2.3**, there is a 1:1 ratio of rare earth ions to nitrogen ions. Vacant nitrogen sites ( $V_N$ ) act as the main electronic dopant (thus forming n-type semiconductors [17,74]), leading to a massive range of possible conductivities [18,73–76]. The level of nitrogen vacancy doping is controllable during the growth process through the partial pressure of nitrogen.

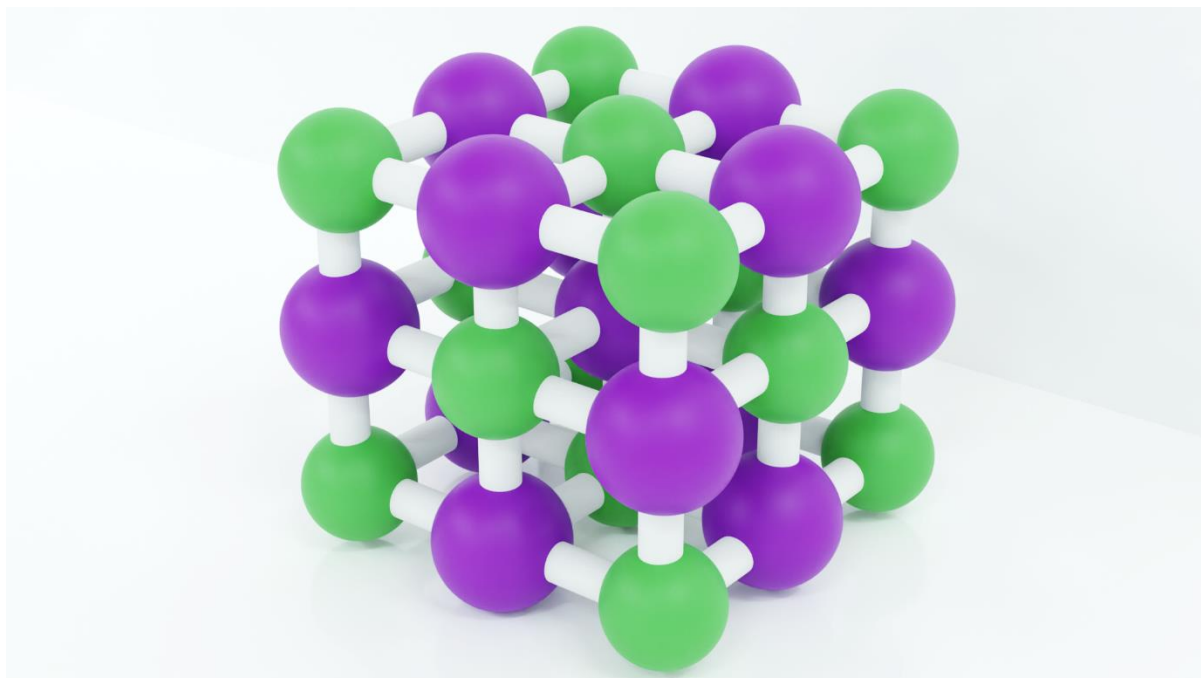


**Figure 2.3:** Schematic of the rock salt structure of the rare earth nitrides.  $L^{3+}$  ions are shown as green while the  $N^{3-}$  ions are shown as purple.

Bulk samples of rare earth nitrides were studied in the early 1960s and 1970s. These early studies were plagued by poor stoichiometry and oxidation issues and so it wasn't until decades later, along with the advent of improvements in vacuum technology, that interest in the rare earth nitrides was re-established. Aerts et al. [77] led this movement with a paper published in 2004 that investigated the electronic structure of the rare earth nitrides using self-interaction corrected (SIC) local-spin-density approximation (LSDA). They predicted that the RENs had a variety of electrical behaviour ranging from half-metallic, to insulating, to semimetallic. Over the years, it has become apparent that the majority of RENs are in fact semiconductors and the historic identifications otherwise are a result of unintended non-unity stoichiometry (i.e.  $LN_{1-\delta}$ ) [17,76]. In particular, the group at VUW have investigated the series and found that the bandgap varies across the series, from  $\sim 0.7$  to  $1.7$  eV, generally increasing with atomic number. The lattice parameter decreases across the series, ranging from  $5.31$  to  $4.76$  Å [17].

As intrinsic ferromagnetic semiconductors, the RENs offer significant advantages over dilute magnetic semiconductors. The magnetic properties can be controlled, mainly, through the

selection of the rare earth while the electronic properties can be controlled through the level of nitrogen vacancy-doping. Both of these are parameters for consideration during the growth process. We now discuss the general electronic and magnetic properties of the rare earth nitrides, before moving on to more specific properties of the particular RENs mentioned throughout this thesis – GdN, SmN, DyN, and LuN – with a focus on GdN and SmN.

### 2.3.2 Electronic Properties

We begin our discussion of the electronic properties of rare earth nitrides by considering recent band structure calculations. Gadolinium nitride is used as an example here for a number of reasons; one being that all of its  $4f$  electrons are spin-aligned resulting in a (relatively) simpler band structure compared to the other RENs. As a result, it is one of the most accessible RENs to study computationally and has served as the prototypical REN in this regard.

The calculated band structure for GdN is shown in **Figure 2.4**, as calculated using local spin density approximation with the Hubbard  $U$  correction (LSDA+ $U$ ). The seven filled majority spin  $4f$  states of the GdN are relatively flat and lie significantly below the valence band maximum around -7 eV. These filled  $4f$  states are the cause of the spin splitting observed in the nitrogen  $2p$  bands, resulting in majority and minority spin bands. The nitrogen  $2p$  bands form the valence band with a maximum at  $\Gamma$ . The conduction band is formed from a Gd  $5d$  band, spin split similarly due to the filled  $4f$  states of Gd. The conduction band minimum occurs at X, resulting in a direct bandgap of  $\sim 1$  eV – depending on the paramagnetic (1.31 eV) or ferromagnetic (0.9 eV) phase – and an indirect bandgap of 0.43 eV.

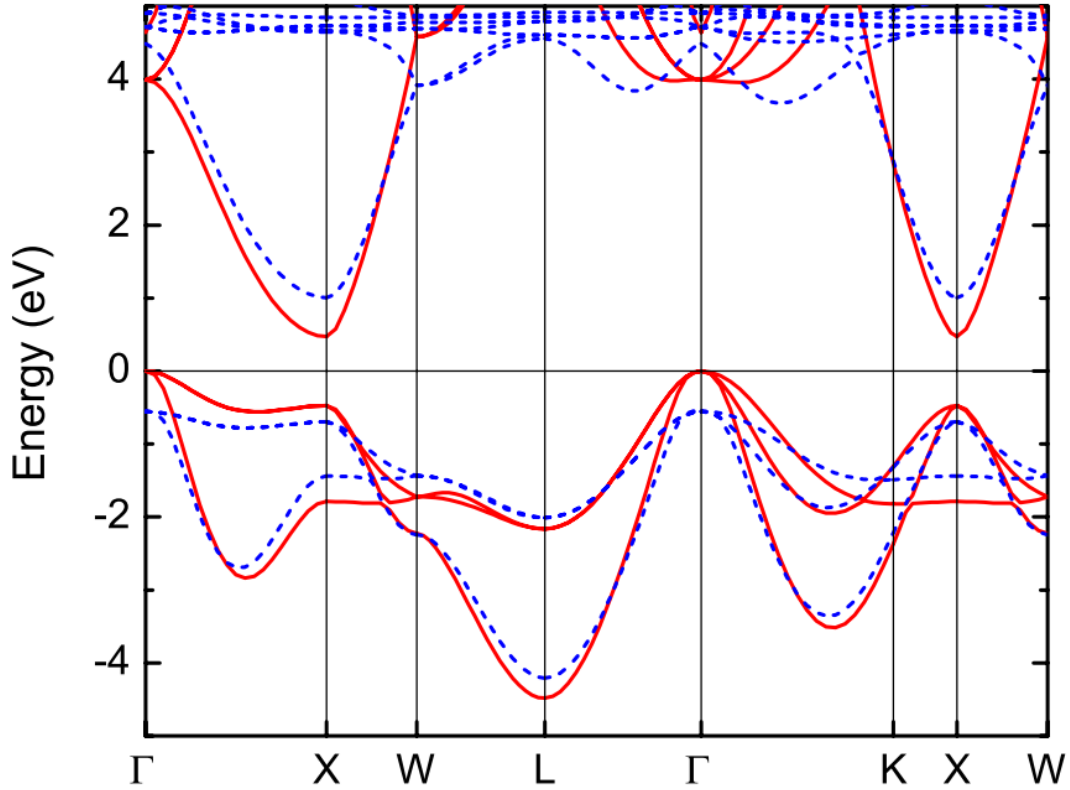


**Figure 2.4:** Calculated band structure of stoichiometric GdN, with majority- and minority-spin bands shown in **red** and **blue** respectively. Figure reproduced with permission from reference [78].

Similar computational results were obtained for other RENs [73,76,79]. While the band structure changes across the REN series, largely due to changes in the filling of the  $4f$  orbitals, the valence band maximum and conduction band minimum typically still occur at  $\Gamma$  and X respectively. The majority of band structure calculations for the RENs consider the stoichiometric form, but as nitrogen vacancies are introduced into the system, defect states begin to appear [73,76]. This can introduce states above and/or below the valence and/or conduction bands, potentially changing the bandgap as compared to the stoichiometric crystal. However, there are very few theoretical studies on nitrogen vacancy-doped RENs [73], and instead the experimental studies more greatly encompass the behaviour of the doped RENs.

RENs can be doped with  $V_N$  during the growth process by controlling the nitrogen partial pressure used [18,75,76,80]. In this way, REN thin films can be grown with varying conductivities: over six orders of magnitude change in conductivity with only one order of magnitude change in



the nitrogen growth partial pressure [75]. This conductivity range spans from insulating (light to no doping) to metallic-like (heavy doping) conductivity [76].

### 2.3.3 Magnetic Properties

The conventional image of magnetism is based on electron spin. However, the series of rare earth materials introduce an additional magnetic moment originating from the electrons' orbital motion [17]. This leads the series to possess a range of magnetic properties – including opposite spin and orbital moments, resulting in a vanishing net magnetisation [81] – that permits opportunities in device structures that are not accessible with the typical ferromagnetic materials. Here we discuss the empirical Hund's rules as a way to understand how these two moment contributions of the  $4f$  electrons affect the magnetic behaviour across the series.

The spin and orbital magnetic moments are related to the total spin and orbital angular momentum quantum numbers respectively. The total spin angular momentum quantum number,  $S$ , is given by:

$$S^2 = \hbar^2 s(s + 1) \quad (2.1)$$

where  $\hbar$  is the reduced Planck's constant ( $\sim 1.055 \times 10^{-34} \text{ m}^2 \text{ kg s}^{-1}$ ) and  $s$  is the spin quantum number, with each electron having  $s = 1/2$ . The total orbital angular momentum quantum number,  $L$ , is given by:

$$L^2 = \hbar^2 l(l + 1) \quad (2.2)$$

where  $l$  is the angular momentum quantum number. This leaves the total angular momentum quantum number,  $J$ , as:

$$J^2 = \hbar^2 j(j + 1) \quad (2.3)$$

where  $j$  is the angular momentum quantum number (given by  $j = |l \pm s|$ ).

Hund's rules are a set of three rules:

**First rule:** The total spin angular momentum quantum number,  $S$ , must be maximised. For this, we assume that subsequent electrons filling an orbital are spin-aligned until all orbits are filled, where anti-aligned pairing then takes place.

**Second rule:** The total orbital angular momentum quantum number,  $L$ , should be maximised, while adhering to the First rule. This reduces the repulsion between electrons.

**Third rule:** The total angular momentum quantum number,  $J$ , should be minimised. This means that for less than half-filled orbitals,  $J = L - S$ , while for more than half-filled orbitals,  $J = L + S$ . In the RENs, this means that less than half-filled orbitals (CeN to EuN) will have their spin and orbital magnetic moments anti-aligned, while those with more than half-filled orbitals (TbN to YbN) will have their spin and orbital moments aligned. GdN, with its half-filled orbital, would have zero orbital magnetic moment.

Indeed, Larson *et al.* found that the REN series generally obeys all three of Hund's rules [79]. The second rule is broken by EuN and YbN where a cubic symmetry results in a lower energy configuration. The calculated contributions of each moment and the resulting total magnetic moment are shown in **Figure 2.5**. Experimentally, the total magnetic moment is sometimes found to be less than expected for some RENs [18,81].

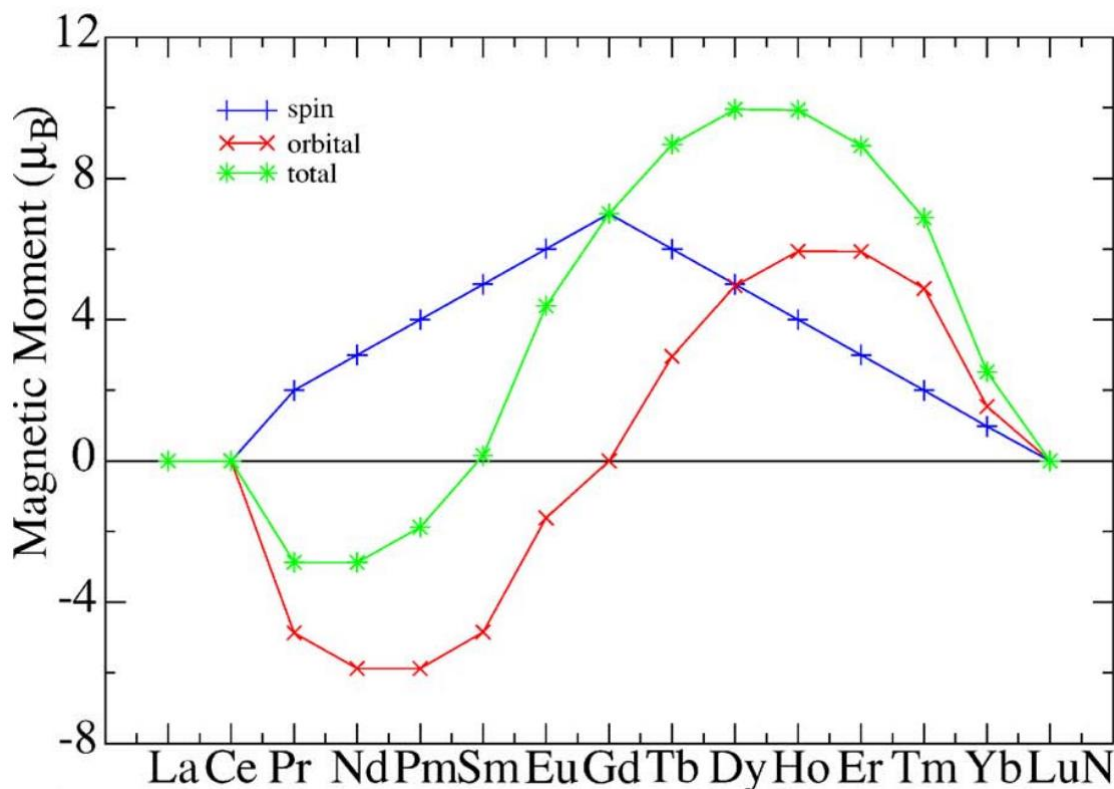


**Figure 2.5:** Calculated spin (blue), orbital (red), and total (green) magnetic moments for the REN series. Figure reproduced with permission from reference [79].

## 2.3.4 Relevant Rare Earth Nitrides

### 2.3.4.1 Gadolinium Nitride

GdN has been introduced earlier in this chapter and serves as the prototypical rare earth nitride. As a result, it is the most studied of the series. Its magnetic moment is purely spin-dominated and very strong with an expected saturation magnetisation of 7  $\mu_B$ /ion according to Hund's rules ( $L = 0$ ,  $S = 7/2$ ). GdN exhibits a ferromagnetic phase below  $\sim 50$  K, though this can be pushed higher to  $\sim 70$  K through doping with nitrogen vacancies [69,82]. The coercive field at low temperatures is very small, on the order of tens to hundreds of millitesla, and therefore greatly influenced by the crystallinity of the film [83]. Larger coercive fields are generally found for more polycrystalline GdN samples, while epitaxial films have smaller coercive fields [84].

### 2.3.4.2 Samarium Nitride

SmN has two fewer electrons than GdN, with the electron configuration  $4f^5$ . Interestingly, these electrons produce both a spin and orbital magnetic moment of  $\sim 2 \mu_B/\text{ion}$  [85] which point in opposite directions due to the spin-orbit coupling. As a result, the two antiparallel contributions yield a net magnetic moment of near-zero, approximately  $0.035 \mu_B/\text{ion}$ , below the Curie temperature of  $\sim 27$  K [81,86]. At even lower temperatures, below 4 K, SmN has also been shown to exhibit superconductivity [87].

SmN has a very large coercive field of over 6 T at 2 K, a result of a weak Zeeman interaction due to the small magnetic moment [81,88]. This means that SmN can, and has, been used as the hard FM layer in MTJ structures, as the large coercive field largely prevents a change in magnetisation at low magnetic fields. Additionally, the near-zero moment reduces any stray fringe fields, the reduction of which would be useful in real world application [27,28].

### 2.3.4.3 Dysprosium Nitride

DyN is a heavy REN with 9  $4f$  electrons and approximately equal spin- and orbital-moments that are in the same direction. This means that the spin and orbital magnetic moments are aligned in the same direction and therefore contribute additively to the total magnetic moment. It has both a theoretical orbital and spin magnetic moment of  $5 \mu_B/\text{ion}$ , resulting in an expected total net magnetic moment of  $10 \mu_B/\text{ion}$  in the paramagnetic state, falling to  $\sim 5 \mu_B/\text{ion}$  under the exchange interaction below its Curie temperature at  $\sim 30$  K [18,70,75].

Bulk DyN is found to have a  $T_C$  of 17-25 K [89] and the value for thin films is reported as slightly higher between 24-32 K [18,75,90]. The coercive field of DyN has been reported as on the order of 100 mT at 5 K [18] making it a suitable FM pair with GdN, which has a coercive field on the order of 10 mT at the same cryogenic temperature [83,91]. As will be discussed in **Chapter 6**, these contrasting properties of DyN and GdN can be used to determine whether the FM layers in a trilayer structure are magnetically isolated through the measurement of two distinct ferromagnetic transition temperatures (using magnetisation as a function of temperature) or two coercive field values (using magnetisation as a function of external magnetic field).

#### 2.3.4.4 Lutetium Nitride

LuN is the end member of the rare earth nitride series. It possesses a completely full  $4f$  orbital and is one of two RENs that are non-magnetic, along with LaN. It is relatively under-studied as compared to the other RENs, likely due to the lack of any prominent magnetic properties. However, it is exactly this lack of magnetism that makes it interesting from a device perspective, for example as a non-magnetic spacer layer in heterostructures or multilayers. In this thesis, we perform a fundamental study of LuN in a combined experimental and theoretical approach in **Chapter 5**.

## Chapter 3

# Device Fabrication and Experimental Techniques

### 3.1 Introduction

The large majority of samples presented in this thesis consist of single- or multi-layer thin films. These films may be unpatterned – simply grown on the entirety of the chosen substrate – or patterned, using photolithography to selectively cover part of the substrate and restrict film growth to a certain shape or area for device applications.

In this chapter, the growth, fabrication, and characterisation of these samples is detailed. We begin with a description of the growth systems used throughout this project followed by the various growth parameters for different samples. The photolithography process is then outlined, with a full description of the multi-step recipe that was used to fabricate magnetic tunnel junctions. We then move on to general sample characterisation, with techniques such as X-ray diffraction, followed by the equipment and techniques used for electrical transport and magnetic measurements.

### 3.2 Thin Film Deposition

#### 3.2.1 Ultra-High Vacuum System

All of the thin films, so-called layers, were grown in ultra-high vacuum (UHV) systems by physical vapour deposition (PVD). The ultra-high vacuum method has been the technique of choice for the growth of REN materials because the high vacuum and inert gas environment ensure that good crystal quality and material purity are achieved.

A Thermionics ultra-high vacuum system with a base pressure of  $\sim 1 \times 10^{-9}$  mbar was used to grow the majority of the single- and multi-layer REN thin films discussed in this thesis. A schematic of the chamber is shown in **Figure 3.1**. Substrates up to 2 inches in diameter could be loaded onto a molybdenum substrate holder and transferred from the load lock chamber to the growth/deposition chamber via a transfer arm. The load lock chamber allowed the loading of

substrates without venting the growth chamber to the atmosphere. Once the sample was loaded, the load lock chamber was pumped down for several hours (often overnight) to a pressure of  $\sim 1 \times 10^{-7}$  mbar before transferring the substrate into the growth chamber in order to minimise contamination to the growth chamber.

The holder was transferred into the growth chamber via the transfer arm and attached to a central manipulator, still oriented film-side down. This manipulator had both a water-cooling system to cool the substrate during growth and an installed heat coil to heat the substrate if desired (for substrate outgassing or epitaxial growth for example). It was also able to rotate continuously to assist with uniform film deposition. After film deposition, the reverse of this procedure was performed to remove the sample and holder from the chamber.

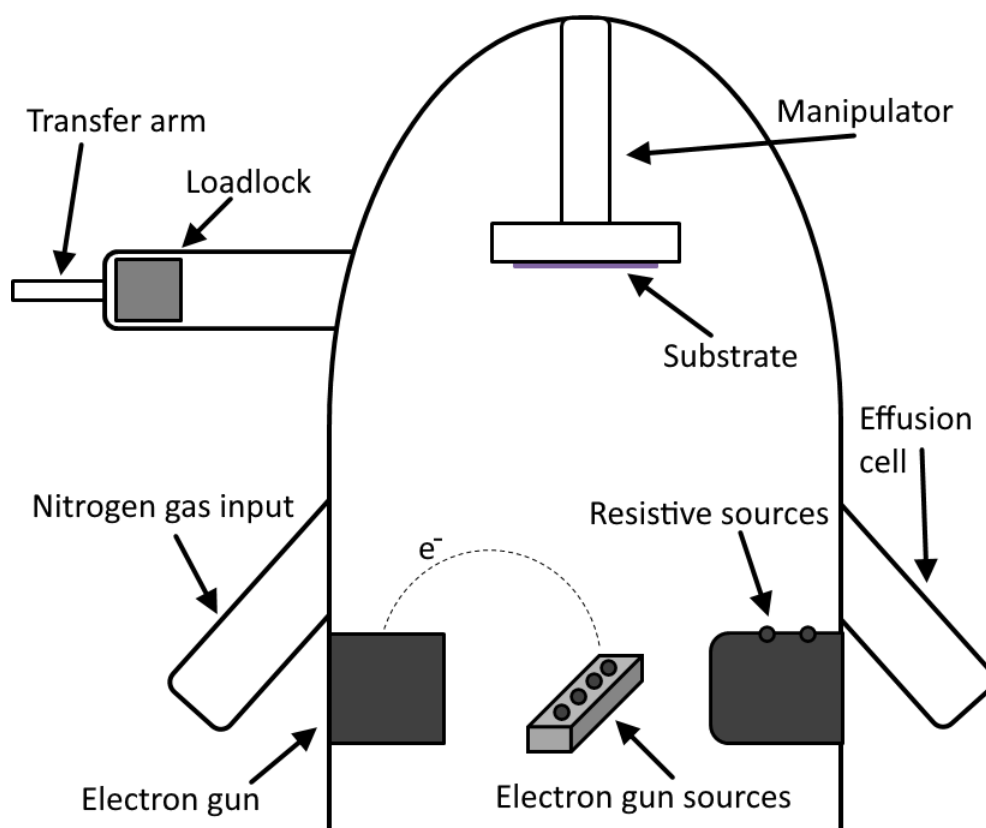


**Figure 3.1:** Schematic of thermionics system, not to scale, showing the relative position of various elements about the stainless-steel main chamber.

The chamber had space for four sources heated by an electron beam, two sources for resistive evaporation, and various ports for effusion cell attachments. During this thesis, one effusion cell was installed and used for Al evaporation. Molecular nitrogen ( $N_2$ ) could be carefully introduced into the system via a mass flow controller, typically at a rate of  $\sim 1$ -4 sccm as needed. Two quartz microbalance crystals were installed inside the chamber and used to monitor the deposition rate during growth. There was also a Kaufman ion source within the chamber, sometimes used to ionise the nitrogen gas, namely for materials like GaN and AlN, that do not catalytically break the molecular nitrogen bond.

### 3.2.2 Substrates and Growth Parameters

Samples in this thesis were grown mainly on two different substrates: Sapphire ( $Al_2O_3$ ) and thermally oxidised silicon (Si/SiO<sub>2</sub>).  $Al_2O_3$  substrates were used as 1x1 cm<sup>2</sup> chips for optical and electrical transport measurements. Si/SiO<sub>2</sub> substrates were used as 2" diameter wafers for patterning and deposition of the magnetic tunnel junctions. These substrates were electrically insulating as to not affect electrical transport measurements.

For the growth of REN thin films, rare earth sources were evaporated in the presence of nitrogen gas. Rare earth sources with sufficiently low evaporation temperatures (e.g. Sm, Dy) could be heated using a resistive heating source, while an electron gun was used to heat the rare earth sources with a higher evaporation temperature (e.g. Gd, Lu). Note that the rare earths with relatively lower evaporation temperatures could still be evaporated using the electron gun setup. Effusion cells could also be utilised to evaporate the source materials. The growth rate of all layers was typically in the range of 100 nm hr<sup>-1</sup> to 400 nm hr<sup>-1</sup>.

A standard growth procedure began by loading and outgassing (if possible) a substrate. Substrate outgassing was dependant mainly on any previous depositions on the substrate, such as photoresist, which could not be heated without hardbaking, or Cr/Au bottom contacts, which could not be heated above  $\sim 400$  °C. With the shutter still closed, the chosen source material was heated up to its evaporation temperature until the desired growth rate was achieved. At this point, nitrogen gas could be introduced into the system to create the desired nitrogen partial pressure.



Typically, the nitrogen partial pressure was maintained at a constant value, somewhere in the range of  $1 \times 10^{-6}$  to  $5 \times 10^{-4}$  mbar, with higher nitrogen partial pressures used to obtain more resistive REN thin films [18,75,76]. The nitrogen catalytically reacted with the rare earth ions to form the corresponding rare earth nitride [72]. Eu and Yb are the only rare earth ions that are known to not catalytically break the nitrogen bond and so required the nitrogen to be activated using the ion source within the chamber. Contaminants in the chamber were monitored via their partial pressure using a Pfeiffer Prisma mass spectrometer. The nitrogen gas was passed through a Materson PUR-Gas in-line purifier prior to its introduction in the chamber to remove any contaminants.

The growth continued under the chosen, constant growth parameters until the desired thickness was reached. This was inferred through the deposition rate controller (DRC) which measured the deposition rate of the rare earth in  $\text{\AA s}^{-1}$ . The thickness as measured by the DRC was calibrated with *ex-situ* thickness measurements, such as Dektak or scanning electron microscopy (SEM). Immediately after the REN thin film growth was completed, a capping layer was grown directly on top.

### 3.2.3 Capping Layer

A capping layer was required to prevent oxidation of the REN thin films once removed from the chamber. The material used for the capping layer was dependent on the purpose of the film. Insulating capping layers were used for optical and single-layer electrical transport measurements, while conducting materials were mainly used for the electrical transport of MTJs which required a conductive top contact. The most common capping layer materials used were Al and AlN for conductive and insulating layers respectively. Other materials included Gd, Dy, Sm, and GaN where relevant.

### 3.2.4 Other Systems

#### 3.2.4.1 Evaporator System for Pre-deposited Bottom Contacts

An Angstrom Engineering evaporator system was also used for the deposition of electrical bottom contacts on  $1 \times 1 \text{ cm}^2$  sapphire substrates used for van der Pauw electrical transport measurements, and to deposit the gold bottom contacts for MTJs in the *caisson* geometry. The *caisson* geometry will be described in detail later in this chapter. Prior to Au deposition,  $\sim 5 \text{ nm}$  of Cr was deposited onto the substrate to aid in the adhesion of the Au layer.

The evaporator system was made of a single stainless-steel chamber. The door opened directly to atmosphere and had a base pressure of  $\sim 1 \times 10^{-6} \text{ mbar}$ . Samples were loaded onto a large round plate which could accommodate several (7+) 2" wafers at a time, allowing for a much higher throughput compared to depositing bottom contacts in our Thermionics UHV system. This plate was loaded into the system along with the desired evaporation materials and then pumped down for several hours, usually overnight, before contact deposition could begin.

## 3.3 Fabrication of Magnetic Tunnel Junctions

### 3.3.1 Photolithography

As mentioned earlier in this chapter, photolithography has been used to grow patterned films. Simple patterning was performed using shadow masks, as in the case for the evaporated electrical Cr/Au bottom contacts. More complex and high-resolution lithography was achieved through the use of photolithography.

Photolithography is the process in which a light-sensitive chemical called photoresist is used to create a patterned layer. The photoresist was spread in a thin layer to coat a wafer or substrate and a number of photoresist-specific heating/exposure steps were then performed to selectively etch a pattern into the photoresist layer. The photoresist layer was then removed with acetone, leaving behind the patterned resist. The specific recipe used in this thesis will be described later in this section in detail. **Figure 3.2** below shows a flow diagram of an example process to deposit a patterned gold square.

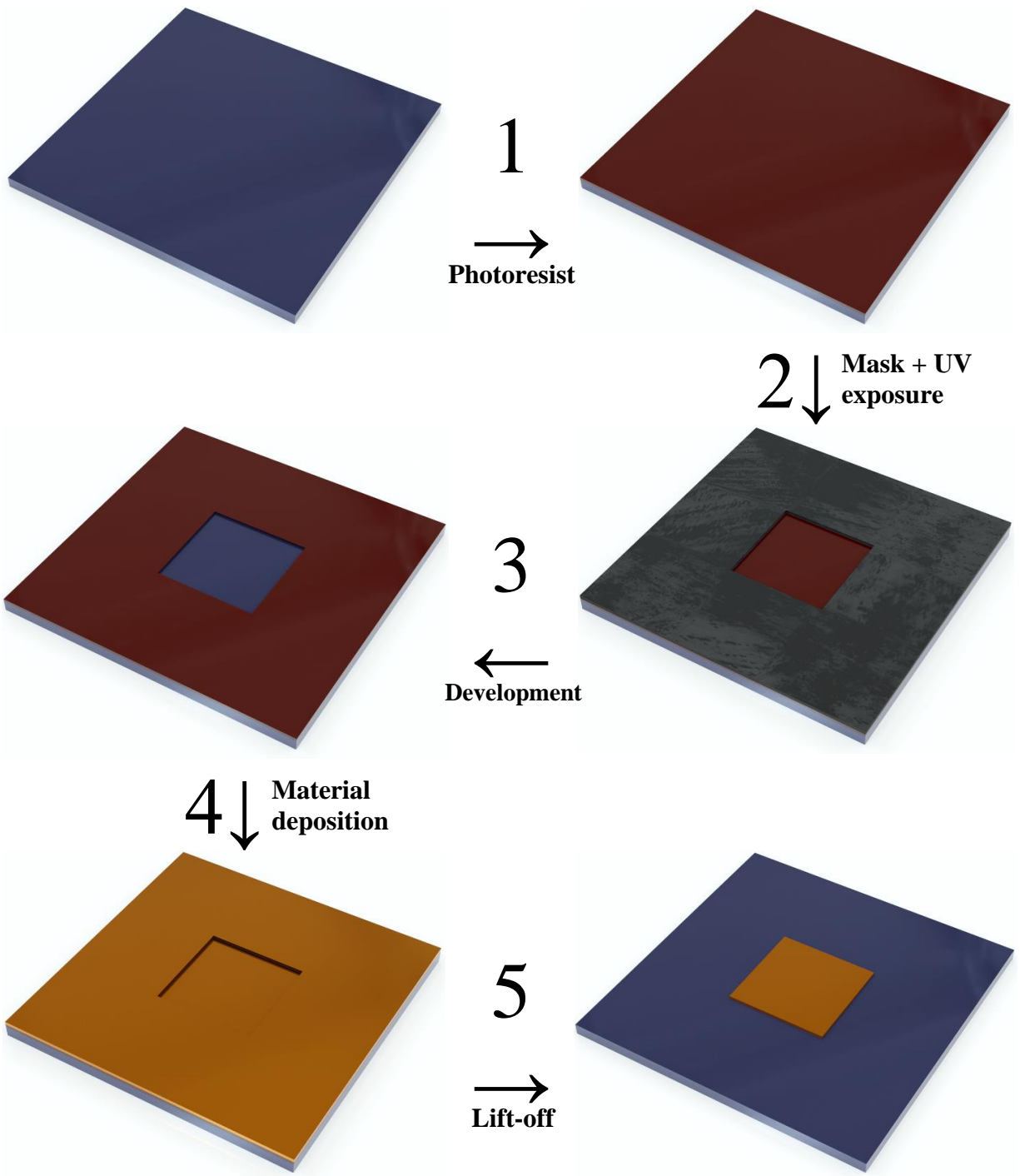


**Figure 3.2:** A flowchart showing the basic photolithography process from substrate to patterned layer. The substrate is shown as metallic **blue**, the photoresist is shown as **red**, the photomask is shown as **grey**, and the deposited material is shown as **gold**.

In the example process shown above in **Figure 3.2**, a clean substrate is first covered in photoresist (Step 1). A patterned photomask is then positioned on top of the substrate (Step 2). By exposing the uncovered area to UV light and performing a subsequent development step, the exposed photoresist is washed away, leaving the photomask pattern imprinted on the photoresist layer (Step 3). The desired material is then deposited onto the patterned substrate (Step 4). The remaining photoresist – and any material deposited on top of it – is then washed away by placing the patterned substrate in acetone, leaving behind the deposited material in the pattern of the photomask (Step 5).

The chemical structure of photoresists changes upon exposure to certain wavelengths of light – in our case, UV light – and sometimes require a subsequent thermal baking step. A photomask made of chrome and soda lime glass was used to expose some parts of the photoresist to UV light, while leaving other parts unexposed. Upon exposure, the photoresist's chemical structure changed such that the dissolution rate of the exposed and unexposed sections of photoresist was different in the appropriate developer solution. In this way, a physical photomask could be used to create patterned photoresist layers on the sample.

Photoresists could be either positive or negative, meaning the area exposed to the UV light was the area with an increased or decreased dissolution rate respectively. In this thesis, the main photoresist used was AZ5214E [92]. This is an image reversal photoresist, which acted initially as a positive photoresist, however, upon a subsequent heating step was reversed into a negative photoresist. More simply, it acted as a negative photoresist overall. The benefit of the image reversal step was that the side profile of the photoresist was undercut, which allowed for sharper features of the subsequently deposited material.

### 3.3.1.1 Magnetic Tunnel Junctions

The photolithographic process used to fabricate the magnetic tunnel junctions described in this thesis was a multi-step process consisting of three photolithography processes. The recipe for each of the three processes was identical except for the photomask used.

The full photolithographic recipe used was previously optimised [93] and was as follows:

1. Clean wafer with acetone and blow dry with N<sub>2</sub>
2. Spincoat AZ5214E photoresist on wafer at 4000 rpm for 60 s
3. First heating step at 95 °C for 60 s
4. UV expose full wafer for 0.25 s
5. Second heating step at 110 °C for 120 s
6. UV expose wafer through patterned mask for 12 s
7. Develop in a 4:1 ratio of 351B developer for 20 s
8. Double rinse in deionised water
9. Blow dry with N<sub>2</sub>

Over the course of this thesis, small corrections were made to the exposure time, development time etc. to adjust for variations in equipment, such as the mercury vapour lamp used for exposure. For samples with aluminium present, 351B developer could not be used in Step 7 as it eroded aluminium. Instead, AZ Developer was used for these samples, which is optimised for minimum attack of Al species [94].

This process produced a growth-ready substrate. Alternatively, the patterned substrate could be stored in atmosphere, out of UV light, for up to two months. After film deposition, a lift-off step was required to remove the photoresist template by soaking the wafer in instrument grade acetone and sonicating for up to 10 minutes.

The full growth of an MTJ sample required three photolithography steps, three growth steps, and three lift-off steps. All samples were grown on a 2-inch silicon wafer with a nominally

300 nm layer of oxidised silicon ( $\text{Si}/\text{SiO}_2$ ) and each wafer provided ten chips with two devices per chip, for a total of twenty devices per wafer.

The first step was to pattern ten dumbbell-shaped bottom contacts of a conductive metal, as shown in **Figure 3.3**. The deposited material was typically gold using the evaporator, but other materials considered were copper and niobium. For the gold deposition,  $\sim 5$  nm of Cr was first deposited on the substrate surface for better adhesion of the  $\sim 50$  nm gold layer. At the bottom of the wafer, below the ten dumbbell-shaped bottom contacts, were four rectangular pieces that could be used for magnetic or structural measurements. The dumbbells as grown from the photomask were intended to be 9 mm by 10 mm and the inner strip had a nominal width of 0.5 mm.

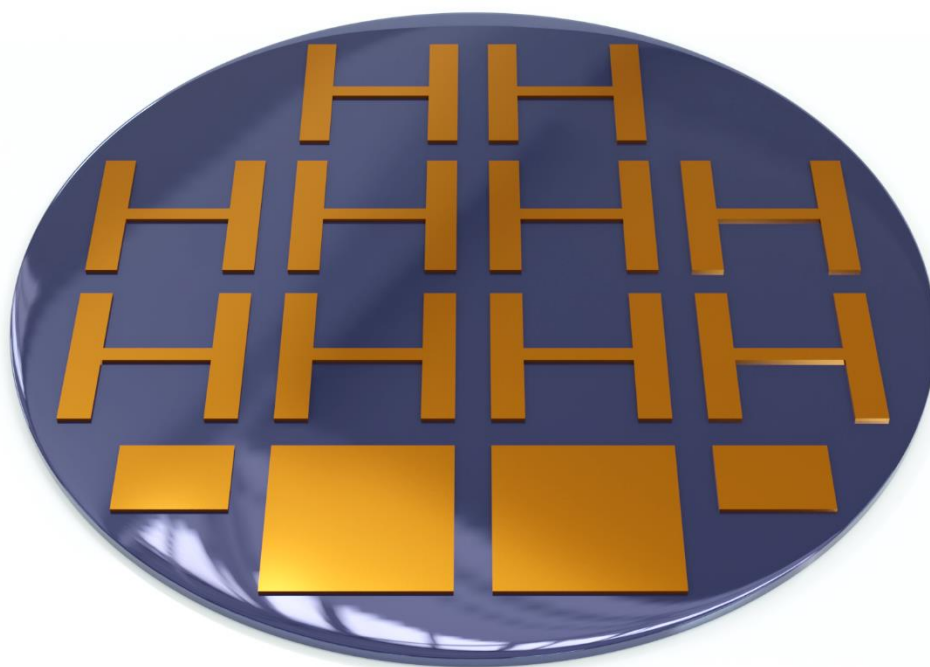


**Figure 3.3:** A 2-inch  $\text{Si}/\text{SiO}_2$  wafer (purple) with ten dumbbell-shaped patterned Au contacts (gold) and four rectangular Au thin films.

The second step was an area restriction layer, as shown in **Figure 3.4**. We used an insulating layer to cover the gold contact which allowed the electric current to only flow through a small square-shaped hole. This square hole defined the so-called *caisson*. The size of this *caisson*

was designed to vary for each device, so in this way, devices ranging from  $10 \times 10 \mu\text{m}^2$  to  $200 \times 200 \mu\text{m}^2$  could be fabricated using a single wafer. To perform competitively in an industrial setting, the *caisson* size must be reduced to at least  $1 \times 1 \mu\text{m}^2$ , however for the proof-of-concept testing of REN-based MTJs, this larger size was sufficient and offered more reliable fabrication of devices. Materials used for this layer needed to be electrically insulating and included GaN, AlN, and  $\text{Al}_2\text{O}_3$ , with the thickness was grown to be  $\sim 40 \text{ nm}$  thick. The Thermionics system was used for GaN and AlN *caisson* growths, while the sputter coater was used for  $\text{Al}_2\text{O}_3$  growths. The area restriction layer had a nominal size of  $10 \text{ mm}$  by  $7 \text{ mm}$ .

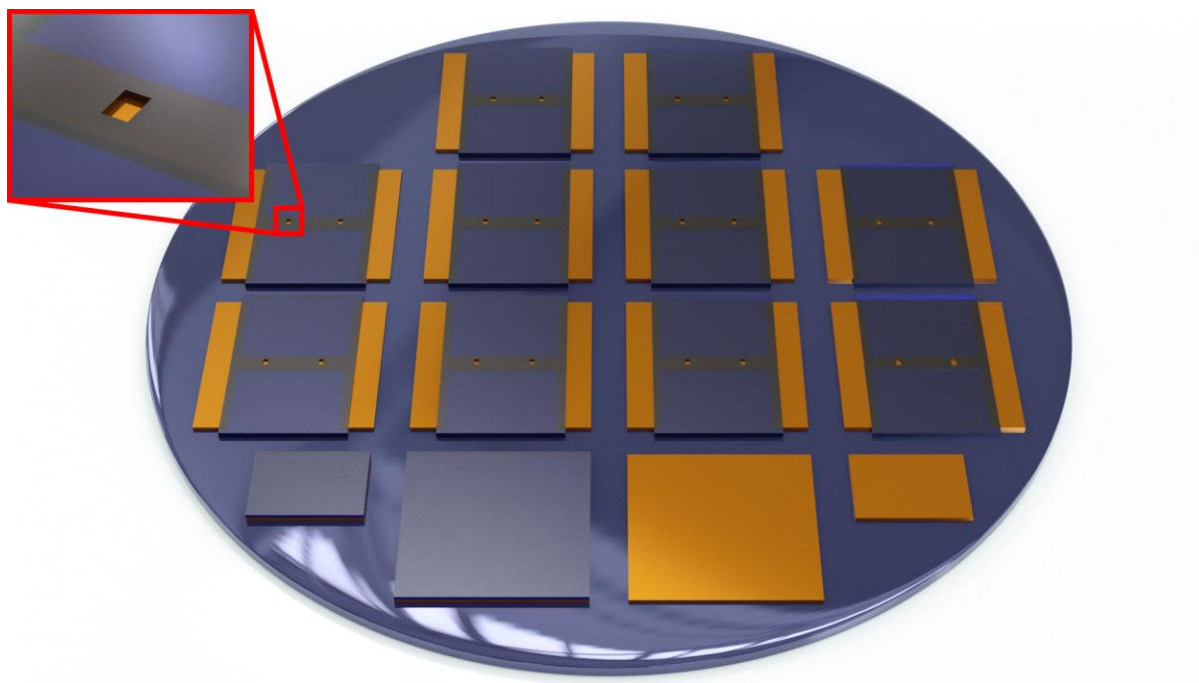


**Figure 3.4:** The area restriction layer (blue) was grown on top of the dumbbell-shaped gold bottom contacts. On each area restriction layer, two squares (not to scale) could be seen about one third of the way in from each side, revealing the gold underneath. This is highlighted in the inset. These squares were the so-called *caissons*. The insulating layer covered two of the four larger rectangles to investigate film quality while two were left bare.

The third and final step was the growth of the multilayer MTJ structure that resulted in the dumbbell shape-like devices – two on each chip – perpendicular to the gold bottom contacts, as shown in **Figure 3.5**. The multi-layered MTJ structure grown in the UHV system consisted

typically of a stack made of a 100 nm thick REN layer, a 2 nm thick AlN or GaN tunnel barrier layer, a 100 nm thick REN layer, and a 100 nm thick Al or Gd capping layer (notated as REN/I/REN/C). The metallic layer was used both as a protective layer for the REN layer and as a top electric contact. Each dumbbell had an inner waist of 1 nm width and were different lengths as to more easily distinguish the *caisson* size at a glance.

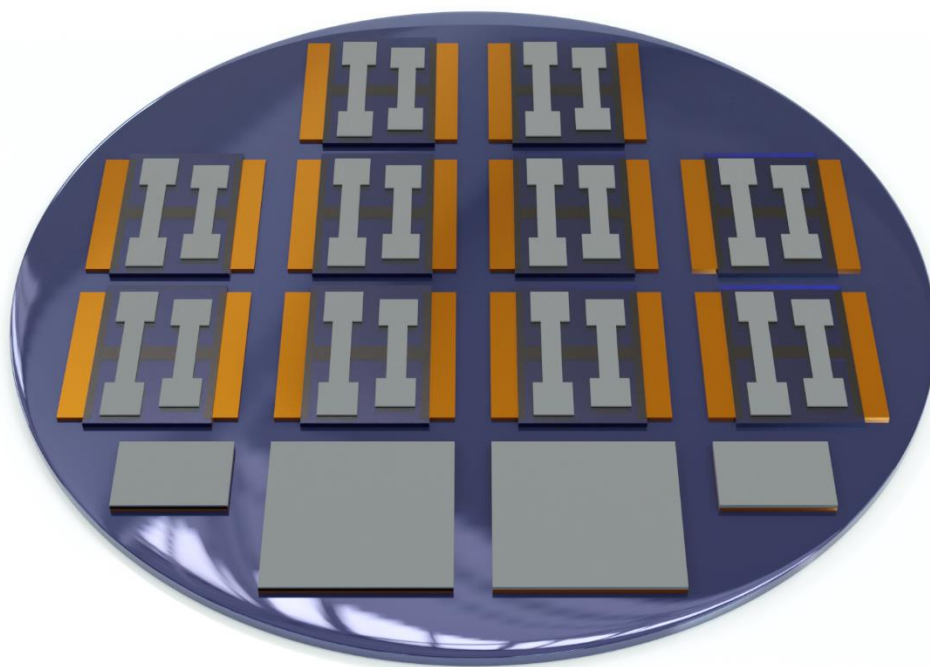
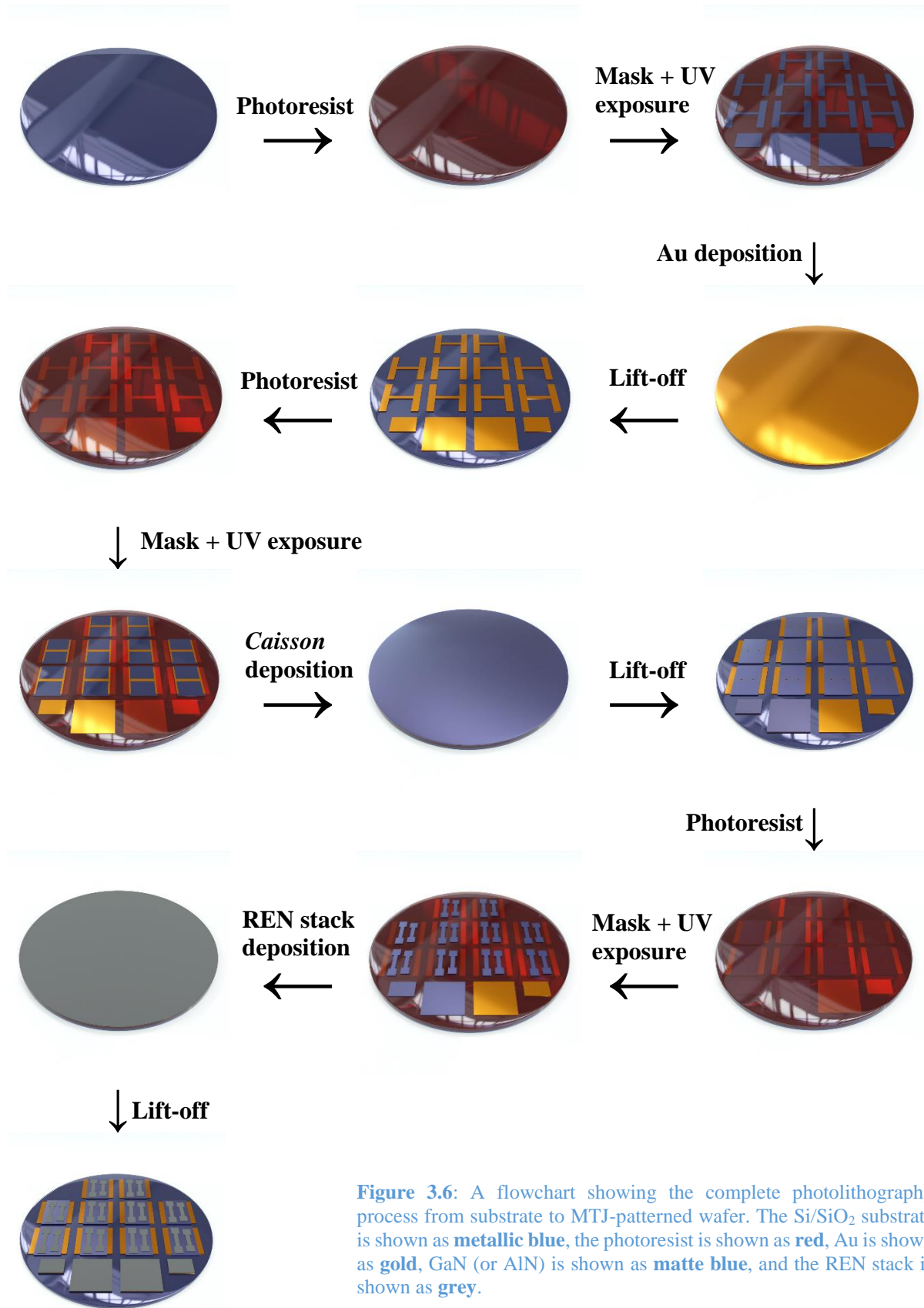


**Figure 3.5:** The REN layer consisted of twenty dumbbells (grey) grown perpendicular to the bottom contacts and on top of the area restriction layer, covering the caisson. In this way, the REN layer made direct contact with the bottom gold contact in a size-controlled fashion. The REN layer was also deposited onto the four bottom rectangles.

The complete photolithography process is outlined in **Figure 3.6**.





Finally, a cross-section of the *caisson* area is shown in **Figure 3.7** to demonstrate how the layers are structured around this feature. Note that this schematic is not to scale. The aspect ratio was much much greater than depicted here, with the *caisson* width on the order of 100  $\mu\text{m}$  and the layer thicknesses on the order of 100 nm. This meant that the layers above the caisson are likely continuous over the *caisson* edges.

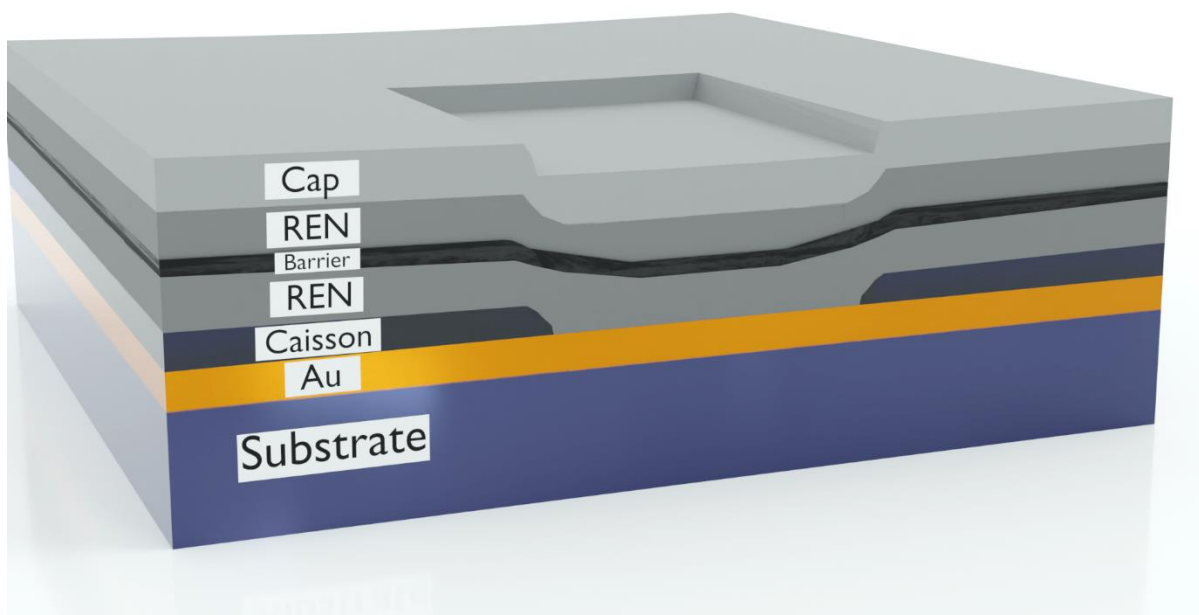


**Figure 3.7:** Cross-section side view of the *caisson* after all steps are completed, not to scale. The layers from bottom to top are the Si/SiO<sub>2</sub> substrate (light blue), Au bottom contacts (gold), insulating *caisson* (dark blue), MTJ stack of REN/barrier/REN (dark grey/black/dark grey), and conductive capping layer (light grey). The device active area can be seen as a break in the *caisson* layer, allowing the MTJ to make electrical contact with the gold layer below.

One wafer yielded ten chips, each with two devices per chip, for a total of twenty devices per wafer. These devices were subsequently characterised using various techniques as described in the following section.

## 3.4 Structural Characterisation

### 3.4.1 Dektak Profilometry

The predominant method used to characterise the profile of the device features was profilometry using a Veeco Dektak 150 Profilometer. This was used due to ease of access and quick measurement times that allowed, for example, the depth profile of all twenty caissons to be characterised in quick succession. After *caisson* layer growth and subsequent photoresist lift-off in acetone, each of the twenty *caissons* were measured using the Dektak. Photoresist was sometimes problematic to remove from the smaller *caissons* and so this measurement gave indication to whether photoresist remained in the *caisson*. An example of a successful development of photoresist from the caisson is shown below in **Figure 3.8**.

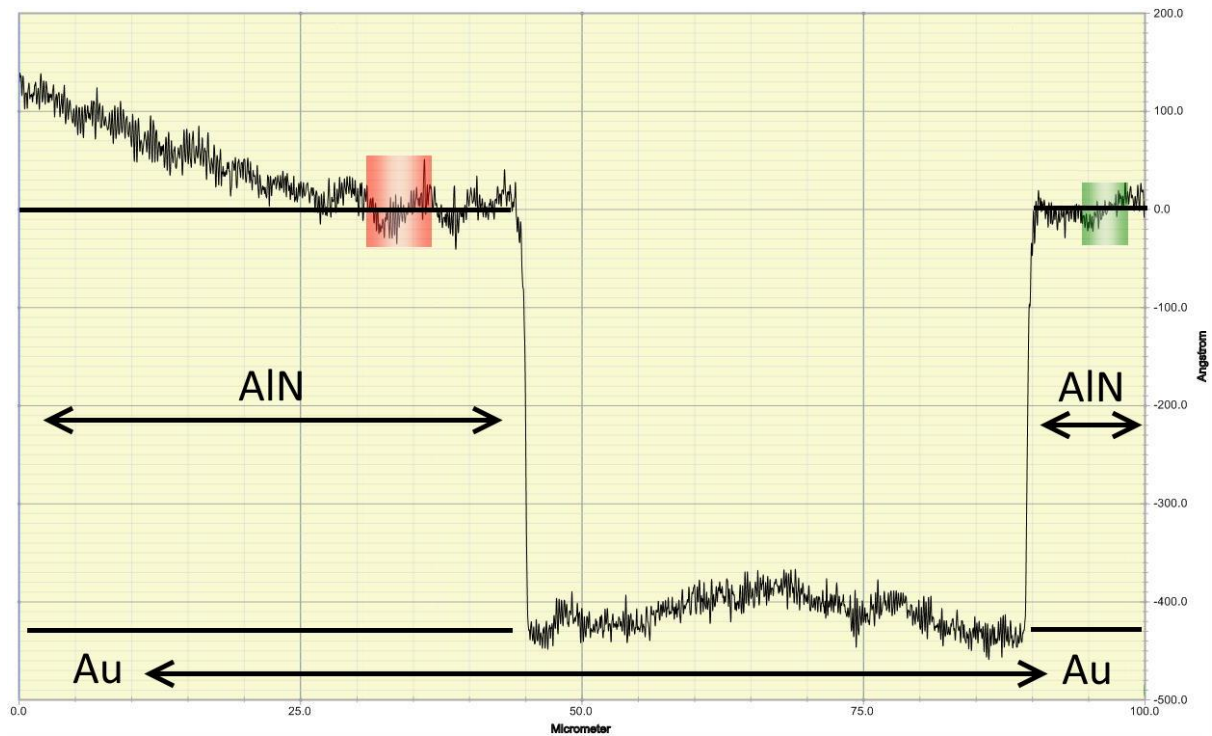


**Figure 3.8:** Surface profile across the *caisson* of a sample after deposition of the Au and AlN *caisson* layers. The red and green bars are software markers. Labels have been added to show the Au layer (bottom layer) and the AlN layer (top layer). The gap in the AlN layer is the future active area of the device, which had a side length of approximately 45  $\mu\text{m}$ .

The AlN *caisson* layer was measured to typically be just over 40 nm thick and sat on top of the Au bottom contacts. The photoresist thickness after spin-coating was approximately  $\sim 1\text{ }\mu\text{m}$  and so was very noticeable, if present, on this size scale.

### 3.4.2 Optical Microscope

An optical microscope was used in a similar way to monitor the cleanliness of layers throughout the photolithography process. First, shown in **Figure 3.9** is a *caisson* with photoresist still present after the standard lift-off procedure (**left**) and after excessive ( $\sim 120$  mins) sonication in acetone (**right**). The extended sonication time damaged some of the layers, with black dots appearing on the surface of the AlN.

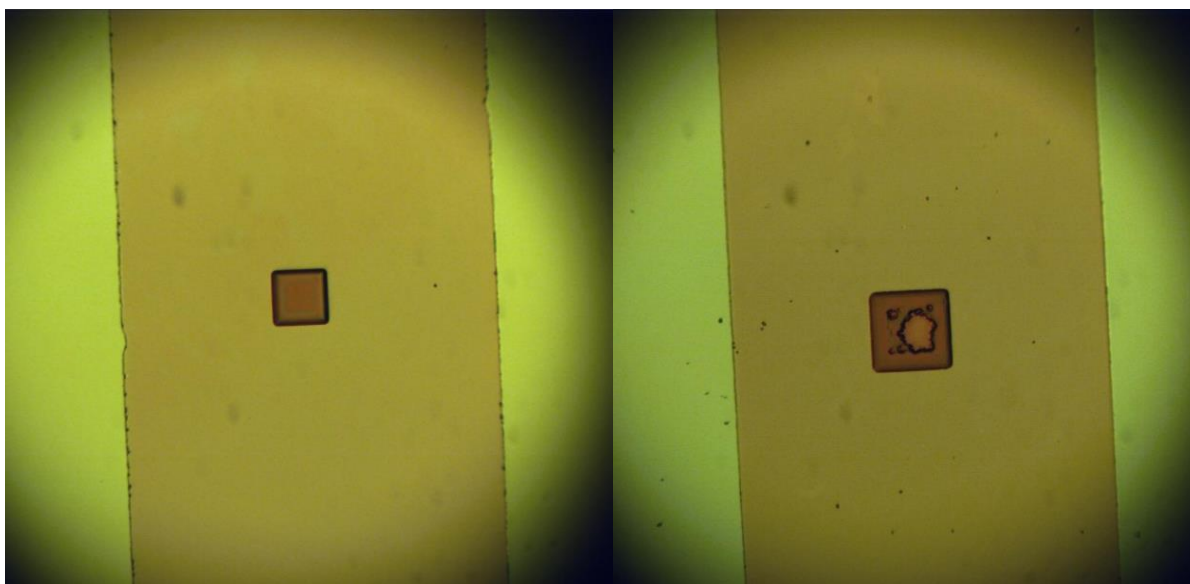


**Figure 3.9:** Optical microscope images of a *caisson* after 1 minute of sonication (**left**) and  $\sim 120$  minutes of sonication (**right**). The gold bottom contact can be seen running vertically in the centre of each image and an AlN layer covered everywhere in the image except for the square *caisson*.

The photoresist in the centre of the *caisson* had begun to dissolve with this extended lift-off procedure but at the cost of structural damage to the deposited materials. This was most likely

due to the photoresist hardbaking, as this particular sample was grown without active sample cooling. In contrast, **Figure 3.10** shows a *caisson* for which the photoresist was successfully removed, after growth with active sample cooling.

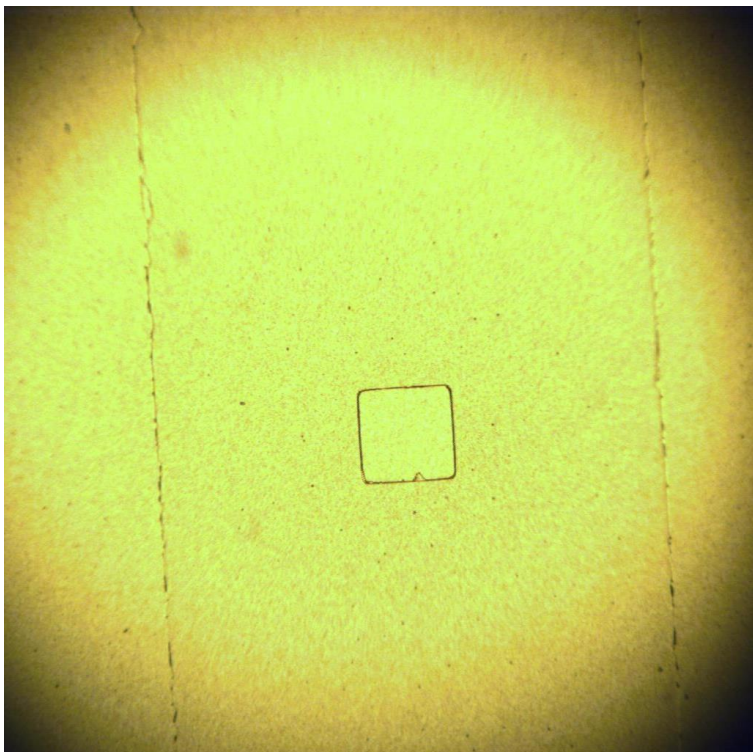


**Figure 3.10:** An optical microscope image of a *caisson* after a successful lift-off step with no photoresist remaining in the active area. The reflective gold surface can be seen clearly through the gap in the AlN layer. The graininess is due to issues with the microscope camera at the time.

### 3.4.3 X-Ray Diffraction

X-ray diffraction (XRD) measurements were performed using a PAN-alytical X'Pert PRO equipped with a Cu X-ray source with wavelength  $\lambda = 1.54 \text{ \AA}$ . Samples were measured using  $2\theta$  scans. As our samples are polycrystalline the XRD measurements showed that growth occurred along the REN (111) direction, as expected for a material with a rock-salt structure. Two diffractogram examples from a bare Si/SiO<sub>2</sub> substrate and a polycrystalline single-layer GdN thin film are shown in **Figure 3.11** and **Figure 3.12** respectively. As labelled in **Figure 3.11**, peaks

related to the copper  $k_\alpha$  and  $k_\beta$  of the silicon [400] occur at approximately  $66^\circ$ , and  $62^\circ$  respectively. Peaks due to the silicon substrate can be seen at approximately  $33^\circ$ ,  $44^\circ$ , and  $69^\circ$ .

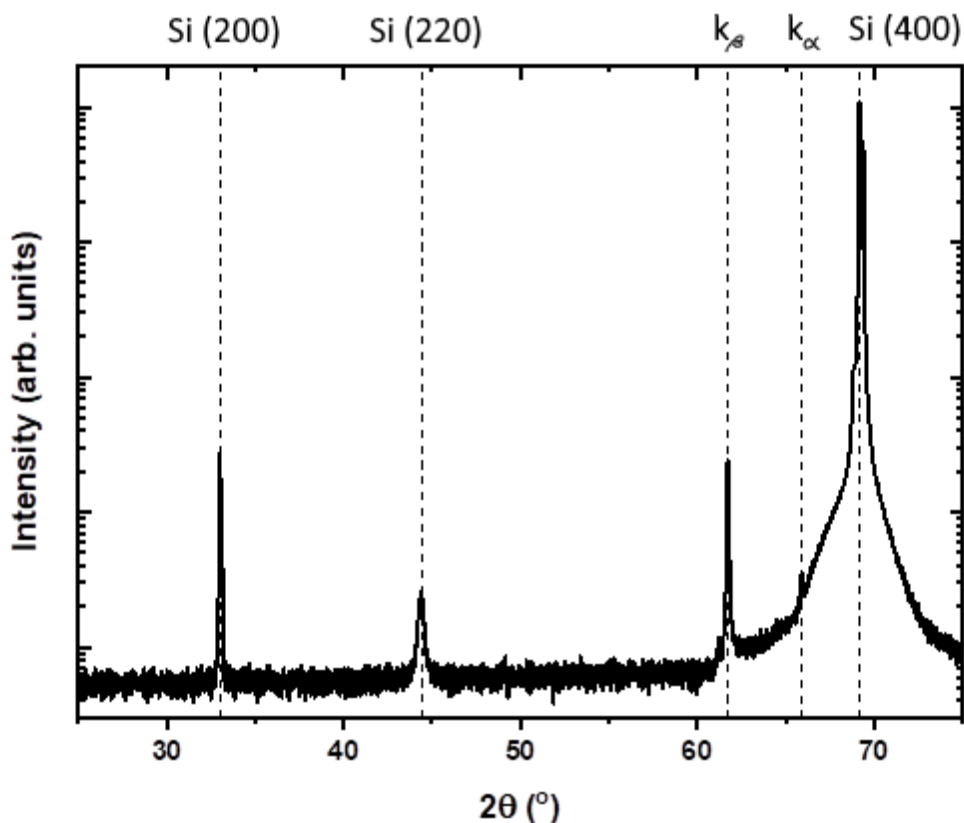


**Figure 3.11:** Typical  $2\theta$ - $\theta$  X-ray diffractogram of a bare Si/SiO<sub>2</sub> substrate used for the thin film growths in this thesis. The dashed lines indicate the position for various peaks.

For the polycrystalline GdN thin film, a strong preferential orientation, along the (111) direction can be clearly observed for all samples grown, with other directions, such as (200) and (311) also present. Coincidentally, the broad GdN (311) peak occurred at a similar angle to the Si (400)  $k_\beta$  peak (sharper, higher intensity), around  $62^\circ$ , highlighting the importance of identifying these peaks that are unrelated to the thin film sample in question.



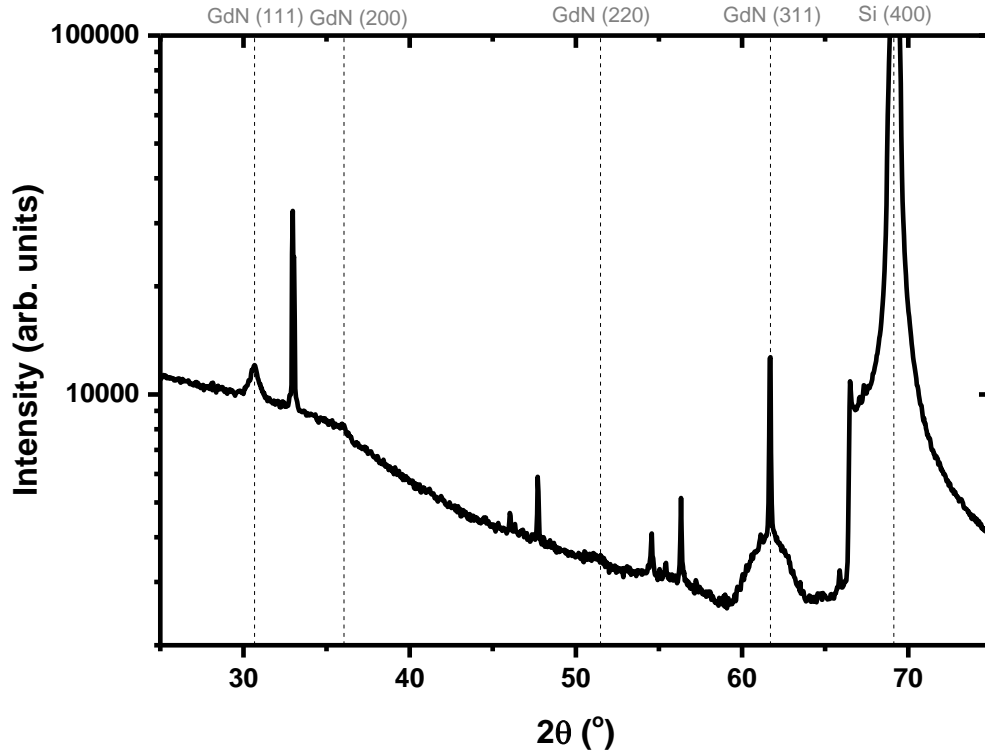


**Figure 3.12:** 2 $\theta$ -X-ray diffractogram of a typical GdN thin film. The dashed lines indicate the position for various GdN orientations, as well as for the silicon substrate.

The peak position provided information on the lattice parameter of the crystal, while the peak width could be used to estimate the average crystallite size. This was achieved using Bragg's formula (**Equation 3.1**) and the Scherrer equation (**Equation 3.2**) respectively.

$$n\lambda = 2d \sin\theta \quad (3.1)$$

here  $n$  is the order of diffraction,  $\lambda$  is the X-ray wavelength,  $d$  is the atomic spacing of the sample, and  $\theta$  is the angle of reflection.

$$\tau = \frac{K\lambda}{\beta \cos\theta} \quad (3.2)$$

Where  $\tau$  is the average crystallite size,  $K$  is a dimensionless shape factor (often taken to be 1), and  $\beta$  is the width of the peak at half of its intensity (FWHM).

Other techniques for structural characterisation were performed from time to time, such as Raman spectroscopy and scanning electron microscopy (SEM). These techniques will be described where relevant.

## 3.5 Electrical Transport Measurements

The electrical transport of samples was primarily characterised using a Janis research closed cycle cryostat. A QuantumDesign Physical Property Measurement System (PPMS) was also used, though this system used a magnetic field in combination with electrical transport and will be described later in the chapter.

### 3.5.1 Closed Cycle Cryostat

The closed cycle cryostat was used for temperature-dependent resistance measurements at different applied currents, as well as current-voltage (IV) characteristic measurements. Samples were mounted onto a copper cold finger using Apiezon N-grease, which was cooled using a Sumitomo heavy industries F-50 helium compressor. The temperature of the cold finger was controlled by a Lakeshore 340 temperature controller. A Keithley 182 Sensitive digital voltmeter, a Keithley 224 programmable current source and a Keithley 196 System DMM multimeter were used for the electrical measurements and controlled via a LabView program. The LabView program was also used to control the temperature. Measurable sample resistance was limited by the voltmeter which could measure a maximum of 3 V, corresponding to a sample resistance of 300 M $\Omega$  when using 0.01  $\mu$ A, the minimum suppliable by the current source.



Electrical contact between the MTJ devices and the electronics was achieved through copper wires attached to the MTJ devices via silver paint, as shown in **Figure 3.13**. This was the configuration for MTJs grown in the *caisson* geometry, with charge pushed along the top contact of one dumbbell, down through the *caisson* device active area, and along the bottom gold contact. Voltage was measured across the active area in a similar manner using the opposite contact pads.

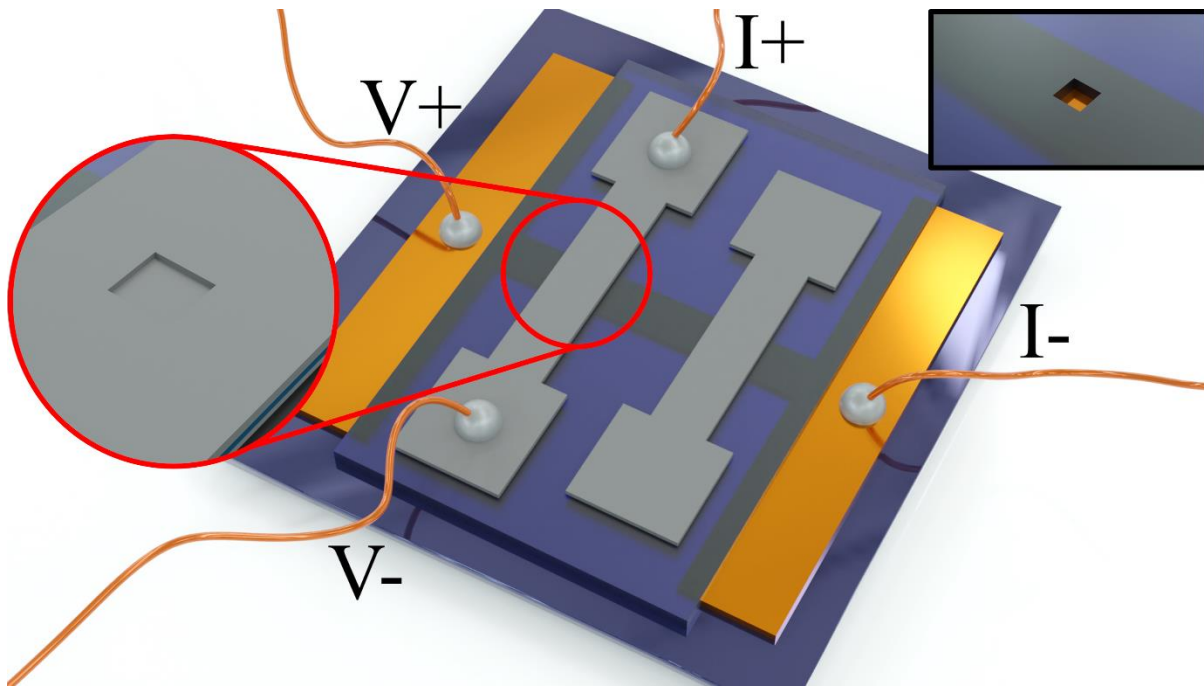


**Figure 3.13:** Schematic showing the electrical contacts on a device in the caisson geometry. The inset in the top right shows the caisson prior to the magnetic tunnel junction deposition and the gold bottom contact can be seen underneath. The MTJ fills the caisson, as shown by the zoom of the cross-contact area.

Temperature-dependent resistance measurements were performed by applying a set current and sweeping the temperature from 300 K to ~4 K (or vice versa). The current was reversed – to the negative of the set value – at certain intervals to check any potential offset in the measurement. The average of these positive and negative data sets was used as the final result. The temperature was set to stabilise at a range of temperature values, which would prevent the build-up of thermal lag between the copper hearth (from which the temperature was measured) and the sample itself.

The current-voltage characteristics of samples was measured using a LabView script. For a set temperature, the current range was chosen as desired (e.g.  $\pm 10 \mu\text{A}$ ) along with the number of steps which would define the current increments. The measurement would then begin at the lowest current value, measuring the voltage a number of times, and moving up in increments to the maximum current value (e.g.  $-10 \mu\text{A}$  to  $+10 \mu\text{A}$  in 20 step sizes of  $1 \mu\text{A}$ ).

## 3.6 Magnetic Measurements

Magnetic measurements of samples were performed using two different systems: a QuantumDesign Physical Property Measurement System (PPMS) and a QuantumDesign Magnetic Property Measurement System (MPMS).

### 3.6.1 Physical Property Measurement System

The Physical Property Measurement System could be used to measure a range of electrical and magnetic properties. For the measurements in this thesis, we focussed on using the resistivity option in applied magnetic fields. This setup had a set voltage limit of 95 mV and was optimised for samples between  $4 \mu\Omega$  to  $4 \text{ M}\Omega$ . The use of the Electrical Transport Option (ETO) setup was explored, which allowed for samples with resistances of up to  $5 \text{ G}\Omega$  to be measured, however this option applied an alternating current (AC) and so was incompatible with testing of magnetic tunnel junctions. An external magnetic field of  $\pm 9 \text{ T}$  could be applied and the temperature could be controlled between 2-400 K.

Samples were mounted onto a puck, as shown in **Figure 3.14**, wired up in a configuration similar to that shown in **Figure 3.13** above for the cryostat measurements using copper wire and silver paint. Here two devices on a single chip were connected and measured independently.

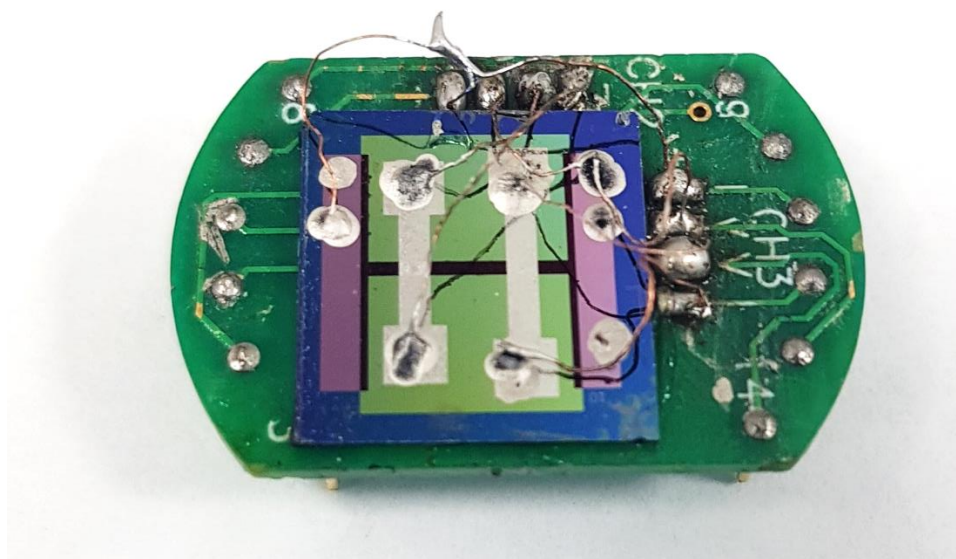


**Figure 3.14:** A 10x10 mm<sup>2</sup> chip with two MTJ patterned devices is mounted on top of a PPMS mounting puck using GE varnish. Silver paint is used to connect copper wires to the device surface at one end, while the other end of the wires is soldered to the puck. There are electrical connectors on the bottom side of the puck which slot into the PPMS.

The PPMS was used to obtain all magnetoresistance measurements in this thesis. A typical magnetoresistance measurement involved cooling the sample down to a chosen temperature and applying a constant current to the device while measuring the voltage across it. An external magnetic field was applied, sweeping between a chosen field range. For hysteretic materials/structures, the direction of the magnetic field sweep is important as it may have an effect on the resistance value. Note that in the case of MTJs, what is stated here as resistance is simply a calculated  $V/I$ ; though the tunnelling current and non-linear IV characteristics of the devices means this is not strictly the case.

Full field magnetoresistance sweeps were obtained by sweeping the field from +8 T to -8 T and then back to +8 T. The coercive fields of the RENs span a wide range of values, GdN for instance has a coercive field on the order of 0.1 mT while the coercive field of SmN is above this 8 T limit at 2 K. In multilayer structures – here MTJs with a soft and a hard ferromagnetic layer – it is valuable to probe the appropriate applied field values in order to assess the behaviour of each individual layer. In this regard, partial field magnetoresistance sweeps were performed, where the

field was swept from +8 T down to a value near the coercive field of the soft ferromagnetic layer and then reversed back to +8 T.

### 3.6.2 Magnetic Property Measurement System

The Magnetic Property Measurement System measured the magnetic moment of samples using a superconducting quantum interference device (SQUID). It operated between ambient temperature and  $\sim 2$  K, with fields of up to  $\pm 7$  T. Samples for this system needed to be roughly  $5 \times 10 \text{ mm}^2$  to be inserted into a plastic straw which was then loaded into the system. The exact area or weight of the sample were noted to facilitate calculation of the magnetic moment per ion after measurements.

Typical measurements in the MPMS included so-called zero-field cooling (ZFC) and field cooling (FC), along with magnetic hysteresis (MH) measurements at different temperatures. ZFC and FC measurements are temperature-dependent magnetisation measurements in zero- or constant applied field respectively, while MH measurements record the magnetic moment as a function of the applied magnetic field at a constant temperature. Careful selection of the applied field in FC measurements and the temperature in MH measurements allowed for subsequent calculations of several magnetic properties of the sample including Curie temperature, susceptibility, coercive field, and saturation magnetisation moment.

## Chapter 4

# Rare Earth Nitrides in Magnetic Tunnel Junctions

### 4.1 Introduction

It has been previously mentioned that there are many reasons to motivate research of novel types of non-volatile memory elements and solid-state devices. In this chapter, results from magnetic tunnel junctions (MTJs) with gadolinium nitride as the ferromagnetic electrodes will be presented and discussed. GdN is an intrinsically ferromagnetic semiconductor, which, in contrast to the conventional ferromagnetic metals commonly used in magnetic tunnel junctions, allows for much greater control over the magnetic and electronic properties via doping with nitrogen vacancies. As well as this, there is also the potential for 100% spin polarisation with the use of ferromagnetic semiconductors in magnetic tunnel junctions, leading to potentially infinite tunnelling magnetoresistance (TMR) values.

In this chapter we first report on the previous work of the VUW REN group regarding magnetic tunnel junction structures using RENs. This serves as a useful starting point in identifying the successes – as well as the shortcomings – of these structures and materials. Given this, we will explore the conduction paths in such devices using a mathematical model to probe how the layer conductivities and *caisson* geometry affect experimental measurements. We investigate the conduction path in single- and multi-layered structures using the *caisson* geometry and develop a model to determine specific minimum requirements to assume that electrical measurements meaningfully represent the sample active area. It is found that single layer thin films introduce much greater error in electrical measurements as compared to MTJ structures due to the much lower resistance of the single layer film. The inclusion of a tunnel barrier layer greatly reduces this error and allows for meaningful interpretation of the results.

Following this, we present the fabrication and characterisation of REN-based MTJs using the *caisson* geometry. The MTJs presented in this chapter consist of two ferromagnetic layers of GdN separated by tunnel barriers of either GaN or AlN. The top GdN layer is magnetically pinned by a subsequent Gd layer that acts as both a metallic top contact and a passivation layer. Electrical

and magnetic measurements are performed to characterise the devices at a range of temperatures and used to satisfy the Rowell criteria for tunnelling.

We show that our MTJs display a tunnelling magnetoresistance (TMR) of 135% for magnetic fields of  $\pm 8$  T at 5 K, with a low-field hysteretic behaviour consistent with the coercive field of the free GdN layer. By sweeping the field to this coercive field ( $\sim 0.04$  T) and then reversing the direction of the magnetic field sweep, this high-resistance state is able to be preserved at 0 T. The difference between the high- and low-resistance states of the MTJ at 0.04 T and 0 T respectively is  $\sim 0.53\%$ . This is the first known report of a REN-based MTJ retaining its resistive state at zero field and showcases the viability of these materials in future non-volatile memory devices at cryogenic temperatures.

The work in this chapter was presented as a poster at the 8<sup>th</sup> International Conference on Nanoscience and Nanotechnology (ICONN) 2020 and was awarded the Best Poster Award in Nanoelectronics.

## 4.2 Previous REN Group Work on Magnetic Tunnel Junctions

The REN group at VUW have been incorporating RENs into MTJs for several years [27,28], with a main focus on GdN-based devices due to the low coercive field and the extensive research on single layers of GdN [78,80,82,83,91,95]. SmN has also been investigated as a FM layer material [26–28,96]. Areas of interest have been in the growth and fabrication of these devices, as well as their electrical and magnetic characteristics [19,25,26]. It is noted that while extensive electrical measurements have been performed on these devices, the magnetic measurements have been somewhat limited to date, focussing on the broad, high-field behaviour whilst neglecting the finer low-field behaviour, especially around the coercive field of GdN. This low-field behaviour is important as it is exactly this switching of the GdN magnetisation that would provide the memory storage element of the REN-based MTJ. Initial structures were grown using a simple cross contact geometry; however, this was later refined through the use of photolithography to the *caisson* geometry [25,27,28].

### 4.2.1 GdN-based Magnetic Tunnel Junctions

A single thin layer film was typically used for probing the properties of a material. In this case, horizontal transport was used where a current was passed through the film layer. This compared to heterostructures which concerned vertical transport through a stack of thin layers. The main difference in these two measurements is shown in **Figure 4.1** and a consequence of this was the requirement of patterning for vertical transport.

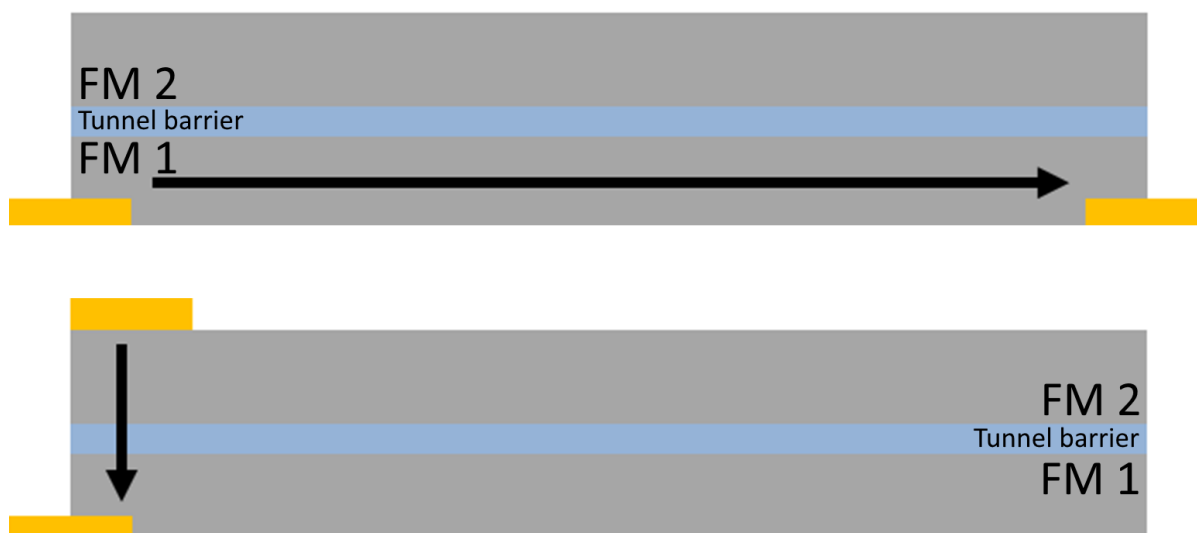


**Figure 4.1:** Horizontal transport (**top**) could be used to probe single layer (grey) films, but the current (black arrow) would not pass through the much more resistive tunnel barrier (light blue) when measuring an MTJ. Vertical transport (**bottom**) placed the current contacts (gold) on either side of the tunnel barrier, forcing the current to pass through the tunnel barrier layer.

The standard geometry for vertical transport measurements is a cross-contact geometry (as shown in **Figure 4.2**), often in conjunction with a four-point contact measurement which is used to minimise/mitigate resistance from the contact wires. Using this design, GdN/GaN/GdN tunnel junctions have been previously constructed. The measured resistance through the stack was considerably more than a single GdN layer in the same cross contact geometry, suggesting that the high resistance measured was due to the GaN tunnel barrier [25]. The devices made using this

geometry displayed promising tunnelling characteristics but did not exhibit the required hysteresis and retention – that is, no sharp switching events – at zero-field [28].

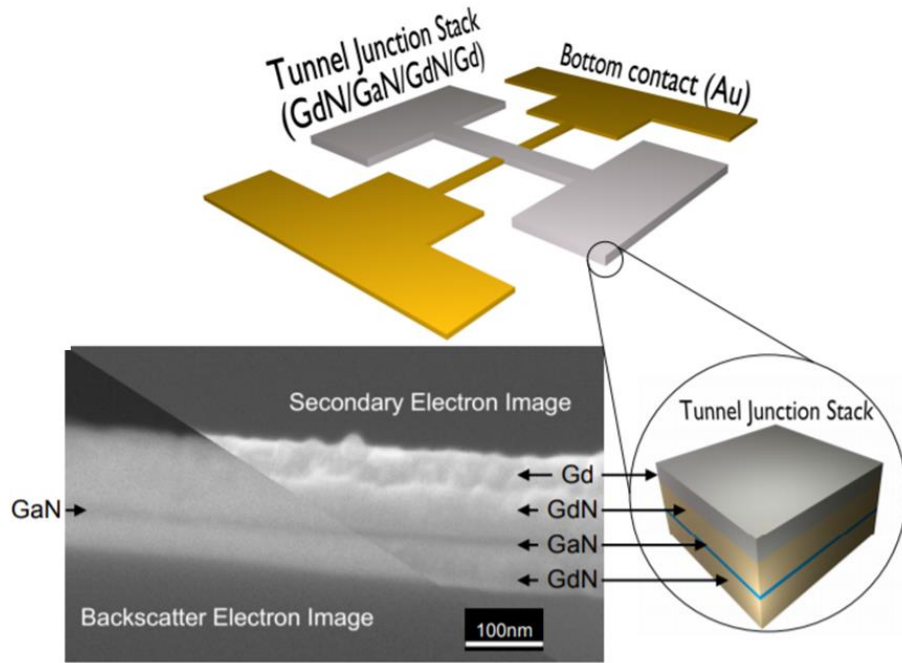


**Figure 4.2:** Schematic (**top**) of the cross-contact geometry used previously [25]. The bottom contact is made solely of gold and the tunnel junction consists of the MTJ and capping layer, highlighted in the zoom. Each layer can be seen in the SEM cross-section of the tunnel junction stack (**bottom**). Figure reproduced from reference [25].

Towards the goal of producing devices with sharper switching events, MTJs were also fabricated with GdN as one FM layer and SmN as the other. These materials were chosen mainly due to the vastly different coercive fields (GdN  $\sim 0.04$  T, SmN  $> 7$  T) meaning that the magnetisation direction in one layer – the GdN layer – could be switched using a magnetic field without significantly influencing the magnetisation of the other (SmN) layer. It was found that the magnetic response of such a MTJ showed a more complicated behaviour than would be expected from simply the switching of magnetisation directions in the FM layers, with a spin-twisted phase in the SmN layer potentially coupling to the Gd pinning layer [25,96]. This is further complicated due to the opposite – and almost equal – spin and orbital moments in SmN [86].



One practical concern with the cross-contact geometry was that the air-sensitive REN layers also quickly deteriorated due to oxidation, limiting the number of possible measurements on each device. To overcome this, the patterning geometry was refined via the introduction of a *caisson* layer [19,28]. This is an insulating layer (typically GaN or AlN) with a square hole in it of fixed area that defines the *caisson*. As well as defining device area, the insulating layer also provides protection to the sides of the active stack area from air oxidation. A three-step photolithography process was developed, as previously described in **Chapter 3**, which yielded a much higher throughput of the *caisson* geometry [26]. This design allows for the production of 20 devices per wafer, each with varying device active areas sizes, a huge improvement compared to the one device using the cross-contact geometry. The size of the devices was also significantly reduced through the use of the *caisson* geometry, down from  $200 \times 100 \mu\text{m}^2$  to a minimum size of  $10 \times 10 \mu\text{m}^2$ .

Using this new design, a number of GdN/GaN/SmN MTJs were fabricated. These devices showed some evidence of hysteresis, but were mainly probed using larger magnetic field increments [27]. Switching of the free GdN layer would likely occur below 0.1 T [84] – which is preferable for device application, as low-fields require less power to generate – so exploration of the low-field behaviour is essential.

In the section 4.2.1.1 below we show data of the GdN/I/GdN and GdN/I/SmN MTJs just introduced in this chapter. Here we briefly discuss examples of previously collected magnetic measurements and electrical transport of GdN-based MTJs.

#### 4.2.1.1 Magnetic Data

We begin with the magnetic response of a GdN/GaN/GdN/Gd structure. Device resistance was measured while placed in an external magnetic field. By sweeping continuously from a large, positive field to a large, negative field (or vice versa), the full magnetoresistive behaviour can be observed. As shown in **Figure 4.3**, the GdN-based MTJs exhibit a strong magnetic response, where the resistance decreases with increasing magnetic field strength [25]. At high magnetic fields, the two FM layers have their magnetisation aligned, resulting in a low resistance state. At a low

magnetic field – around the coercive field of the soft FM layer – the magnetisation of one FM layer will switch. The device is now in an anti-aligned state which results in a measured high resistance.

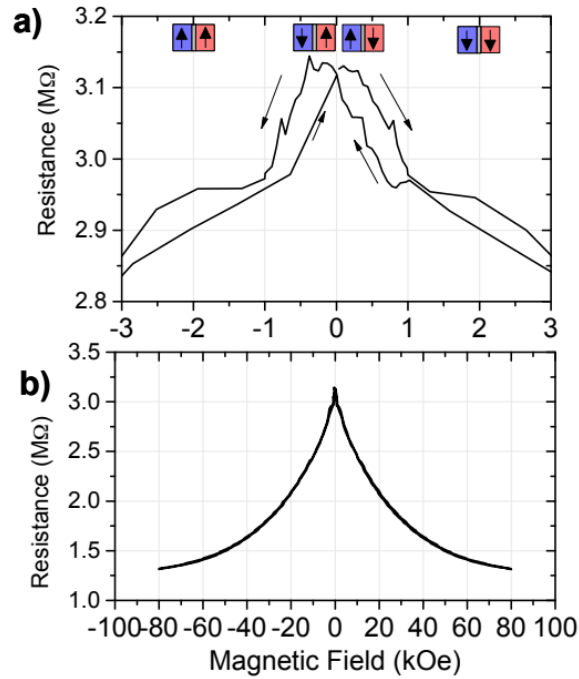


**Figure 4.3:** Magnetoresistance measurements of a GdN/GaN/GdN/Gd magnetic tunnel junction between (a)  $\pm 3$  T and (b)  $\pm 8$  T. Hysteresis is observed at low-field – highlighted in (a) – and the assumed relative alignment of the two ferromagnetic layers is shown above the plot. Figure reproduced from reference [25].

Temperature-dependent magnetoresistance measurements are shown in **Figure 4.4** for a GdN/GaN/SmN device [26]. Here we see that the resistance decreases with increasing magnetic field as before, however, the extent of the change in resistance is different for different temperatures. The maximum TMR occurs at 50 K and is almost 400% for a magnetic field of 8 T. No hysteresis was observed in this particular device at any temperatures, however other GdN/GaN/SmN MTJs have displayed small hysteresis at low fields. No demonstration of retention was observed at any fields.

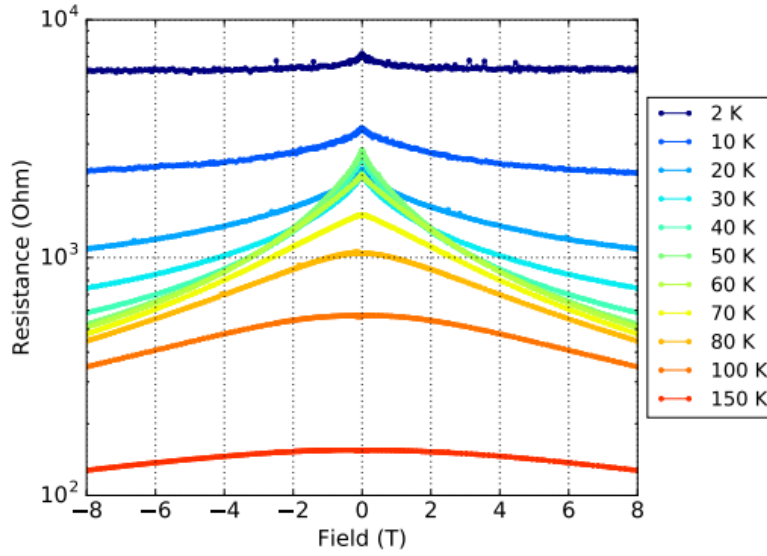


**Figure 4.4:** Magnetoresistance measurements of a GdN/GaN/SmN magnetic tunnel junction between  $\pm 8$  T at varying temperatures. The highest resistance values occur at 2 K, while the greatest magnetoresistance occurs around 50 K near the ferromagnetic transition temperatures of the ferromagnetic layers. A constant current of  $1 \mu\text{A}$  was used in all sweeps. Figure reproduced from reference [26].

#### 4.2.1.2 Electrical Data

We now turn to the electrical transport of these devices. **Figure 4.5** shows how there is a non-linear relationship between current and voltage, deviating from Ohm's Law. The non-linearity becomes more pronounced at higher voltages, and this is highlighted in the log-scale plot (**Figure 4.5 right**), especially at voltages above 100 mV. The low temperature 4 K curve was able to be fit using the Simmons model and yielded a barrier width of 2.45 nm, within 0.5 nm of the intended thickness. Details of the Simmons model will be discussed later in this chapter.

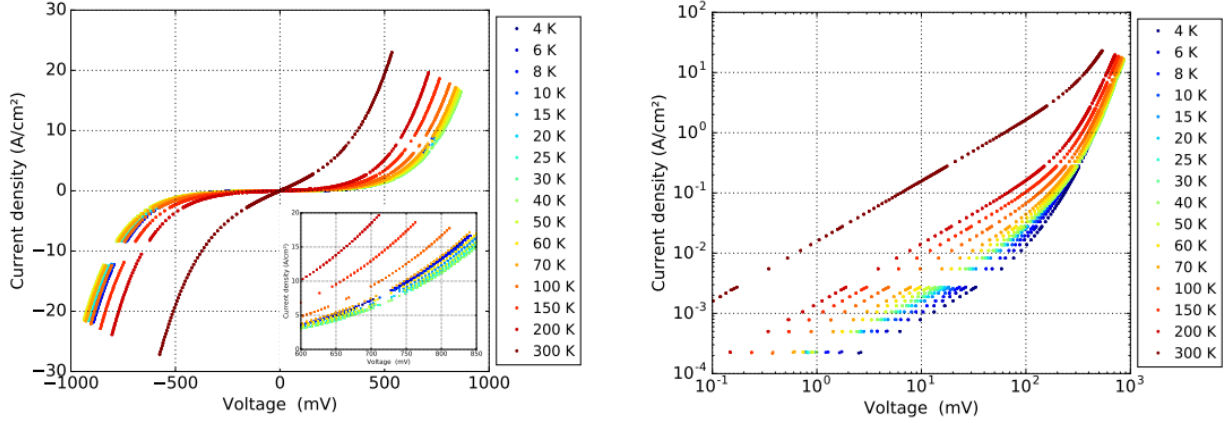


**Figure 4.5:** JV measurements of a GdN/GaN/SmN magnetic tunnel junction at varying temperatures up to 1000 mV plotted on a linear (**left**) and log (**right**) scale. The inset on the linear plot show a magnification of the positive high voltage data. Figure reproduced from reference [26].

These devices used two different RENs as the ferromagnetic MTJ layers, compared to the early devices consisting of two GdN layers, showing that there is promise in exploring the many combinations of RENs in MTJs. It is noted that significant progress has been made previously towards device manufacturing; the next step is demonstrating a device that exhibits memory retention at zero-field with read/write capabilities. In this regard, we first present data in this chapter for a MTJ with two GdN FM electrodes. MTJs with different REN FM layers are explored later in this thesis, in **Chapter 6**.

In the remainder of this chapter, we will explore the theory of tunnel barriers and conduction paths in the *caisson* geometry by considering a simplified model. Next, results on GdN/I/GdN MTJs are presented with a focus on the low-field magnetisation data, where I = GaN or AlN. We probe the magnetic response of each layer individually and show data for the switching of one layer, with the MTJ in the anti-aligned configuration. Retention of this state is demonstrated at zero-field, with a resistance difference of 0.53% between the high- and low-resistance state. This is the first demonstration of a REN-based MTJ exhibiting memory retention at zero field.

### 4.3 Tunnel Barrier Theory

First, we will discuss some characteristics of tunnel barriers. Rowell describes three principles for tunnelling behaviour, so-called “Rowell criteria”, to determine whether the conduction mode is dominated by tunnelling or otherwise [97,98]. Note that here I use terms of resistance, simply the inverse of conductance. The first criterion is that the conduction should depend on the thickness of the barrier, with an exponential dependence in accordance with

$$R(t) \propto e^{\frac{t_{\text{barrier}}}{t_0}} \quad (4.1)$$

where  $R(t)$  is the barrier resistance as a function of the barrier thickness,  $t_{\text{barrier}}$  is the barrier thickness, and  $t_0$  is the Wentzel–Kramers–Brillouin decay length (order  $\sim 1$  Å) [99,100]. Second, there should be a parabolic (or at least non-linear) relationship between the voltage and the current which can be described using a tunnelling model such as Brinkman–Dynes–Rowell (BDR) or Simmons [97,101]. This non-linearity is the most common ‘proof’ used in literature for demonstration of tunnelling behaviour [23,98,102,103]. The final criterion is that the resistance should have a negative temperature coefficient, whereby the resistance increases as temperature decreases.

It should be stated that structures which do not have tunnelling conductance have still been shown to fulfil these criteria [98,102,104,105]. In Nb/AlO<sub>x</sub>/Fe devices (with an alumina barrier), Jönsson-Åkerman *et al.* intentionally introduced pinholes into the barrier and found that the current-voltage relation could still be reasonably fit using the Simmons formula regardless of pinholes or not [102]. **Figure 4.6** from Åkerman *et al.* [105] shows how both shorted and non-shortened tunnel junction devices display non-linear IV characteristics, although it is worth noting that the shorted tunnel barriers displayed lower resistance values compared to the functioning tunnel barriers. Similarly, the conductance was found to vary exponentially with barrier thickness for devices with pinholes. Only the third criterion, the temperature dependence of the devices, was found to differ between barriers with and without pinholes, as the resistance for devices with pinholes was found to decrease with temperature.

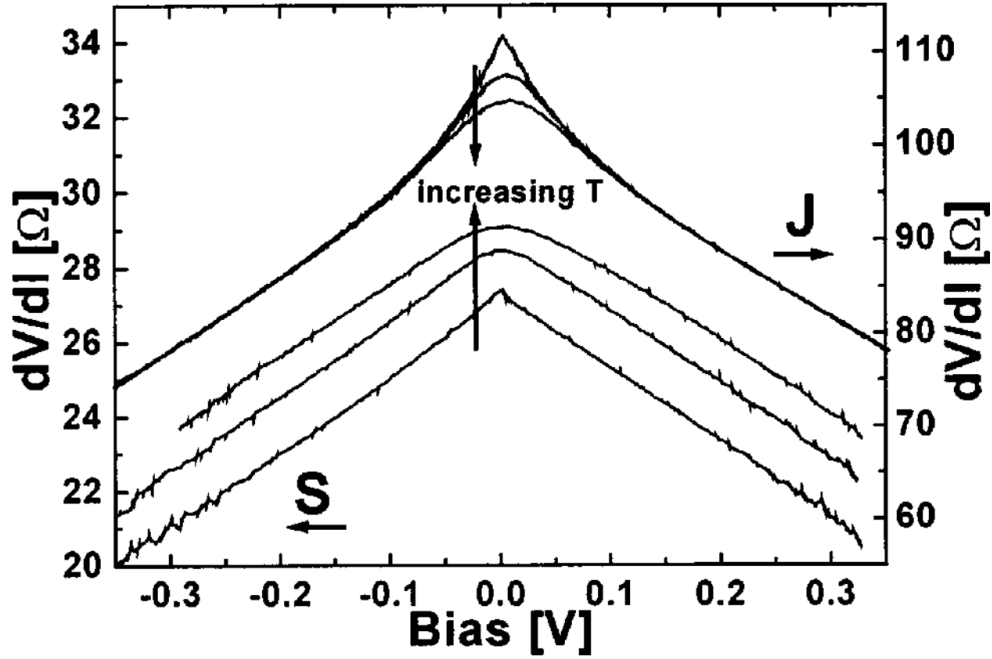


**Figure 4.6:** Electrical measurements of  $\text{AlO}_x$  tunnel barrier devices from Åkerman *et al.* that shows intentionally shorted (S) tunnel junctions display similar non-linear IV characteristics to standard junction (J) systems. Figure reproduced from reference [105].

However, Oliver *et al.* later showed that all three criteria can still be satisfied for a device with intentionally created pinholes in the tunnel barrier [98]. Specifically in contrast to Jönsson-Åkerman *et al.*, their alumina barrier devices demonstrated a negative temperature coefficient of resistance after pinholes were created via device breakdown [98,102]. It wasn't until successive breakdowns (i.e., the creation of excessive pinholes) that the device exhibited a positive temperature coefficient of resistance. They go on to suggest that a demonstration of device breakdown is sufficient to demonstrate the presence of a tunnel barrier but note that this is a destructive test and not always reasonable to perform.

Pinholes in REN-based MTJs have been previously suggested [25,26]. It was noted that while pinholes are a valid concern in any multi-layered thin film structure, the fabrication process used to produce REN-based MTJs yields devices largely free of pinholes. For example, some  $\text{GdN}/\text{GaN}/\text{SmN}$  structured-devices of different active areas – as defined by the *caisson* geometry

– had different measured voltages measured for the same applied current density [26]. This could be a result of regions of higher conductivity – so-called hotspots – around the tunnel barrier, where the layer thickness is slightly thinner than the surrounding areas. Pinholes would be the extreme case, where the hotspot area is very small and concentrated on a discontinuity in the tunnel barrier itself where the electrode materials are in contact with each other. This was the case for a very few number of samples, so was worth considering on a batch-by-batch basis, rather than for every individual device. The vast majority of samples showed characteristics that suggested no pinholes were present in the tunnel barrier: the high voltage region was dominated by non-linearity so, if anything, it would be the low voltage region that would show the pinhole contributions, but this typically displayed behaviour consistent with the high voltage region. The absolute resistance was also very large and was found to increase with increasing barrier thickness [25]. Indeed, devices with thinner barriers were more often found to display pinhole characteristics, as the thinner barriers were more affected by inhomogeneities across the layer and more likely to be discontinuous at some point.

The inclusion of a tunnel barrier greatly increases any magnetoresistive effects already present in the MTJ layer materials. This is known as tunnel magnetoresistance (TMR) and was first reported by Jullière in 1975 [106]. He found that the relative orientation of the ferromagnetic electrodes in a tri-layer of iron and cobalt separated by an insulating germanium layer (i.e.. Fe/Ge/Co) affected the tunnelling conductance of the tunnel junction. Magnetoresistance is the observed change in resistance with an applied magnetic field and has the general formula:

$$TMR = \frac{(R_{AP} - R_P)}{R_{AP}} \quad (4.2)$$

where  $R_{AP}$  is the resistance when the FM electrodes are in the anti-parallel (AP) configuration, and  $R_P$  is when the FM electrodes are in the parallel (P) configuration. Due to the effects of band splitting in the ferromagnets, TMR values are often much greater than MR, and can be influenced by the spin polarisation of the ferromagnet. In fact, spin polarisations of 100% can theoretically lead to infinite TMR, according to **Equation 4.3** [106]:

$$TMR = \frac{2P_1P_2}{1 - P_1P_2} \quad (4.3)$$

where  $P_1$  and  $P_2$  refer to the spin polarisations of the two ferromagnetic layers in the MTJ.

While we have been discussing the characteristics of ferromagnet-insulator-ferromagnet (FM/I/FM) MTJs, it is worth noting that much of the theory and understanding of tunnel barriers is based on metal-insulator-metal structures, whereas here we are dealing with semiconductor-insulator-semiconductor structures. The current theories serve as a useful starting point to explain the observed phenomena, though this distinction should be kept in mind going forward.

## 4.4 Voltage Drop

### 4.4.1 Background

The cross-contact geometry is a standard across literature for fabrication of MTJs and provides a simple way to test material properties [16,25,107]. However, the air-sensitivity of the RENs prompted the development of the *caisson* geometry that has been described previously in **Chapter 3**. In this section we investigate the conduction paths in each layer and develop a model to determine how accurately experimental measurements using the *caisson* geometry reflect the electrical behaviour of the MTJ. We then use this model to investigate the effect that various parameters – such as conductivity, temperature etc. – have on the measurement.

In the previous measurements of electron transport through thin layers between high-conductivity electrodes performed by our group, some of them showed clear evidence of influence from the contact resistances; for example, in the crossed-contact geometry there has been some evidence of the temperature dependence of the top Gd contact. Here the current was fed along a top Gd strip of 200  $\mu\text{m}$  width, then vertically down through the MTJ, – a more resistive stack consisting of two GdN layers separated by an AlN tunnel barrier, on the order of 10's of nm thickness – and finally out along an Au strip of 100  $\mu\text{m}$  width. The potential difference was



measured across the ends of the crossed strips opposite to the ends used for current injection and drain. The electrical contacts used in a similar manner for the *caisson* geometry are shown in **Figure 4.7**.

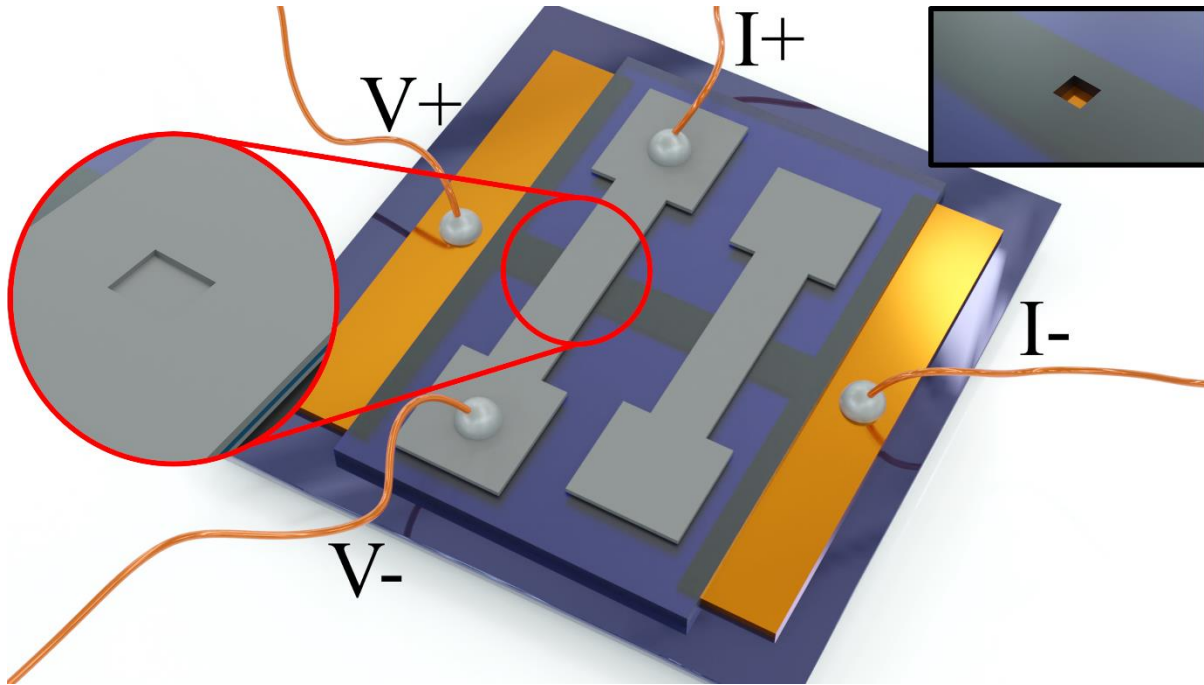


**Figure 4.7:** Schematic showing the electrical contacts on a device in the *caisson* geometry. The inset in the top right shows the *caisson* prior to the magnetic tunnel junction deposition and the gold bottom contact can be seen underneath. The MTJ filled the *caisson*, as shown by the zoom of the cross-contact area.

In the situation where the top and bottom contact materials have infinite conductivity, they will define equipotential surfaces. This means that the measured voltage is exactly the same as that which is applied across the entire active area, giving reliable IV data. However, if the contact materials have a non-negligible resistance, the potential difference is then reduced at the voltage-measurement ends of the contacts, as is the current down through the MTJ. This results in an apparent resistance through the REN stack which is somewhat reduced in comparison with the actual resistance. For meaningful insight into the device characteristics, it is imperative that the measured current and voltage – and subsequently calculated resistance – are not significantly dissimilar to the actual values, a problem we discuss in this section.

#### 4.4.2 Physical and Geometrical Parameters of the Structure

As previously mentioned in **Chapter 3**, the *caisson* geometry consists of three photolithography steps. The bottom layer is the conductive bottom contact and consists of gold grown onto the Si/SiO<sub>2</sub> wafer in a dumbbell shape. The second layer is an area-restrictive layer, with a small square hole in the centre which allowed us to control the amount of gold surface exposed, and subsequently the active area of the device. This second layer is insulating GaN, with a square area (the *caisson*) of varying dimensions from 10x10  $\mu\text{m}^2$  to 200x100  $\mu\text{m}^2$  where there is no GaN present, exposing the gold underneath. This means that when the third layer – the REN MTJ stack – is grown on top of this, it fills in the *caisson* and makes contact with the gold, forming the active area of the device. The REN stack itself consists of three layers (FM/I/FM) and is grown in a dumbbell pattern perpendicular to the gold dumbbell, reminiscent of the original cross-contact geometry. The fourth and final growth layer is the capping layer, another conductive metal such as aluminium. This is grown in the same dumbbell shape as the REN layer and is always done concurrently as the REN stack growth.

When making electrical measurements on any device fabricated using the *caisson* geometry, electrical contact is made in the same manner as for the standard cross-contact geometry: by placing a current contact on each of the dumbbells (one on the aluminium dumbbell and one on the gold dumbbell as shown above in **Figure 4.7**). In this case, the only current path is through the *caisson*, that is, through the active area of the device. However, here we encounter a potential issue. Current is introduced at one end of the dumbbell and the potential is measured at the other end of the dumbbell. As the current flows across the *caisson*, it will be decreased by the amount of current flowing down through the *caisson* (through the device active area) which will subsequently decrease the measured potential difference between the top metal layer and the bottom gold layer. A measured value that is significantly different from the true value is not meaningful and doesn't provide any insight into the actual properties of the material.

#### 4.4.3 Modelling a Simple Case: Gold/REN layer/Aluminium

To model this problem, we will begin by consider a simple cross-contact geometry. As shown in **Figure 4.8 (left)**, our simple structure has a bottom gold layer, with a REN layer and an

aluminium layer placed perpendicular on top. Note that in this simple model, the REN layer is treated as one layer, though this would be the layer relating to the MTJ stack. **Figure 4.8 (right)** defines the active area in the x-direction as  $0 < x < L$ .

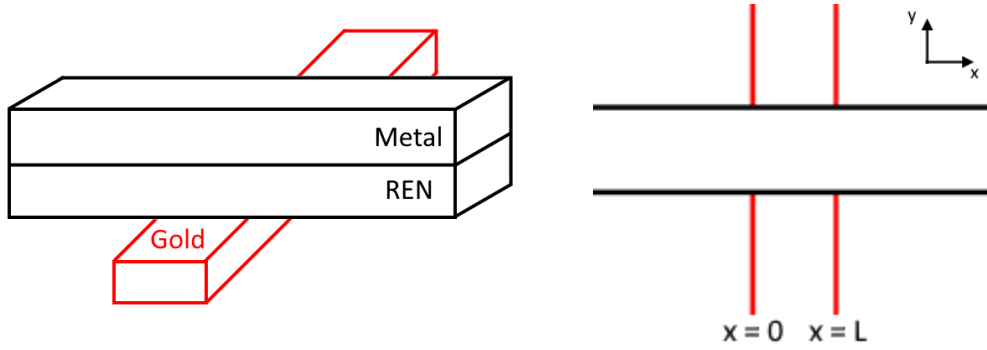


**Figure 4.8:** Top view with the metal/REN layer (black) positioned along the x-direction and the gold (red) layer positioned along the y-direction (**right**), and side 3D view of the same structure (**left**).

The concern is that the potential between the metal and gold layers might not be uniform across the square region – in **Figure 4.8 (right)** this area is defined by  $0 < x < L$  – where all layers overlap and current would be flowing down through the barrier layer. If this concern is valid, we need to know how accurately the measured potential represents the actual potential across the REN layer. We want to be sure that the current versus voltage characteristics measured in the device are solely due to the REN layer. Furthermore, we want to understand how the current and voltage drop horizontally across the square region of width  $L$  where the top and bottom contacts overlap. A simplified schematic of the current source and drain points is shown in **Figure 4.9**.

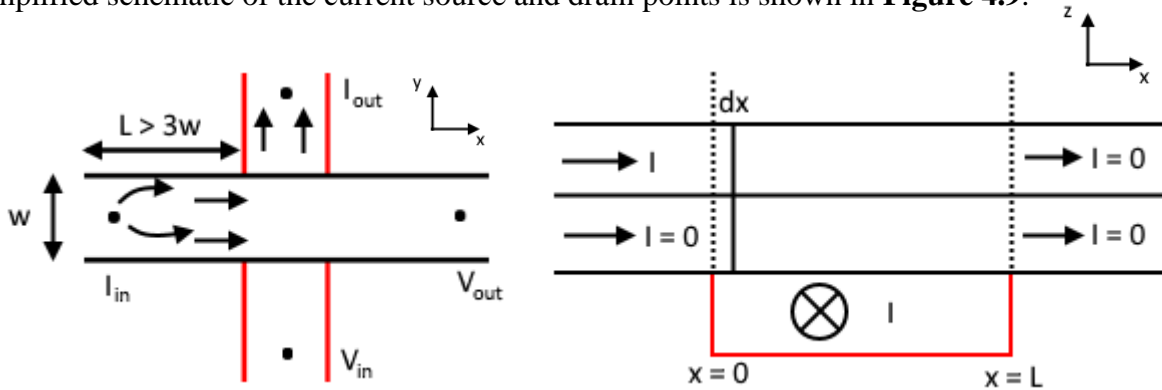


**Figure 4.9:** Top view showing injection and endpoint of current, along with points for measuring the voltage (**left**) and side view depicting current direction and magnitude in each layer (**right**).

Ideally, the top and bottom metal layers would each have an infinite conductivity and result in the REN layer as the only source of resistance in the structure. While this could be achieved by implementing superconducting contact layers, gold and aluminium are used in this model for consistency with experiment and so we approximate infinite conductivity in our simple model as follows.

First, we consider the conductivity of gold as infinite ( $\sigma_{Au} = \infty$ ) so that it can be treated as an equipotential ( $V_{Au} = 0$ ), allowing us to investigate the effects of the top contact and REN layer only. The thicknesses of the layers are given by  $t_{Al}$ ,  $t_{REN}$ , and  $t_{Au}$  for the aluminium, REN, and gold layers respectively. Similarly, conductivities for each layer are given by  $\sigma_{Al}$ ,  $\sigma_{REN}$ , and  $\sigma_{Au}$ .

A second assumption is that the conductivity of the aluminium is much, much greater than the conductivity of the REN such that  $\sigma_{Al} \gg \sigma_{REN}$ . Current  $I_{in}$  is introduced at some point in the aluminium layer (this introduction point is discussed later) and flows horizontally until reaching the edge of the cross-contact area (that is,  $x = 0$ ). The amount of current flowing in the aluminium layer is related to the conductivity of the aluminium and the REN layers. The conductivity of a layer is given by  $\sigma = I/lVA$  (where  $I$  is current,  $l$  is length,  $V$  is voltage, and  $A$  is area. Each layer is subject to the same potential difference and has the same length, so the amount of current flowing through the aluminium layer and REN layer is only dependent on their conductivity and area. In this model, we assume that both layers also have the same thickness – and therefore the same area – so that the current  $I_{in}$  flowing horizontally is only dependent on the conductivity ratio of the two layers.

The conductivity of each layer will vary with temperature, and in different ways too; the conductivity of the metallic aluminium will increase as temperature decreases, while the conductivity of semiconducting REN will decrease. This is actually beneficial for us, as it will mean that even more of the current will be flowing in the top aluminium layer – relative to the REN layer – as temperature decreases. Typical conductivity values for each layer are  $\sigma_{Al} \sim 10^5 \text{ S cm}^{-1}$  and  $\sigma_{REN} \sim 10^2 \text{ S cm}^{-1}$  [17,108], giving a ratio of  $\sigma_{Al}/\sigma_{REN} \sim 1000$ , so we can assume that  $\sim 99.9\%$  of the current will be flowing through the top metal layer in the region  $x < 0$ , as in **Figure 4.9 (right)**. Past this point (that is, in the region  $0 < x < L$ ) the current will begin flowing down through the REN layer to the gold layer.

Our third assumption is that the current density is uniform at the point  $x < 0$ . Following the rule of thumb, for this assumption to be true to within 1%, we introduce current at some point on the aluminium layer that is more than three times the strip width,  $w$ , away from the edge of the gold strip ( $x = 0$ ). We want to know how the current lost down through the REN layer varies with distance along  $x$ , and so we look at a very thin slab of thickness  $dx$  and width  $w$ . Current density is not uniform for  $0 < x < L$ , but across the slab  $dx$  it will be. Here we can use the equations  $J = \sigma E$  and  $E = -\nabla V$ .

#### 4.4.4 Current and Potential Drop in the Region $0 < x < L$

##### 4.4.4.1 Potential in Top Layer

Let us first consider the potential in the top contact. We want to find how the potential driving the current in the  $x$ -direction in the metal layer varies with  $x$ , across the slab  $dx$ . The potential  $V$  will depend on  $x$  (and only  $x$ , as  $\sigma_{Al} \gg \sigma_{REN}$ ), and for the thin slab this varies as  $dV(x)/dx$ . Using  $J = \sigma E$  and  $E = -\nabla V$ , we get:

$$\frac{dV(x)}{dx} = -\frac{J_x(x)}{\sigma_{Al}} \quad (4.4)$$

Where  $J_x(x)$  is the current density in the top metal layer in the  $x$ -direction and can be expressed in terms of the current ( $I$ ) and the area that the current is flowing through ( $A$ ). The area is given by the product of the layer width ( $w$ ) and the metal layer thickness ( $t_m$ )

$$J_x(x) = \frac{I_x(x)}{A} = \frac{I_x(x)}{wt_{Al}} \quad (4.5)$$

So, substituting **Equation 4.5** into **Equation 4.4** gives:

$$\frac{dV(x)}{dx} = -\frac{I_x(x)}{\sigma_{Al}wt_{Al}} \quad (4.6)$$

This gives an expression for the change in potential in the top metal layer in terms of the current in the top metal layer, allowing us to relate the current at any point  $x$  in the metal layer to the potential at the same point.

#### 4.4.4.2 Current Through REN Layer

We now consider the current through the REN layer. We want to find how the current in the  $x$ -direction in the metal layer decreases across slab  $dx$ , due to current flowing down through the REN layer. The electric field driving the current down through the REN layer will be given by the potential difference across this layer (with  $E_z$  as the electric field in the REN layer):

$$E_z = \frac{V(x) - V_{Au}}{t_{REN}} = \frac{V(x)}{t_{REN}} \quad (4.7)$$

$V(x) - V_{Au} = V(x)$  as we set  $V_{Au} = 0$ . The current density flowing down through the REN layer (given as  $j_z(x)$ ) across slab  $dx$  will depend only on  $x$ , and will be equal to the REN conductivity multiplied by the electric field in the  $z$ -direction:

$$j_z(x) = \sigma_{REN} E_z = \sigma_{REN} \frac{V(x)}{t_{REN}} \quad (4.8)$$

The amount that current,  $I(x)$ , flowing in the top layer is reduced over distance  $dx$  is given by  $-dI(x)$  and is equal to the amount of current flowing down through the REN layer. Here the area is given by the width multiplied by  $dx$ :

$$-dI(x) = j_z(x) w dx \quad (4.9)$$

We substitute in our expression for  $j_z(x)$  and rearrange to yield the following **Equation 4.10**, where we now have the change in current in the top metal layer in terms of the potential in the top metal layer:

$$\frac{dI(x)}{dx} = -\frac{\sigma_{REN} V(x) w}{t_{REN}} \quad (4.10)$$

#### 4.4.4.3 An Expression for Potential

We now have two equations (**Equation 4.6** and **Equation 4.10**) that link the potential and current in the top metal layer, which can be solved as a set of differential equations. This is done in terms of  $V(x)$ , starting by rearranging **Equation 4.6**:

$$I(x) = -\sigma_{Al} w t_{Al} \frac{dV(x)}{dx} \quad (4.11)$$

$$\frac{dI(x)}{dx} = -\sigma_{Al} w t_{Al} \frac{d^2 V(x)}{dx^2} \quad (4.12)$$

Setting this equal to **Equation 4.10**:

$$-\frac{\sigma_{REN}V(x)w}{t_{REN}} = -\sigma_{Al}wt_{Al}\frac{d^2V(x)}{dx^2} \quad (4.13)$$

$$\frac{d^2V(x)}{dx^2} - \frac{\sigma_{REN}}{\sigma_{Al}t_{Al}t_{REN}}V(x) = 0 \quad (4.14)$$

A solution of this differential equation is given by:

$$V(x) = V_0e^{-\lambda x} \quad (4.15)$$

$$\frac{dV(x)}{dx} = -\lambda V_0e^{-\lambda x} \quad (4.16)$$

$$\frac{d^2V(x)}{dx^2} = \lambda^2 V_0e^{-\lambda x} \quad (4.17)$$

So:

$$\lambda^2 V_0e^{-\lambda x} = \frac{\sigma_{REN}}{\sigma_{Al}t_{Al}t_{REN}}V_0e^{-\lambda x} \quad (4.18)$$



$$\lambda^2 = \frac{\sigma_{REN}}{\sigma_{Al} t_{Al} t_{REN}} \quad (4.19)$$

$$\lambda = \sqrt{\frac{\sigma_{REN}}{\sigma_{Al} t_{Al} t_{REN}}} \quad (4.20)$$

So, substituting this into **Equation 4.15**:

$$V(x) = V_0 e^{-\sqrt{\frac{\sigma_{REN}}{\sigma_{Al} t_{Al} t_{REN}}} x} \quad (4.21)$$

#### 4.4.4.4 An Expression for Current

We can obtain a similar solution in terms of the current, starting by setting **Equation 4.6** equal to **Equation 4.16**:

$$\frac{dV(x)}{dx} = -\lambda V_0 e^{-\lambda x} = -\frac{I(x)}{\sigma_{Al} w t_{Al}} \quad (4.22)$$

$$I(x) = \lambda \sigma_{Al} w t_{Al} V_0 e^{-\lambda x} \quad (4.23)$$

And now using the expression for  $\lambda$  from **Equation 4.20**:

$$I(x) = \sqrt{\frac{\sigma_{Al}\sigma_{REN}t_{Al}}{t_{REN}}} w V_0 e^{-\sqrt{\frac{\sigma_{REN}}{\sigma_{Al}t_{Al}t_{REN}}}x} \quad (4.24)$$

#### 4.4.4.5 Analysis using Realistic Parameters

Using **Equation 4.21** and some rough values for the thicknesses and conductivities of the aluminium and REN layers, we can see how the potential measured using the cross-contact geometry as described compares with the real potential across the device area. From the *caisson* photolithography process, twenty devices are produced, with realistic device widths ranging from 10  $\mu\text{m}$  to 100  $\mu\text{m}$  from one growth. Looking ahead, shrinkage of the device size is a future goal of the project, eventually down to widths of 1  $\mu\text{m}$  or even 0.1  $\mu\text{m}$ .

In **Figure 4.10**, we see how changing the thickness of each layer (but keeping each layer of equal thickness) affects the measured voltage. In practice, the thicknesses of each layer cannot be changed by much more than an order of magnitude and so, while this greatly increases the measured voltage for any given device width, even the smallest device width of 10  $\mu\text{m}$  and layer thicknesses of 100 nm only results in a 4.2% reading of the applied voltage. For larger devices widths – and, typically, those that are fabricated more consistently – the measured voltage is many many orders of magnitude smaller than what is applied, likely below the sensitivity range of the voltmeter being used in the experiment.

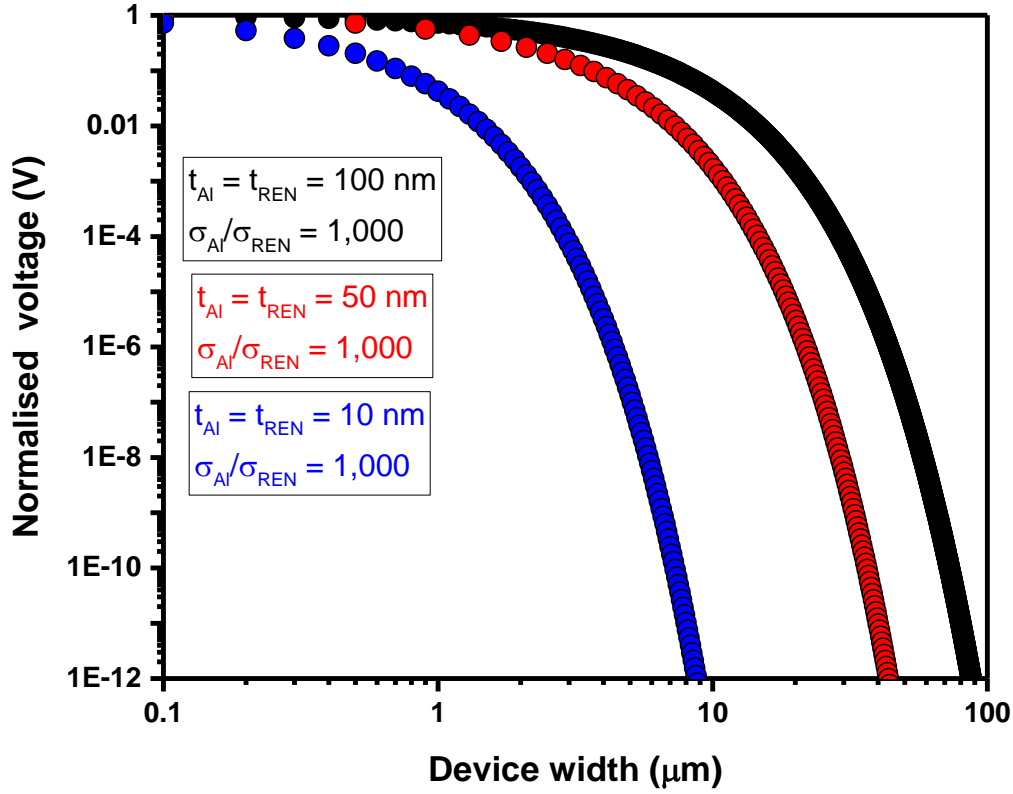


**Figure 4.10:** The measured potential difference (V) compared with the normalised applied voltage for devices of different thicknesses. The Al:REN conductivity ratio was taken to be 1,000 in all cases (using  $\sigma_{\text{Al}} \sim 10^5 \text{ S cm}^{-1}$  and  $\sigma_{\text{REN}} \sim 10^2 \text{ S cm}^{-1}$ ) and the thickness of each layer was varied for 10 nm (**blue**), 50 nm (**red**), and 100 nm (**black**).

We are limited experimentally by the layer thickness to only one, or maybe two, orders of magnitude. However, the conductivity of the REN layer can be tuned over six orders of magnitude [18] by controlling various growth parameters. This will have a much greater effect on the measured voltage than can be achieved by varying the thickness, as highlighted in **Figure 4.11**. In this plot, layer thickness is kept constant at 100 nm for each layer, but the conductivity ratio is varied between 1,000 and 100,000. Note that the y-axis scale is different to that in **Figure 4.10**, and that the blue curve in **Figure 4.11** is the same as the black curve in **Figure 4.10**.

It can be seen from **Figure 4.11** that decreasing the REN conductivity results in an increase of the measured voltage. With a  $\sigma_{\text{Al}}/\sigma_{\text{REN}}$  ratio of 100,000 – requiring a  $\sigma_{\text{REN}}$  of  $\sim 10^0 \text{ S cm}^{-1}$  [91]

– devices with a width of 100  $\mu\text{m}$  now yield a measured voltage of 4.2% of the applied voltage, although this is still much too low to provide any useful insight into the vertical transport of the REN layer. By combining this high  $\sigma_{\text{Al}}/\sigma_{\text{REN}}$  ratio of 100,000 and small device width of 10  $\mu\text{m}$ , we can achieve a measured voltage that represents 72.9% of the applied voltage.

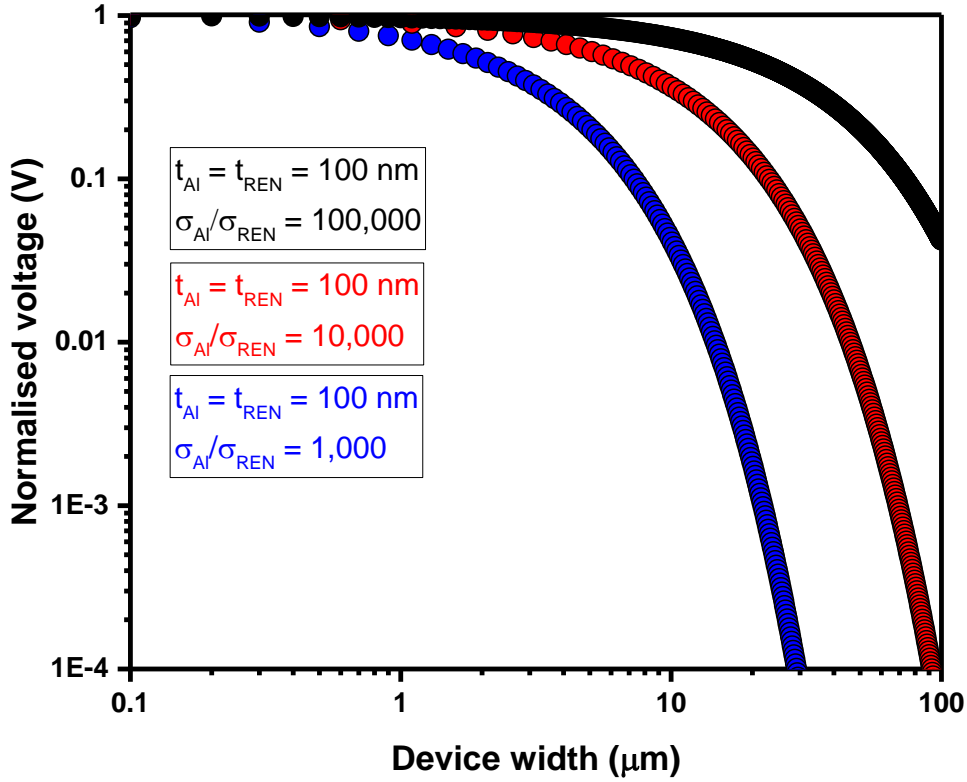


**Figure 4.11:** The measured potential difference (V) compared with the normalised applied voltage for devices of different sizes. The thickness of each layer was set to 100 nm and the Al:REN conductivity ratio was varied between 1,000 (**blue**), 10,000 (**red**), and 100,000 (**black**).

All devices with a width of less than 30  $\mu\text{m}$  and a  $\sigma_{\text{Al}}/\sigma_{\text{REN}}$  ratio of 100,000 result in a measured voltage that is greater than 90% of the applied voltage. This is approaching a value that gives a meaningful insight into the vertical transport of the REN layer and can potentially be pushed further by exploiting the temperature dependent behaviour of these materials.

#### 4.4.5 Temperature Effects

The conductivity values stated previously are for  $\sim 300$  K, whereas these devices will be operational at much lower temperatures of  $\sim 2$  K. This decrease in temperature will result in an increase in the conductivity of the aluminium, due to a reduction in phonon vibrations, while the conductivity of the REN will decrease due to a reduction in carrier motion. This effect will be about 10x for aluminium and about 100x for REN [95,108], so overall the ratio will change by about 1000x.

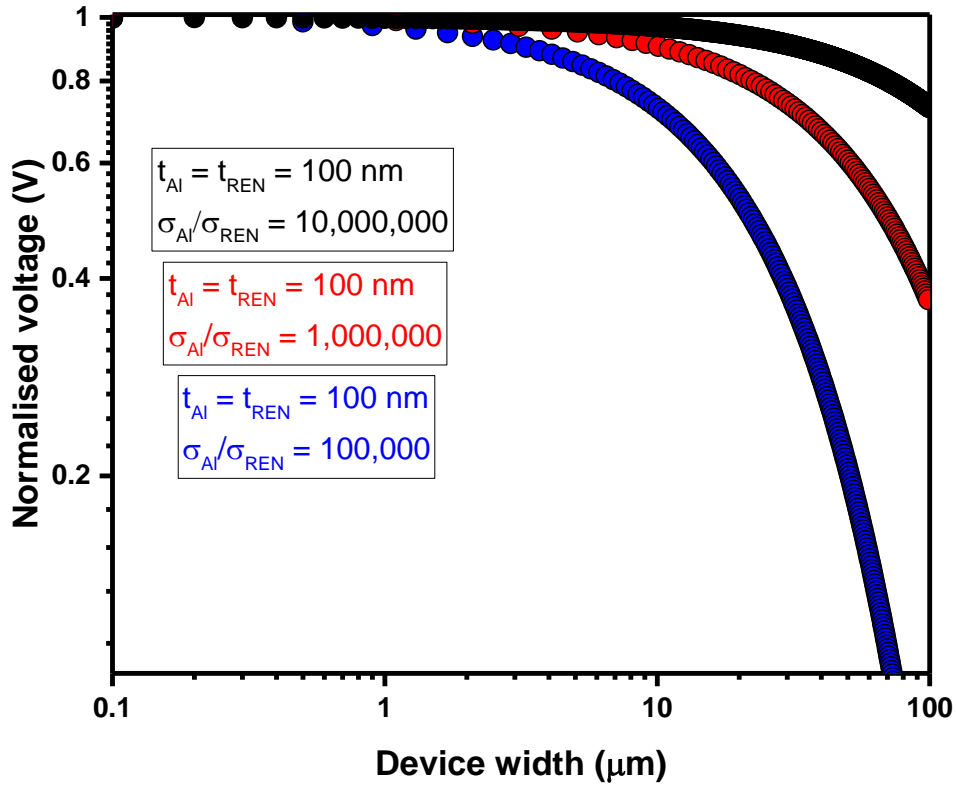


**Figure 4.12:** The measured potential difference (V) compared with the normalised applied voltage for devices of different sizes. The thickness of each layer was set to 100 nm and the Al:REN conductivity ratio was varied for 100,000 (blue), 1,000,000 (red), and 10,000,000 (black) to simulate an ambient temperature of  $\sim 2$  K.

The black curve in **Figure 4.12** is the most extreme case plotted, where both layers have a thickness of 100 nm and a  $\sigma_{\text{Al}}/\sigma_{\text{REN}}$  ratio of 10,000,000, still easily achievable with a  $\sigma_{\text{Al}}$  of  $\sim 10^6$  S

$\text{cm}^{-1}$  and a  $\sigma_{\text{REN}}$  of  $\sim 10^{-1} \text{ S cm}^{-1}$  at  $\sim 2 \text{ K}$ . It shows that the largest device width of  $100 \mu\text{m}$  will yield a measured voltage of 72.9% of the actual voltage, and a value of 96.9% for a device width of  $10 \mu\text{m}$ .

Replacing the aluminium layer with a metal that is superconducting at this low temperature would make the  $\sigma_{\text{Al}}/\sigma_{\text{REN}}$  ratio become infinite, eliminating the voltage drop issue in this simple model, with a value of 100% regardless of device size. This could be something to work towards with materials such as Nb or NbN.

#### 4.4.6 Resistance of the Device Active Area

In the simplest case, this is a problem of two resistors. From **Figure 4.13** we can see there is a resistance from current travelling horizontally through the top aluminium layer and a resistance from current travelling vertically down through the REN layer. The current travels through much more of the top metal aluminium layer than it does through the REN layer; the current must pass through some length of aluminium with a given area which will provide a resistance and then also travel down through the more resistive REN layer, through the device area with a much smaller length.

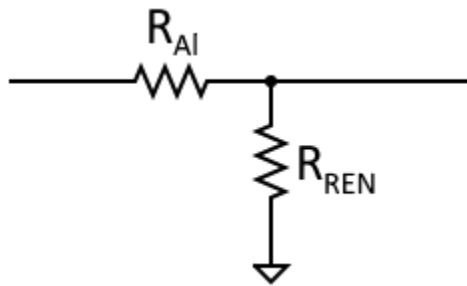


**Figure 4.13:** Resistor diagram of the aluminium layer and REN layer.

Ideally, we want all the measured potential to be across the resistance in the REN layer. For this, we need the situation that  $R_{\text{Al}} \ll R_{\text{REN}}$  where  $R_{\text{Al}}$  and  $R_{\text{REN}}$  are the resistances of the

aluminium and REN layer respectively. Resistance is given by  $R = l/\sigma A$  and so – in the region  $0 < x < L$  – for each layer we get:

$$R_{Al} = \frac{L}{L\sigma_{Al}t_{Al}} = \frac{1}{\sigma_{Al}t_{Al}} \quad (4.28)$$

$$R_{REN} = \frac{t_{REN}}{L^2\sigma_{REN}} \quad (4.29)$$

To satisfy  $R_{Al} \ll R_{REN}$ , we get:

$$\frac{1}{\sigma_{Al}t_{Al}} \ll \frac{t_{REN}}{L^2\sigma_{REN}} \quad (4.30)$$

Which can be rearranged to:

$$\frac{\sigma_{REN}}{\sigma_{Al}t_{Al}t_{REN}}L^2 \ll 1 \quad (4.31)$$

This gives the term in the square root for **Equation 4.21** – alternatively, given as  $\lambda^2$  – for the case  $x = L$ . To satisfy **Equation 4.28**, we can see that this term must be much much less than 1 and, similarly for **Equation 4.21**, making this term as small as possible results in an exponential with a decay in measured voltage that is much less steep with respect to device width.

Considering some values for a physical device – including the aluminium layer before  $x = 0$  – we can consider the ratio of resistances for each layer. A  $R_{Al}:R_{REN}$  of 0.01 would mean that 99% of the resistance measured is due to the REN layer, for example, and so using some real geometric values for this specific structure, we can get a rough idea for the resistance ratio due to each layer's contribution. The resistance ratio for aluminium to REN is therefore given by **Equation 4.29**, so using  $l_{Al} = 10^{-2}$  m,  $l_{REN} = 10^{-7}$  m,  $A_{Al} = 10^{-10}$  m<sup>2</sup>, and  $A_{REN} = 10^{-8}$  m<sup>2</sup>, to get a resistance ratio of  $R_{Al}:R_{REN}$  of 0.01, we require that  $\sigma_{REN} = 10^{-1}$  S cm<sup>-1</sup> (with  $\sigma_{Al} = 10^6$  S cm<sup>-1</sup>, as at low temperature). This is a reasonable and realistic value for typical REN layers and provides an achievable upper limit in REN conductivity for valid measurements:

$$\frac{R_{Al}}{R_{REN}} = \frac{\sigma_{REN} l_{Al} A_{REN}}{\sigma_{Al} l_{REN} A_{Al}} \quad (4.32)$$

#### 4.4.7 Closing Thoughts

This model provides a simplified view and insight into the current paths involved in the caisson geometry. The main assumptions used in this model are that the top contact does not introduce any resistance into the circuit and that current density is uniform across the strip. The model also assumes that all layer surfaces are smooth and so does not account for any variations in the thickness of the layers which would result in the current density being much greater at the thinnest parts of the REN layer, especially with a tunnel barrier present due to the exponential dependence of resistance on layer thickness. For a more accurate description of the current pathways in such a geometry, a number of improvements could be made to this model, namely through mathematical consideration of some of these listed assumptions.

Still, from the simple model analysis performed in this section, there is the possibility of a large discrepancy between the potential being measured using the *caisson* (and/or cross-contact) geometry. This is dependent on a number of factors, including device width, layer thickness, and Al:REN conductivity ratio, highlighted in **Equation 4.28**. The easiest and most effective way to experimentally deal with this problem (other than using superconducting contacts) is to increase the Al:REN conductivity ratio by growing a REN layer that is more resistive. It was shown that



ratios of over  $10^7$  could be achieved, especially at low temperatures, reducing the voltage drop to less than 23% for all devices less than 100  $\mu\text{m}$  in width. Other options include reducing device width or increasing layer thickness, but these have added experimental challenges such as photolithography resolution limits.

Another way to realise this high conductivity ratio is by using a MTJ stack instead of a single REN layer. The implementation of a tunnel barrier greatly increases the resistance of the REN layer (technically now a REN *stack*) by several orders of magnitude, diminishing the effects of the voltage drop described above. Therefore, the *caisson* geometry is unsuitable for measuring a single REN thin film reliably – such as when testing for Ohmic or Schottky contacts – but has application when measuring MTJ structures.

## 4.5 GdN/I/GdN/Gd Devices

We now move to experimental results of MTJ structures incorporating GdN as the FM electrodes. GdN-based MTJs have been grown using the *caisson* geometry to investigate their low-field and switching behaviour. Two structures are presented in this chapter, with the only difference being the barrier material. The two structures of devices were GdN/GaN/GdN/Gd, where two GdN ferromagnetic layers were separated with a GaN barrier, and GdN/AlN/GdN/Gd, where two GdN layers were separated with an AlN barrier. In both cases, the top GdN layer was capped with ferromagnetic Gd which was in contact – and therefore exchanged coupled – with the top GdN layer. This helped to pin the magnetisation of the top FM layer, making it magnetically harder relative to the bottom FM layer.

### 4.5.1 Fabrication, growth, and Experimental Methods

Magnetic tunnel junctions consisting of GdN electrodes separated by a thin GaN or AlN tunnel barrier were grown using molecular beam epitaxy (MBE) at room temperature in a vacuum system with base pressure  $1 \times 10^{-8}$  mbar. To grow the GdN layers, gadolinium metal was evaporated at a rate of  $\sim 0.3 \text{ \AA/s}$  using an electron gun under a nitrogen partial pressure of  $1 \times 10^{-4}$  mbar. The GaN barrier layer was grown in a similar manner, additionally using a Kaufman ion source to

activate the nitrogen (in a partial pressure of  $2.4 \times 10^{-4}$  mbar) as gallium does not catalytically break the  $N_2$  triple bond as the rare earth metals do. The AlN barrier was also grown using activated nitrogen, and the aluminium was evaporated from an effusion cell.

Devices were grown using the *caisson* geometry as described previously, with 20 potential devices produced per wafer, as shown in **Figure 4.14**. Briefly, 50 nm gold bottom contacts and a 40 nm thick GaN area restriction layer were patterned in two separate steps beforehand with photoresist addition and lift-off processes. The MTJ was then formed as a REN stack in one final growth: 80 nm GdN/3 nm GaN/80 nm GdN (sample name **A626**) and 20 nm GdN/2 nm AlN/20 nm GdN (sample name **A774**) followed by a 100 or 40 nm Gd cap respectively. The Gd capping layer helped to prevent oxidation of the REN layers and pinned the magnetisation of the top GdN FM layer, as well as acting as a conductive top contact for the device. A schematic of the two MTJ structures is shown in **Figure 4.15**.

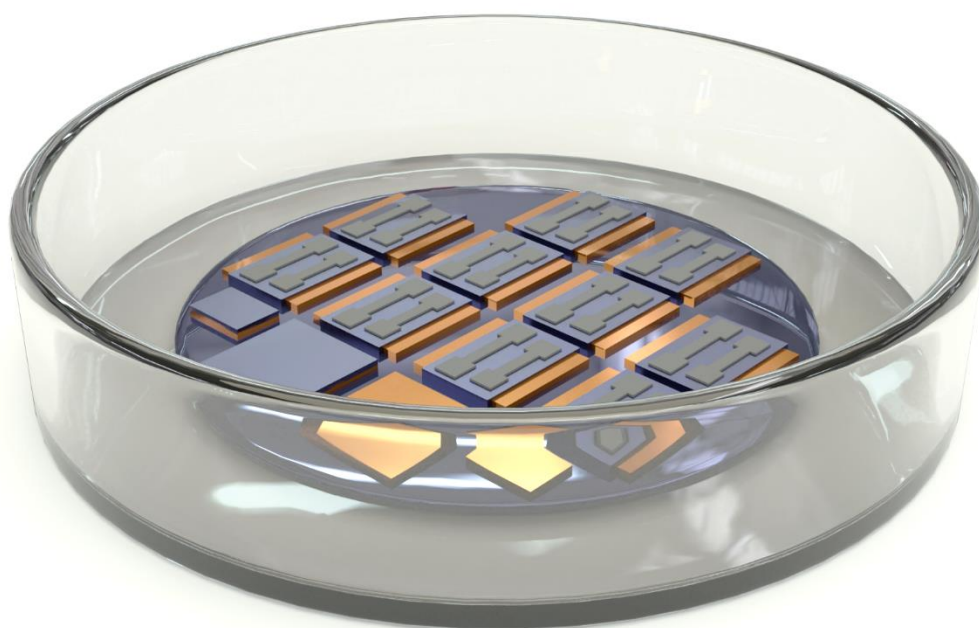


**Figure 4.14:** Render of a 2" Si/SiO<sub>2</sub> wafer with a fully patterned set of 20 devices. The REN MTJ stack can be seen as **grey** dumbbells, on top of **blue** GaN *caissons*, on top of **gold** bottom contacts. Render thicknesses are not to scale.

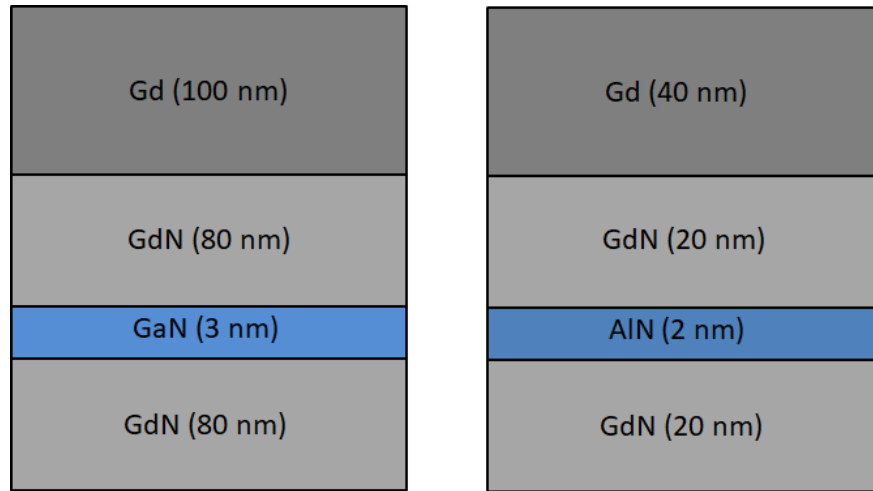


**Figure 4.15:** Schematic of the GdN/GaN/GdN (**left**) and GdN/AlN/GdN (**right**) MTJ structures described in this chapter. Layer thicknesses are given as expected from the growth conditions. Schematic is not to scale.

A cross-section scanning electron microscope (SEM) image showing the GdN/AlN/GdN/Gd device is displayed in **Figure 4.16**. The SEM image shows the GdN layers to be about 30 nm thick, in close agreement with the growth parameters. This sample was an unpatterned film from the same growth as a patterned MTJ and so the MTJ can be seen on top of the GaN *caisson*, whereas in an actual device, the active area of the MTJ would be within a small gap of this *caisson* layer. While the barrier layer was visible in the SEM image, it was too thin for the SEM measurement software to accurately distinguish on this scale. Instead we can use the Simmons model to fit electrical data of the tunnel barrier and subsequently calculate a barrier height and width [101].

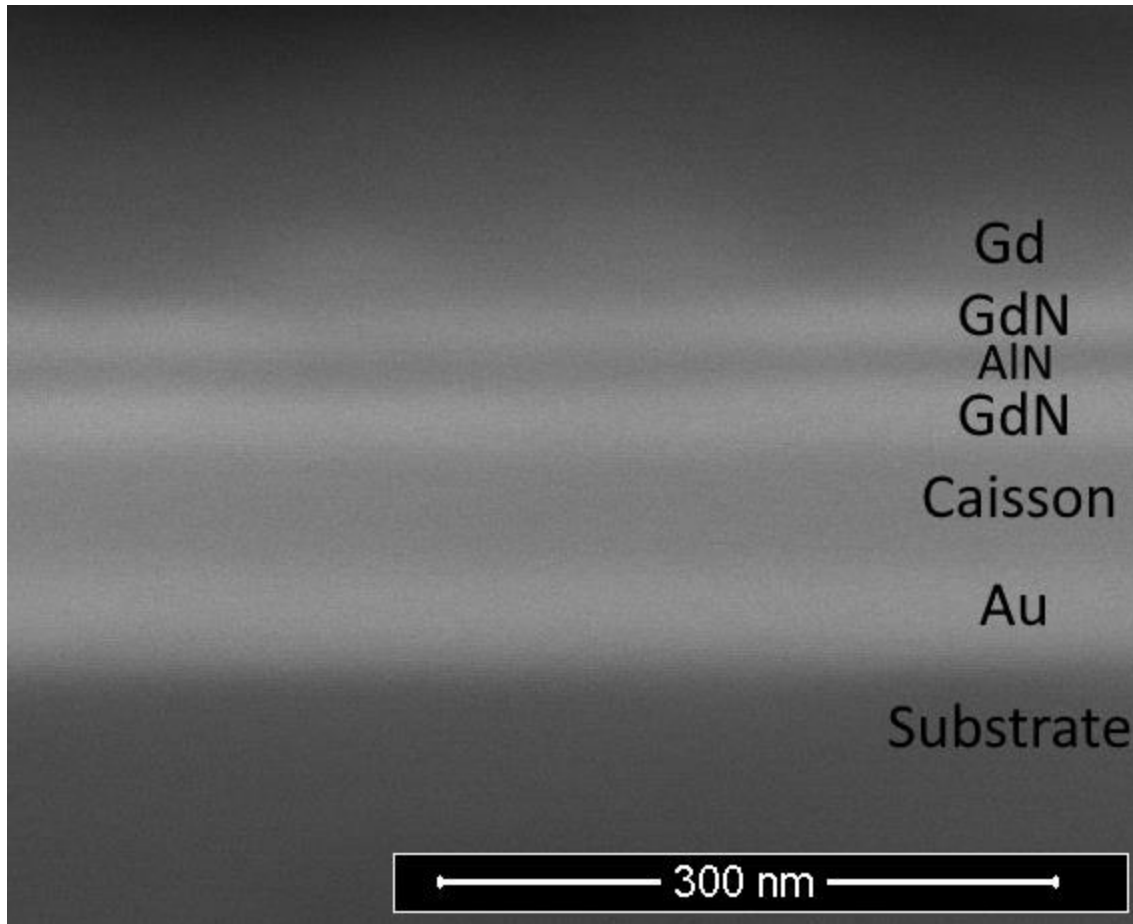


**Figure 4.16:** Cross-section SEM image of the GdN/AlN/GdN MTJ. The device is grown on Si/SiO<sub>2</sub> substrate and a layer of gold and GaN (*caisson*) can also be seen, as the bottom contact and *caisson* layers respectively.

X-ray diffraction was used to characterise the films grown on all substrates using a PANalytical X'Pert PRO x-ray diffractometer with Cu K-alpha source.

#### 4.5.2 Results

We now present results on the characterisation and measurement of GdN-based MTJs. We begin with the electrical transport of devices including current-voltage (IV) behaviour at a range of temperatures between ambient and 5 K. The non-linear, low temperature IV data was subsequently fitted using the Simmons model to determine the expected barrier width. Following this, the magnetic properties of the devices are discussed with an emphasis on the

magnetoresistance properties, especially at the lowest 5 K temperature range. Devices are shown to exhibit switching of single ferromagnetic layers, with a retention of the resistive state observed at zero-field.

#### 4.5.2.1 Electrical Transport

Electrical measurements of devices were performed in no external field using a Janis research closed cycle cryostat, and with an external magnetic field using a Quantum design Physical Property Measurement System. We will first consider here the electrical transport without a magnetic field. The *caisson* geometry means that all measurements of devices presented here are in the current perpendicular to plane (CPP) geometry.

All device structures demonstrated non-linear current-voltage behaviour at all temperatures, indicative of a tunnelling current, with the non-linearity generally becoming more pronounced at higher voltages and lower temperatures. These curves were fitted using the Simmons model to determine barrier height and barrier width. The devices also exhibited a negative temperature coefficient of resistance, meaning that the device resistance increased as temperature decreased. While an anomaly in the resistance around  $T_C$  for GdN was observed, reminiscent of the shape seen for single layer GdN thin films, the absolute resistance values are orders of magnitude greater for the MTJ than the single layer suggesting that the tunnel barrier is the dominant source of resistance in the MTJ structure. Devices of the same structure were not grown with varying barrier thickness, and so this particular criterion could not be confirmed.

The resistance of a GdN/AlN/GdN device as a function of the temperature is shown in **Figure 4.17**. Resistances for two different currents were plotted, and it is noted that for any given temperature, the resistance value was different for the two currents. This was due to the tunnelling current which has non-linear IV characteristics – and will be discussed in detail next – as a result of the AlN barrier layer. In general, the resistance increased as the temperature decreased, with an anomaly just below 50 K which corresponded to the Curie temperature of GdN.

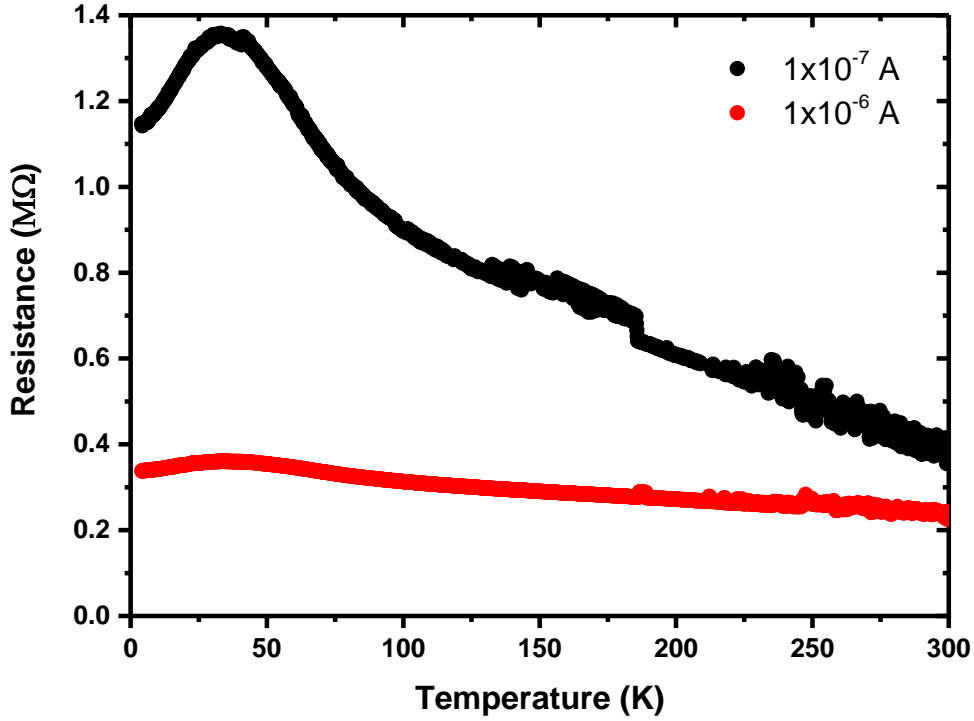


**Figure 4.17:** Temperature dependent resistance for a  $100 \times 100 \mu\text{m}^2$  GdN/AlN/GdN/Gd structured MTJ at  $0.1 \mu\text{A}$  (black) and  $1 \mu\text{A}$  (red). The resistance increases for both currents as the temperature decreases. A peak in the resistance can be seen just below 50 K, near the ferromagnetic transition of the GdN electrodes which is due to the band splitting of GdN around this temperature where the band edges are shifted.

The magnetic anomaly was relatively less pronounced at higher currents, where effects of band splitting become reduced relative to the effects of the applied voltage. This shows that, while the AlN tunnel barrier was the dominant source of resistance in the device, the density of states in the GdN FM layers also influenced the electrical behaviour.

Looking further at the current-voltage characteristics of these devices, we can see the non-linearity highlighted in **Figure 4.18** and **Figure 4.19**. Note that the scale on these plots uses current density ( $J$ ) rather than current ( $I$ ) where the current has been scaled by the assumed device active area of  $80 \times 80 \mu\text{m}^2$ . First, the GdN/AlN/GdN device was found to exhibit non-linearity at all temperatures measured. The non-linear regime typically begins above 0.1 V where it can be seen in **Figure 4.19** that the curves deviated from the unity gradient of the dashed line on a logarithmic

scale. The positive and negative voltage behaviour was largely symmetric, as would be expected for two similar electrode materials (GdN and GdN) as the density of states in relation to the AlN tunnel barrier would be similar.

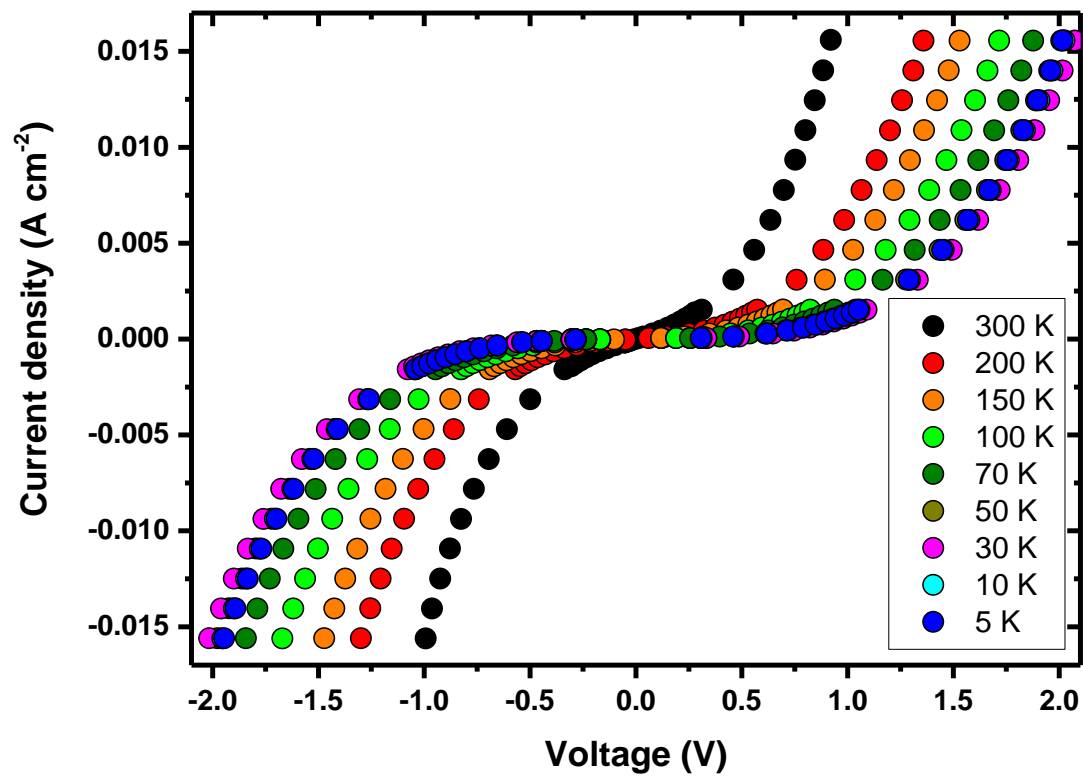
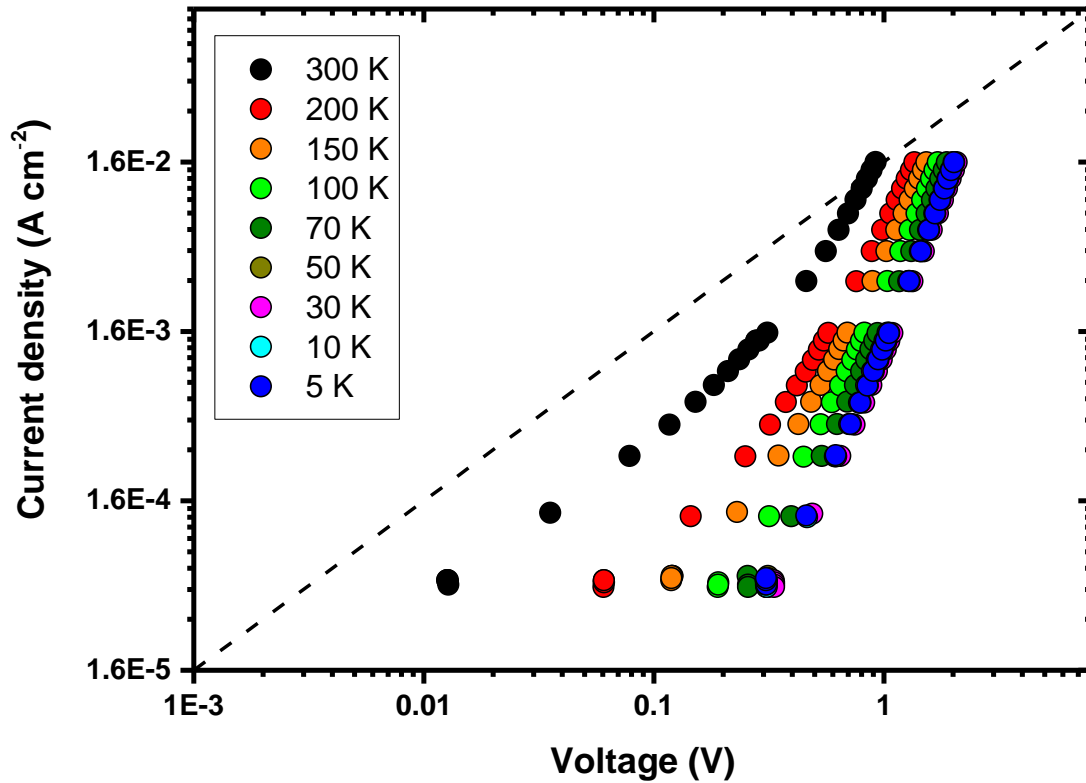


Figure 4.18: JV curves of an 80x80  $\mu\text{m}^2$  GdN/AlN/GdN MTJ device at varying temperatures.



**Figure 4.19:** JV curves of an  $80 \times 80 \mu\text{m}^2$  GdN/AlN/GdN MTJ device at varying temperatures. Data is the same as in Figure 18, now presented using a log-log scale to highlight the linear and non-linear regimes. The dashed line is added as a guide with a gradient following that of Ohm's Law.

As temperature was decreased, voltage generally increased for the same current density value. This reached a maximum for the 30 K curve, corresponding to the Curie temperature of GdN. As GdN transitioned into the ferromagnetic regime, band splitting occurred and resulted in an increase of resistance before further decreasing with temperature [109–111]. This behaviour is in agreement with that observed in the temperature-dependent resistance plot shown in **Figure 4.17**.

The data presented in this section go some way towards satisfying Rowell's three criteria for tunnelling. To further this, and determine some barrier parameters, we now use the Simmons model to fit the previously presented current-voltage data.



#### 4.5.2.2 Simmons Model

There are many models which exist that attempt to describe the current-voltage (IV) characteristics of tunnel barriers [97,101]. The Simmons model is one such model that is often utilised in literature due to its expression of terms in parameters that relate to measurable aspects of devices such as barrier height and current density etc. [19,23,26,101–104]. The model is a generalised formula based on the Wentzel-Kramers-Brillouin (WKB) approximation and can be used in several situations to account for asymmetric/symmetric barriers, images charges, and different voltage regimes [100].

Simmons provides equations for three voltage regimes. One for low voltage (where the voltage bias across the barrier is approximately zero), one for intermediate voltages (where  $V < \phi_0/e$ ), and one for high voltages (where  $V > \phi_0/e$ ). Here  $V$  is the applied voltage bias across the barrier,  $\phi_0$  is the potential height of the barrier (in eV), and  $e$  is the elementary charge ( $\sim 1.602 \times 10^{-19}$  C). Simmons often interchanges units for practicality, even within the same manuscript, and so attention must be given to the units for each term. In the low voltage regime ( $V \sim 0$ ), the current density,  $J$  (A cm<sup>-2</sup>), is defined by **Equation 4.33**:

$$J = 3.16 \times 10^{10} \bar{\phi}_0^{\frac{1}{2}} \left( \frac{V}{s} \right) \exp \left( -1.025 s \phi_0^{\frac{1}{2}} \right) \quad (4.33)$$

Where  $\phi_0$  is barrier height (eV) and  $s$  is barrier width (Å). When there is an applied voltage across the barrier, the shape of the barrier is distorted due to a change in the energy bands of the barrier and electrodes. This is accounted for in the two other regimes. For the intermediate voltage range where the applied voltage is less than the barrier height ( $V < \phi_0/e$ ), the current density:

$$J = \left( \frac{6.2 \times 10^{10}}{s^2} \right) \left\{ \left( \phi_0 - \frac{V}{2} \right) \exp \left[ -1.025 s \left( \phi_0 - \frac{V}{2} \right)^{\frac{1}{2}} \right] - \left( \phi_0 + \frac{V}{2} \right) \exp \left[ -1.025 s \left( \phi_0 + \frac{V}{2} \right)^{\frac{1}{2}} \right] \right\} \quad (4.34)$$

and for the high voltage range where  $V > \phi_0/e$ , we have:

$$J = 3.38 \times 10^{10} \left( \frac{F^2}{\phi_0} \right) \left\{ \exp \left( -\frac{0.689 \phi_0^{3/2}}{F} \right) - \left( 1 + \frac{2V}{\phi_0} \right) \exp \left[ -0.689 \frac{\phi_0^{3/2}}{F} \left( 1 + \frac{2V}{\phi_0} \right)^{\frac{1}{2}} \right] \right\} \quad (4.35)$$

where  $F$  is the Faraday constant ( $\sim 96485 \text{ C mol}^{-1}$ ). Data in this chapter was largely fitted using **Equation 4.34** where the applied voltage is less than the potential barrier height.

Note that the Simmons model assumes metallic electrodes on either side of the tunnel barrier and an operating temperature of 0 K. Here we are applying it to semiconducting electrodes at 5 K. The Simmons model represents a reasonable first step for extracting barrier parameters as it has been used previously for REN MTJs with extracted parameters being in good agreement with SEM-derived thicknesses and expected growth parameters. It serves as a characterisation method which allows for comparison between similar device structures fabricated both in this thesis and in literature. Expanding on this, one could envision a model designed for a tunnelling current between semiconducting electrodes which, for example, considers the non-zero bandgap of these electrodes which would affect the relative barrier height experienced by a tunnelling electron. This would make for an interesting project, however, was not the focus of this present study. When applying and interpreting subsequent extracted barrier parameters for devices with semiconducting electrodes, these points should be taken into consideration; the Simmons model is used in this thesis simply to give some idea of the barrier characteristics and allow for comparison with existing and future metallic electrodes from literature.

JV data from an  $80 \times 80 \text{ } \mu\text{m}^2$  GdN/AlN/GdN MTJ at 5 K is shown as a representative device to demonstrate the Simmons model fitting (see **Figure 4.20** below). All curve fitting was performed using a custom function on Origin software. The curve was fitted reasonably well ( $R^2 = 0.990$ ), with a larger deviation occurring at low voltages. The Simmons fit gave a barrier height of 3.38 eV and a barrier width of 1.54 nm. The Simmons barrier height of 3.38 eV was around half

that of the bandgap of AlN (6.0 eV at 300 K) [112]. The Simmons barrier width was slightly under the expected barrier thickness of 2 nm; however, this was unsurprising as the Simmons model often underreports barrier widths as there is an exponential dependence on barrier thickness and tunnelling through the barrier will be overly dominated by the thinnest parts of the barrier. Barrier parameters determined using the Simmons model are approximate values. The barrier was unlikely to be a perfectly uniform layer – in either width (thickness) or height (energy gap) – and so the values should be interpreted more as average values. This was especially true of polycrystalline layers, such as those grown in the devices presented in this chapter.

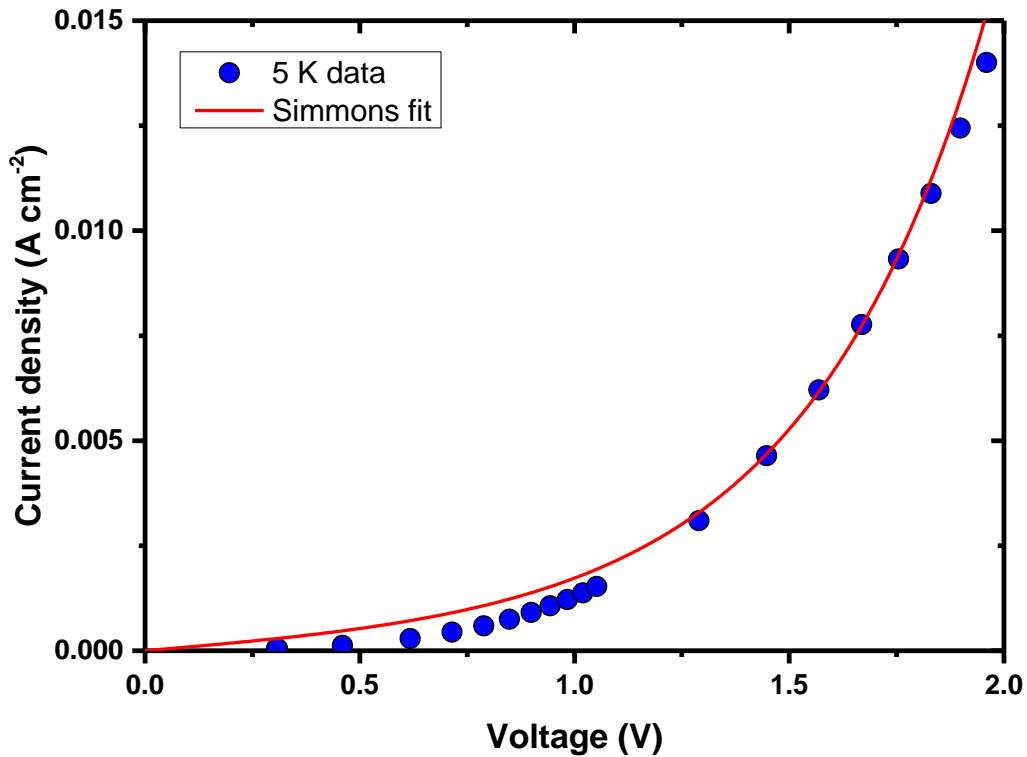


**Figure 4.20:** Positive voltage data for the JV characteristics of an 80x80  $\mu\text{m}^2$  GdN/AlN/GdN/Gd MTJ (blue dots) fitted with the Simmons model (red line).

A linear term was added to the fitting equation to account for the deviation at low-voltage bias. The difference between the Simmons fit with and without this linear term is shown in **Figure**

**4.21** for the same  $80 \times 80 \text{ } \mu\text{m}^2$  GdN/AlN/GdN/Gd device above. The addition of the linear term corrected for much of the fit deviation at low voltage and lowered the Simmons barrier width to 1.19 nm from 1.54 nm. This suggested that there is some contribution of an Ohmic current within the device, potentially pinholes in the barrier, as pinholes would further reduce the perceived average barrier thickness. However, this is maybe not so surprising as tunnelling systems are expected to be in the linear regime at low voltages. The Simmons barrier height was increased to 5.22 eV from 3.38 eV when fitting with the additional linear term.

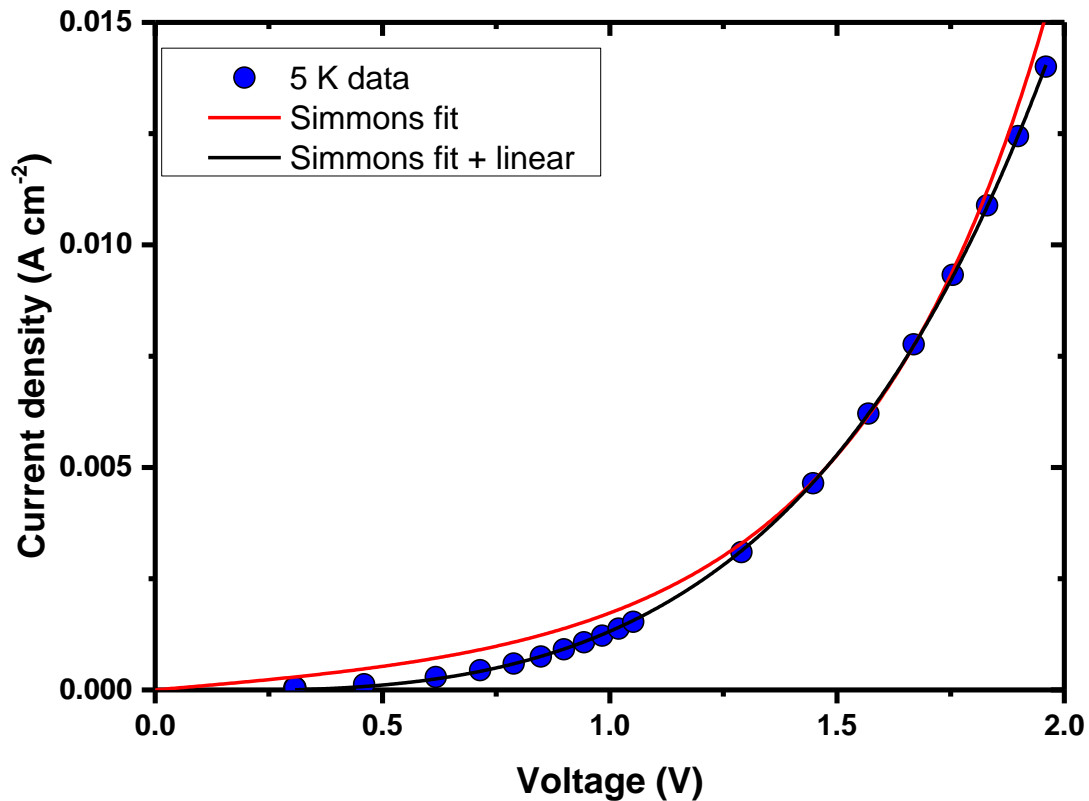


**Figure 4.21:** Positive voltage data for the JV characteristics of an  $80 \times 80 \text{ } \mu\text{m}^2$  GdN/AlN/GdN/Gd MTJ (blue) fitted with the Simmons model (red) and the Simmons model with an additional linear term (black).

The difference between the Simmons fit with and without this linear term is shown in **Figure 4.22** for a  $100 \times 100 \text{ } \mu\text{m}^2$  device from the same growth as the GdN/AlN/GdN/Gd device above.

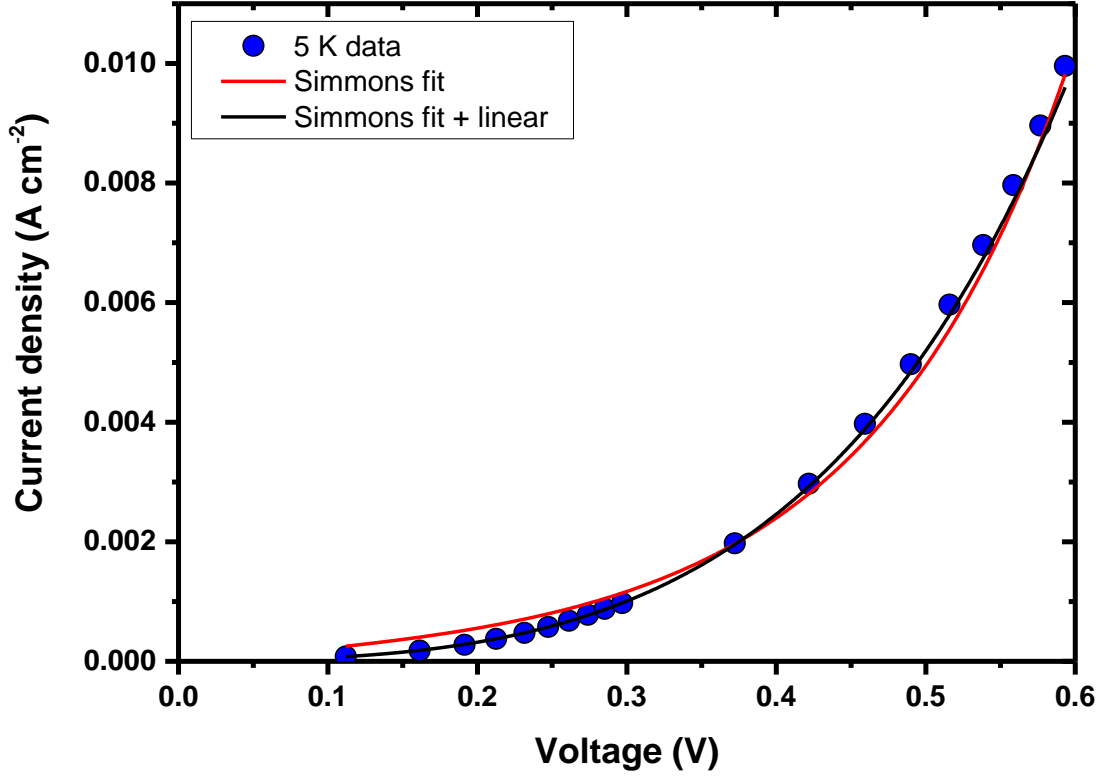


**Figure 4.22:** Positive voltage data for the JV characteristics of a  $100 \times 100 \mu\text{m}^2$  GdN/AlN/GdN/Gd MTJ (**blue**) fitted with the Simmons model (**red**) and the Simmons model with an additional linear term (**black**).

The addition of a linear term to correct for the low voltage JV behaviour made little difference to the extracted barrier parameters in this case. The Simmons barrier width changed from 2.65 nm to 2.45 nm for the  $100 \times 100 \mu\text{m}^2$  device, moving closer to the nominal barrier thickness of 2 nm, while the Simmons barrier height changed more significantly from 0.98 eV to 1.96 eV.

#### 4.5.2.3 Magnetic Behaviour

We now turn to the magnetic behaviour of devices in the presence of an external magnetic field. A GdN/AlN/GdN heterostructure was grown with an Al cap to probe the magnetic response

of just the GdN layers without influence of the usual Gd cap. Gd is ferromagnetic (for the measured temperature range) and is used to couple with the top GdN layer in order to break the magnetic symmetry of the two FM layers, however in previous magnetic measurements, the presence of a Gd layer meant that it was difficult to separate the contributions from Gd and GdN layers [25,26,113].

**Figure 4.23** shows the in-plane temperature-dependent magnetisation of such a structure when cooled in no applied field (black) and when cooled in a field of 200 Oe (red). The transition to ferromagnetic could be clearly seen for the GdN layers, with an onset around 70 K and the transition appeared to be complete by around 60 K. This was in agreement with the paramagnetic Curie temperature, as determined by the inverse susceptibility plot in **Figure 4.24**. The data between 75 K and 120 K was fit using a linear fit which extracted a paramagnetic Curie temperature of 61.8 K.

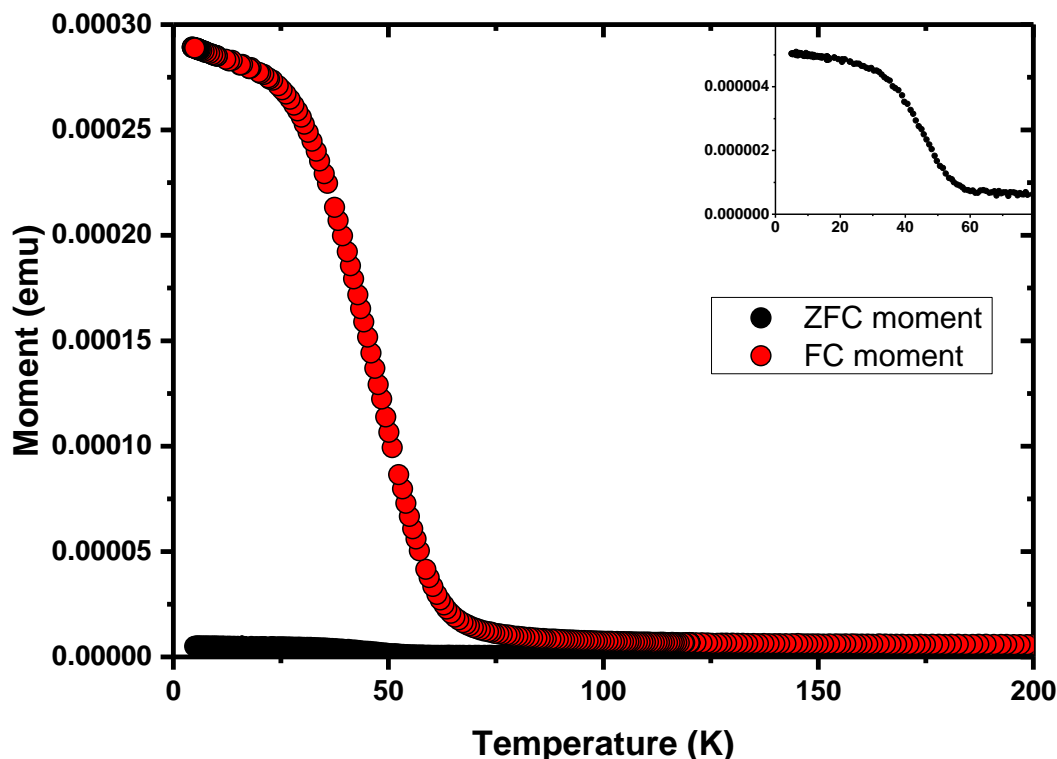


**Figure 4.23:** Temperature-dependent magnetisation of a GdN/AlN/GdN MTJ cooled in no applied magnetic field (black, ZFC) and cooled in a field of 200 Oe (red, FC). The inset is a zoom of the low temperature ZFC data.

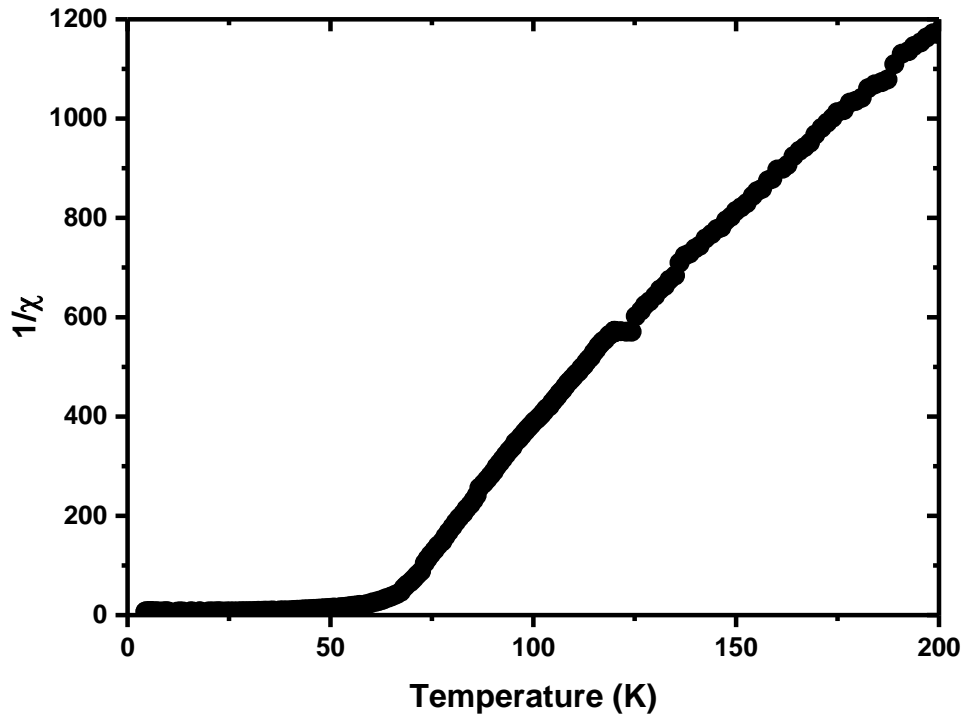


**Figure 4.24:** Inverse susceptibility as a function of temperature of a GdN/AlN/GdN MTJ cooled in in a field of 200 Oe.

Field-dependent magnetisation measurements for the same unpatterned GdN/AlN/GdN/Al heterostructure are shown in **Figure 4.25** as magnetic hysteresis (MH) loops between  $\pm 7$  T. The loops had the expected shape for polycrystalline GdN thin films, with a sloped, non-square transition and reached saturation at a field below 7 T [82]. The moment at saturation increased as the temperature decreased, with the loop at 70 K displaying weak ferromagnetism as it was likely that only a fraction of the GdN layer was ferromagnetic at this temperature. The saturation moment of  $\sim 1.5 \mu_B/\text{ion}$  at 5 K was also much lower than would be expected from epitaxial GdN thin films of  $7 \mu_B/\text{ion}$ , but among samples grown within our group, it was not uncommon for polycrystalline GdN thin films to be lower in moment.

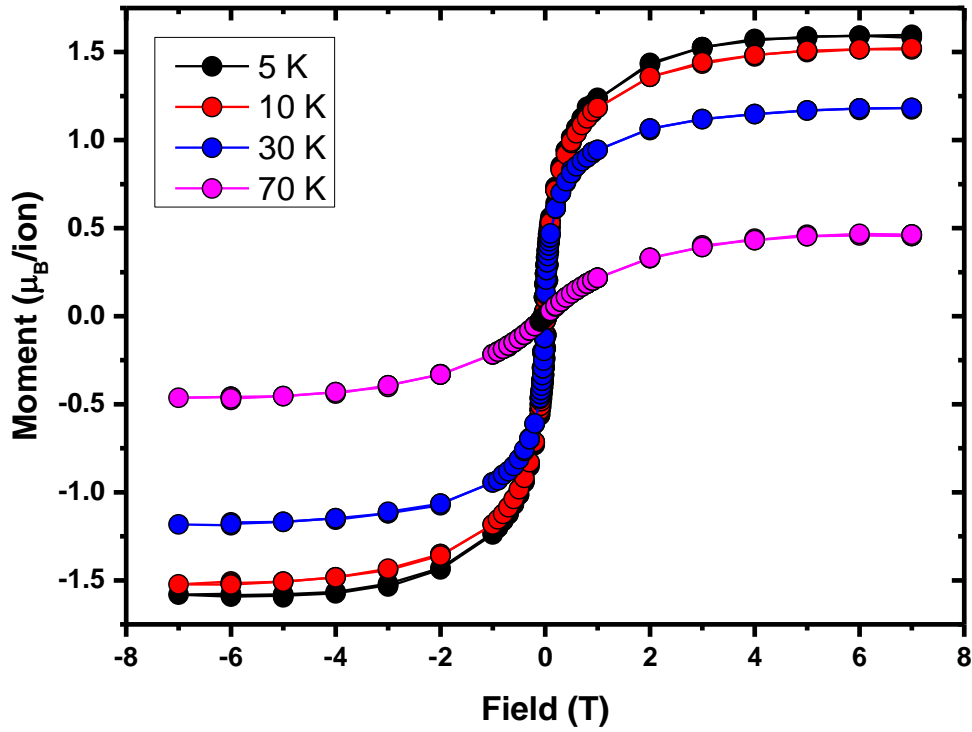


**Figure 4.25:** Field-dependent magnetisation of a GdN/AlN/GdN MTJ capped with Al for varying temperatures.

A zoom of the low-field response is shown below in **Figure 4.26** and here the MH loops can be seen to gradually open up with decreasing temperature around the coercive field of GdN.



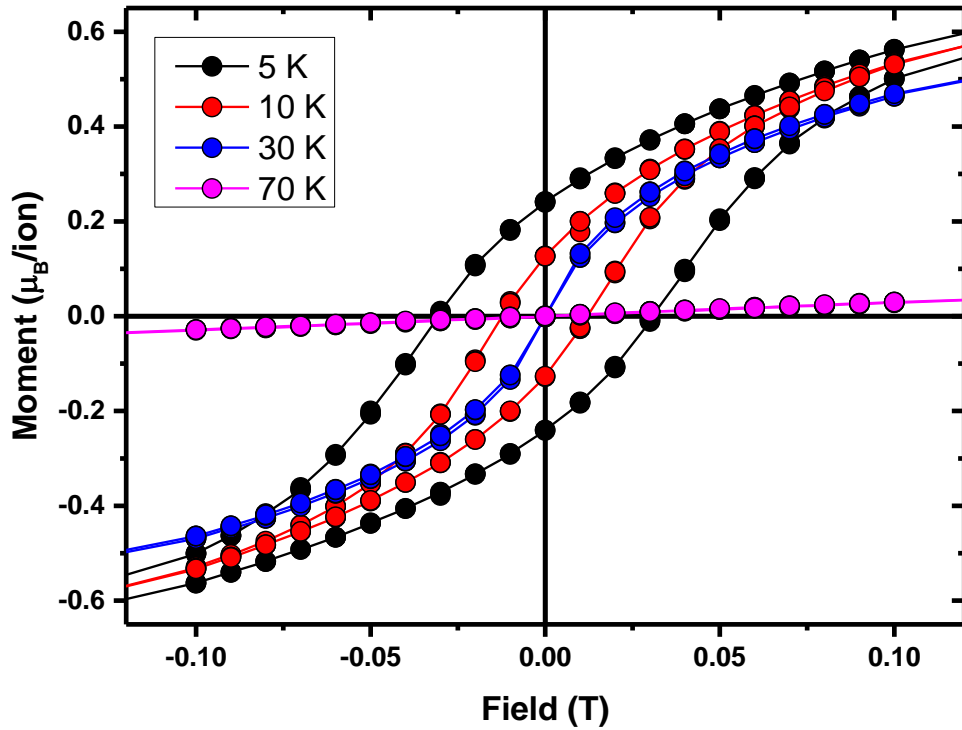


**Figure 4.26:** A zoom of the field-dependent magnetisation as shown above for a GdN/AlN/GdN MTJ capped with Al for varying temperatures.

The zoomed data in **Figure 4.26** show how the MH loop opened up with decreasing temperature. The MH loops give a good indication of the coercive field of GdN, the field at which the magnetic moment is zero. It can be seen that this value increased with decreasing temperature, up to a maximum of 0.03-0.04 T at 5 K. This information on the coercive field in device structures can be used to inform magnetoresistance measurements.

#### 4.5.2.4 Magnetoresistance

Electrical transport of devices was measured in the presence of an external magnetic field. The magnetic field was applied in-plane to the device – that is, in-plane with the FM layers – and measurements were typically performed at 2 K unless otherwise stated.

First, we consider a GdN/GaN/GdN/Gd MTJ. The magnetoresistance for this heterostructure is shown in **Figure 4.27** between  $\pm 8$  T, where the device was cooled to 2 K in a field of +8 T and then swept continuously to -8 T (in blue). Here the field direction was then reversed and swept back up to +8 T (in red). A strong magnetic response was observed, with the resistance decreasing with increasing magnetic field values. Hysteresis was observed, highlighted in **Figure 4.28**, which is a zoom of the low-field data presented in **Figure 4.27**. The resistance reached a peak value around  $\pm 0.04$  T, near the coercive field found for GdN in such a structure. This suggested that the resistance peak corresponded to the anti-aligned configuration, where one GdN layer had switched magnetisation, resulting in a high resistance state. As the magnetic field continued to sweep, the second GdN layer switched, although this feature was lost in the larger overall magnetoresistance. It is noted that a feature around both positive and negative 4 T ( $\pm 4$  T) was observed, which may correlate with the switching of the second, Gd-coupled GdN layer, although the origin of this feature is not resolved here.

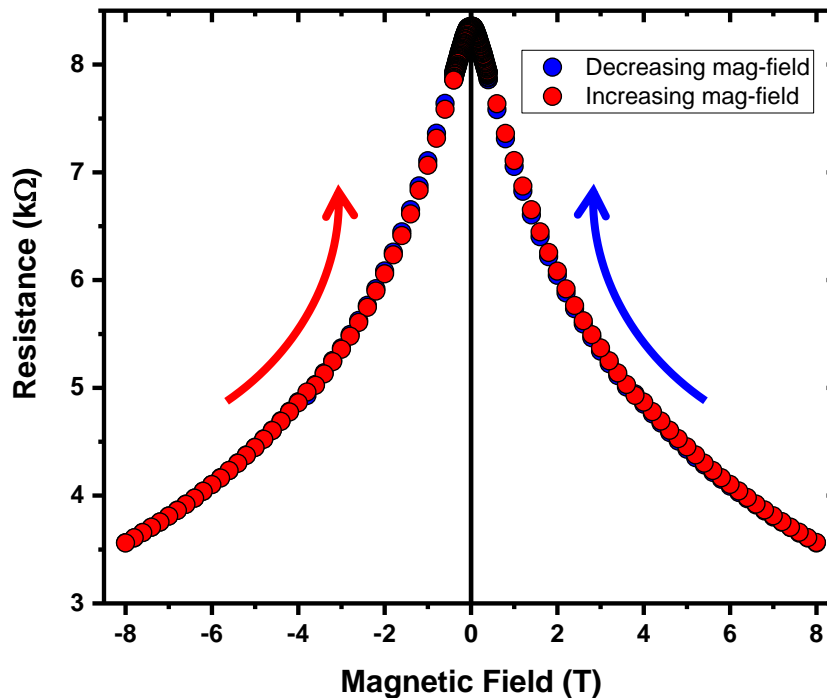


**Figure 4.27:** Magnetoresistance for a GdN/GaN/GdN/Gd MTJ at 2 K. Field direction is swept from positive to negative (**blue**) from +8 T to -8 T, before reversing direction from negative to positive (**red**) from -8 T to +8 T.

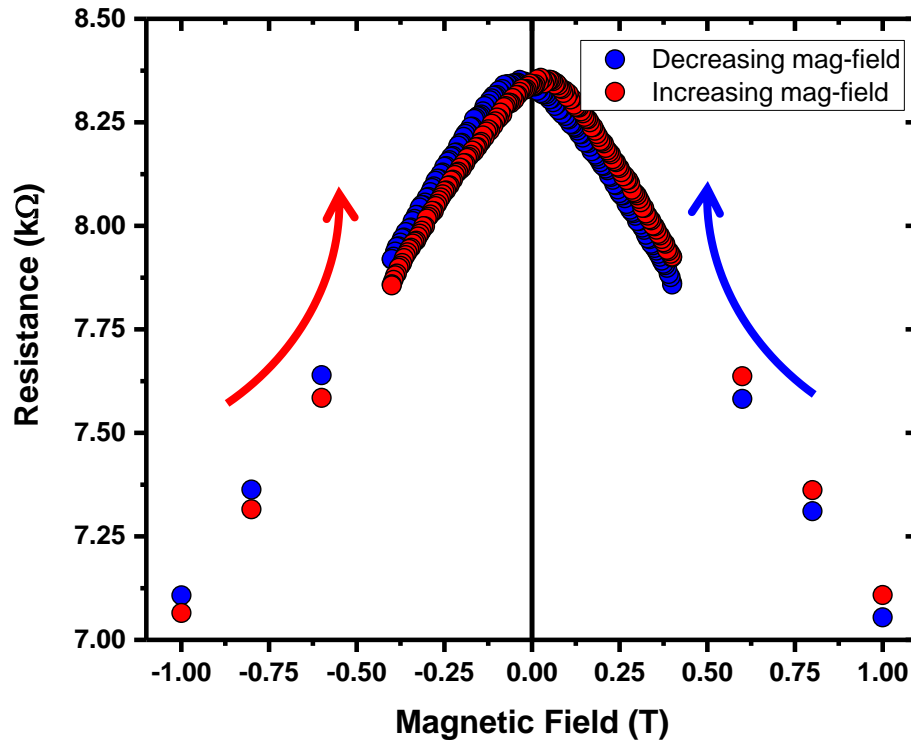


**Figure 4.28:** Low-field zoom of magnetoresistance for a GdN/GaN/GdN/Gd MTJ at 2 K. Field direction is swept from positive to negative (**blue**) from +8 T to -8 T, before reversing direction from negative to positive (**red**) from -8 T to +8T. Hysteresis is observed with the resistance value dependant on the direction of magnetic field sweep.

The TMR is reported in **Figure 4.29**. Using the TMR equation (**Equation 4.2**) and values near 0 T and 8 T for  $R_{AP}$  and  $R_P$  respectively, we found a maximum TMR magnitude of 135% at 8 T for 2 K. It had previously been reported that TMR for GdN-based MTJs reached a maximum at around 50 K and increased using lower applied currents, so this 135% value could be even greater under different conditions [26].

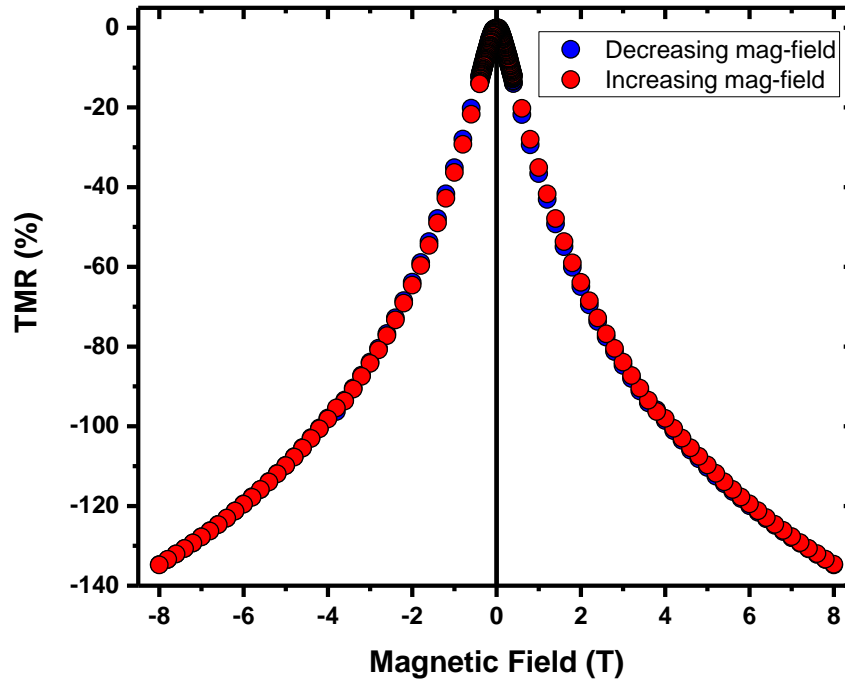


**Figure 4.29:** Magnetoresistance of a GdN/GaN/GdN/Gd MTJ at 2 K, reported as a TMR percentage.

This magnetoresistive behaviour and shape was typical of GdN/I/GdN MTJ structures (and indeed REN-based MTJs in general). For an AlN-barrier device, **Figure 4.30** below shows the low-field magnetoresistance behaviour of a GdN/AlN/GdN/Gd device between  $\pm 0.25$  T and the same hysteretic behaviour can be seen at magnetic fields close to the coercive field of GdN. To probe the switching behaviour of the FM layers, we now look at magnetoresistance data where the field was reversed near the resistance maximum ( $\sim -0.04$  T) instead of the full-field -8 T value. In doing so, the device was taken to a field strong enough to switch one GdN layer, without switching the other.

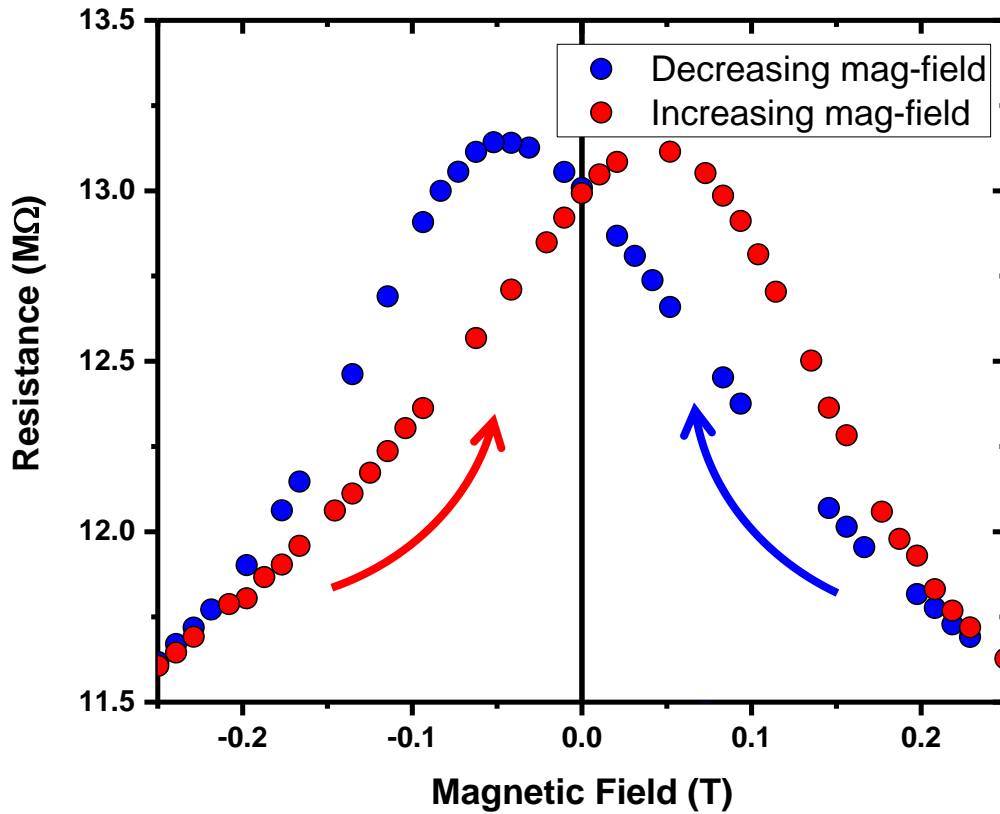


**Figure 4.30:** Magnetoresistance of a GdN/AlN/GdN/Gd MTJ at 2 K. Field direction is swept from positive to negative (blue) from +0.25 T to -0.25 T, before reversing direction from negative to positive (red).

**Figure 4.31 (left)** below shows the low-field magnetoresistance behaviour of a GdN/AlN/GdN/Gd device which had been taken to +8 T and swept down in magnetic field to -0.04 T. Here the field was reversed and swept back to +8 T. A difference in resistance was observed at zero-field (0 T) – highlighted in **Figure 4.31 (right)** – for the two different field sweep directions, in contrast to the full field ( $\pm 8$  T) sweeps shown above. The difference in resistance value at zero field was found to be 0.53% and signified a retention of the resistive state at zero-field. This was the first demonstration of memory retention at zero-field in a REN-based MTJ.

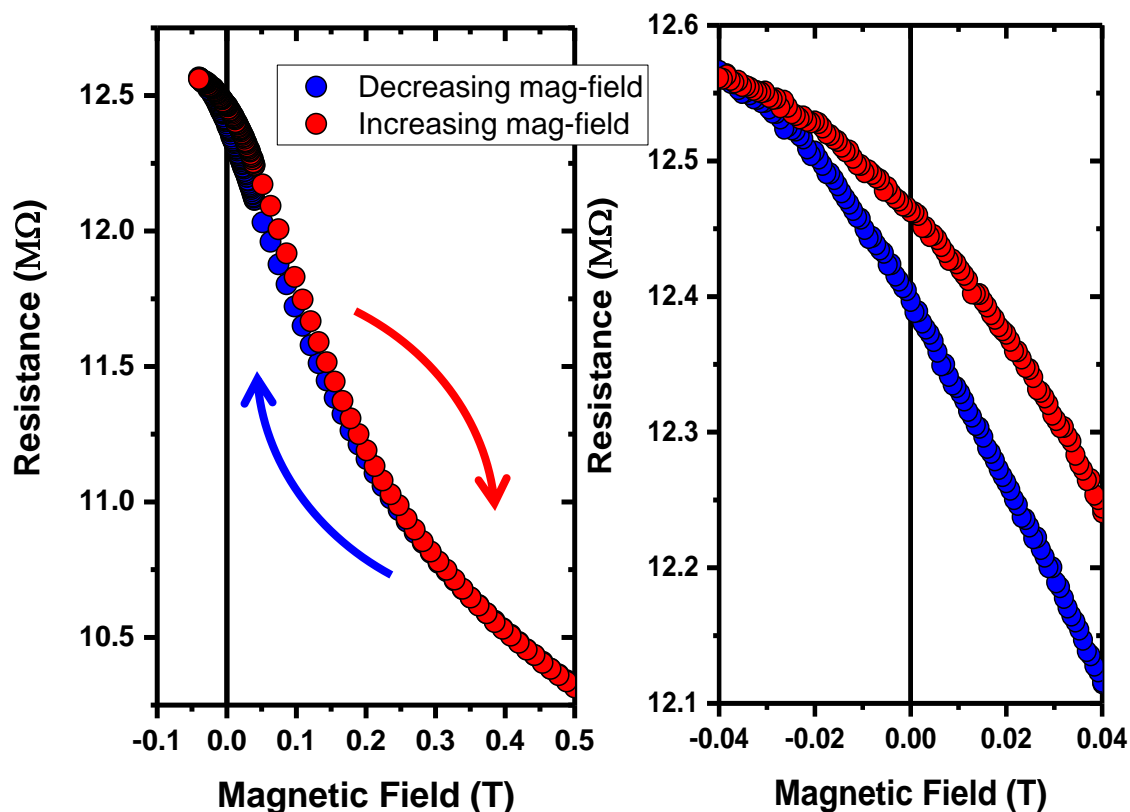


**Figure 4.31:** Magnetoresistance of a GdN/AlN/GdN/Gd MTJ at 2 K. Field direction is swept from positive to negative (**blue**) from +8 T to -0.04 T, before reversing direction from negative to positive (**red**) from -0.04 T to +8T. **Left** is the full sweep between -0.04 T and +0.5 T and **right** is a zoom of the same data between  $\pm 0.04$  T. Note that the resistance value at 0 T is dependent on the field sweep direction, implying a difference in alignment of the ferromagnetic layer in the MTJ.

This demonstrated that RENs are a viable material choice for use as FM layers in MTJs for magnetic memory storage. Low-field hysteresis has been shown, along with zero-field retention of the anti-aligned, high-resistance state. This was achieved in a structure using two GdN layers as the FM electrodes (albeit with one coupled to Gd) and so it is expected that the use of layers with contrasting magnetic, but similar electronic, states would result in even stronger retentive effects. This could be realized by incorporating a hard FM to pair with the relatively soft GdN layer, such as SmN (as done previously) or DyN (as shown in **Chapter 6**).

## 4.6 Conclusion

In this chapter, we have investigated the conduction path in single- and multi-layered structures using the *caisson* geometry and determined specific minimum requirements to assume that electrical measurements meaningfully represent the sample active area. For single layer thin films, a conduction ratio of 10,000,000 between the top metal contact and sample layer is required for films with an active area of  $10 \times 10 \text{ } \mu\text{m}^2$  to have a measured resistance that represents ~97% of the actual resistance. Alternatively, MTJ heterostructures provide a large enough resistance contribution due to the insulating tunnel barrier layer as to avoid this concern.

REN-based MTJs were fabricated using the *caisson* geometry with two ferromagnetic layers of GdN separated by tunnel barriers of either GaN or AlN. Devices displayed TMR of 135% for magnetic fields of  $\pm 8 \text{ T}$  at  $5 \text{ K}$  and showed low-field hysteretic behaviour consistent with the coercive field of the free GdN layer. By deactivating the magnetic field when the device resistance value is maximised, we were able to demonstrate a retention of this resistive state at zero field, with a difference in resistance of 0.53% between the high- and low-resistance states of the MTJ. This is the first known report of a REN-based MTJ retaining its resistive state at zero field and demonstrates the viability of these materials in future non-volatile memory devices.

GdN served as a useful proof of concept to assess the viability of RENs in heterostructures such as MTJs. However, to further develop the applicability of these devices, consideration must be given to the careful selection of each layer material. Another consideration could be in the optimisation of layer growths via minimisation of the lattice mismatch between layers. This could be achieved by making use of other RENs, and one could imagine a fully REN-based MTJ where the FM and I layers are all some REN. Towards this end, the following chapter looks at the structural, electronic, and magnetic properties of LuN.

Another path forwards could be the use of FM layers with much more contrasting coercive fields as to switch one layer completely while leaving the other layer as unaffected as possible (such is the case in GdN/I/SmN devices). This could further increase the resistance difference between the aligned and anti-aligned states, leading to a larger retention difference at zero-field. For this, DyN is paired with GdN as a second FM layer in tri-layer structures in **Chapter 6**.

## Chapter 5

# Lutetium Nitride: A Non-Magnetic Semiconducting Rare Earth Nitride

### 5.1 Introduction

As mentioned in previous chapters, a variety of opportunities has motivated the development of the rare earth monpnictides in general, and rare earth nitrides in particular, over the last few decades due to their unusual and unique range of electronic, magnetic, and optical properties [17,77]. Particular interest has been in their potential practical applications in areas such as spintronics, topological and cryogenic electronics, and high-performance computing, among others [114,10,27,28,115]. Two of the rare earths which have yet to be explored in more detail are the end members: lanthanum and lutetium.

While other rare earth monpnictides display interesting magnetic and electronic properties that correlate with their partially filled  $f$ -shell electrons, lutetium, as the last member of the rare earth series, has no net magnetic moment as a result of the filled  $4f$  shell. In terms of device application of rare earth nitrides, the nitrated form of lutetium (lutetium nitride) could be a suitable material to be used as a tunnel barrier in magnetic tunnel junctions (MTJs), provided that the material is sufficiently insulating and has an appropriate bandgap. Most RENs have a bandgap of  $<1$  eV [116,117] and so, in REN-based MTJs, GaN or AlN have been the prototypical materials used for tunnel barriers due to their bandgaps at 300 K of 3.4 eV [118] and 6.0 eV [112] respectively [28]. Conflicting reports on the conductive nature of LuN from semimetallic to semiconducting can be found in the literature, with the semiconducting reports listing a bandgap of 1.55-1.6 eV [117,119–121]. Evidently clarification on the electrical properties of LuN is needed here, but LuN shows promise as a suitable barrier material for REN MTJs with lower lattice mismatch and potential epitaxial compatibility between layers.

Previous computational [116,122–127] and experimental [117,119,128–131] studies have mainly focussed on the structural, elastic, mechanical, and phonon properties of LuN, but largely neglected the electrical transport properties, a gap we aim to fill in this chapter.



Of particular interest is to gain a more fundamental understanding of the conductive nature of LuN – metallic vs semiconducting, direct vs indirect bandgap, etc. – and the role of nitrogen vacancies on the structural and electronic properties. In this chapter, we address the electronic properties of LuN in a combined experimental and computational study. We start with a brief historical background and a literature review of the recent results on LuN. We then report on the growth of polycrystalline LuN thin films and the effect of the  $\text{N}_2\text{:Lu}$  flux ratio during growth on the structural properties and stoichiometry of the LuN films. Optical measurements on the stoichiometric film are used to determine the optical band gap, and this is compared to the films doped with nitrogen vacancies (non-stoichiometric LuN) which show a free carrier response consistent with a semiconductor doped to degeneracy. A clear ambient-temperature absorption edge and indirect bandgap near 1.7 eV is observed for the undoped LuN film, while a tail develops at lower energies in the nitrogen vacancy-doped films. Electrical transport measurements show a shift from insulating to metallic-like conductivity with increasing nitrogen vacancy concentration.

Finally, we use the experimental results to inform density functional theory (DFT)-based band structure calculations on both stoichiometric LuN and lightly doped LuN crystals. These calculations are then used alongside the experimental data to make an informed conclusion about the electronic properties of LuN. We find that, upon doping, each nitrogen vacancy releases three electrons into the crystal: one electron into the Lu 5d extended state conduction band minimum, facilitating electrical transport, while the other two electrons are largely localised to the vacancy site, in deep donor levels at the valence band maximum.

One publication related to the results of this chapter has been published; the article was promoted as a Featured Article on the journal's homepage [76]:

S. Devese, K. Van Koughnet, R. G. Buckley, F. Natali, P. P. Murmu, E.-M. Anton, B. J. Ruck, and W. F. Holmes-Hewett, *Probing the Defect States of  $\text{LuN}_{1-\delta}$ : An Experimental and Computational Study*, AIP Advances **12**, 035108 (2022).

### 5.1.1 LuN: A Brief Historical Review

The earliest studies of LuN are from the 1960s where samples were produced by nitriding chunks of rare earth metals or rare earth hydrides with ammonia gas at elevated temperatures [117,119,128]. They were aware of the air-sensitivity of the RENs and, in one study by Didchenko and Gortsema, used gloveboxes and techniques such as storing samples in bags with dry ice to minimise the exposure to air. [119] It is not clear whether these samples would have been exposed to air when transferring to the setups required for magnetic and resistivity measurements, however it is fair to assume that these uncapped samples are not perfectly stoichiometric crystals. They found LuN, in particular, to have a room temperature resistivity of  $\sim 300 \mu\Omega \text{ cm}$  and concluded that all rare earth nitrides – except for YbN – demonstrated semimetallic behaviour, which suggested that these samples were compromised with nitrogen vacancies, rather than oxidative damage. It was also noted that LuN was paramagnetic [119] and had a lattice parameter of  $4.76 \text{ \AA}$  [128].

As previously mentioned, a historic review by Hulliger listed LuN as having a bandgap of  $\sim 1.6 \text{ eV}$ , the highest bandgap of the RENs, and it was stated that ‘one is tempted to deduce non-metallic properties’ for LuN [117] based largely on contemporary work by Busch *et al.* and Dismukes *et al.* [120,121]. Interestingly, Dismukes *et al.* noted that LuN is the most stable REN in air from their investigation, which is in stark contrast to Didchenko and Gortsema who stated LuN to be the most reactive REN [119], highlighting a probable discrepancy in sample purity. There is clear uncertainty about the electronic properties of LuN – and indeed the RENs in general – and this is likely due to the difficulty in controlling nitrogen vacancy doping levels during synthesis at the time.

### 5.1.2 LuN Since 2004

There has been a renewed interest in rare earth nitrides since the seminal paper by Aerts *et al.* [77]. Using self-interaction correction local spin-density (SIC-LSD) calculations, they predicted half-metallic, insulating, and semimetallic behaviour across the REN series. They also predicted that some RENs have mobile electrons all with the same spin alignment, that is, there would be no ‘minority spin’ electrons among the conducting charge carriers. These predictions

offered an entire series of materials with promising properties for spintronics application, and encouraged a second boom of REN research, with much of the middle RENs (GdN, SmN etc.) being the focus of experimental work due to their unique and unusual magnetic properties [17,83,96,132,133].

The majority of research on LuN, however, has been computational studies, looking at the electrical and structural properties. LuN was calculated to have a direct band gap of 0.9 eV and indirect bandgap of 1.55 eV [123], and the lattice constant ranging from 4.7-4.9 Å [116,124–126]. The behaviour of the partially-filled *f*-shell electrons across the rare earth nitride series makes modelling the system more complicated than can be calculated using a straight forward local spin density approximation (LSDA), and so other terms must be taken into account; for example, Larson *et al.* used a Hubbard-U correction to allow the *f*-orbitals to break cubic symmetry and push them away from the fermi level [116]. They also used the relatively abundant experimental GdN literature to inform the size of the U correction term, by matching the computational results for GdN to the experimental GdN properties and then used this as a basis for the other REN calculation parameters. Interestingly, LaN, GaN, and LuN are the three RENs from the series that have filled shells and thus reduce the complexity of these calculations, making them a realistic entry point in REN band structure calculations. As a sidenote, a few groups have investigated the structural properties of LuN, mainly phase transitions and mechanical properties, and have found the occurrence of pressure-dependent structural transitions though this is not so relevant for the work in this chapter [123–125,134].

Although there have been a handful of LuN samples synthesised more recently, most of the analysis in these studies focus on the synthesis procedure and structural properties [129–131]. The direct nitridation of a lutetium ingot resulted in LuN with a lattice parameter of 4.76 Å, similarly to the historical data, however this experiment used bulk lutetium, and their “highly nitrided” samples were found to be only 85-97% nitrided [131]. This effectively means that the LuN was doped with 3-15% nitrogen vacancies, which – as will be discussed in this chapter – is more than significant enough to change the material properties compared to stoichiometric LuN. Granville *et al.* [129] looked at the vibrational properties of various RENs via Raman spectroscopy and found a peak associated with LuN at 582 cm<sup>-1</sup>, corresponding to the LO(*L*) mode. We will discuss Raman spectroscopy of RENs in more detail in **Section 5.3.2** of this chapter.

It is known that historic samples of the rare earth nitrides are typically compromised via reaction with oxygen and/or contain a significant amount of nitrogen vacancies, a result of the less-advanced vacuum technology of the time. This is shown through the commonly reported distorted lattice parameters and reduced resistivity of grown samples. Shaib *et al.* have shown clearly how decreased nitrogen pressure during growth of SmN and GdN thin films results in a shift of the (111) XRD peak position towards high angle in  $2\theta$ - $\theta$  measurements, corresponding to a decrease in the lattice parameter [75,80]. Nitrogen vacancy concentration in these films also affects the magnetic properties, though this effect is not specifically applicable to paramagnetic LuN.

The electronic properties of rare earth nitrides are largely driven by the concentration of nitrogen vacancies in the material, each of which dopes the conduction band with, at most, three electrons. As demonstrated through our group studies of the other rare earth nitrides [18,69,75], we can intentionally control the level of nitrogen vacancy doping through selective growth parameters, namely the nitrogen partial pressure during sample growth. In this chapter, we will show that polycrystalline thin films ranging from stoichiometric LuN through to metallic Lu can be grown by controlling the  $N_2$ :RE flux ratio during growth. Findings from Raman, optical, and electrical transport measurements show that increased doping via nitrogen vacancies increase the conductivity of the films, and this is supported by theoretical calculations on the band structure for the doped and undoped film. Compared to historical data, we note that the properties reported for historic samples correspond to films from our study that were intentionally doped with nitrogen vacancies, suggesting that many samples of LuN reported in literature actually contain significant concentrations of nitrogen vacancies.

## 5.2 LuN Thin Film Growth

Five LuN samples and one Lu sample were grown for this study. ~80 nm thick LuN layers were deposited at ambient temperature in a molecular beam epitaxy system onto Si/SiO<sub>2</sub> and 1x1 cm<sup>2</sup> sapphire substrates with pre-deposited gold contacts in a van der Pauw geometry. Before the growth the substrates were outgassed at 600 °C for one hour. Lu metal was evaporated using an electron beam in the presence of a molecular nitrogen partial pressure ranging from  $1 \times 10^{-6}$  to  $1 \times 10^{-4}$  mbar, exploiting the catalytic activity of Lu ions to spontaneously drive the reaction between the Lu surface and molecular N<sub>2</sub>. This resulted in the formation of a LuN layer, confirming the

catalytic activity for Lu, as has been exhibited by most of the other rare earth elements [72]. Film thicknesses were measured using Dektak profilometry and Rutherford Back Scattering (RBS) spectroscopy. A constant deposition rate of  $360 \text{ nm h}^{-1}$  was monitored in real-time using a quartz crystal microbalance, corresponding to  $\text{N}_2\text{:Lu}$  flux ratio from 0.77 to 77 for the pressure ranges used. RBS measurements on films grown at the highest  $\text{N}_2\text{:Lu}$  flux ratio showed a 1:1 ratio of  $\text{N}_2\text{:Lu}$  present, suggesting a stoichiometric film. This result is consistent with reported growth parameters used to grow stoichiometric thin films of other RENs, such as GdN and DyN [18, 75]. RBS data for films grown at lower  $\text{N}_2\text{:Lu}$  flux ratios showed a smaller ratio of  $\text{N}_2\text{:Lu}$  present in the film; consistent with the idea that the number of nitrogen vacancies in REN thin films increases with decreasing nitrogen growth pressure, as will be demonstrated in this chapter.

The  $\text{N}_2\text{:Lu}$  flux ratio is calculated from the impingement rate of each precursor species. The  $\text{N}_2$  flux rate,  $\Gamma$ , is derived from the ideal gas law, and is inferred from the nitrogen partial pressure during growth according to the following formula:

$$\Gamma = \frac{P}{(2\pi mk_B T)^{\frac{1}{2}}} \quad (5.1)$$

Where  $P$  is the partial pressure of the gas,  $m$  the mass of the gas molecule,  $k_B$  the Boltzmann constant, and  $T$  the temperature. For convenience and specificity to nitrogen gas at 300 K, the molecular flux of nitrogen in units of  $\text{N}_2/\text{nm}^2/\text{s}$  is given as:

$$\Gamma_{(\text{N}_2, 300 \text{ K})} = P \times 2.87 \times 10^6 \quad (5.2)$$

The flux rate for Lu is also inferred indirectly, this time using the growth rate – thickness, as determined by Dektak, divided by the growth time – and atomic density of Lu within LuN.

$$\Gamma_{(Lu, 300\text{ K})} = \frac{t}{\tau} \times \rho \quad (5.3)$$

Where  $t$  is the film thickness in nm,  $\tau$  is the growth time in s, and  $\rho$  is the atomic density of Lu within LuN, which is approximately  $37\text{ Lu nm}^{-3}$ . The flux ratio referred to in this chapter is the impingement rate ratio of  $\text{N}_2$  molecules to Lu atoms; a higher flux ratio is equivalent to a higher nitrogen growth partial pressure.

To prevent the oxidation of the LuN films and allow further *ex-situ* physical characterisation, a polycrystalline 50 nm thick AlN cap was deposited *in-situ*. A single layer of Lu metal was grown in a similar manner, without molecular nitrogen present, for comparison.

Sample name	$\text{N}_2$ growth partial pressure (mbar)	$\text{N}_2$ :Lu flux ratio	LuN thickness (nm)
A845	$1 \times 10^{-4}$	77	70
A848	$5 \times 10^{-5}$	39	95
A846	$1 \times 10^{-5}$	7.7	65
A849	$5 \times 10^{-6}$	3.9	90
A847	$1 \times 10^{-6}$	0.77	80
A850	No nitrogen flow	0	100

**Table 5.1:** The sample names,  $\text{N}_2$  growth pressure,  $\text{N}_2$ :Lu flux ratio, and thickness parameters for each LuN and Lu film in this chapter.

## 5.3 Structural Properties

### 5.3.1 X-Ray Diffraction

$2\theta$ - $\theta$  XRD diffractograms for LuN samples grown at different nitrogen pressures are shown in **Figure 5.1**. For the sample grown at the lowest nitrogen partial pressure,  $1 \times 10^{-6}$  mbar, the XRD suggests that the film is mainly comprised of Lu metal with the characteristic Lu (100), (002) and (101) reflections all present, though the large Lu (002) peak may obscure a small LuN (111) feature. Small contributions of Lu metal are also detected on the sample grown at  $5 \times 10^{-6}$  mbar. By contrast there are clear signatures of LuN in all samples grown with  $N_2$  pressure  $1 \times 10^{-5}$  mbar and above. The films are polycrystalline by nature, with a rock-salt structure. A strong texture along the (111) direction is observed, while other weak contributions from orientations (200, 220, and 311) can be seen at higher angles. A zoom of the (111) peak is highlighted in **Figure 5.2**. Said texture is common for rare earth nitride materials grown in similar conditions of pressure and deposition rate; rock salt materials are known to have the propensity to grow along the (111) close-packed plane rather than the (002) direction.

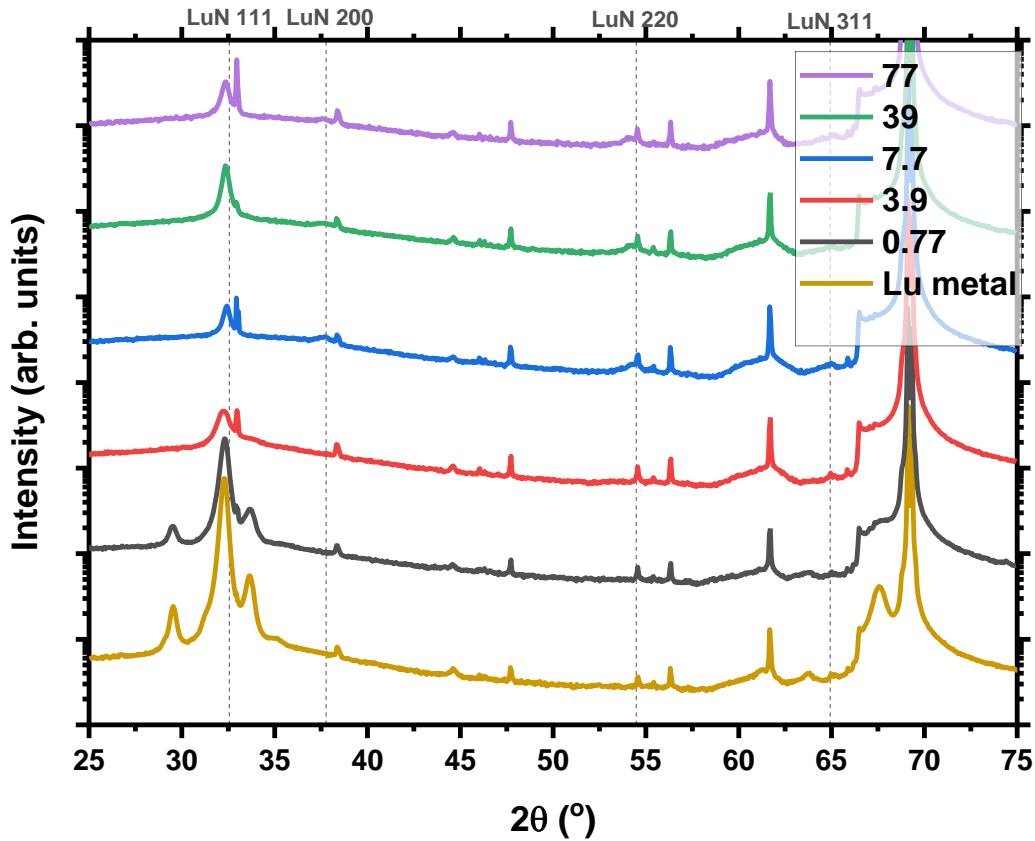


**Figure 5.1:**  $2\theta$ - $\theta$  X-ray diffractograms of LuN and Lu metal thin films grown at different  $N_2$ :Lu flux ratios of  $R_{N_2/Lu} = 77$  (purple), 39 (green), 7.7 (blue), 3.9 (red), 0.77 (black), and 0 (gold). Dashed vertical lines indicate the position of various orientations for historical LuN with a lattice constant of  $4.76 \text{ \AA}$  [128,129].

We note that additional peaks due to the substrate and X-ray source are present in these measurements. As discussed in **Section 3.4.3 X-ray Diffraction**, peaks due to the Si (200), Si (211), and Si (400) reflections are all present and occur at approximately  $33^\circ$ ,  $44^\circ$ , and  $69^\circ$  respectively. Peaks from the copper  $k_\beta$  and  $k_\alpha$  of the Si[400] occur at approximately  $62^\circ$  and  $66^\circ$ . These peaks are present across all thin films, regardless of  $N_2$ :Lu flux ratio.



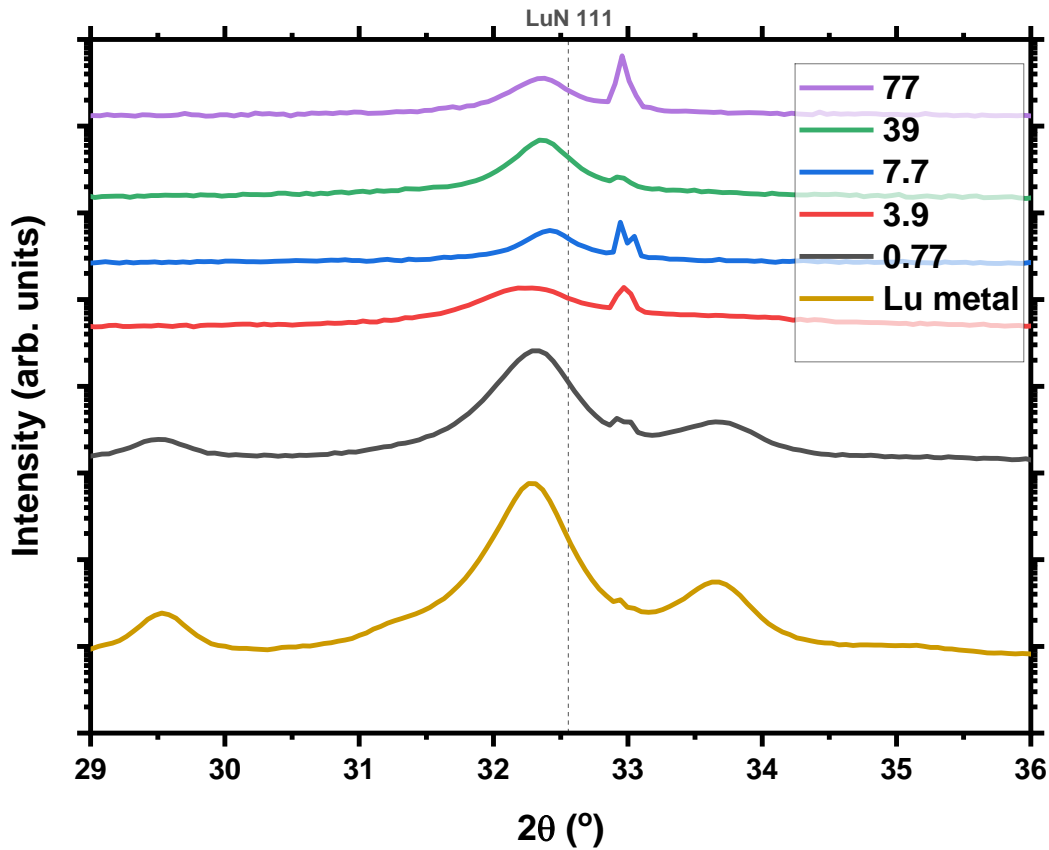


**Figure 5.2:** Zoom of the  $2\theta$ - $\theta$  XRD LuN (111) peak for LuN thin films grown at different  $N_2$ :Lu flux ratios of  $R_{N_2/Lu} = 77$  (purple), 39 (green), 7.7 (blue), 3.9 (red), 0.77 (black), and 0 (gold). The sample grown at  $R_{N_2/Lu} = 0$  corresponds to the Lu metal thin film. Dashed vertical lines indicate the position of (111) for historical LuN with a lattice constant of 4.76 Å [128,129].

The (111) XRD peak could be fitted using a single Lorentzian function for all LuN samples, as shown in **Figure 5.3**, meaning the growth is mostly dominated by grain size effects rather than strain. Using the Scherrer equation [135], we calculate a grain size of 33.1, 39.5, and 39.0 nm for the  $R_{N_2/Lu} = 77$ , 39, and 7.7 thin films respectively, which corresponds to approximately one half of the film thickness. The extracted lattice parameter is  $4.79 \text{ Å} \pm 0.01 \text{ Å}$  for the three films grown at highest nitrogen pressure. It is worth pointing out that we do not observe a noticeable shift towards reduced lattice parameters when increasing the growth nitrogen pressure, as has been reported for other rare earth nitrides [75]. Indeed, Shaib *et al.* [80] reported on a high angle shift in the GdN (111)  $2\theta$ - $\theta$  XRD peak position as the  $N_2$ :Gd flux ratio ( $R_{N_2/Gd}$ ) increases, accompanied

by a progressively developing asymmetry of the peak. It was suggested that two structural phases were present in the film – called GdN I (stoichiometric) and GdN II (non-stoichiometric) – and could subsequently be fitted using two Lorentzian functions, one fixed to the stoichiometric GdN I position and the other free to vary, related to the nitrogen vacancy concentration. For the SmN thin film series, Shaib *et al.* [75] did not observe the presence of a second phase in the  $2\theta$ - $\theta$  XRD angle and could only fit the SmN (111) peak position with a pseudo-Voight function. For all LuN thin film samples grown here, the LuN (111) peak position could be reasonably fit using one Lorentzian function, implying no presence of a second structural phase.

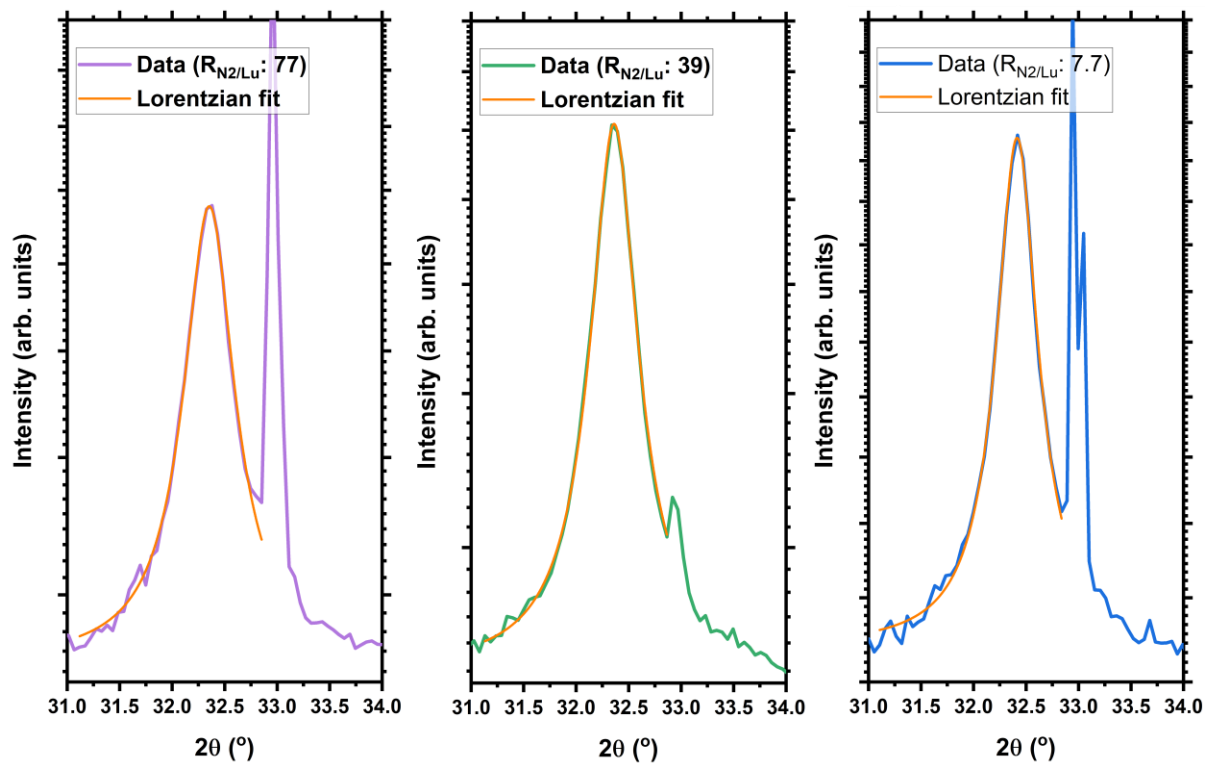


**Figure 5.3:** Lorentzian fitting (orange) of the  $2\theta$ - $\theta$  XRD LuN (111) peak for LuN thin films grown at different  $N_2$ :Lu flux ratios of  $R_{N_2/Lu} = 77$  (purple), 39 (green), and 7.7 (blue). Each peak could be fitted using one Lorentzian function.

N <sub>2</sub> :Lu flux ratio	N <sub>2</sub> growth partial pressure (mbar)	Peak position (°)	Lattice parameter (Å)
77	1x10 <sup>-4</sup>	32.35	4.789
39	5x10 <sup>-5</sup>	32.36	4.788
7.7	1x10 <sup>-5</sup>	32.41	4.780
3.9	5x10 <sup>-6</sup>	32.26	4.803
0.77	1x10 <sup>-6</sup>	32.31	4.796

**Table 5.2:** Values of the 2θ-XRD LuN (111) peak position and corresponding calculated lattice parameter for LuN thin films grown at different N<sub>2</sub>:Lu flux ratios of R<sub>N<sub>2</sub>/Lu</sub> = 77 (purple), 39 (green), 7.7 (blue), 3.9 (red), and 0.77 (black).

It is worth pointing out that the uncertainty associated with this measurement is namely in the resolution of the XRD measurement, which translates to  $\sim \pm 0.001$  Å in lattice parameter. To further clarify the presence/absence of any shift in peak position, and subsequently lattice parameter, it would be worth growing a new series of LuN thin film samples, focusing on higher N<sub>2</sub>:Lu flux ratios that do not yield samples with the presence of Lu signals in the XRD measurement which potentially obstruct or distort the analysis of LuN peaks (e.g. Lu (002) and LuN (111) which both occur around 32.4°).

As listed in **Table. 5.3**, our lattice parameter for stoichiometric LuN is slightly larger than most of the experimental values reported in the literature, somewhat unsurprisingly, as reduced lattice parameters are often reported for rare earth nitride films – namely GdN, DyN, and SmN – with unintentionally high levels of nitrogen vacancies and oxidation. Additionally, among the lattice parameter values reported in literature for LuN, there is greater spread in the computational samples as compared to the experimental samples. One reason for this could be the different ways of accounting for the localised behaviour of the *f*-orbitals, leading to larger discrepancies in lattice parameter between studies.

Lattice parameter (Å)	Type	Year	Reference
<b>4.79</b>	Experimental	2022	This work
<b>4.76</b>	Experimental	1956	[128]
<b>4.76, 4.88</b>	Experimental, computational	2009	[129]
<b>4.87</b>	Computational	2007	[116]
<b>4.76</b>	Computational	2011	[124]
<b>4.76</b>	Computational	2015	[125]
<b>4.72</b>	Computational	2016	[126]

**Table 5.3:** Literature values of lattice constants for LuN determined by experimental or computational means over the years.

### 5.3.2 Raman

Raman vibrations have previously been reported for rare earth nitride thin films, despite the RE-N crystal structure expected to be Raman inactive due to the inversion symmetry in the rock salt structure [80,129].

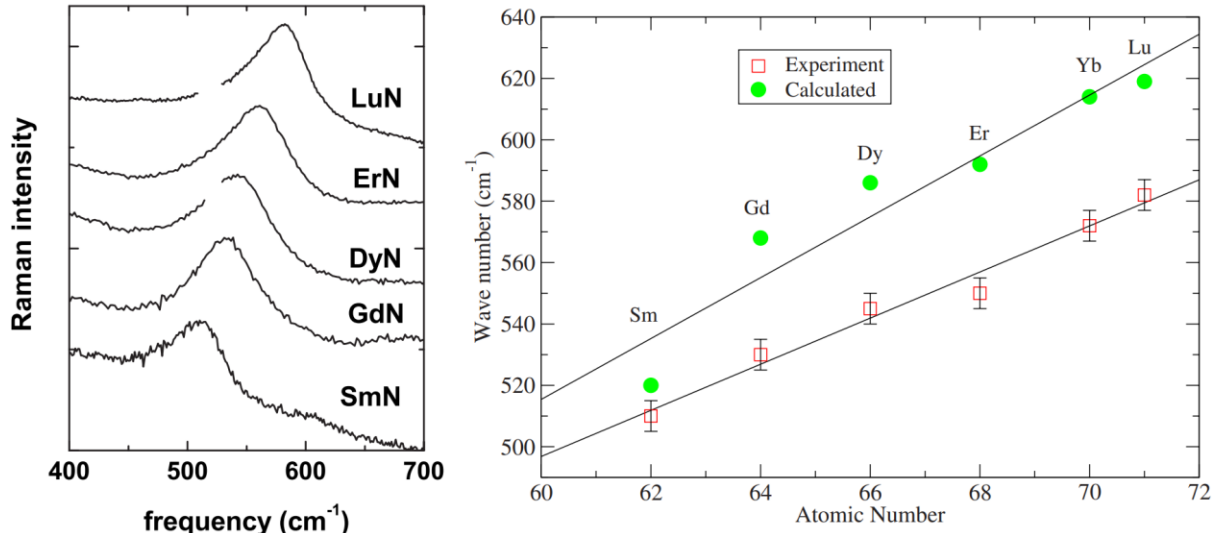


**Figure 5.4:** From Granville *et al.* [129]: **(left)** Raman spectra of SmN, GdN, DyN, ErN, and LuN and **(right)** experimental and calculated LO(L) phonon frequencies versus atomic number. The solid lines are a linear guide for the eyes. Figures reproduced from reference [129].

Historically, Granville *et al.* [129] attributed the appearance of these Raman modes, seen in **Figure 5.4 (left)**, from the nitrogen vacancies within the crystal structure, where the nitrogen vacancy induces a loss of the inversion symmetry, rendering the vibration Raman active. However more recently, Shaib *et al.* have shown that the Raman signal in GdN thin films actually decreased with increasing nitrogen vacancy concentration [80]. They suggested that it is not the vacancies that play a role in the Raman activity and instead proposed the formation of a superlattice structure, which doubles the unit cell in the (111) direction. Currently it is not fully understood what the origin of the rare earth nitride Raman signal is.

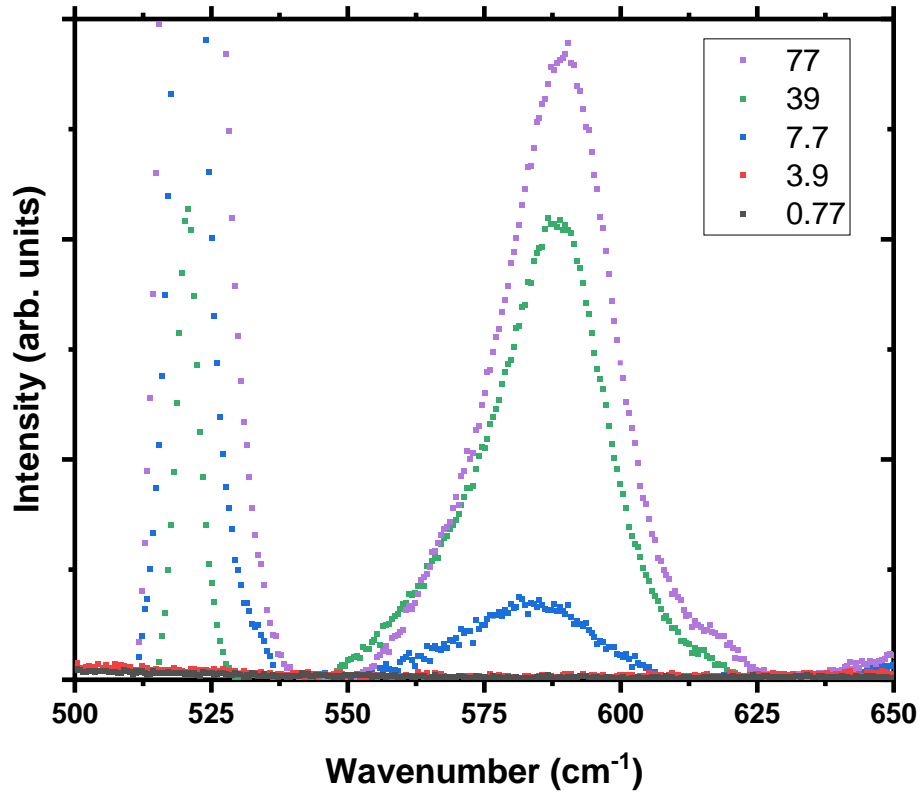


**Figure 5.5:** Raman spectra of LuN films grown at different  $N_2:Lu$  flux ratios. A linear background subtraction has been performed on each spectrum. Note that the films grown at the two lowest  $N_2:Lu$  ratios do not display the REN peak at  $\sim 590\text{ cm}^{-1}$ , likely due to excessive reflectivity.

Raman spectra for the LuN films are shown above in **Figure 5.5**, with the LuN peak at  $\sim 590\text{ cm}^{-1}$ . Clearly for the two samples grown at the lowest nitrogen pressure, no peak is observed. It is worth pointing out that there is also no silicon peak detected ( $\sim 520\text{ cm}^{-1}$ ) for these two films, which suggests that the films are too reflective for the laser to probe the crystal.

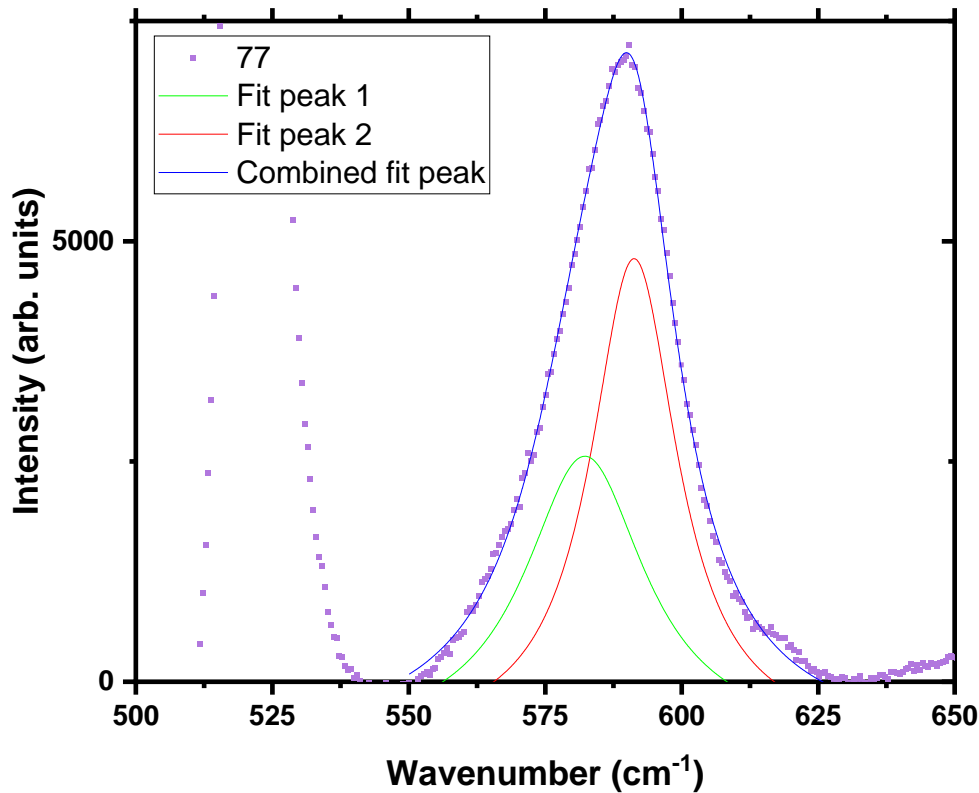


**Figure 5.6:** Raman spectra of LuN films grown at a  $\text{N}_2\text{:Lu}$  flux ratio of 77. A linear background has been subtracted and two Lorentzians (green and red) have been fitted to the raw data (purple), with the combined fit shown (blue). This fit serves as an example fit for the other two films, grown at 39 and 7.7 flux ratios, that have been treated in the same manner.

For the three samples with a Raman signal, the LuN LO(*L*) feature could be fitted using two Lorentzians; one such fit is shown in **Figure 5.6**. The values for peak position and amplitude ratio of the two fits for each sample are shown in **Table 5.4**. The Lorentzian at higher wavenumbers (here called ‘peak 2’) is the dominant peak with a higher intensity, and this dominance increases with increasing nitrogen vacancies, as shown through the increasing value of the amplitude ratio. This suggests that there is a feature of the Raman signal (peak 2) associated with LuN that becomes relatively stronger as the nitrogen vacancy concentration increases, indicating that it is in fact the nitrogen vacancies that provide the loss of inversion symmetry necessary for the observed Raman signal.

<b>N<sub>2</sub>:Lu flux ratio</b>	<b>N<sub>2</sub> growth partial pressure (mbar)</b>	<b>Lorentzian fit peak 1 position (cm<sup>-1</sup>)</b>	<b>Lorentzian fit peak 2 position (cm<sup>-1</sup>)</b>	<b>Amplitude ratio (peak 1:peak 2)</b>
77	1x10 <sup>-4</sup>	582	591	1.22
39	5x10 <sup>-5</sup>	576	589	1.47
7.7	1x10 <sup>-5</sup>	560	584	5.75

**Table 5.4:** The N<sub>2</sub>:Lu flux ratio, N<sub>2</sub> growth pressure, peak positions for peak 1 and peak 2, and peak 1:peak 2 amplitude ratio for the three LuN thin films grown at the highest N<sub>2</sub>:Lu flux ratio.

However, there is an observed decrease in overall peak intensity with decreasing N<sub>2</sub>:Lu flux ratio during growth, which, counterintuitively, seems to indicate that higher densities of nitrogen vacancies result in a weaker Raman signal, though this may be a result of the increased reflectivity of the samples. This would agree with the results of the GdN thin film study by Shaib *et al.* [80] where it is seen that the Raman signal decreased as the nitrogen vacancy concentration increased. Though it is important to note that the reflectivity of the films also increases with decreasing N<sub>2</sub>:Lu flux ratio so the Raman spectroscopy findings here are largely inconclusive.

## 5.4 Magnetic Properties

A quick mention is given to the magnetic properties of, what is reported in literature to be, a non-magnetic compound [136]. One single layer LuN thin film (N<sub>2</sub>:Lu flux ratio of 77) was measured in a Magnetic Properties Measurement System (MPMS) using fields of up to 7 T over a temperature range of 2-300 K.



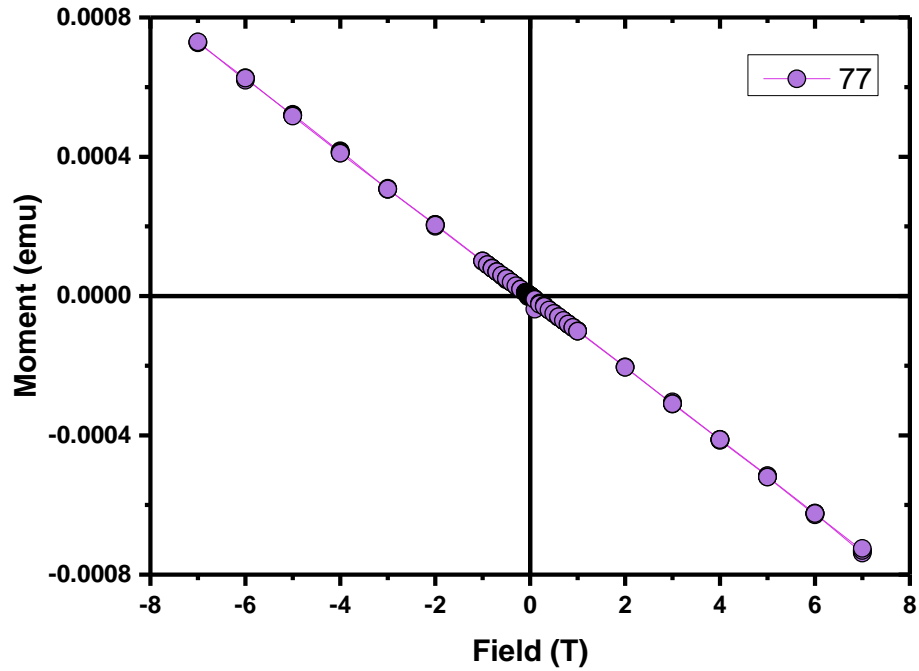


**Figure 5.7:** Magnetic hysteresis loop at 5 K for a LuN thin film grown at a  $\text{N}_2\text{:Lu}$  flux ratio of 77. The field is swept from +7 T to -7 T and then back up to +7 T.

The magnetic hysteresis (MH) loop at 5 K, shown in **Figure 5.7**, is at the lowest measured temperature for this film, so is most likely to be below the Curie temperature of LuN if it were ferromagnetic. However, no ferromagnetic contribution is observed. Instead, we see a weak diamagnetic response, likely from the silicon substrate, and this is consistent across all temperature ranges measured. From this we affirm that LuN is a non-magnetic material; In the completely undoped, stoichiometric LuN thin film, all electron orbitals are full and so there is no spin imbalance to give any ferro- or paramagnetic moment.

## 5.5 Electronic Properties

We begin our discussion of the electronic properties of LuN with ambient temperature optical transmission and reflection measurements conducted from 0.1 eV to 3.5 eV from which

the optical conductivity has been extracted. The following optical conductivity measurements and fitting for the LuN film series were performed in collaboration with Kiri van Koughnet at Robinson Research Institute. Both the substrate and capping layers were independently measured, from which the optical conductivity has been extracted and their optical properties determined to enable the separation of the optical properties of the rare earth nitride layer in isolation.

**Figure 5.8** shows the real part of the optical conductivity for the five LuN films with an increasing concentration of nitrogen vacancies moving from the top panel (a) to the bottom panel (d). In the most insulating film in panel (a), there is no indication of any zero-frequency absorption associated with free carriers at the lowest energies measured. The optical conductivity remains negligible through the mid-infrared region until  $\sim 1.7$  eV where a steep rise indicates the onset of inter-band optical transitions. The shaded area under the curve here represents the intrinsic optical absorption from the undoped material, which is used as a comparison in the following panels. This value of 1.7 eV is slightly higher than the 1.55 eV from historical samples reported in literature, suggesting again that historic samples were not stoichiometric LuN and instead were at least slightly doped with nitrogen vacancies. Additionally, the behaviour shown here for stoichiometric LuN is more consistent with that of a semiconductor, rather than a semimetal, with an observed decrease in bandgap with increased doping via nitrogen vacancies.

Moving down **Figure 5.8** to the next film in panel (b), the onset of optical absorption can be seen at a slightly lower energy, near  $\sim 1.5$  eV. A tail develops, indicating the presence of lower energy transitions, likely due to the introduction of nitrogen vacancies doping the bandgap with defect states. The moderately doped film in panel (c) has a finite zero-frequency conductivity associated with free charge carriers. The free-carrier term centred at zero frequency ( $\omega = 0$ ) has been separated from the inter-band optical transitions, which now begin near  $\sim 1$  eV. These are shown separately as the coloured dashed lines in **Figure 5.8**. The inter-band absorption now also shows an enhancement over the intrinsic absorption from panel (a) at all energies. Finally, the heavily doped film in panel (d) shows an optical conductivity which is dominated by the zero-frequency free-carrier term. The onset of inter-band transitions is now at much lower energy near  $\sim 0.5$  eV, indicating significant changes to the band structure in this heavily doped film. The optical absorption in this film is strongly enhanced compared to the absorption in the undoped film. Using a simple free electron picture, the carrier concentration can be extracted from the part of the optical conductivity centred at  $\omega = 0$ , which is possible for the films in panels (c) and (d). We find carrier

concentrations of  $1 \times 10^{21} \text{ cm}^{-3}$  and  $4 \times 10^{22} \text{ cm}^{-3}$  for these films respectively. The former is comparable to other moderately doped rare earth nitrides [18] while the latter is more similar to the expected carrier concentration of Lu metal.

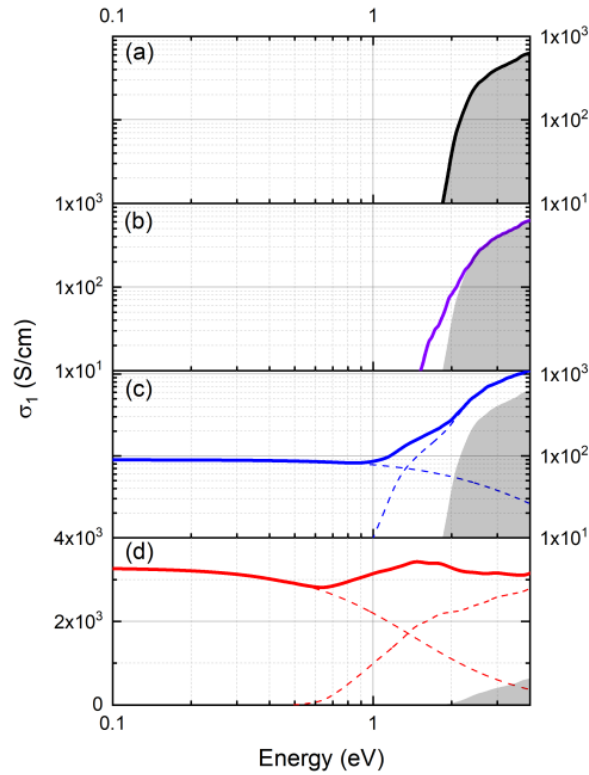


**Figure 5.8:** Optical conductivity measurements of LuN films grown at (a)  $1.4 \times 10^{-4}$  mbar, (b)  $1 \times 10^{-4}$  mbar, (c)  $5 \times 10^{-5}$  mbar, and (d)  $5 \times 10^{-6}$  mbar nitrogen pressure. The shaded area represents the intrinsic optical absorption of the undoped film and is copied consistently across panels for comparison [75].

Clearly as these films are doped with nitrogen vacancies, there are significant changes to the electronic properties. At low energy the development of the zero-frequency free-carrier term is apparent which implies that nitrogen-deficient films have mobile charge carriers, at least at ambient temperature. The red-shift of the optical absorption energy is particularly interesting, as this is opposite to the conventional Moss–Burstein shift and implies some band re-normalisation or additional transitions that are not present in the undoped material [137]. This is discussed later when looking at the calculated band structures.

We now turn to the temperature-dependent DC resistivity of the LuN thin films. Each sample was measured in a Janis closed cycle cryostat from ambient temperature down to 5 K using a Sumitomo F-50 helium compressor using a 4-wire van der Pauw configuration. Across the series, resistivity increases with increasing N<sub>2</sub>:Lu ratio during growth. Looking at the top four samples in **Figure 5.9**, we see the room temperature resistivity increases by over 5 orders of magnitude for an increase of only 2 orders of magnitude for the nitrogen growth pressure, implying massive control over the material conductivity, as seen in the other rare earth nitrides [75]. This is in line with the optical data and the view that the nitrogen vacancies provide free electrons to act as carriers in these films. The room temperature carrier concentration as determined by Hall effect measurements is shown in **Figure 5.10** and shows that the carrier concentration decreases with increasing N<sub>2</sub>:Lu flux ratio, as expected for the observed increase in resistivity. From Hall effect measurements, we find carrier concentrations for the more conductive films grown at a flux ratio of 3.9 and 7.7 of  $5.7 \times 10^{21}$  and  $1.3 \times 10^{22} \text{ cm}^{-3}$  respectively, which is comparable to the range determined from optical measurements ( $1 \times 10^{21} \text{ cm}^{-3}$  and  $4 \times 10^{22} \text{ cm}^{-3}$  respectively).

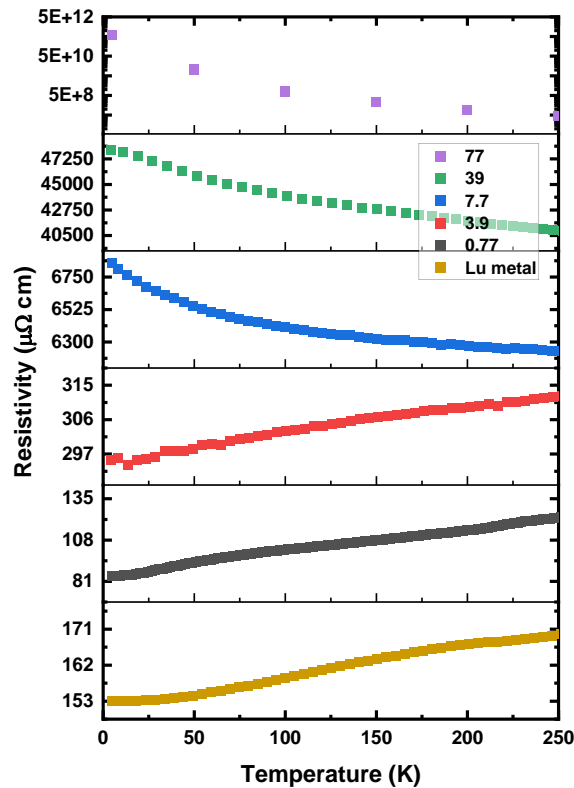


**Figure 5.9:** Temperature-dependent resistivity as a function of the N<sub>2</sub>:Lu ratios for LuN and Lu thin films.

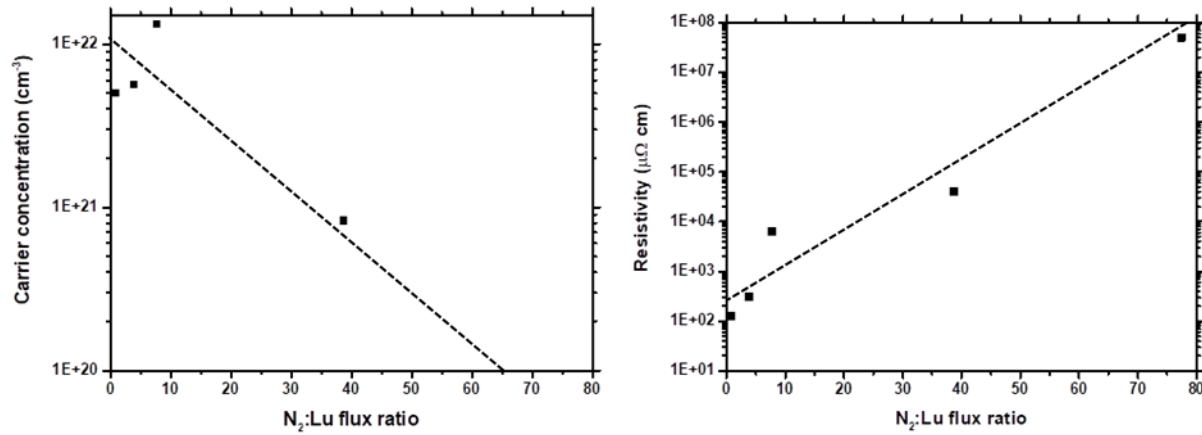


**Figure 5.10:** Ambient temperature carrier concentration (**left**) and resistivity (**right**) of LuN thin films as a function of the N<sub>2</sub>:Lu flux ratio during growth. The dashed lines are added as a guide for the eye. Note the LuN sample grown at a N<sub>2</sub>:Lu flux ratio of 77 was too resistive to measure for Hall effect.

Compared to the ferromagnetic RENs, there is no ‘bump’ in the temperature-dependent resistivity, as is the case for GdN for example [91]. As seen in **Figure 5.11**, the same negative coefficient of temperature is observed for a GdN thin film, down to a temperature near  $T_C$ , at which point the resistivity increases due to the onset of conduction band exchange splitting. As the temperature continues to decrease, the typical thermally activated behaviour is seen again, as resistivity decreases. The absence of such a peak – commonly associated with an onset in magnetic disorder – in the resistivity data for LuN further demonstrates that LuN is a non-ferromagnetic material, as there is no anomaly in resistivity due to magnetic disorder at any temperature.

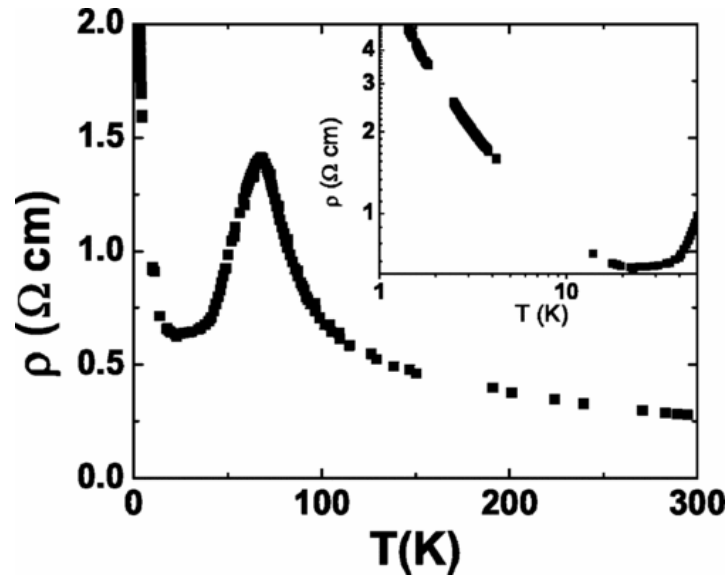


**Figure 5.11:** Temperature-dependent resistivity of a GdN thin film from Granville et al. [91] demonstrating a peak in resistivity around 68 K, corresponding to the measured  $T_C$  for this film. The inset shows the low temperature behaviour of the resistivity. Figure reproduced from reference [91].

For the samples grown at the three highest nitrogen pressures, there is a clear negative temperature coefficient of resistance (TCR), in agreement with behaviour for insulating/slightly doped-semiconducting materials, with the resistivity looking to diverge at the lowest temperatures measured for the most resistive sample. The two least resistive LuN films and the Lu metal film all show a positive TCR and metallic/heavily doped-semiconductor behaviour, in agreement with the optical conductivity data. The Lu metal sample shown here displays slightly higher resistivity than expected (by an order of  $\sim 3$ ), likely due to the lack of annealing and growth parameter optimisation [138].

The resistivity data in **Figure 5.9** above are consistent with electrons being doped into disorder-driven localised states forming in the bottom of the conduction band [82,139]. At low levels of doping with nitrogen vacancies, carriers occupy states below a mobility edge, and as the doping increases, these occupied states cross and eventually lie above the mobility edge, becoming delocalised. The film grown at the highest  $N_2:Lu$  ratio (purple) in **Figure 5.9** has a diverging resistivity implying only a small population of carriers in localised states near the bottom of the conduction band below a mobility edge. The two moderately doped films (green and blue) appear

to have a finite zero temperature conductivity which implies the Fermi energy lies above the mobility edge, however the small negative temperature coefficient of resistivity suggests there is still sufficient disorder to drive localisation effects, rather than full extended state conduction. Finally, the two films grown at the lowest (non-zero)  $\text{N}_2\text{:Lu}$  ratios (red and black) have a metallic-like temperature dependence, highlighted by the similar shape to the temperature-dependent resistivity of the Lu metal thin film (gold), indicating that the Fermi energy lies in extended states well above the mobility edge. Having found the bandgap of stoichiometric LuN to be  $\sim 1.7$  eV, we can use this value to inform band structure calculations.

## 5.6 Computational Band Structure

### 5.6.1 Background

We now turn to the computational band structure calculations. The  $4f$  electrons of the rare earth nitride series are strongly correlated and thus require careful treatment beyond the basic density functional theory (DFT) [116,136]. To account for this, we must consider additional corrections, known as U parameters.

In DFT, the functional is the electronic density, in contrast to the electronic wavefunction used in other computational theories. This greatly reduces the computation time when using DFT, allowing for calculations on larger, many-bodied systems as the electronic density is a function of just three spatial variables, compared to electronic wavefunction which has  $3N$  variables depending on the number ( $N$ ) of electrons in the system. To describe the RENs, we use the local-spin density approximation (LSDA) – which is an extension of the local-density approximation (LDA) – that considers electron spin to allow for more accurate calculations on, for example magnetic materials. Both of these approximations assume that the exchange-correlation energy of the system can be described by the local energy density at the point where the functional is evaluated.

In the basic DFT, using solely local spin density approximation, the  $4f$  states in the rare earth nitride would mostly be found at the Fermi energy. However, the strongly correlated nature of these electrons actually pushes the filled states below and unfilled states above the Fermi energy. It has been shown that this physics can be largely captured using the DFT+U method [140–143],

and so here we use two  $U$  parameters:  $U_f$  which accounts for the strongly correlated  $4f$  states and  $U_d$  which is an empirical correction applied to the  $5d$  states which has been extensively used to match the optical band gap to the experimental value, as for GdN and SmN [78,116,136].

A common method to estimate  $U_f$  is to match the location of the  $4f$  states in the valence band to experimental photo-emission data. However, as we do not have photo-emission data available for LuN, either for the samples in this chapter or in literature, to overcome this issue we used the same approach as Larson *et al.* [116]: We completed a separate band structure calculation of GdN with  $U_f(\text{Gd})$  matched to the available photo-emission data [144], and from there we have scaled  $U_f(\text{Gd})$  by the ratio of the Slater-Coulomb integrals  $F_0$  for  $\text{Gd}^{3+}$  and  $\text{Lu}^{3+}$  to estimate  $U_f(\text{Lu})$ . This gave us a value of  $U_f(\text{Lu}) = 7.14$  eV. The  $U_d$  parameter is chosen to match the bandgap as found from our LuN optical data, in the same way as done by Trodahl *et al.* for GdN [78]. We have not changed the value of  $U_d$  and  $U_f$  between the undoped and vacancy-doped cell of LuN.

## 5.6.2 Computational Details

Calculations were undertaken using Quantum Espresso and the rare earth pseudo-potentials used were developed by Topskał *et al.* [145]. For the undoped stoichiometric crystal, calculations were undertaken on the primitive unit cell with a two-atom basis in the FCC rock-salt structure. To model the nitrogen vacancy-doped material, one N atom was removed from a  $3 \times 3 \times 3$  super-cell, which is comprised of 27 Lu atoms and 26 N atoms and corresponds to a vacancy concentration of  $\sim 3\%$ . The supercell was fully relaxed to accommodate this vacancy. The supercell band structure was unfolded so that it can be easily compared to the band structure of the primitive unit cell [146]. For self-consistent calculations, the primitive cell Brillouin zone was sampled with a grid of  $12 \times 12 \times 12$  k-points, supercell calculations were sampled on a  $4 \times 4 \times 4$  grid. The wave function and charge density cut-off energies were 50 Ry and 200 Ry respectively for all calculations. Non-self-consistent calculations for the density of states (DOS) were sampled on  $16 \times 16 \times 16$  grids for both the primitive and supercell calculations.



### 5.6.3 Results

The calculated band structure is shown in **Figure 5.12** for the stoichiometric (left) and doped (right) crystals, including the DOS on the right panel. Looking first at the band structure of stoichiometric LuN, the Lu  $4f$  electrons can be found in flat bands roughly 8 eV below the valence band maximum (maximum at  $\Gamma$ ), while the remainder of the valence band shown here consists of the Lu  $5d$  and N  $2p$  band, which hybridise between 0 and -4 eV. The conduction band is formed largely from the Lu  $5d$  bands with the minimum found at X, the point where optical transitions begin, which has been matched to the optical data from **Figure 5.8**.

By introducing one nitrogen vacancy into the lattice, defect states are created throughout the band structure (**Figure 5.12 right**) and three electrons are provided to the system, as inferred by the fact that the Lu and N ions all retain their  $3+$  and  $3-$  charges respectively. This is similar to results obtained for calculations on doped SmN, where inclusion of a nitrogen vacancy introduced substantial disorder to the calculated band structure. The six Sm ions nearest to the nitrogen vacancy shared one of the released electrons, each having an intermediate valence state of between  $2-3+$ , however the majority of Sm ions retained their  $3+$  state [73].

One electron can be found in a defect state at the bottom of the Lu  $5d$  band,  $\sim 1$  eV above the conduction band minimum. This suggests that increasing nitrogen vacancies in the crystal dopes the system with electrons available for electrical transport, decreasing the resistivity, in line with the experimental electrical transport presented above.

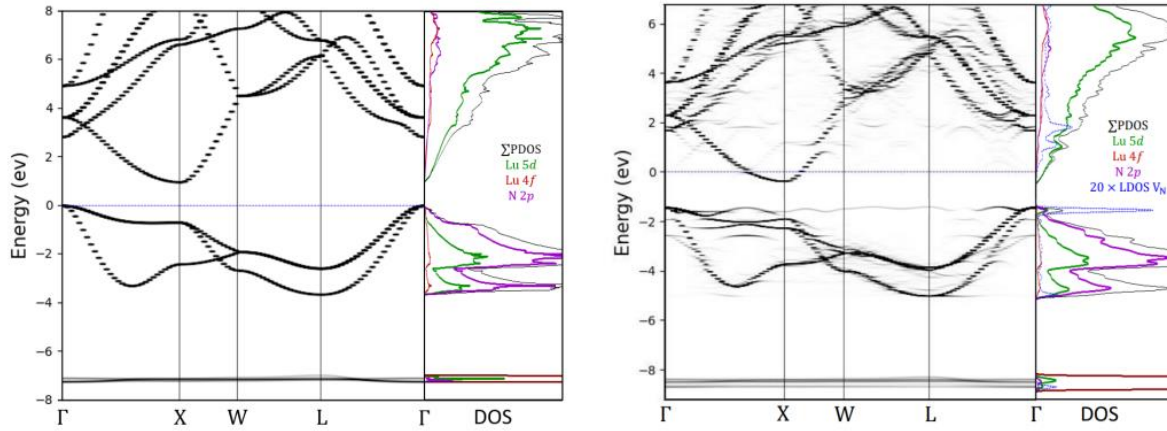


**Figure 5.12:** Calculated band structure for undoped (**left**) and doped (**right**) LuN crystal lattices. The undoped film has a simulated nitrogen vacancy concentration of ~3%. The density of states is shown on the right of each band structure [76].

It is worth pointing out that there is a particularly prominent defect state that is flat and localised near the valence band maximum. The DOS is shown to the right of the calculated band structure in **Figure 5.12**, as well as the localised DOS (LDOS) and it can be seen that this defect state corresponds to two electrons localised to the nitrogen vacancy site, subsequently representing the other two electrons provided by the nitrogen vacancy.

This defect band now forms the initial state of the minimum optical gap, just above the valence band maximum, with the final state located at the Fermi energy in the Lu 5d band. The energy of this transition is ~1.5 eV, matching the value found from experimental optical transitions in **Figure 5.8**. These defect states are a result of the inclusion of nitrogen vacancies, so with increased doping of these vacancies, we would expect a higher density of these states, leading to the enhanced optical absorption observed in the doped films. That is, the presence of nitrogen vacancies increases both the concentration of filled initial states near the valence band maximum as well as the density of final states in the conduction band. At high enough doping levels, an extended metallic-like state could arise, in line with the electrical behaviour observed for LuN films grown at the lowest nitrogen growth pressures, through the filling of these defect states that form the optical gap.

## 5.7 Conclusion

In this chapter, we have investigated the effect of the  $\text{N}_2\text{:Lu}$  flux ratio during the growth of LuN polycrystalline thin films on the structural, electrical, and optical properties.

We observe a non-changing lattice constant of 4.79 Å across LuN samples. We have found stoichiometric LuN to be a non-magnetic semiconductor with an indirect bandgap of ~1.7 eV. We have shown that the doping of LuN thin films via nitrogen vacancies can be controlled through consideration of the  $\text{N}_2\text{:Lu}$  flux ratio during growth and the introduction of each vacancy dopes the crystal lattice with three electrons that reside in defect states about the valence band maximum and conduction band minimum.

Electrical transport measurements show that stoichiometric LuN is an insulating material with an indirect bandgap and diverging resistivity at low temperature which changes as the films are doped with nitrogen vacancies to become increasingly conductive, eventually with a metallic-like, finite resistivity at low temperature.

Through band structure calculations of one undoped LuN crystal and one LuN crystal doped with ~3% nitrogen vacancies, we show that each nitrogen vacancy provides three electrons to the cell: one in a defect state at the bottom of the conduction band minimum, and two in the valence band maximum.

Finally, we propose that the bandgap of LuN is suitable to be used as a tunnel barrier in a REN-based MTJ structure. The bandgap of stoichiometric LuN is found to be 1.7 eV, higher than many of the other RENs, including GdN (0.98 eV), SmN (0.7 eV), and DyN (0.91 eV) [116,117]. This opens further paths and opportunities for REN-based devices and potentially epitaxial compatibility with existing REN device structures in the future.

## Chapter 6

# Gadolinium Nitride and Dysprosium Nitride as Ferromagnetic Materials in Trilayer Structures

### 6.1 Introduction

The development of cryogenic memory storage devices using semiconducting materials is crucial for providing a scalable and energy efficient solution for integration with future superconducting computing platforms and the next generation of data centres [1,7,50,57,147]. In this chapter we describe a number of trilayer structures incorporating GdN and DyN as FM layers. We have constructed a fully REN-based magnetic tunnel junction (MTJ) using LuN as the tunnel barrier layer and two giant magnetoresistance (GMR)-style devices using Lu and Al as the exchange blocking (EB) layers. Temperature- and field dependent-magnetic measurements confirmed that the two FM layers were magnetically isolated from one another. Retention of the anti-aligned state at zero-field was observed in both device structures. The LuN MTJ had a resistance difference of  $\sim 1.2\%$  at 0 T between the aligned and anti-aligned states, while the Lu GMR-style device had a difference of  $\sim 0.04\%$ . The GMR-style device using Al as an EB layer did not exhibit hysteresis in the magnetoresistance measurements.

One publication related to the results of this chapter has been published [148]:

S. Devese, C. Pot, F. Natali, S. Granville, N. Plank, B. J. Ruck, H. J. Trodahl, and W. Holmes-Hewett, *Non-Volatile Memory Storage in Tri-Layer Structures Using the Intrinsically Ferromagnetic Semiconductors GdN and DyN*, Nano Ex. **3**, 045007 (2023).

### 6.2 Device Structure

So far, in this thesis, we have focussed on magnetic tunnel junctions as the building block structure to demonstrate the potential use of RENs in memory storage devices. Of course, many other device structures exist [1,11,41,50,58]. The inherent high resistance of the MTJ limits its

incorporation with superconducting electronics as an energy efficient memory element platform, as the step up in resistance between components will negate any benefits of the hybrid circuitry. Here, we present a low resistance alternative that utilises a similar trilayer structure with two REN FM layers, but now is in the form of a current in-plane (CIP) giant magnetoresistance-style geometry with a metallic layer between the FM layers.

### 6.2.1 Giant Magnetoresistance

The giant magnetoresistance effect is the phenomenon observed in magnetic materials whereby the resistance of a multilayer structure changes greatly when exposed to an external magnetic field as compared to the magnetic material by itself. Its discovery is often attributed independently to both Albert Fert in 1988 [14] and Peter Grünberg in 1989 [47]. The first observation of GMR was using multilayers of ferromagnetic Fe and non-magnetic Cr, each layer on the order of 10 nm, with current passed in-plane relative to the film (CIP). This is highlighted in **Figure 6.1**, which compares the relative change in resistance as a function of magnetic field between an Fe/Cr multi-layered structure and an Fe thin film.

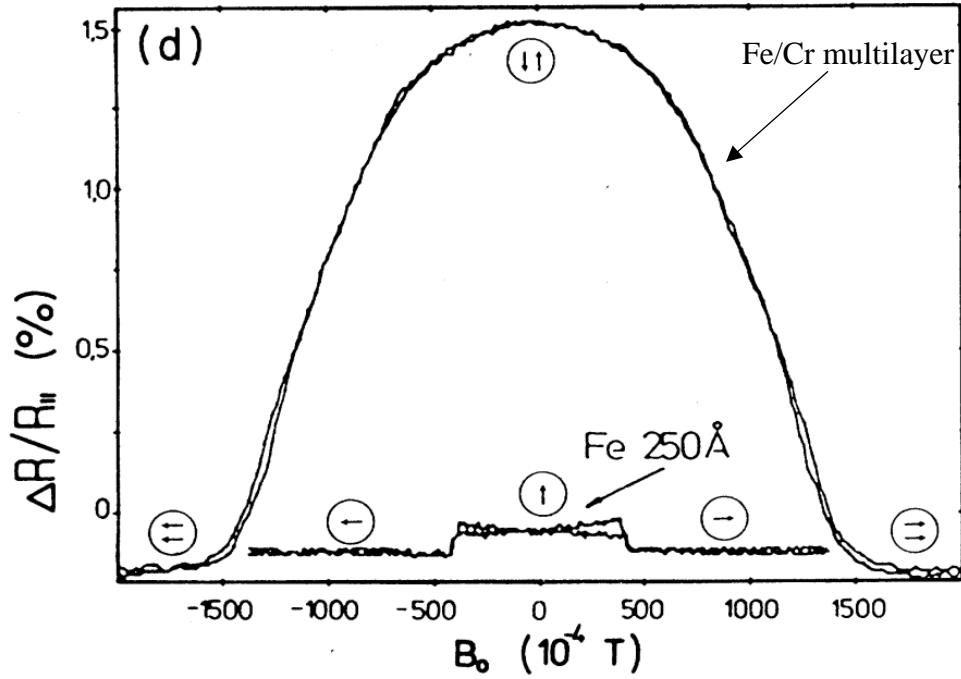


**Figure 6.1:** Relative change in resistance as a function of magnetic field for a Fe/Cr multi-layered structure (**top**) and a single-layered Fe thin film (**bottom**). The overall change in magnetoresistance is much greater for the multi-layered structure. The relative magnetic alignment for each structure is shown where relevant. Figure reproduced from reference [47].

As with TMR, the magnitude of the GMR is characterised by:

$$GMR = \frac{(R_{AP} - R_P)}{R_{AP}} \quad (6.1)$$

where  $R_{AP}$  is the resistance when the FM layers are in the anti-parallel (AP) configuration, and  $R_P$  is when the FM are in the parallel (P) configuration. GMR values tend to decrease as individual layer thickness increases but increases with the number of layers [149]. Specifically, GMR decreases exponentially with the non-magnetic layer thickness and as the inverse of the thickness of the magnetic layers. This is a result of scattering that occurs within the non-magnetic layer.

Descriptions of electron scattering in materials exist for cases with and without spin-flipping – the phenomena where propagating electrons change their spin orientation [150–152]. The mean distance over which electrons travel without flipping their spin is known as the spin-diffusion length of a material. Early experiments measured the spin diffusion length in Al and found it to be  $\sim 450$   $\mu\text{m}$  at 4 K, which was relatively long compared to the thicknesses of the thin film layers being measured and thus spin-flipping effects were assumed to be negligible [152–154]. Estimates of the spin diffusion length of Al at 4 K were later reassessed and modified to the order of  $\sim 500$  nm [155,156].

As the spin-diffusion length for more materials was measured, it was found that Al had a longer spin-diffusion length than most other materials, and so this effect needed to be taken into more consideration for systems where preservation of the electrons' spin orientation was of importance, such as for GMR-style structures. The presence of spin-orbit coupling tends to decrease spin diffusion lengths in materials and so the rare earths don't immediately present themselves as the obvious choice for the conductive layer in a GMR-style device [157–159]. However, Lu has a fully filled  $4f$  orbital and therefore relatively reduced spin-orbit coupling as compared to the rest of the rare earth series [160]. The spin diffusion length in Lu should be comparable to other non-magnetic heavy metals, such as Pt or Pd, on the order of 10 nm [152].

In a trilayer structure with two FM layers, the magnetisation of the FM layers influences the spin of the electrons flowing in the conductive EB layer. The exact influence depends on the geometry of the structure, namely the direction of current flow relative to the plane of the layers, as discussed below.

### 6.2.2 Current Perpendicular-to-Plane vs Current-In-Plane

The previously discussed magnetic tunnel junction utilises a trilayer structure with electrical measurements performed using current in the direction perpendicular to the plane of the film layers, so-called CPP. This is highlighted in **Figure 6.2a** and forces the electrons to tunnel across the insulating tunnel barrier between the two FM electrodes. In contrast, we introduce a second trilayer structure where current is passed in-plane to the film layers, so-called CIP,

highlighted in **Figure 6.2b**. We have used LuN and Lu as example EB layers for these schematics but will also present a third device in the CIP geometry which uses Al as an EB layer.

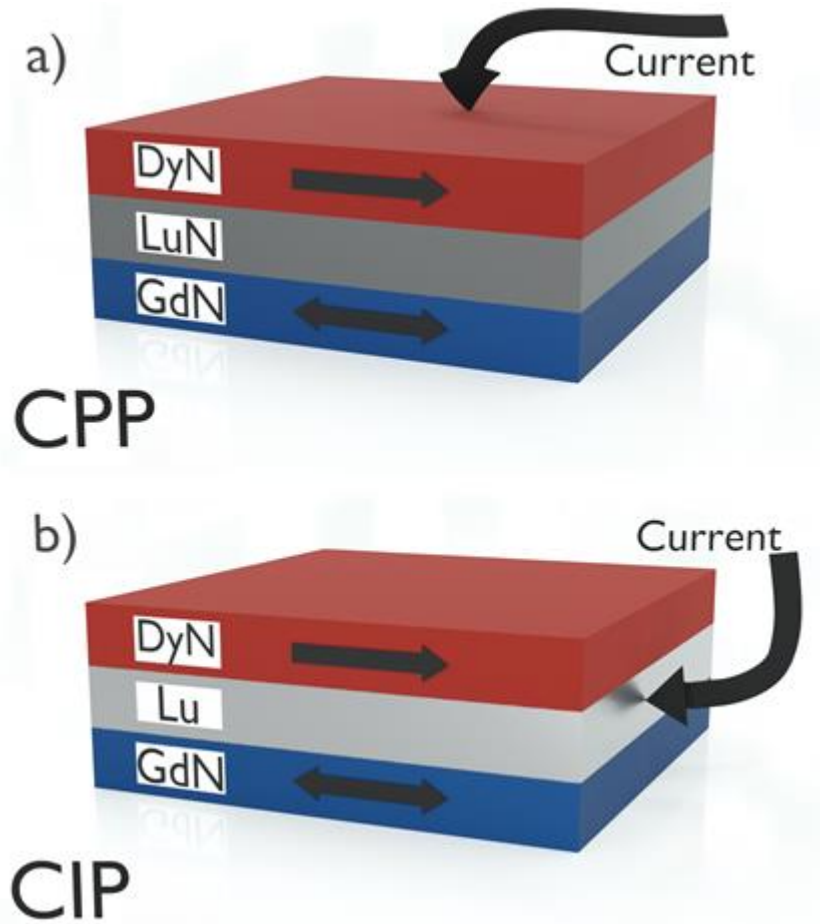


**Figure 6.2:** Schematic showing the current flow direction and relative magnetisation (**black arrows**) of the GdN (**blue**) and DyN (**red**) layers (not to scale). The high resistance magnetic tunnel junction is shown with an insulating LuN barrier (**grey**) and current perpendicular to plane (**a**). The low resistance in-plane conduction device is shown with a conductive Lu (**silver**) exchange-blocking layer (**b**). Note that the second CIP device with Al as the blocking layer was of the same general structure.

The effect of the magnetisation direction in the FM layers on the spin of electrons (and subsequent device resistance state) for the MTJ CPP geometry has been previously discussed in **Chapter 4**. Briefly, the relative alignment of the two FM layers facilitates majority-majority or



majority-minority band transport across the insulating barrier for the aligned or anti-aligned states respectively, resulting in a relatively low- or high-resistance state.

For the CIP geometry, the magnetisation in the FM layers influences the electrons' spin through scattering effects at the interface of the EB and FM layers [161,162]. Electrons that collide with the interface have a chance to be spin flipped to the same orientation as the magnetisation in the FM layer. For the aligned state, this means that electrons scattered by both FM interfaces would be flipped to the same orientation, resulting in nominally fewer flipping events, and therefore relatively lower measured resistance in the conductive EB layer. In the anti-aligned state, electrons scattering off one interface would then be spin-flipped at the other interface, yielding a relatively higher measured resistance.

The in-plane conduction of the CIP geometry removes the requirement of patterning via photolithography and here we use a van der Pauw electrical measurement setup, shown in **Figure 6.3**.

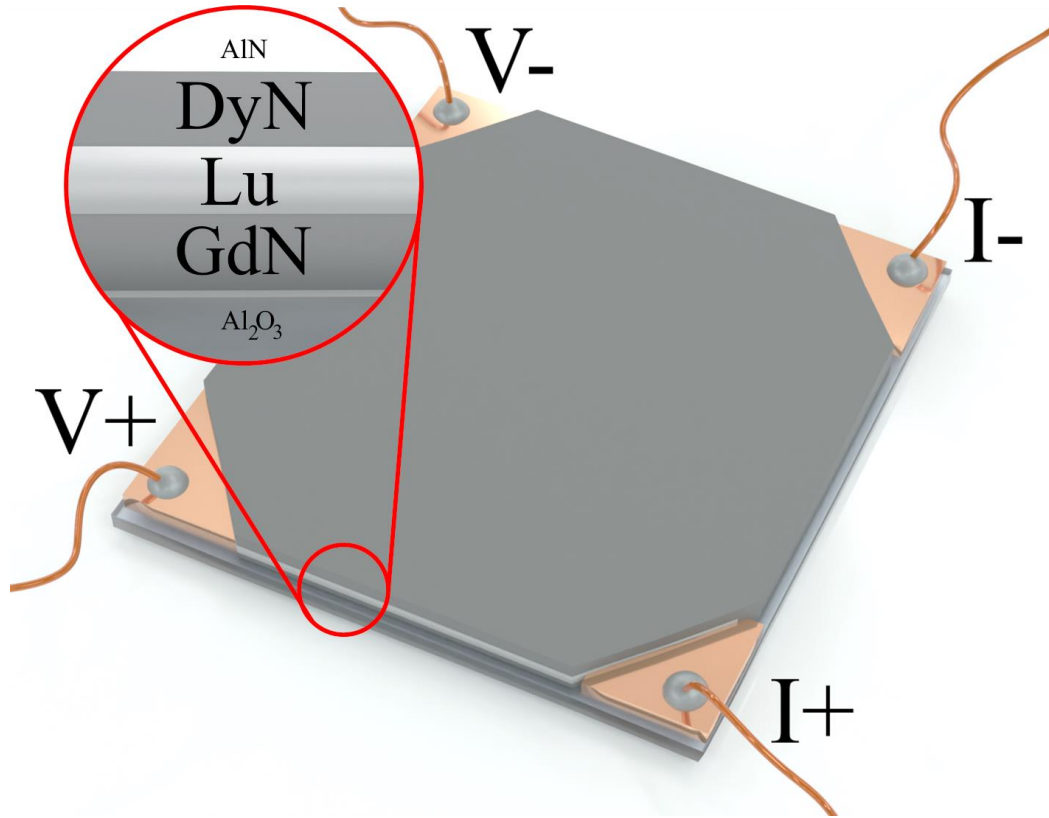


**Figure 6.3:** Schematic showing the electrical van der Pauw contacts on a device in the GMR-style geometry used for the in-plane conductivity device. Copper wires are attached to pre-deposited gold contacts using silver paint. The zoom highlights the trilayered structure for the in-plane conductivity device, with Lu as the example blocking layer, on top of the Al<sub>2</sub>O<sub>3</sub> substrate and capped with a layer of AlN. Layers are not to scale.

It is worth noting that GMR devices can be made using the CPP geometry, and indeed tend to exhibit higher GMR effects [150,163,164]. This is typically done using metallic ferromagnets which are electrically conductive and do not contribute significant resistance to the overall measurement. Here, we used semiconducting ferromagnets which would introduce non-negligible resistance if the current was measured perpendicular to plane. To reduce this effect, the RENs could be made to be more conductive by doping with nitrogen vacancies during the growth process, although this was not explored here. Instead, we focussed on in-plane conduction through the conductive EB layer for the GMR-style devices.

For the CIP geometry, the majority of the current needs to be flowing through the conductive EB layer. To attain this, the REN FM layers were grown to be stoichiometric, or at

most, lightly doped with  $V_N$ . For the CCP geometry, the opposite is desired: the EB layer must be the dominant source of resistance. We have shown that this can be achieved with an appropriate tunnel barrier that induces a tunnelling current (**Chapter 4**). In this way – for the conductivity range of doped RENs and the active areas of the *caissons* used – any level of doping will be sufficient for the measured resistance to be an accurate representation of the barrier layer. We have also shown that LuN has a bandgap of  $\sim 1.7$  eV, larger than any of the other RENs and in particular GdN ( $\sim 1$  eV) and DyN ( $\sim 0.9$  eV) (**Chapter 5**) [76,78,79,89]. In this chapter we combine these findings and construct a MTJ trilayer where all three layers are RENs.

## 6.3 GdN/EB/DyN Devices

### 6.3.1 Fabrication, Growth, and Experimental methods

All layers were grown in a molecular beam epitaxy (MBE) system with a base pressure of  $\sim 1 \times 10^{-9}$  mbar. The FM rare earth nitride layers were grown by evaporating metallic Gd or Dy in an atmosphere of  $\sim 2 \times 10^{-4}$  mbar of  $N_2$ . While the FM layers for all devices were grown using similar/identical conditions, the differing nature of the two device structures required significantly different growth conditions for their respective EB layers.

As mentioned, one high impedance MTJ device was grown using an insulating EB layer and two low impedance GMR devices were grown using a conductive EB layer. The insulating EB layer,  $\sim 8$  nm of LuN, was grown by evaporating Lu in an atmosphere of  $N_2$  (partial pressure  $\sim 2 \times 10^{-4}$  mbar), similar to the FM rare earth nitride layers described above. The conductive Lu EB layer ( $\sim 20$  nm thick) was grown by evaporating Lu at the base pressure of  $\sim 1 \times 10^{-9}$  mbar while the  $\sim 40$  nm thick Al layer was grown by evaporating Al from an effusion cell set to  $1140^\circ\text{C}$ . Each GMR-style device was simultaneously grown on polished  $Al_2O_3$  and Si substrates, which were held at ambient temperature throughout the growth. The MTJ was grown using the previously described *caisson* geometry on Si/SiO<sub>2</sub> substrates. A protective layer of  $\sim 40$  nm thick AlN or Al was used to protect all the devices from oxidation. Insulating AlN was used for the low-impedance device to prevent current flow through the capping layer, while conductive Al was used for the high-impedance devices to act as a top electrical contact and allow current flow.

These materials were chosen as capping layers because the different geometries of the two device structures meant that different electrical contacts were needed. Electrical contact was made to the low-impedance GMR devices via Au bottom contacts in a van der Pauw configuration, which were deposited using a shadow mask in a separate growth before the trilayer deposition. In contrast, electrical measurement for the high-impedance tunnelling device comprised of vertical transport from the pre-deposited Au layer, through the device in the *caisson* structure, to the metallic Al protective layer, as described in previous chapters.

## 6.3.2 Results

We begin by discussing the magnetic results in general for both devices. This is followed by a discussion of the electronic behaviour without an external magnetic field and the magnetoresistance characteristics with an external magnetic field, including memory facilities for both the high- and low-impedance devices.

### 6.3.2.1 Magnetic Behaviour

The temperature-dependent magnetisation is shown in **Figure 6.4** for the GdN/Lu/DyN trilayer structure (grey) of the low impedance device. Also shown are the same measurements for single-layer GdN (blue) and DyN (red) polycrystalline thin films. The first derivative, shown in the inset, highlights the distinct magnetic transitions of GdN near 60 K and DyN near 30 K. The two distinct transitions in the trilayer data indicate that the two layers were magnetically isolated from each other by the non-magnetic EB layer, in this case Lu. Similar behaviour was observed for the high impedance device using LuN as the EB layer.

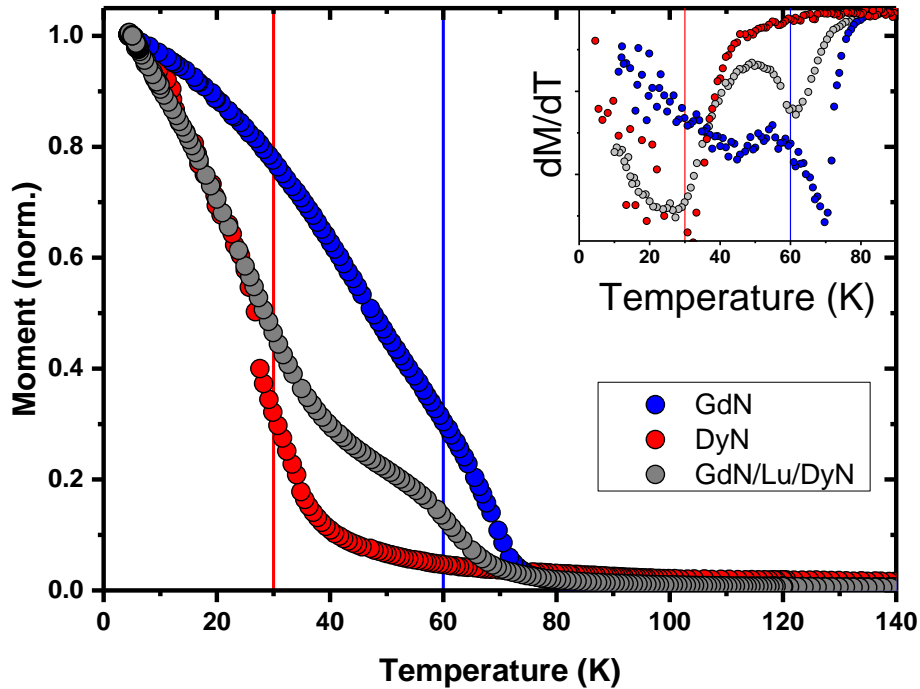


**Figure 6.4:** Temperature-dependent magnetic moment for the GdN/Lu/DyN tri-layer structure (grey) when cooled in an external magnetic field of 0.025 T. Similar measurements for GdN (blue) and DyN (red) are shown with the ferromagnetic transition temperatures for GdN (blue line at ~60 K) and DyN (red line at ~30 K) shown to highlight the two transitions seen in the tri-layer structure. The inset shows the first derivative of each curve.

The field-dependent magnetisation at 5 K is shown in **Figure 6.5**. The saturation magnetisation has been normalised for the three samples, though it is noted that the absolute saturation magnetisation was largest for the GdN film, with the GdN film having the relatively smaller coercive field compared to DyN (~0.04 T vs. ~0.16 T). The sloping shape of the overall hysteresis loop was consistent with the films being polycrystalline in nature. There was the presence of a slight ‘wasp-waist’ feature in the trilayer structure, where there is a narrowing and subsequent expanding of the hysteresis loop around low-field, which is indicative of two different magnetic contributions. Similar measurements were made for the other trilayer structures GdN/Lu/DyN and GdN/LuN/DyN suggesting that the FM layers have similar magnetic properties between devices, though the wasp-waist feature in these structures was noticeably less pronounced.

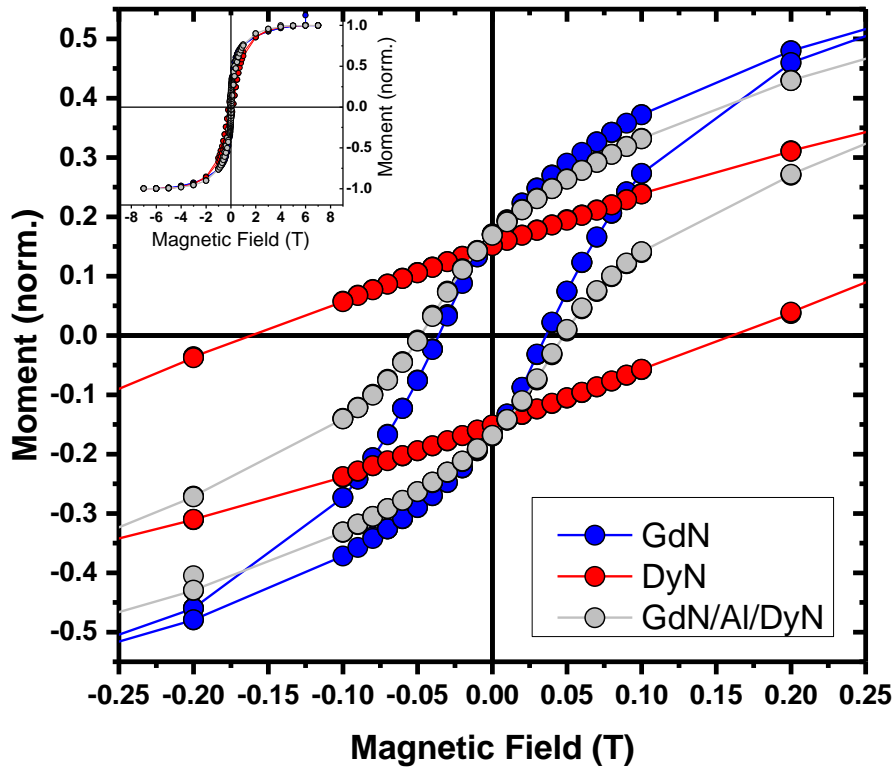


**Figure 6.5:** Field-dependent magnetisation of the GdN/Al/DyN trilayer structure (grey) at 5 K. A so-called wasp-waist can be seen at low fields, due to the different coercive fields of each ferromagnetic layer. Data for single layer GdN (blue) and DyN (red) thin films grown in similar conditions are also shown. The inset shows the same measurement over the full  $\pm 7$  T range.

These magnetic measurements show that the FM layers in all devices are sufficiently decoupled from one another and so we now move on to the electrical transport through the EB layer.

### 6.3.2.2 Electrical Transport

We will discuss the electrical transport of the high- and low-impedance devices separately, starting with the high-impedance device. The temperature-dependent resistance for the GdN/LuN/DyN device is shown in **Figure 6.6** and varied depending on the applied current. This

was consistent with previously shown MTJs in this thesis and the deviation from Ohm's Law signalled a tunnelling current [165,166]. The device exhibited a negative temperature coefficient of resistance with a noticeable peak around 30 K. This feature is commonly attributed to the onset of magnetic order associated with the FM transition in RENs [87,91].

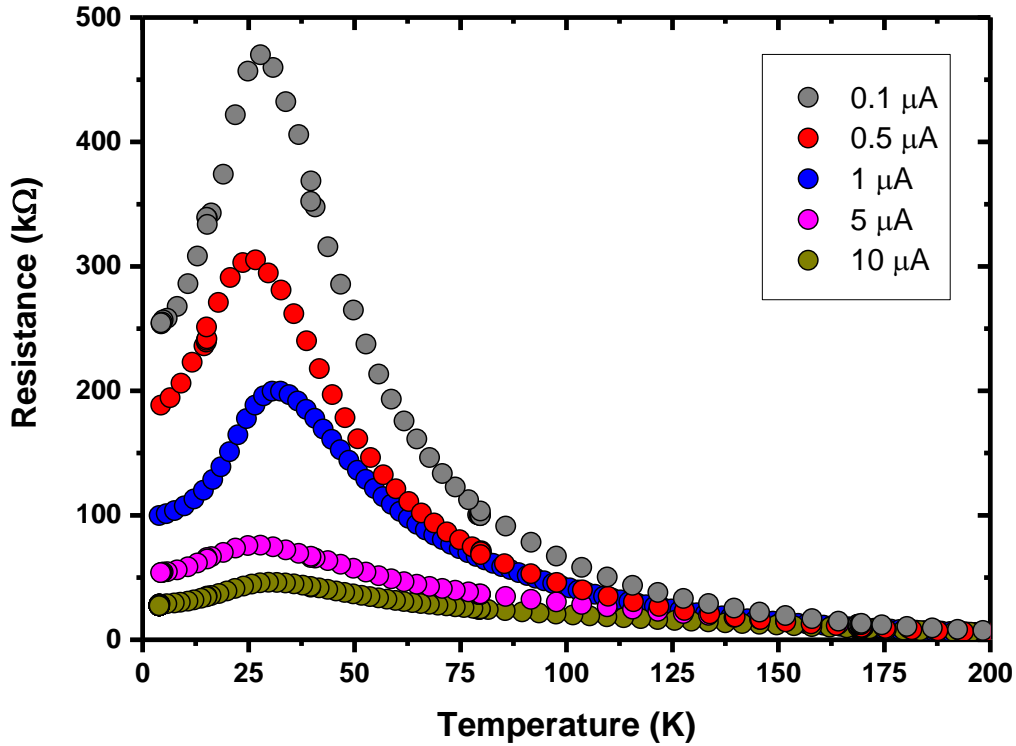


**Figure 6.6:** The temperature-dependent resistance for the  $100 \times 100 \mu\text{m}^2$  GdN/LuN/DyN magnetic tunnel junction measured at different applied currents.

The non-linearity is further highlighted in the current-voltage plot shown in **Figure 6.7**. Linear behaviour was observed at low voltages at all temperatures measured. However, for voltages above  $\sim 0.1$  V it can be seen that the MTJ exhibited non-linear current-voltage characteristics at all temperatures measured, with stronger non-linearity at lower temperatures.

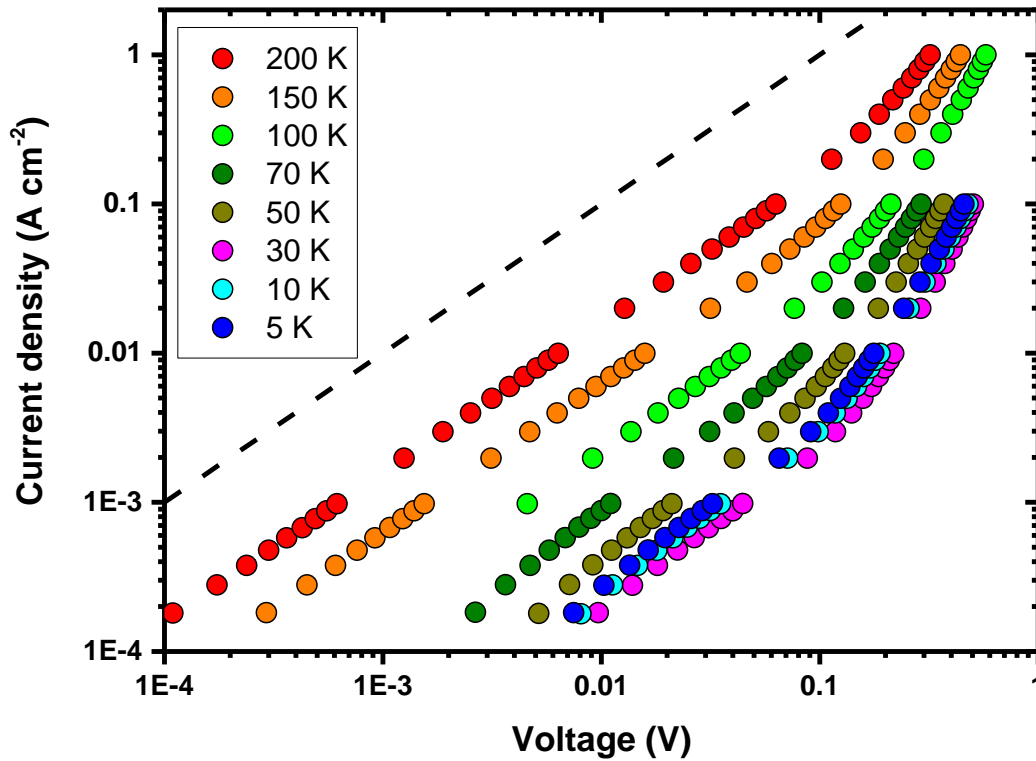


**Figure 6.7:** Logarithmic plot of the current-voltage behaviour for the  $100 \times 100 \text{ } \mu\text{m}^2$  GdN/LuN/DyN magnetic tunnel junction. A linear relationship can be seen at lower voltages, with a non-linear regime developing above voltages of  $\sim 0.1 \text{ V}$ . The dashed line is added as a guide to the eye for a gradient of unity.

The lowest temperature (5 K) data was fitted using the Simmons model, as shown in **Figure 6.8**, yielded a fit with  $R^2 = 0.996$ . The Simmons barrier width from this fit was 3.0 nm, compared to the nominal 8 nm, and the Simmons barrier height was 1.14 eV. As with previous MTJs, a deviation in the fit from the data occurred at low voltages. By adding a linear term to the Simmons model to account for any Ohmic current within the device (e.g. pinholes), the Simmons model fit the data with  $R^2 = 0.999$ , and the Simmons barrier width decreased to  $\sim 1 \text{ nm}$  while the Simmons barrier height increased to 10.0 eV. Despite the better fit, the Simmons parameters moved further away from the expected values.



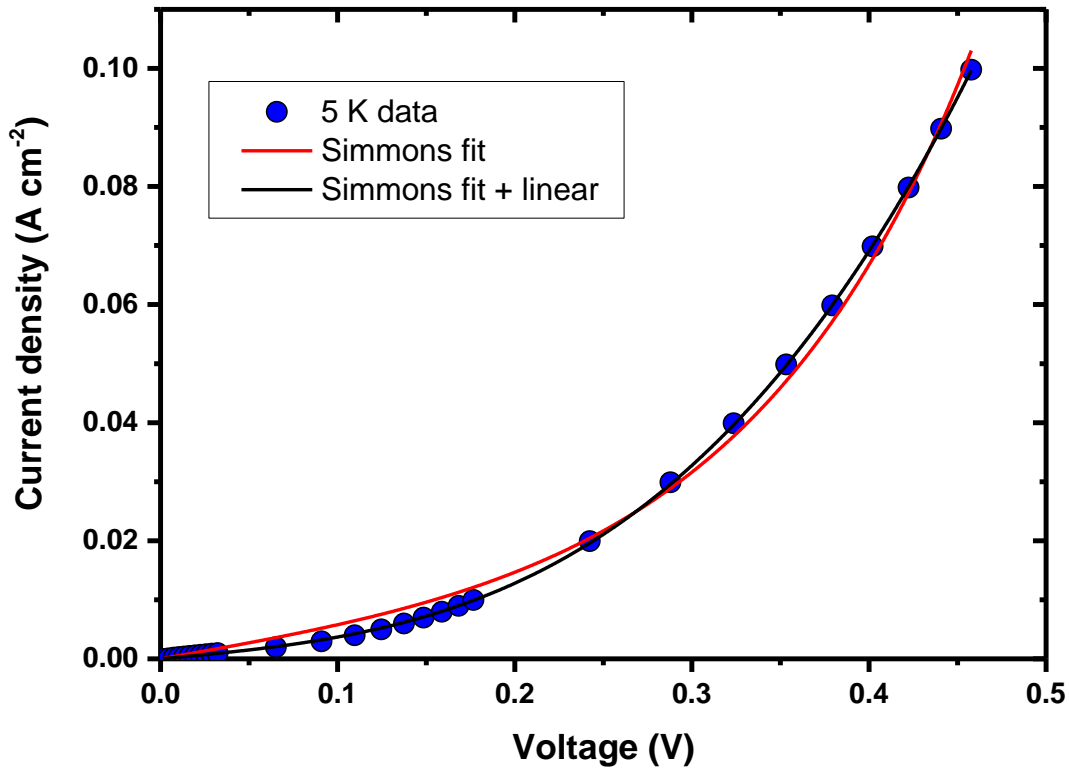


**Figure 6.8:** Positive voltage data for the JV characteristics of a 100x100  $\mu\text{m}^2$  GdN/LuN/DyN MTJ (blue) fitted with the Simmons model (red) and the Simmons model with an additional linear term (black).

As shown below in **Figure 6.9**, the positive and negative voltage IV behaviour was asymmetric. This is due to the use of two dissimilar electrode materials (GdN and DyN) which would introduce differences in the density of states at the boundary with the LuN layer. The negative portion of the IV curve was fit separately and in a similar manner to the positive portion, shown in **Figure 6.10**, giving a Simmons barrier width and height of 1.7 nm and 3.0 eV respectively using the additional linear term. These values are comparable to the values obtained above for the positive data, however the uncertainty in using the Simmons model to fit for semiconducting electrodes (vs the standard metallic electrodes) is likely greater than the slight variations in material differences between the FM REN layers.

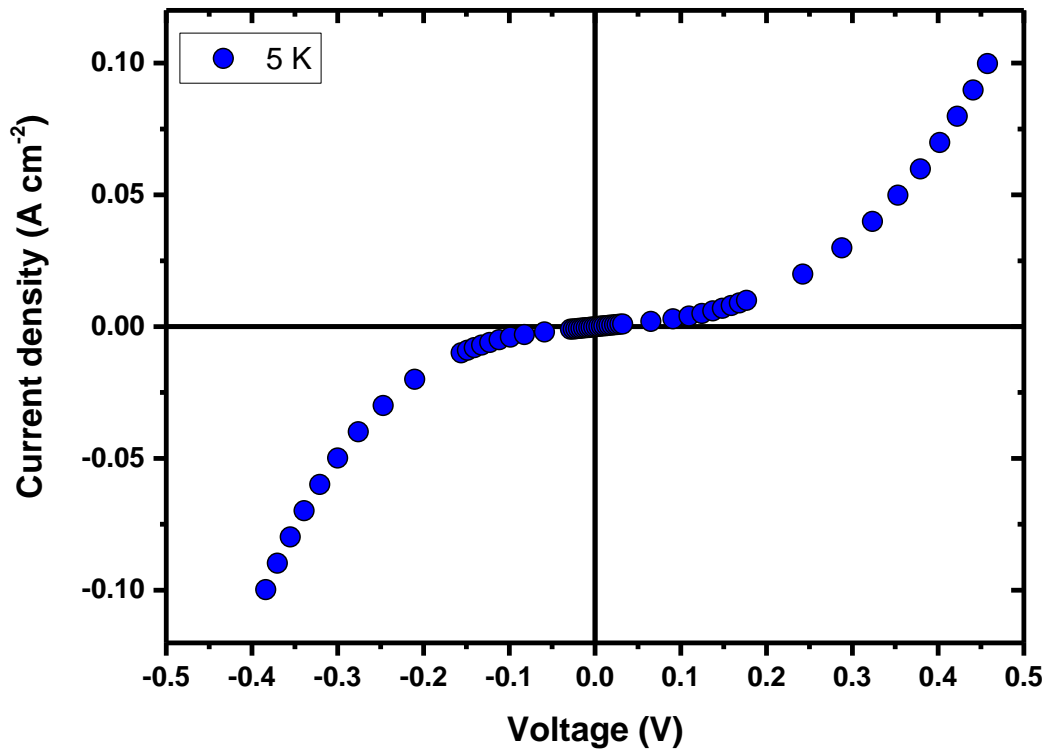


**Figure 6.9:** Positive and negative voltage data for the JV characteristics of a 100x100  $\mu\text{m}^2$  GdN/LuN/DyN MTJ. In this measurement, current was swept from -10  $\mu\text{A}$  to +10  $\mu\text{A}$ . Note that different voltage values are obtained based on the sign of the current, most noticeable at  $\pm 10 \mu\text{A}$ .

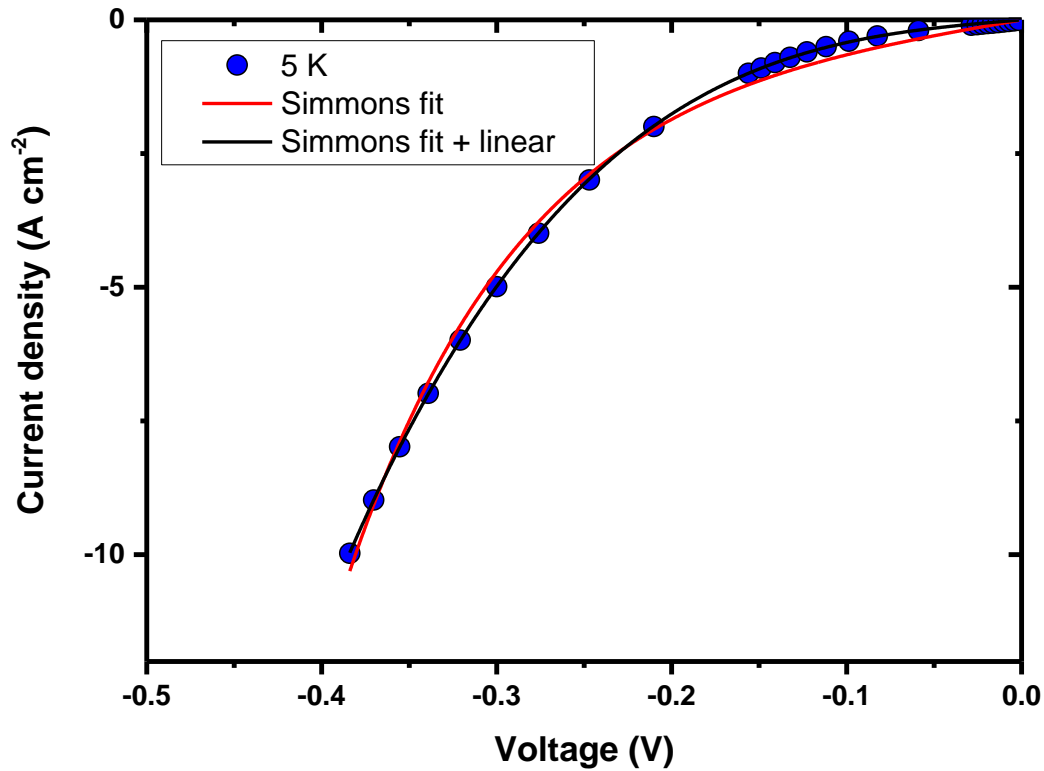


**Figure 6.10:** Negative voltage data for the JV characteristics of a  $100 \times 100 \mu\text{m}^2$  GdN/LuN/DyN MTJ (blue) fitted with the Simmons model (red) and the Simmons model with an additional linear term (black).

The Simmons barrier width in both directions is less than the nominal thickness of the LuN layer expected from the growth parameters, regardless of the additional linear term. This is not unexpected of the Simmons model, as discussed in **Chapter 4**, and within the same order of magnitude for the nominal thickness as expected from the growth rate and time.

We now turn to the low-impedance GMR devices. The temperature-dependent resistance for both the GdN/Lu/DyN and GdN/Al/DyN devices is shown in **Figure 6.11**. Both devices exhibited a positive temperature coefficient of resistance, which suggested that the majority of the resistance measured was due to the conductive EB layer, rather than the semiconducting FM layers. The Al-barrier device was  $\sim 2$  orders of magnitude lower in resistance than the Lu-barrier device with a room temperature resistivity of  $\rho(\text{Al}, 300 \text{ K}) = 53.54 \mu\Omega \text{ cm}$  compared to  $\rho(\text{Lu}, 300$

K) = 2.83 m $\Omega$  cm using the van der Pauw method [167–169] (assuming EB layer thicknesses of 40 nm and 20 nm respectively and that all current flow is through the EB layer). The Lu-barrier device exhibited an additional upturn in resistance at low temperature with a local resistance minimum at ~20 K.

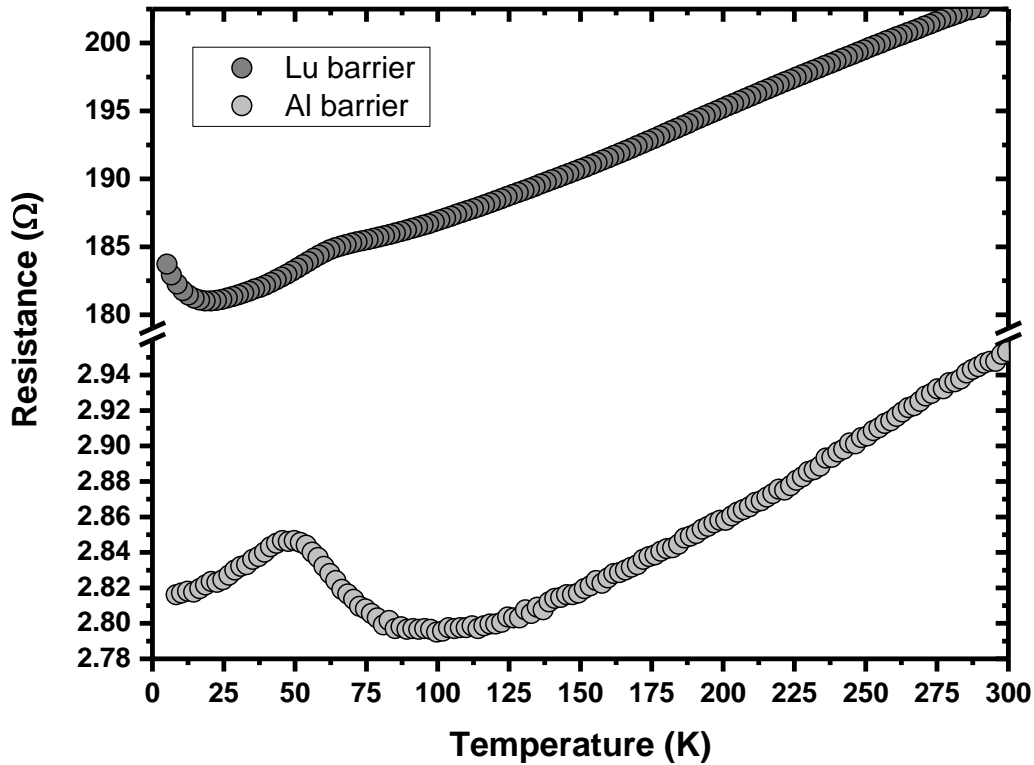


**Figure 6.11:** Resistance as a function of temperature for the two low-impedance devices with Lu (dark grey) and Al (light grey) as the conductive blocking layers using a current of 0.1 mA and 1 mA respectively.

Note that the resistivity in the GdN/Lu/DyN tri-layer is higher than would be expected from a ~20 nm thick Lu single layer film of the typical ~54  $\mu\Omega$  cm [138]. It is possible that some nitrogen from the adjacent REN layers had diffused out of those layers and subsequently reacted with the two surfaces of the Lu layer, catalytically forming LuN. With the very basic assumption of conduction solely through the Lu and not through any LuN (or GdN or DyN), the Lu layer would need to be ~0.4 nm thick to yield a comparable resistivity value to literature. However, this

is assuming that the LuN formed is heavily doped, which is very unlikely given the low amount of nitrogen available from the neighbouring REN layers. If we assume that the increase in resistivity is due to nitridation of the Lu layer, and compare this to the LuN series resistivity study in **Chapter 5**, the resistivity value places this film at a degree of nitridation between the samples grown at a  $N_2$ :Lu flux ratio of 3.9-7.7, likely closer to 3.9.

It can be noted that the peak associated with the FM phase transition in the RENs is shifted to higher temperatures for the device with Lu as a conductive blocking layer compared to the Al-barrier device. This is further evidence that nitrogen may have migrated from the GdN and/or the DyN layers as it has been shown that N-deficient GdN has a slightly higher Curie temperature than stoichiometric GdN [69] and this effect could reasonably be extrapolated to DyN as well.

### 6.3.2.3 Magnetoresistance Measurements

We now present the magnetoresistance measurements of the three trilayer structures. All measurements shown were performed at 2 K using a Quantum design Physical Property Measurement System (PPMS) with the external magnetic field in-plane with the device layers. We begin with the GdN/LuN/DyN magnetic tunnel junction. The full-field sweep between  $\pm 8$  T is shown in **Figure 6.12** and a strong magnetic response was observed. The absolute resistance was on the order of 100's of  $k\Omega$ , in-line with the expected value for such a tunnel barrier structure. Resistance was lowest at the extreme positive and negative field values and reached a maximum around approximately zero-field, with a maximum magnetoresistance of  $\sim 20\%$ . A zoom of the low-field behaviour is shown in **Figure 6.13**.

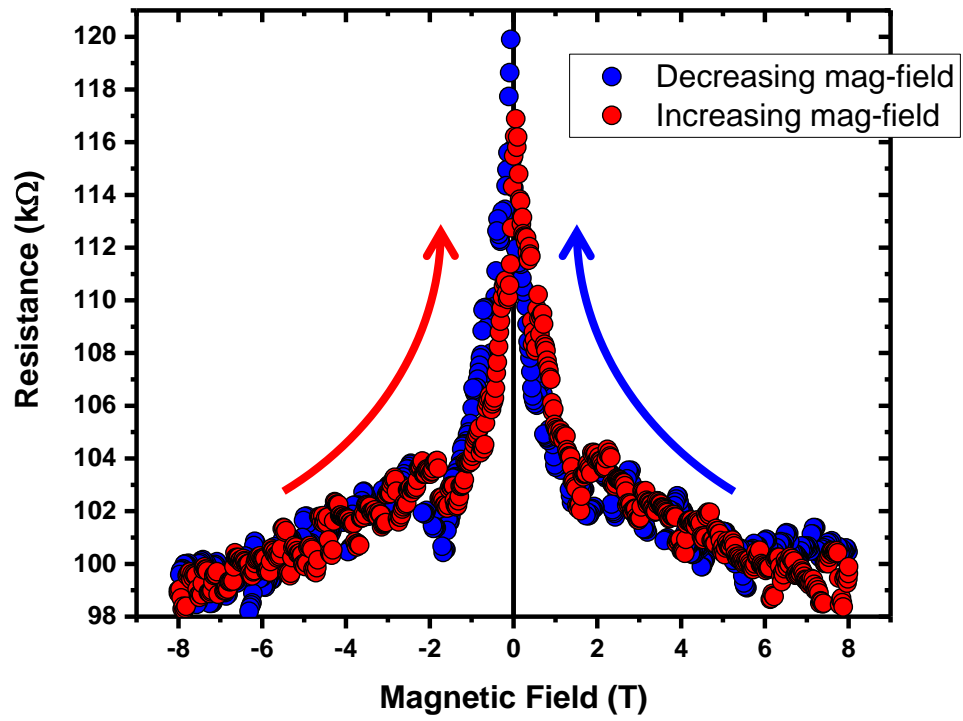


**Figure 6.12:** Magnetoresistance for the GdN/LuN/DyN MTJ at 2 K. Field direction is swept from positive to negative (**blue**) from +8 T to -8 T, before reversing direction from negative to positive (**red**) from -8 T to +8 T.

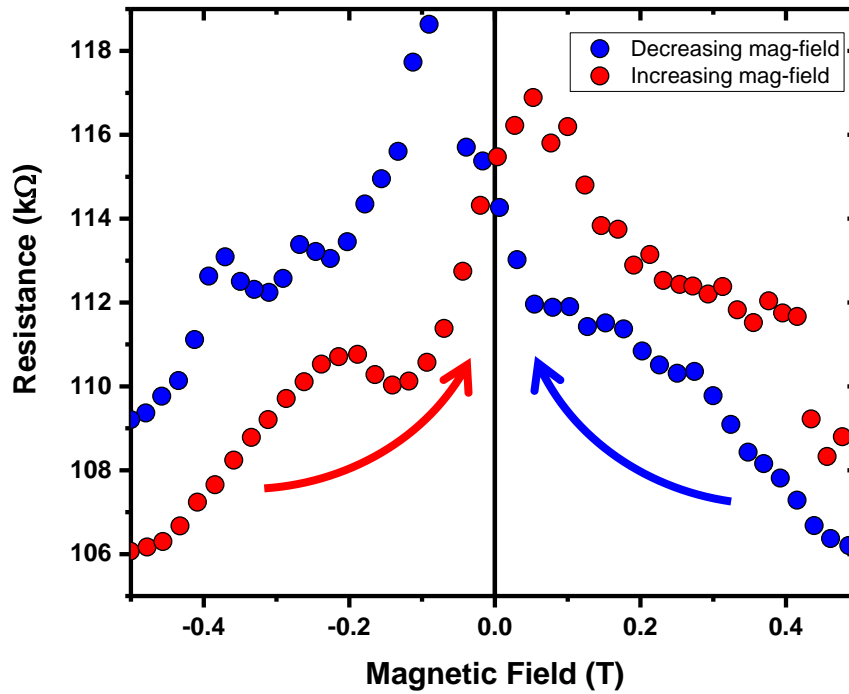


**Figure 6.13:** Zoom of the low-field magnetoresistance for the GdN/LuN/DyN MTJ at 2 K. Field direction is swept from positive to negative (**blue**) from +8 T to -8 T, before reversing direction from negative to positive (**red**) from -8 T to +8 T. Hysteresis is observed with the resistance value dependant on the direction of magnetic field sweep.

The resistance maximum was found to occur at a magnetic field of around  $\pm 0.06$  T, near the coercive field expected for polycrystalline GdN in similar growth conditions. This suggested that the resistance peak corresponded to the anti-aligned configuration, where the magnetisation direction of the GdN layer had switched, resulting in a high resistance state. There was evidence of an additional feature at around  $\pm 0.3$  T which may be related to the switching of the magnetisation orientation of the DyN layer. To probe the switching of each individual layer, minor sweeps were performed, sweeping down in magnetic field from +8 T to low-negative field values, before switching field direction and sweeping back to +8 T. The first of these measurements is shown in **Figure 6.14**.

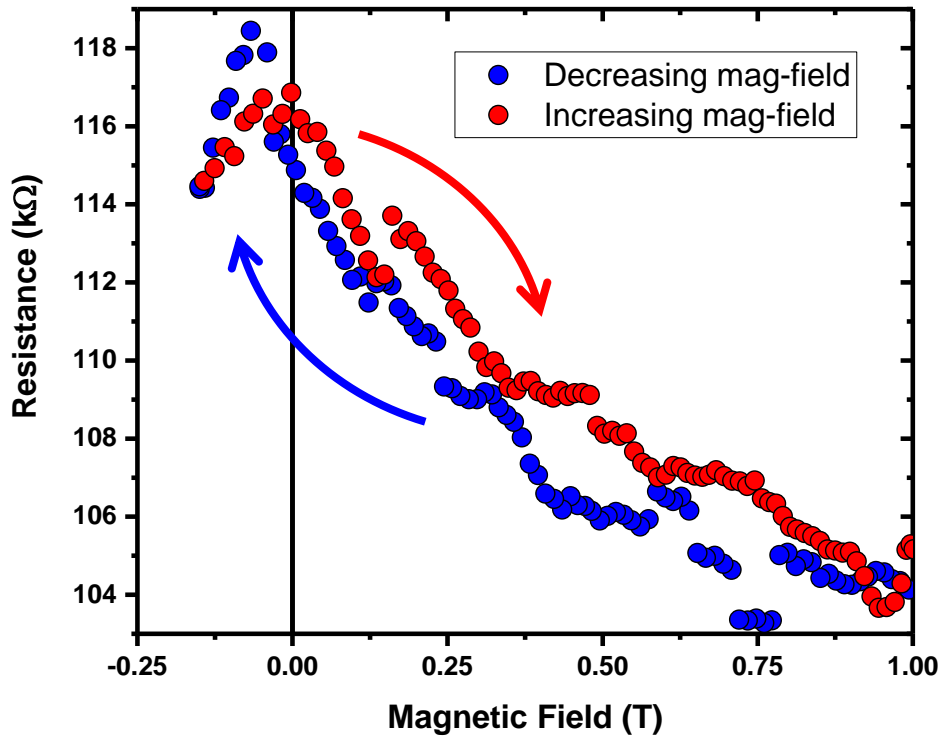


**Figure 6.14:** Magnetoresistance for a GdN/LuN/GdN MTJ at 2 K. Field direction is swept from positive to negative (**blue**) from +8 T to -0.15 T, before reversing direction from negative to positive (**red**) from -0.15 T to +8 T. This sweep takes the MTJ past the resistance maximum at -0.06 T. Data shown for the range -0.15 T to +1.0 T

In the measurement shown in Figure 6.14, the magnetic field was swept from +8 T down to -0.15 T (blue). This took the sample past the resistance maximum measured in the full-field sweep (-0.06 T) and this same feature can be seen here. At -0.15 T, the magnetic field sweep direction was reversed, from -0.15 T to +8 T (red). The relative orientation of the two FM layers should not be affected by the negative field values in this up-sweep and so the increase in resistance was assumed to be due to the overall background magnetoresistance. A small difference in resistance was observed at zero-field between the two magnetic field sweep directions (~0.95 %) indicating that the DyN layer had not, at least completely, switched at this field. To optimise the difference in resistive states at zero-field, a sweep was performed that reversed at the resistance maximum of -0.06 T, shown in **Figure 6.15**.



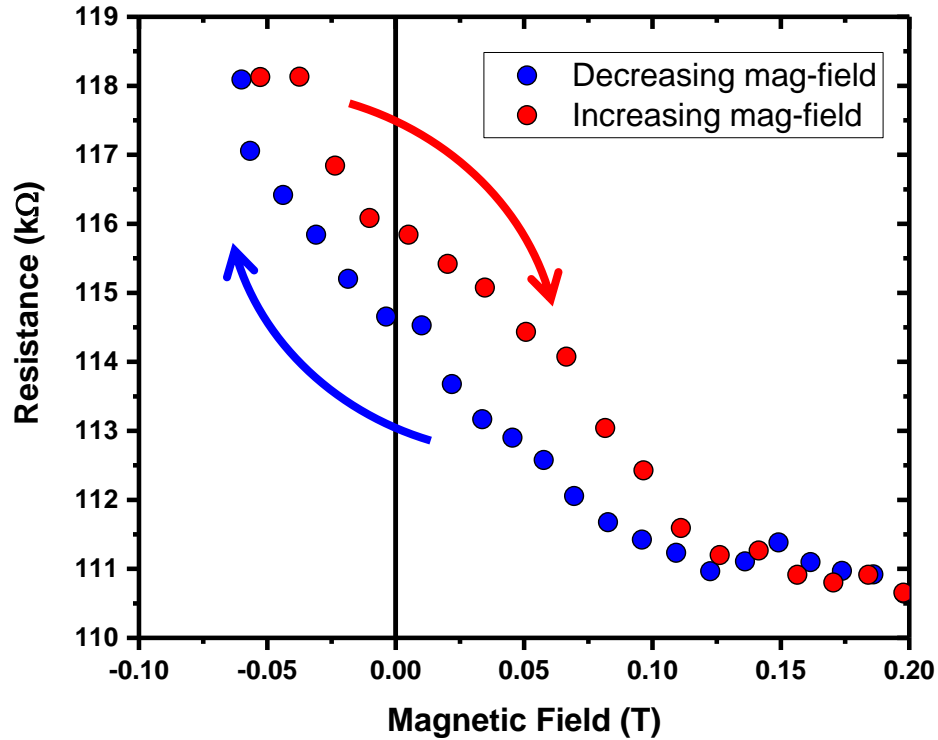


**Figure 6.15:** Magnetoresistance for a GdN/LuN/GdN MTJ at 2 K. Field direction is swept from positive to negative (**blue**) from +8 T to -0.06 T, before reversing direction from negative to positive (**red**) from -0.06 T to +8T. Note that the resistance value at 0 T is dependent on the field sweep direction, implying a difference in alignment of the ferromagnetic layer in the MTJ. Data shown for the range -0.06 T to +0.20 T.

Here the magnetic field was swept down from +8 T and reversed at -0.06 T. When sweeping down from +8 T, the sample should be in the aligned configuration with the magnetisation direction of both FM layers in the same orientation. At this resistance maximum at -0.06 T, the sample was in the anti-aligned configuration. By reversing the field-sweep direction at this point, the anti-aligned state should be preserved until the positive field value associated with the coercive field of the GdN layer is reached. In this way, at zero-field, the up- and down-sweeps represent different resistance states of the device. The measured resistance difference at zero-field was  $\sim 1.37$  k $\Omega$ , corresponding to a difference of  $\sim 1.2\%$  between the aligned and anti-aligned state with no applied field. This measurement demonstrated both the memory retention and non-volatility possible with such a MTJ using GdN and DyN as the FM layers and LuN as the tunnel

barrier. Also of note is that the value of 1.2% is greater than the 0.5% obtained for the GdN/AlN/GdN/Gd device shown in **Chapter 4**, showing that the use of FM layers with more contrasting magnetic properties can be used to increase the resistance difference at zero-field.

We now turn to the GMR-style devices, first with Lu as the EB layer (GdN/Lu/DyN). As before, the full-field magnetoresistance is shown in **Figure 6.16**, sweeping between  $\pm 8$  T. The absolute resistance was on the order of 100s of  $\Omega$ s, consistent with earlier temperature-dependent resistivity measurements. Hysteresis was observed with a resistance maximum at  $\sim 0.3$  T, which is much higher than occurred in the LuN-barrier MTJ above. As highlighted in the low-field zoom in **Figure 6.17**, there are no noticeable features between 0 T and  $\pm 0.30$  T that could correspond to the switching of the GdN layer. The crystal quality of the GdN layer could have been affected by the suspected nitrogen migration to the Lu layer, which could have resulted in the increased coercive field for this GdN layer.

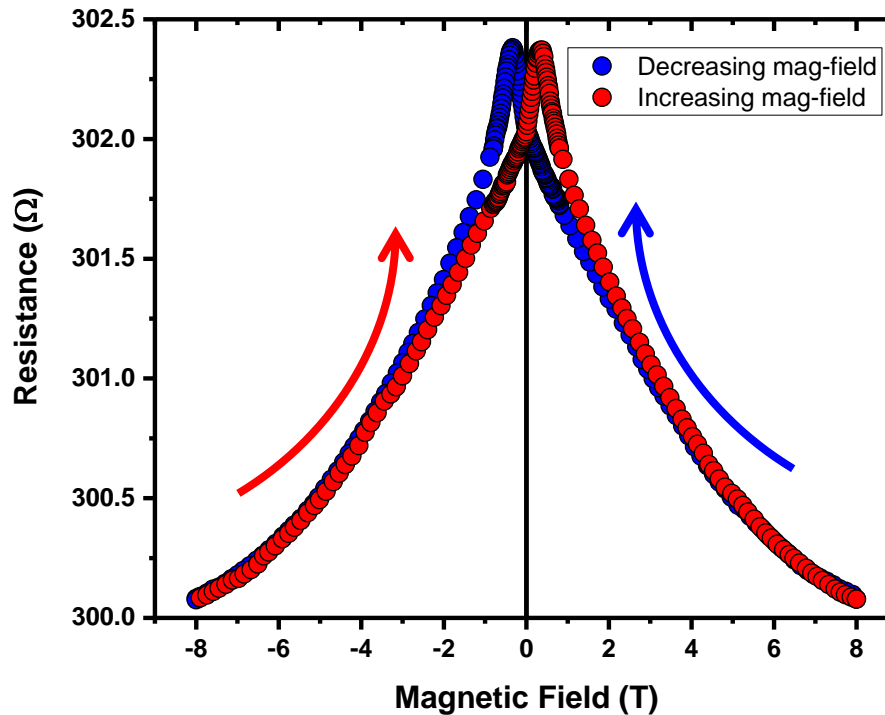


**Figure 6.16:** Magnetoresistance for the GdN/Lu/DyN GMR-style device at 2 K. Field direction is swept from positive to negative (**blue**) from +8 T to -8 T, before reversing direction from negative to positive (**red**) from -8 T to +8 T.

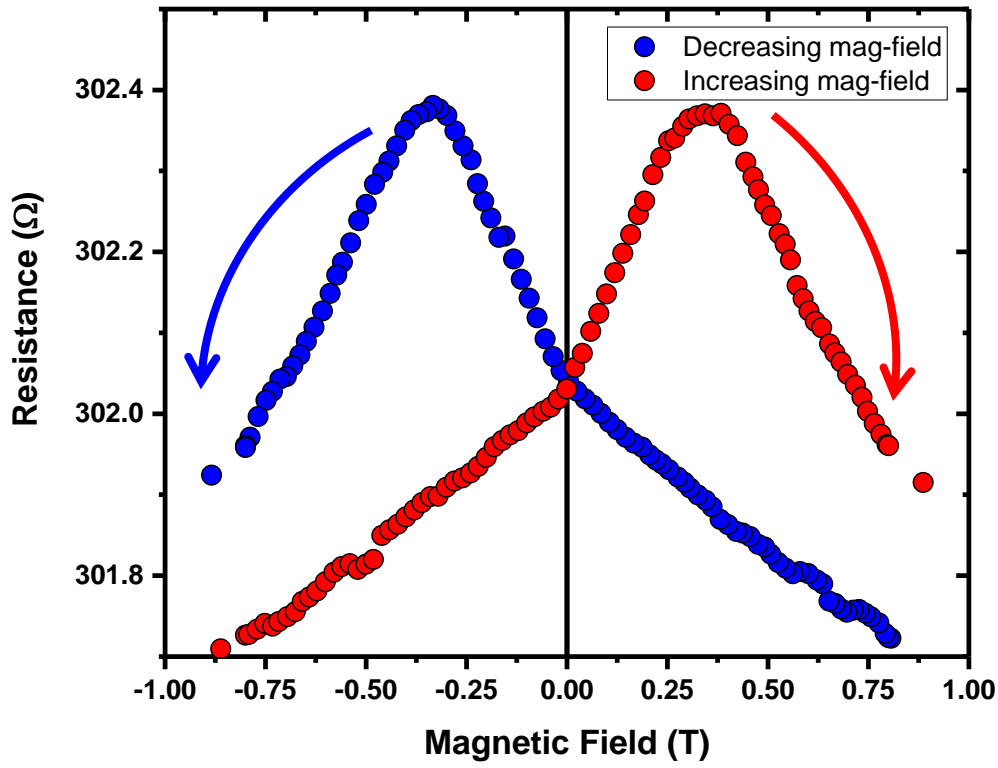


**Figure 6.17:** Zoom of the low-field magnetoresistance for the GdN/Lu/DyN GMR-style device at 2 K. The magnetic field direction is swept from positive to negative (**blue**) from +8 T to -8 T, before reversing direction from negative to positive (**red**) from -8 T to +8 T.

The resistance maximum at 0.3 T was used as the target magnetic field value for the minor sweep of this sample. This measurement is shown in **Figure 6.18**. As with the MTJ shown previously, a difference in resistance at zero-field was obtained. The absolute resistance difference between the up- and down-sweep was found to be  $\sim 0.14 \, \Omega$ , corresponding to a  $\sim 0.04\%$  difference.

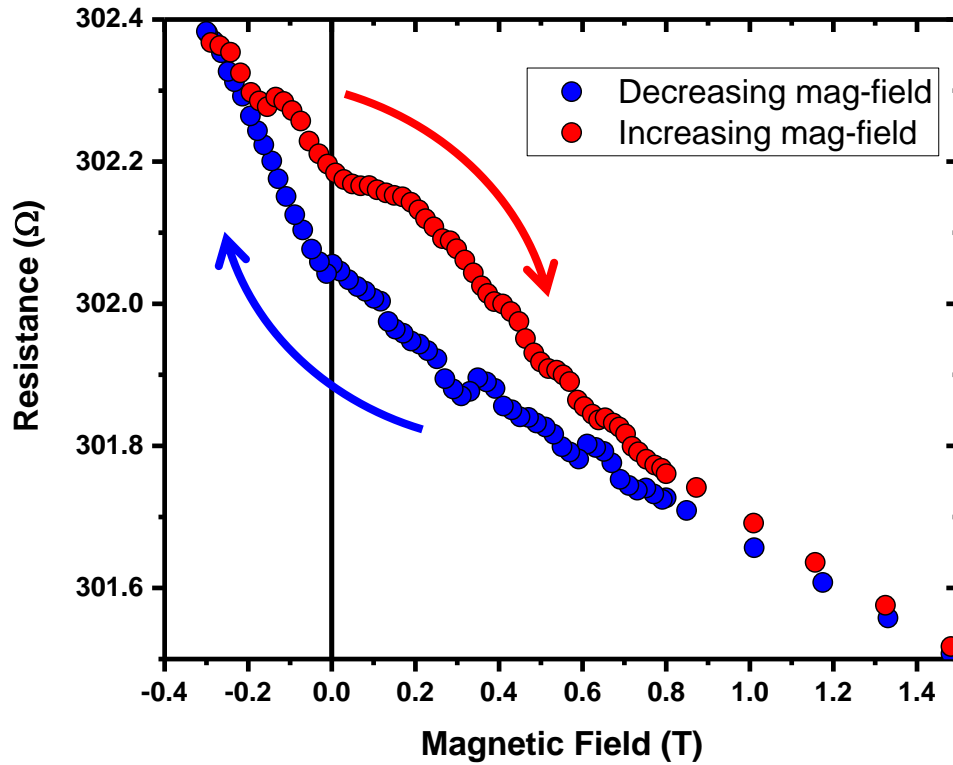


**Figure 6.18:** Magnetoresistance for a GdN/Lu/DyN GMR-style device at 2 K. Field direction is swept from positive to negative (**blue**) from +8 T to -0.3 T, before reversing direction from negative to positive (**red**) from -0.3 T to +8T.

The fact that retention was observed is worth noting – as well as being noteworthy in itself as the first demonstration of such a GMR-style device using RENs as the FM layers – as it suggests that the feature at -0.30 T was likely not solely due to the background magnetoresistance of the REN layers as this behaviour would not be observed for a single layer or coupled layers of material.

While a retention of ~0.04% is very low, even compared to the LuN MTJ, this is on the order of other trilayer GMR-style devices [63,170]. There are several paths forward to improve the retention of such a device using these materials including growing a multilayer (vs. the trilayer used here) structure or using an EB layer that does not react with the FM layers to preserve their integrity.

Here we now present data for the device using Al as an EB layer. The full-field sweep between  $\pm 8$  T is shown in **Figure 6.19**. A similar overall profile is observed, with resistance reaching a maximum and minimum at  $\sim 0$  T and  $\pm 8$  T. However, as highlighted in the zoom of the low-field behaviour in **Figure 6.20**, no hysteresis was observed for this structure.

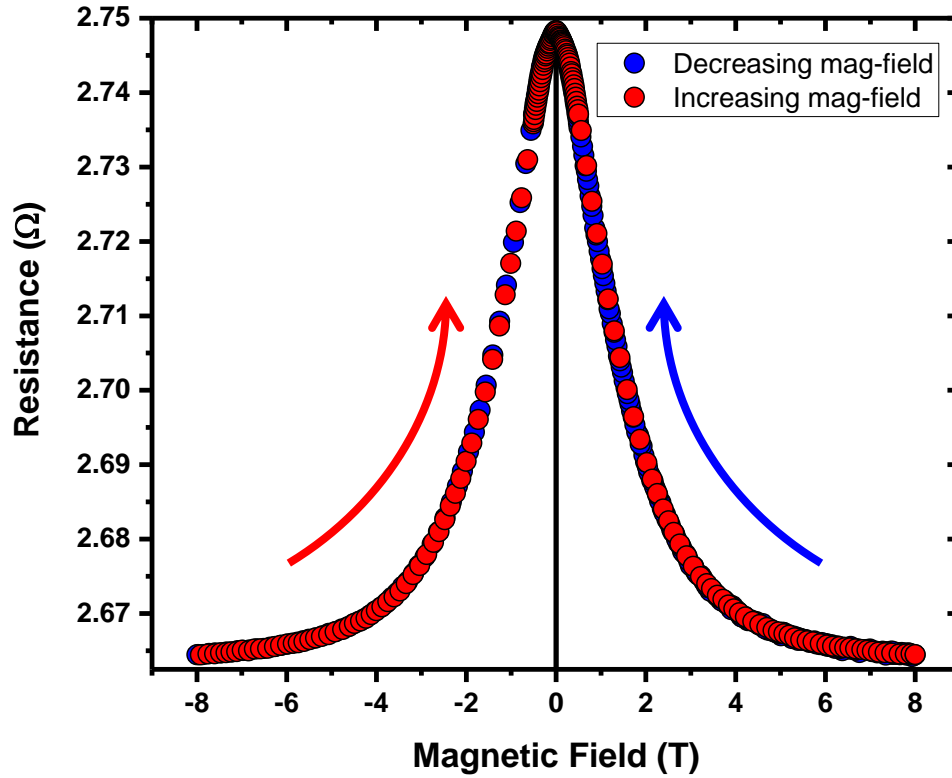


**Figure 6.19:** Magnetoresistance for a GdN/Al/DyN GMR-style device at 2 K. Field direction is swept from positive to negative (**blue**) from +8 T to -8 T, before reversing direction from negative to positive (**red**) from -8 T to +8 T.

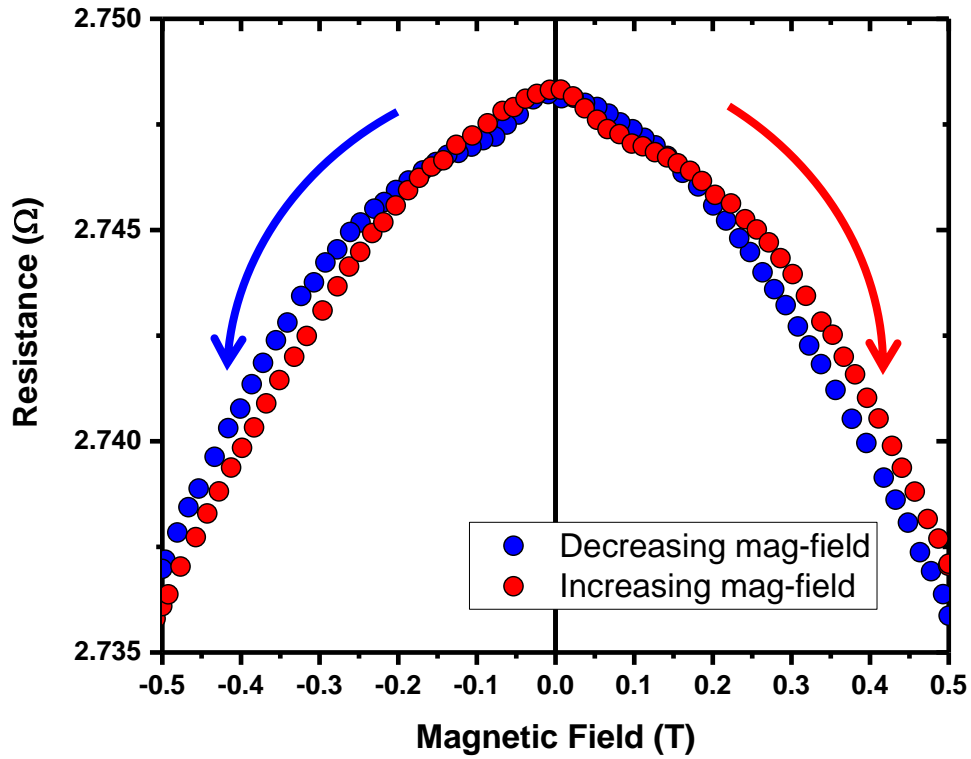


**Figure 6.20:** Zoom of the low-field magnetoresistance for the GdN/Al/DyN GMR-style device at 2 K. The magnetic field direction is swept from positive to negative (**blue**) from +8 T to -8 T, before reversing direction from negative to positive (**red**) from -8 T to +8 T.

There are some features at values below 0.1 T and a very slight difference in resistance between the up- and down-sweeps but no discernible peaks were identified. All minor sweeps probing different reversal magnetic fields did not yield any retention/difference in resistance at zero-field.

The Al-barrier device demonstrated the most distinct magnetic properties out of the three structures shown in this chapter, as shown earlier in the magnetic hysteresis at 5 K, but the least distinct electrical transport properties for magnetoresistance. From this, we can conclude that the FM REN layers were of sufficient quality, but potentially it was the Al layer that was of poor growth quality and drastically reduced the spin diffusion length of this layer. In this situation, the FM layers would still switch as expected but this would not be detected in an electrical

measurement through the conductive Al layer as any effect the FM layers have on the spin of the electrons would not be preserved in their movement to the other FM layer. To overcome this, the growth of Al would need to be optimised for the growth chamber used, with an additional annealing step suggested to form high-quality Al.

## 6.4 Conclusion

In this chapter, we have demonstrated both a cryogenic non-volatile magnetic tunnel junction and two in-plane conduction devices using GdN and DyN as the ferromagnetic layers. GdN and DyN layers were shown to be sufficiently decoupled and individual magnetic transitions were observed for each ferromagnetic layer. A maximum difference in resistive states of  $\sim 1.2\%$  at zero-field was observed for the MTJ.

This is the first reported use of LuN as a tunnel barrier in a MTJ, as well as demonstration of non-volatility with LuN as a tunnel barrier and with GdN and DyN as the FM layers. This is also the first use of using REN FM materials in a GMR-style device. The retention values reported here are respectable already but could benefit from various improvements to the device structure.

For the MTJ structure, improvements in the magnetic properties of the FM layers could lead to more distinct switching events. The coercive fields of DyN and GdN were sufficiently different to individually switch the magnetisation of one layer without switching the other, although the possibility of overlap exists depending on the crystalline quality of each layer. Exploration of other RENs, or even REN solid solutions (combinations of RENs e.g.  $\text{Gd}_x\text{Sm}_{1-x}\text{N}$ ), is encouraged for use in these structures.

The GMR-style structures would similarly benefit from this exploration but, maybe more readily, these structures could be grown as multilayers rather than trilayers. Alternating FM and EB layers stacked on top of each other would increase the GMR effect and therefore the contrast between the aligned and anti-aligned state of the layers. Lu and Al were used as the EB layers in this study. Al is well studied in terms of spin diffusion, but the layers grown here were of poor quality and so could not be thoroughly assessed in this regard. Lu had the issue of reacting with the FM layers but was of high enough quality to demonstrate the GMR effect. It would be

interesting to do an isolated study on the spin diffusion properties of Lu, and the results of this could be used to better inform appropriate growth parameters such as thickness or annealing times.



## Chapter 7

### Summary and Outlook

#### 7.1 Conclusions

In this thesis we have investigated the use of rare earth nitrides as materials for use in non-volatile memory elements to operate at cryogenic temperatures. We began by developing a model to assess the conductivity requirements of materials in the *caisson* geometry, before fabricating magnetic tunnel junctions using GdN as the two ferromagnetic electrodes which demonstrated a retention of the high-resistance anti-aligned state in the absence of an external magnetic field. We then used a series of LuN thin films variously doped with nitrogen vacancies, as well as band structure calculations, to resolve the electronic properties of LuN. Finally, we have fabricated high-resistance magnetic tunnel junctions and low-resistance in-plane conduction devices using GdN and DyN as the two ferromagnetic layers.

In **Chapter 4**, we fabricated and characterised magnetic tunnel junctions using two GdN ferromagnetic electrodes, one pinned by direct contact with Gd. This structure exhibited hysteretic magnetoresistance with a resistance maximum at  $\sim 0.04$  T, near the coercive field of polycrystalline GdN. By reversing the magnetic field sweep at this point, the magnetic state of the device was retained at zero-field, demonstrating the use of these materials in such a structure as a non-volatile memory element. The difference in measured resistance of the two states (aligned vs. anti-aligned) at 0 T was found to be  $\sim 0.53\%$ . This measurement demonstrated both the writing and reading operation of a memory element through the setting of the resistance state using an external magnetic field and the application of an electric current through the device respectively. In the future, one could imagine both operations being controlled purely by electrical means, relying on spin torque to set the magnetisation orientation in the free ferromagnetic electrode. Demonstrating a memory element with all-electrical read and write operations that is controlled by a basic Josephson junction circuit would be a step forward for a memory element with lower power consumption and scalability towards the goal of superconductor integration.

In **Chapter 5** we investigated the effects of nitrogen vacancies in rare earth nitrides through a fundamental study of LuN using experimental and computational techniques. We have reported

on the electrical and optical properties of LuN, as well as its band structure, to clarify on the sparse and conflicting research of this material. We found that stoichiometric LuN is a semiconductor with an indirect bandgap of  $\sim 1.7$  eV and lattice parameter of  $4.79 \text{ \AA}$ , suggesting that previous reports on LuN were likely affected by nitrogen vacancies. Upon doping with nitrogen vacancies, defect states were introduced into the conduction band minimum and valence band maximum, lowering the bandgap. Electrical transport results showed that undoped films, with a low concentration of nitrogen vacancies, were insulating with a diverging resistivity at low temperature. As the films were doped and the nitrogen vacancy concentration increased, the form of the temperature dependent resistivity became metallic-like with a finite resistivity at low temperature, implying that charge carriers reside in the conduction band at zero temperature. Band structure calculations showed excellent agreement with the experimental data; The presence of nitrogen vacancies resulted in defect states at both the conduction band minimum, facilitating electron transport, and the valence band maximum, which reduces the optical gap, consistent with optical spectroscopy measurements.

In **Chapter 6**, we constructed several device structures using GdN and DyN as the FM layers separated by some exchange blocking layer: insulating LuN in the case of the magnetic tunnel junction and Lu and Al in the case of the giant magnetoresistance-style device. This work showed how the use of ferromagnetic layers with contrasting coercive fields (GdN vs. DyN compared to GdN vs. GdN/Gd) could be used to achieve greater distinction between resistance states which is important for the retention at zero-field, as well as reducing write error in a functioning memory element. Here, the GdN/LuN/DyN magnetic tunnel junction exhibited a difference in measured resistance of  $\sim 1.2\%$  at 0 T, higher than the GdN/AlN/GdN/Gd magnetic tunnel junction characterised in **Chapter 4** of  $\sim 0.53\%$ . This was also the first demonstrated use of LuN as the tunnel barrier material in a magnetic tunnel junction. Additionally, giant magnetoresistance-style devices were developed using the current-in-plane geometry in combination with a trilayer structure to explore the use of GdN and DyN in an alternative, low-resistance device structure. Retention of the resistive state at zero-field was achieved, with a measured difference of  $\sim 0.04\%$ . As discussed in the previous chapter, both current perpendicular-to-plane geometries and multilayer structures exhibit stronger giant magnetoresistance effects as compared to those used here, and so this value could likely be improved through the use of multilayers or the current perpendicular-to-plane geometry.

## 7.2 Future Work

From a fabrication point of view, these device structures could benefit from various optimisation procedures. The polycrystalline REN thin films used in these devices tend to exhibit magnetic transitions between the aligned and anti-aligned configurations that are more smeared out – that is, less sharp – as compared to epitaxial films due to the increased number of magnetic domains within the film [83,85,95]. Smearing of this switching event is also found with polycrystalline barriers in MTJs, though in this case it is due to a smearing of the bands as a result of the inhomogeneous layer [171]. A sharper transition would allow for more distinct switching events, potentially enhancing the difference in measured resistance of the two states and reducing any associated write error. However, for the growth of epitaxial REN thin films specifically, high substrate temperatures are required which is incompatible with the photoresist used for the patterning of the devices in this thesis, and so an alternative patterning procedure would be required.

Another possible way to increase the retention difference is through the use of different RENs as the ferromagnetic layers. This was shown in this thesis through the increased retention difference observed using GdN and DyN ferromagnetic electrodes as compared to GdN and GdN/Gd electrodes. This exploration is encouraged as there are many combinations available within the REN series, with recent work on rare earth nitride solid solutions expanding this even further [70]. Solid solutions are a mixture of rare earth nitrides (e.g.  $\text{Gd}_x\text{Sm}_{1-x}\text{N}$ ) which allows for even greater customisation of the coercive field, among other properties. So far, solid solutions containing Gd and Sm ( $\text{Gd}_x\text{Sm}_{1-x}\text{N}$ ) and Gd and Dy ( $\text{Gd}_x\text{Dy}_{1-x}\text{N}$ ) have been realised, with magnetic properties such as coercive field and saturation magnetisation ranging between those of the two parent RENs. The FM pair used in a device structure should be chosen such that the magnetisation direction of the free FM layer can be completely switched – either with an external magnetic field or spin-polarised current – without affecting the magnetisation of the other (fixed) FM layer.

We have recently begun collaborating with a Naples research group who have demonstrated GdN as the barrier layer in a superconducting Josephson junction (JJ) [20], with the aim to incorporate different RENs into Nb-based JJs. As part of this, we have developed a new lithography pattern using laser writing which can reliably create devices with an active area of  $10 \times 10 \mu\text{m}^2$  in order to facilitate size requirements for their measurements. This new process makes

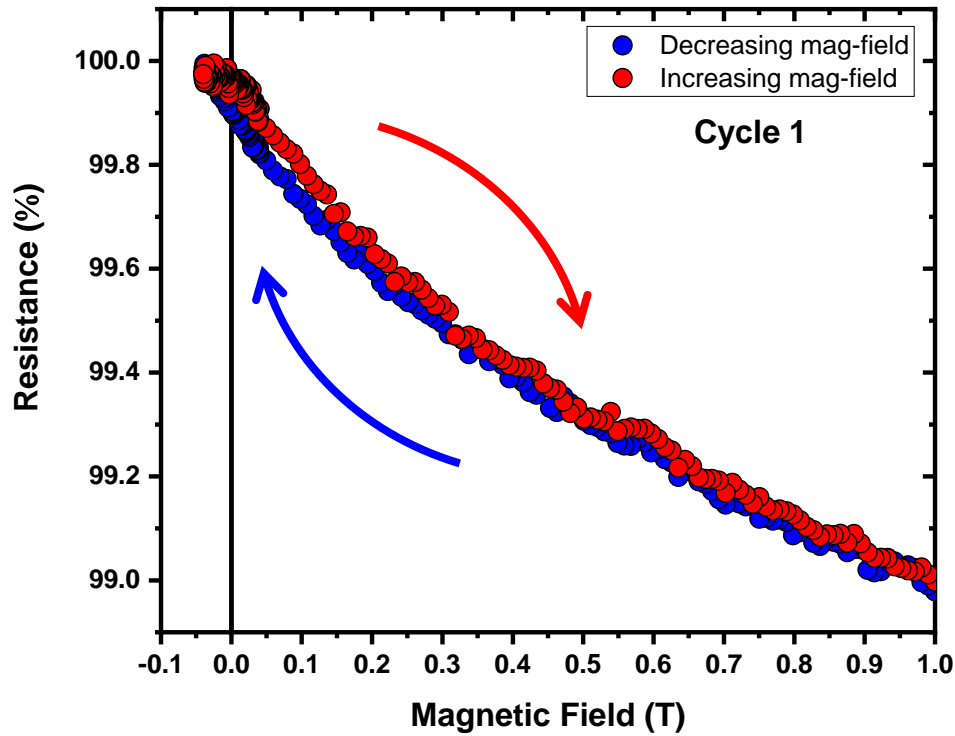
use of a channel-style *caisson* pattern, rather than the isolated square used in this thesis, to assist with the development and lift-off patterning steps. In this thesis, devices ranged from  $10 \times 10 \mu\text{m}^2$  to  $200 \times 200 \mu\text{m}^2$ , with the larger devices often being used for measurements and characterisation. While size reduction of devices was not an area of focus for this thesis, it remains an important aspect towards realisation of an industry-competitive memory element.

## Appendix A Device Performance Over Time

### A.1 Device Cyclability

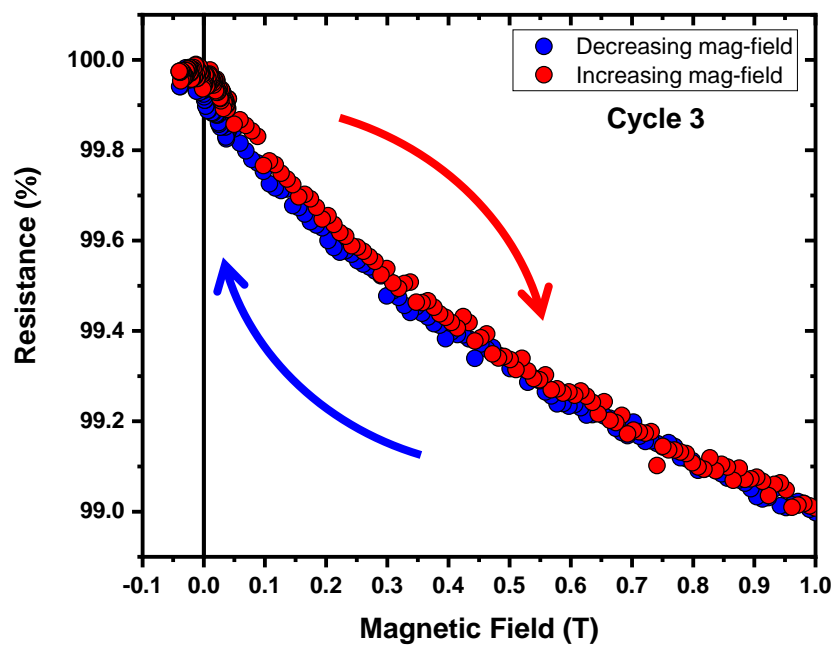
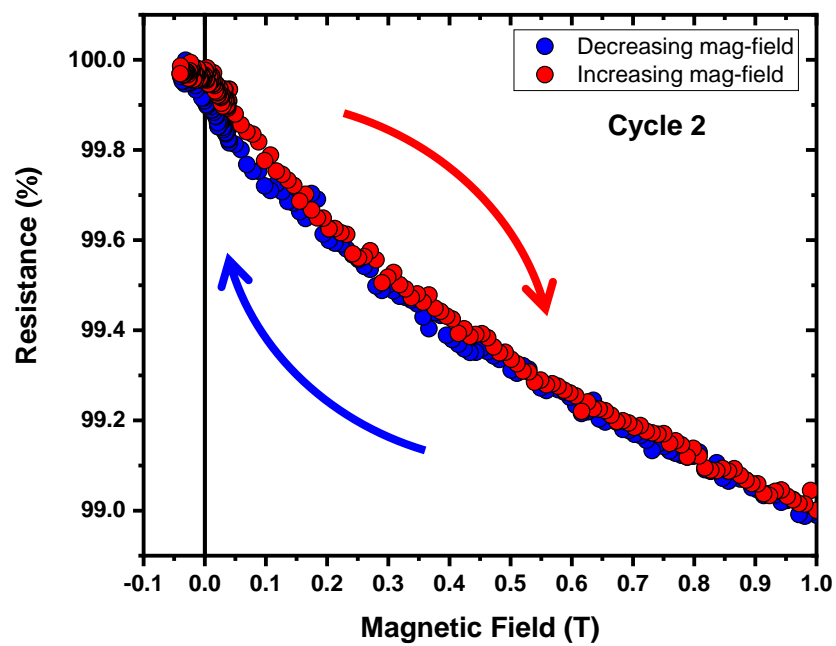
It is an important metric of commercial memory elements to be able to maintain their distinct memory states over millions of read/write cycles. The devices displayed in this thesis are proof-of-concept samples grown in batches of ~20 at a time, rather than manufactured commercial elements. As such, they have not been as thoroughly tested regarding device performance over time, such as for an extended number of cycles or set amount of time. However, shown below are read/write cycles in the form of magnetoresistance plots for a GdN/AlN/GdN/Gd MTJ that was put through four continuous cycles over a 24-hour period.

Shown first, in **Figure A.1**, is the first of the four cycles. During the measurement, the external magnetic field was swept from +1 T down to -0.04 T (**blue**), before reversing direction and sweeping from -0.04 T up to +1 T (**red**). The negative field value was enough to switch the soft GdN layer but not enough to switch the hard GdN/Gd coupled layer, therefore attaining a high-resistance state. This high-resistance state was retained at 0 T during the sweep with increasing magnetic field – on the order of 0.1%, comparable to the GdN/AlN/GdN/Gd device discussed in **Chapter 4** of ~0.53%.



**Figure A.1:** Magnetoresistance for a  $70 \times 70 \text{ } \mu\text{m}^2$  GdN/Al/GdN MTJ device at 2 K. Field direction is swept from positive to negative (blue) from +1 T to -0.04 T, before reversing direction from negative to positive (red) from -0.04 T to +1 T.

Now we show the three magnetoresistance measurements performed immediately following the measurement shown in **Figure A.1**. As can be seen in the three plots in **Figure A.2**, the shape and resistance values varied very little over the three cycles. The ‘100%’ resistance value on the y-axis is the same resistance value across all four cycles and represents the maximum resistance of Cycle 1. Over the four cycles, there was the same increase in resistance as magnetic field decreased from +1 T, peaking around -0.04 T when the device was in the high-resistance state. As the magnetic field increased from -0.04 T, a similar order of retention is observed at 0 T for each subsequent cycle.



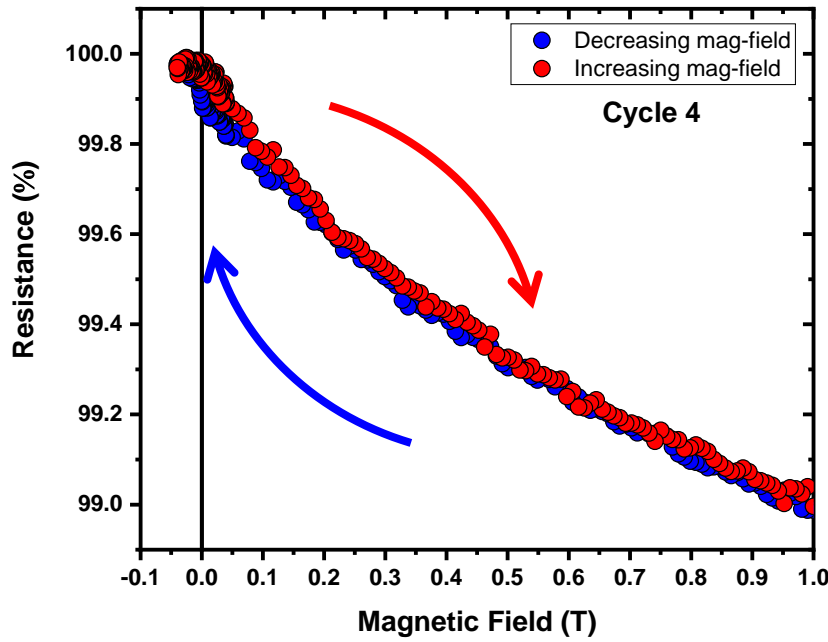


**Figure A.2:** The subsequent three magnetoresistance cycles that were performed in succession following Cycle 1 presented in **Figure A.1** for a  $70 \times 70 \mu\text{m}^2$  GdN/Al/GdN/Gd MTJ device at 2 K. Field direction is swept continuously from positive to negative (**blue**) from +1 T to -0.04 T, before reversing direction from negative to positive (**red**) from -0.04 T to +1 T for the full four cycles.

These measurements were a long way from the level of repetitions and cycles performed in commercial device testing facilities, however, it showed that the retention observed in REN MTJs was not a one-off occurrence and that the devices exhibited some degree of cyclability. Given more equipment time it would be interesting to subject such a device to many more measurement cycles to yield a more detailed insight into how REN MTJs perform read/write operations over time and whether they can sustain a retention of distinct resistance states (as shown here) for an even greater number of cycles.



## Bibliography

- [1] *International Roadmap for Devices and Systems (IRDS™) 2021 Edition - IEEE IRDS™*, <https://irds.ieee.org/editions/2021>.
- [2] I. I. Soloviev, N. V. Klenov, S. V. Bakurskiy, M. Y. Kupriyanov, A. L. Gudkov, and A. S. Sidorenko, *Beyond Moore's Technologies: Operation Principles of a Superconductor Alternative*, Beilstein J. Nanotechnol. **8**, 2689 (2017).
- [3] J. Linder and J. W. A. Robinson, *Superconducting Spintronics*, Nature Physics **11**, 307 (2015).
- [4] O. A. Mukhanov, *Energy-Efficient Single Flux Quantum Technology*, IEEE Transactions on Applied Superconductivity **21**, 760 (2011).
- [5] S. K. Tolpygo, *Superconductor Digital Electronics: Scalability and Energy Efficiency Issues (Review Article)*, Low Temperature Physics **42**, 361 (2016).
- [6] I. V. Vernik, V. V. Bol'ginov, S. V. Bakurskiy, A. A. Golubov, M. Yu. Kupriyanov, V. V. Ryazanov, and O. A. Mukhanov, *Magnetic Josephson Junctions With Superconducting Interlayer for Cryogenic Memory*, IEEE Transactions on Applied Superconductivity **23**, 1701208 (2013).
- [7] M. A. Manheimer, *Cryogenic Computing Complexity Program: Phase 1 Introduction*, IEEE Transactions on Applied Superconductivity **25**, 1 (2015).
- [8] T. Orllepp and T. Van Duzer, *Access Time and Power Dissipation of a Model 256-Bit Single Flux Quantum RAM*, IEEE Transactions on Applied Superconductivity **24**, 1 (2014).
- [9] D. Ielmini and H.-S. P. Wong, *In-Memory Computing with Resistive Switching Devices*, Nature Electronics **1**, 333 (2018).
- [10] R. Sbiaa, H. Meng, and S. N. Piramanayagam, *Materials with Perpendicular Magnetic Anisotropy for Magnetic Random Access Memory*, Physica Status Solidi (RRL) – Rapid Research Letters **5**, 413 (2011).
- [11] S. Z. Peng, Y. Zhang, M. X. Wang, Y. G. Zhang, and W. Zhao, *Magnetic Tunnel Junctions for Spintronics: Principles and Applications*, in *Wiley Encyclopedia of Electrical and Electronics Engineering* (American Cancer Society, 2014), pp. 1–16.
- [12] A. D. Kent and D. C. Worledge, *A New Spin on Magnetic Memories*, Nature Nanotechnology **10**, 187 (2015).
- [13] T. Mikolajick, C. Dehm, W. Hartner, I. Kasko, M. J. Kastner, N. Nagel, M. Moert, and C. Mazure, *FeRAM Technology for High Density Applications*, Microelectronics Reliability **41**, 947 (2001).
- [14] M. N. Baibich, J. M. Broto, A. Fert, F. N. Van Dau, F. Petroff, P. Etienne, G. Creuzet, A. Friederich, and J. Chazelas, *Giant Magnetoresistance of (001)Fe/(001)Cr Magnetic Superlattices*, Phys. Rev. Lett. **61**, 2472 (1988).
- [15] S. N. Kim, J. W. Choi, and S. H. Lim, *Tailoring of Magnetic Properties of Giant Magnetoresistance Spin Valves via Insertion of Ultrathin Non-Magnetic Spacers between Pinned and Pinning Layers*, Sci Rep **9**, 1617 (2019).
- [16] C. Chappert, A. Fert, and F. N. V. Dau, *The Emergence of Spin Electronics in Data Storage*, Nature Mater **6**, 813 (2007).
- [17] F. Natali, B. J. Ruck, N. O. V. Plank, H. J. Trodahl, S. Granville, C. Meyer, and W. R. L. Lambrecht, *Rare-Earth Mononitrides*, Progress in Materials Science **58**, 1316 (2013).
- [18] W. F. Holmes-Hewett, C. Pot, R. G. Buckley, A. Koo, B. J. Ruck, F. Natali, A. Shaib, J. D. Miller, and H. J. Trodahl, *Nitrogen Vacancies and Carrier-Concentration Control in Rare-Earth Nitrides*, Appl. Phys. Lett. **117**, 222409 (2020).
- [19] J. Miller, *Tunnelling in Rare-Earth Nitride Structures*, Master's Thesis, Victoria University of Wellington (2018).

- [20] H. G. Ahmad, R. Caruso, A. Pal, G. Rotoli, G. P. Pepe, M. G. Blamire, F. Tafuri, and D. Massarotti, *Electrodynamics of Highly Spin-Polarized Tunnel Josephson Junctions*, Phys. Rev. Applied **13**, 014017 (2020).
- [21] A. Pal, K. Senapati, Z. H. Barber, and M. G. Blamire, *Electric-Field-Dependent Spin Polarization in GdN Spin Filter Tunnel Junctions*, Advanced Materials **25**, 5581 (2013).
- [22] A. Pal and M. G. Blamire, *Large Interfacial Exchange Fields in a Thick Superconducting Film Coupled to a Spin-Filter Tunnel Barrier*, Phys. Rev. B **92**, 180510 (2015).
- [23] P. K. Muduli, A. Pal, and M. G. Blamire, *Crossover from Diffusive to Tunneling Regime in NbN/DyN/NbN Ferromagnetic Semiconductor Tunnel Junctions*, Phys. Rev. B **89**, 094414 (2014).
- [24] A. Kandala, A. Richardella, D. W. Rench, D. M. Zhang, T. C. Flanagan, and N. Samarth, *Growth and Characterization of Hybrid Insulating Ferromagnet-Topological Insulator Heterostructure Devices*, Appl. Phys. Lett. **103**, 202409 (2013).
- [25] A. H. Warring, *Device Applications of Rare-Earth Nitrides*, Doctor of Philosophy Thesis, Victoria University of Wellington (2016).
- [26] F. Ullstad, *Rare Earth Nitrides and Their Applications in Magnetic Tunnel Junctions*, Doctor of Philosophy Thesis, Victoria University of Wellington (2019).
- [27] H. Warring, H. J. Trodahl, N. O. V. Plank, F. Natali, S. Granville, and B. J. Ruck, *Magnetic Tunnel Junctions Incorporating a Near-Zero-Moment Ferromagnetic Semiconductor*, Phys. Rev. Applied **6**, 044002 (2016).
- [28] J. D. Miller, F. H. Ullstad, H. J. Trodahl, B. J. Ruck, and F. Natali, *Vertical Transport and Tunnelling in Rare-Earth Nitride Heterostructures*, Nanotechnology **31**, 235202 (2020).
- [29] B. A. Butters, R. Baghdadi, M. Onen, E. A. Toomey, O. Medeiros, and K. K. Berggren, *A Scalable Superconducting Nanowire Memory Cell and Preliminary Array Test*, Supercond. Sci. Technol. **34**, 035003 (2021).
- [30] G. E. Moore, *Cramming More Components onto Integrated Circuits*, **38**, 4 (1965).
- [31] S. E. Thompson and S. Parthasarathy, *Moore's Law: The Future of Si Microelectronics*, Materials Today **9**, 20 (2006).
- [32] M. M. Waldrop, *The Chips Are down for Moore's Law*, Nature News **530**, 144 (2016).
- [33] *What the GlobalFoundries' Retreat Really Means - IEEE Spectrum*, <https://spectrum.ieee.org/nanoclast/semiconductors/devices/what-globalfoundries-retreat-really-means>.
- [34] E. Masanet, A. Shehabi, N. Lei, S. Smith, and J. Koomey, *Recalibrating Global Data Center Energy-Use Estimates*, Science **367**, 984 (2020).
- [35] D. S. Holmes, A. L. Ripple, and M. A. Manheimer, *Energy-Efficient Superconducting Computing—Power Budgets and Requirements*, IEEE Transactions on Applied Superconductivity **23**, 1701610 (2013).
- [36] A. S. G. Andrae and T. Edler, *On Global Electricity Usage of Communication Technology: Trends to 2030*, Challenges **6**, 117 (2015).
- [37] *Supercomputer | Definition, Characteristics, Examples, & Facts | Britannica*, <https://www.britannica.com/technology/supercomputer>.
- [38] A. R. H. Stevens, S. Bellstedt, P. J. Elahi, and M. T. Murphy, *The Imperative to Reduce Carbon Emissions in Astronomy*, Nat Astron **4**, 843 (2020).
- [39] C. Aujoux, K. Kotera, and O. Blanchard, *Estimating the Carbon Footprint of the GRAND Project, a Multi-Decade Astrophysics Experiment*, Astroparticle Physics **131**, 102587 (2021).
- [40] T. S. Perry, *The Father of FinFets: Chenming Hu Took Transistors into the Third Dimension to Save Moore's Law*, IEEE Spectrum **57**, 46 (2020).
- [41] P. Gargini, F. Balestra, and Y. Hayashi, *Roadmapping of Nanoelectronics for the New Electronics Industry*, Applied Sciences **12**, 308 (2022).
- [42] P. Kay and P. Powell, *Future Information Technology - 1984 Telecommunications* (1984).

- [43] W. Arden, M. Brillouët, P. Coge, M. Graef, B. Huizing, and R. Mahnkopf, “More-than-Moore” *White Paper*, 31 (n.d.).
- [44] G. Zhao, Z. Deng, and C. Jin, *Advances in New Generation Diluted Magnetic Semiconductors with Independent Spin and Charge Doping*, J. Semicond. **40**, 081505 (2019).
- [45] A. Gupta, R. Zhang, P. Kumar, V. Kumar, and A. Kumar, *Nano-Structured Dilute Magnetic Semiconductors for Efficient Spintronics at Room Temperature*, Magnetochemistry **6**, 15 (2020).
- [46] I. Žutić, J. Fabian, and S. Das Sarma, *Spintronics: Fundamentals and Applications*, Rev. Mod. Phys. **76**, 323 (2004).
- [47] G. Binasch, P. Grünberg, F. Saurenbach, and W. Zinn, *Enhanced Magnetoresistance in Layered Magnetic Structures with Antiferromagnetic Interlayer Exchange*, Phys. Rev. B **39**, 4828 (1989).
- [48] A. Hirohata, K. Yamada, Y. Nakatani, I.-L. Prejbeanu, B. Diény, P. Pirro, and B. Hillebrands, *Review on Spintronics: Principles and Device Applications*, Journal of Magnetism and Magnetic Materials **509**, 166711 (2020).
- [49] L. Rehm, V. Sluka, G. E. Rowlands, M.-H. Nguyen, T. A. Ohki, and A. D. Kent, *Sub-Nanosecond Switching in a Cryogenic Spin-Torque Spin-Valve Memory Element with a Dilute Permalloy Free Layer*, Appl. Phys. Lett. **114**, 212402 (2019).
- [50] M.-H. Nguyen et al., *Cryogenic Memory Architecture Integrating Spin Hall Effect Based Magnetic Memory and Superconductive Cryotron Devices*, Sci Rep **10**, 248 (2020).
- [51] X. Hu and S.-Z. Lin, *Phase Dynamics in a Stack of Inductively Coupled Intrinsic Josephson Junctions and Terahertz Electromagnetic Radiation*, Supercond. Sci. Technol. **23**, 053001 (2010).
- [52] M. F. Gonzalez-Zalba, S. de Franceschi, E. Charbon, T. Meunier, M. Vinet, and A. S. Dzurak, *Scaling Silicon-Based Quantum Computing Using CMOS Technology*, Nat Electron **4**, 872 (2021).
- [53] Q.-Y. Zhao, E. A. Toomey, B. A. Butters, A. N. McCaughan, A. E. Dane, S.-W. Nam, and K. K. Berggren, *A Compact Superconducting Nanowire Memory Element Operated by Nanowire Cryotrons*, Supercond. Sci. Technol. **31**, 035009 (2018).
- [54] V. K. Semenov, Y. A. Polyakov, and S. K. Tolpygo, *Very Large Scale Integration of Josephson-Junction-Based Superconductor Random Access Memories*, IEEE Transactions on Applied Superconductivity **29**, 1 (2019).
- [55] S. Nagasawa, K. Hinode, T. Satoh, Y. Kitagawa, and M. Hidaka, *Design of All-Dc-Powered High-Speed Single Flux Quantum Random Access Memory Based on a Pipeline Structure for Memory Cell Arrays*, Supercond. Sci. Technol. **19**, S325 (2006).
- [56] S. Nagasawa, T. Satoh, K. Hinode, Y. Kitagawa, and M. Hidaka, *Yield Evaluation of 10-KA/Cm<sup>2</sup> Nb Multi-Layer Fabrication Process Using Conventional Superconducting RAMs*, IEEE Transactions on Applied Superconductivity **17**, 177 (2007).
- [57] *IRDS™ 2021: Cryogenic Electronics and Quantum Information Processing - IEEE IRDS™*, <https://irds.ieee.org/editions/2021/cryogenic-electronics-and-quantum-information-processing>.
- [58] M. Tanaka, M. Suzuki, G. Konno, Y. Ito, A. Fujimaki, and N. Yoshikawa, *Josephson-CMOS Hybrid Memory With Nanocryotrons*, IEEE Transactions on Applied Superconductivity **27**, 1 (2017).
- [59] N. Yoshikawa, T. Tomida, M. Tokuda, Q. Liu, X. Meng, S. R. Whiteley, and T. Van Duzer, *Characterization of 4 K CMOS Devices and Circuits for Hybrid Josephson-CMOS Systems*, IEEE Transactions on Applied Superconductivity **15**, 267 (2005).
- [60] G. E. Rowlands, C. A. Ryan, L. Ye, L. Rehm, D. Pinna, A. D. Kent, and T. A. Ohki, *A Cryogenic Spin-Torque Memory Element with Precessional Magnetization Dynamics*, Sci Rep **9**, 1 (2019).
- [61] T. Orllepp, S. R. Whiteley, L. Zheng, X. Meng, and T. Van Duzer, *High-Speed Hybrid Superconductor-to-Semiconductor Interface Circuit With Ultra-Low Power Consumption*, IEEE Transactions on Applied Superconductivity **23**, 1400104 (2013).
- [62] A. Fert, A. Barthélémy, P. Galtier, P. Holody, R. Loloee, R. Morel, F. Pétroff, P. Schroeder, L. B. Steren, and T. Valet, *Giant Magnetoresistance in Magnetic Nanostructures. Recent Developments*, Materials Science and Engineering: B **31**, 1 (1995).

- [63] H. Wang, C. Lu, J. Chen, Y. Liu, S. L. Yuan, S.-W. Cheong, S. Dong, and J.-M. Liu, *Giant Anisotropic Magnetoresistance and Nonvolatile Memory in Canted Antiferromagnet Sr<sub>2</sub>IrO<sub>4</sub>*, *Nat Commun* **10**, 2280 (2019).
- [64] E. C. Ahn, *2D Materials for Spintronic Devices*, *Npj 2D Mater Appl* **4**, 1 (2020).
- [65] S. S. P. Parkin, C. Kaiser, A. Panchula, P. M. Rice, B. Hughes, M. Samant, and S.-H. Yang, *Giant Tunnelling Magnetoresistance at Room Temperature with MgO (100) Tunnel Barriers*, *Nature Materials* **3**, 862 (2004).
- [66] T. Dietl, *A Ten-Year Perspective on Dilute Magnetic Semiconductors and Oxides*, *Nature Materials* **9**, 965 (2010).
- [67] S. Mark, P. Dürrenfeld, K. Pappert, L. Ebel, K. Brunner, C. Gould, and L. W. Molenkamp, *Fully Electrical Read-Write Device Out of a Ferromagnetic Semiconductor*, *Phys. Rev. Lett.* **106**, 057204 (2011).
- [68] M. Tanaka and Y. Higo, *Large Tunneling Magnetoresistance in GaMnAs/AlAs/GaMnAs Ferromagnetic Semiconductor Tunnel Junctions*, *Phys. Rev. Lett.* **87**, 026602 (2001).
- [69] N. O. V. Plank, F. Natali, J. Galipaud, J. H. Richter, M. Simpson, H. J. Trodahl, and B. J. Ruck, *Enhanced Curie Temperature in N-Deficient GdN*, *Appl. Phys. Lett.* **98**, 112503 (2011).
- [70] C. Pot, W. F. Holmes-Hewett, B. J. Ruck, and H. J. Trodahl, *Contrasting Para- and Ferro-Magnetic Responses of (Gd,Dy)N Alloys*, *Appl. Phys. Lett.* **119**, 172406 (2021).
- [71] H. J. Trodahl, F. Natali, B. J. Ruck, and W. R. L. Lambrecht, *Carrier-Controlled Anomalous Hall Effect in an Intrinsic Ferromagnetic Semiconductor*, *Phys. Rev. B* **96**, 115309 (2017).
- [72] F. Ullstad, G. Bioletti, J. R. Chan, A. Proust, C. Bodin, B. J. Ruck, J. Trodahl, and F. Natali, *Breaking Molecular Nitrogen under Mild Conditions with an Atomically Clean Lanthanide Surface*, *ACS Omega* **4**, 5950 (2019).
- [73] W. F. Holmes-Hewett, *Electronic Structure of Nitrogen-Vacancy Doped SmN: Intermediate Valence and 4f Transport in a Ferromagnetic Semiconductor*, *Phys. Rev. B* **104**, 075124 (2021).
- [74] F. Ullstad et al., *Ohmic Contacts of Au and Ag Metals to N-Type GdN Thin Films*, *AIMSMATES* **2**, 79 (2015).
- [75] A. Shaib, W. F. Holmes-Hewett, J. Chan, P. P. Murmu, B. J. Ruck, H. J. Trodahl, and F. Natali, *SmN and DyN: Effect of the Nitrogen to Rare Earth Flux Ratio on the Structural, Transport, and Magnetic Properties*, *AIP Adv.* **11**, 015125 (2021).
- [76] S. Devese, K. Van Koughnet, R. G. Buckley, F. Natali, P. P. Murmu, E.-M. Anton, B. J. Ruck, and W. F. Holmes-Hewett, *Probing the Defect States of LuN<sub>1-δ</sub>: An Experimental and Computational Study*, *AIP Advances* **12**, 035108 (2022).
- [77] C. M. Aerts, P. Strange, M. Horne, W. M. Temmerman, Z. Szotek, and A. Svane, *Half-Metallic to Insulating Behavior of Rare-Earth Nitrides*, *Phys. Rev. B* **69**, 045115 (2004).
- [78] H. J. Trodahl, A. R. H. Preston, J. Zhong, B. J. Ruck, N. M. Strickland, C. Mitra, and W. R. L. Lambrecht, *Ferromagnetic Redshift of the Optical Gap in GdN*, *Phys. Rev. B* **76**, 085211 (2007).
- [79] P. Larson, W. R. L. Lambrecht, A. Chantis, and M. van Schilfgaarde, *Electronic Structure of Rare-Earth Nitrides Using the LSDA+U Approach: Importance of Allowing 4f Orbitals to Break the Cubic Crystal Symmetry*, *Phys. Rev. B* **75**, 045114 (2007).
- [80] A. Shaib, F. Natali, J. R. Chan, F. Ullstad, W. F. Holmes-Hewett, J. D. Miller, B. J. Ruck, and H. J. Trodahl, *Coexisting Structural Phases in the Catalytically Driven Growth of Rock Salt GdN*, *Mater. Res. Express* **7**, 046404 (2020).
- [81] C. Meyer, B. J. Ruck, J. Zhong, S. Granville, A. R. H. Preston, G. V. M. Williams, and H. J. Trodahl, *Near-Zero-Moment Ferromagnetism in the Semiconductor SmN*, *Phys. Rev. B* **78**, 174406 (2008).
- [82] F. Natali, B. J. Ruck, H. J. Trodahl, D. L. Binh, S. Vezian, B. Damilano, Y. Cordier, F. Semond, and C. Meyer, *Role of Magnetic Polarons in Ferromagnetic GdN*, *Phys. Rev. B* **87**, 035202 (2013).
- [83] F. Natali et al., *Molecular Beam Epitaxy of Ferromagnetic Epitaxial GdN Thin Films*, *Journal of Crystal Growth* **404**, 146 (2014).

- [84] F. Natali, N. O. V. Plank, J. Galipaud, B. J. Ruck, H. J. Trodahl, F. Semond, S. Sorieul, and L. Hirsch, *Epitaxial Growth of GdN on Silicon Substrate Using an AlN Buffer Layer*, Journal of Crystal Growth **312**, 3583 (2010).
- [85] J. F. McNulty, K. Temst, M. J. Van Bael, A. Vantomme, and E.-M. Anton, *Epitaxial Growth of (100)-Oriented SmN Directly on (100)Si Substrates*, Phys. Rev. Materials **5**, 113404 (2021).
- [86] E.-M. Anton, B. J. Ruck, C. Meyer, F. Natali, H. Warring, F. Wilhelm, A. Rogalev, V. N. Antonov, and H. J. Trodahl, *Spin/Orbit Moment Imbalance in the near-Zero Moment Ferromagnetic Semiconductor SmN*, Phys. Rev. B **87**, 134414 (2013).
- [87] E.-M. Anton et al., *Superconductivity in the Ferromagnetic Semiconductor Samarium Nitride*, Phys. Rev. B **94**, 024106 (2016).
- [88] W. F. Holmes-Hewett, F. H. Ullstad, B. J. Ruck, F. Natali, and H. J. Trodahl, *Anomalous Hall Effect in SmN: Influence of Orbital Magnetism and 4f-Band Conduction*, Phys. Rev. B **98**, 235201 (2018).
- [89] F. Hulliger, *Chapter 33 Rare Earth Prictides*, in *Handbook on the Physics and Chemistry of Rare Earths*, Vol. 4 (Elsevier, 1979), pp. 153–236.
- [90] A. R. H. Preston et al., *Comparison between Experiment and Calculated Band Structures for DyN and SmN*, Phys. Rev. B **76**, 245120 (2007).
- [91] S. Granville et al., *Semiconducting Ground State of GdN Thin Films*, Phys. Rev. B **73**, 235335 (2006).
- [92] *Photoresist AZ 5214E Photoresists MicroChemicals GmbH*, [https://www.microchemicals.com/products/photoresists/az\\_5214\\_e.html](https://www.microchemicals.com/products/photoresists/az_5214_e.html).
- [93] L. Browning, *Spatial Network Conduction in Carbon Nanotube and Ag-Ag<sub>2</sub>S-Ag Atomic Switch Network Device Platforms*, Doctor of Philosophy Thesis, Victoria University of Wellington (2019).
- [94] *Tds\_az\_developer.Pdf*, (n.d.).
- [95] F. Natali et al., *Epitaxial Growth and Properties of GdN, EuN and SmN Thin Films*, Physica Status Solidi c **9**, 605 (2012).
- [96] J. F. McNulty, E.-M. Anton, B. J. Ruck, F. Natali, H. Warring, F. Wilhelm, A. Rogalev, M. M. Soares, N. B. Brookes, and H. J. Trodahl, *Twisted Phase of the Orbital-Dominant Ferromagnet SmN in a GdN/SmN Heterostructure*, Phys. Rev. B **91**, 174426 (2015).
- [97] W. F. Brinkman, R. C. Dynes, and J. M. Rowell, *Tunneling Conductance of Asymmetrical Barriers*, Journal of Applied Physics **41**, 1915 (1970).
- [98] B. Oliver, Q. He, X. Tang, and J. Nowak, *Tunneling Criteria and Breakdown for Low Resistive Magnetic Tunnel Junctions*, Journal of Applied Physics **94**, 1783 (2003).
- [99] J. J. Åkerman, R. Escudero, C. Leighton, S. Kim, D. A. Rabson, R. W. Dave, J. M. Slaughter, and I. K. Schuller, *Criteria for Ferromagnetic–Insulator–Ferromagnetic Tunneling*, Journal of Magnetism and Magnetic Materials **240**, 86 (2002).
- [100] Y. B. Band and Y. Avishai, *7 - Approximation Methods*, in *Quantum Mechanics with Applications to Nanotechnology and Information Science*, edited by Y. B. Band and Y. Avishai (Academic Press, Amsterdam, 2013), pp. 303–366.
- [101] J. G. Simmons, *Generalized Formula for the Electric Tunnel Effect between Similar Electrodes Separated by a Thin Insulating Film*, Journal of Applied Physics **34**, 1793 (1963).
- [102] B. J. Jönsson-Åkerman, R. Escudero, C. Leighton, S. Kim, I. K. Schuller, and D. A. Rabson, *Reliability of Normal-State Current–Voltage Characteristics as an Indicator of Tunnel-Junction Barrier Quality*, Appl. Phys. Lett. **77**, 1870 (2000).
- [103] M.-S. Kim, Y.-K. Zhou, M. Funakoshi, S. Emura, S. Hasegawa, and H. Asahi, *Tunnel Magnetoresistance in GaCrN/AlN/GaCrN Ferromagnetic Semiconductor Tunnel Junctions*, Appl. Phys. Lett. **89**, 232511 (2006).
- [104] L. S. Dorneles, D. M. Schaefer, M. Carara, and L. F. Schelp, *The Use of Simmons' Equation to Quantify the Insulating Barrier Parameters in Al/AlO<sub>x</sub>/Al Tunnel Junctions*, Appl. Phys. Lett. **82**, 2832 (2003).

- [105] J. J. Åkerman, J. M. Slaughter, R. W. Dave, and I. K. Schuller, *Tunneling Criteria for Magnetic-Insulator-Magnetic Structures*, Appl. Phys. Lett. **79**, 3104 (2001).
- [106] M. Julliere, *Tunneling between Ferromagnetic Films*, Physics Letters A **54**, 225 (1975).
- [107] E. R. Nowak, P. Spradling, M. B. Weissman, and S. S. P. Parkin, *Electron Tunneling and Noise Studies in Ferromagnetic Junctions*, Thin Solid Films **377–378**, 699 (2000).
- [108] P. Duthil, *Material Properties at Low Temperature* (2014).
- [109] E. H. Hwang and S. Das Sarma, *Transport Properties of Diluted Magnetic Semiconductors: Dynamical Mean-Field Theory and Boltzmann Theory*, Phys. Rev. B **72**, 035210 (2005).
- [110] C. Timm, *Disorder Effects in Diluted Magnetic Semiconductors*, J. Phys.: Condens. Matter **15**, R1865 (2003).
- [111] F. Matsukura, H. Ohno, A. Shen, and Y. Sugawara, *Transport Properties and Origin of Ferromagnetism in (Ga,Mn)As*, Phys. Rev. B **57**, R2037 (1998).
- [112] M. Feneberg, R. A. R. Leute, B. Neuschl, K. Thonke, and M. Bickermann, *High-Excitation and High-Resolution Photoluminescence Spectra of Bulk AlN*, Phys. Rev. B **82**, 075208 (2010).
- [113] H. J. M. Swagten, *Chapter One Spin-Dependent Tunneling in Magnetic Junctions*, in *Handbook of Magnetic Materials*, edited by K. H. J. Buschow, Vol. 17 (Elsevier, 2007), pp. 1–121.
- [114] K. Senapati, M. G. Blamire, and Z. H. Barber, *Spin-Filter Josephson Junctions*, Nature Materials **10**, 849 (2011).
- [115] M. Zeng, C. Fang, G. Chang, Y.-A. Chen, T. Hsieh, A. Bansil, H. Lin, and L. Fu, *Topological Semimetals and Topological Insulators in Rare Earth Monopnictides*, ArXiv:1504.03492 [Cond-Mat] (2015).
- [116] P. Larson, W. R. L. Lambrecht, A. Chantis, and M. van Schilfgaarde, *Electronic Structure of Rare-Earth Nitrides Using the LSDA+U Approach: Importance of Allowing 4f Orbitals to Break the Cubic Crystal Symmetry*, Phys. Rev. B **75**, 045114 (2007).
- [117] F. Hulliger, *Chapter 33 Rare Earth Pnictides*, in *Handbook on the Physics and Chemistry of Rare Earths*, Vol. 4 (Elsevier, 1979), pp. 153–236.
- [118] D. Q. Fang, A. L. Rosa, Th. Frauenheim, and R. Q. Zhang, *Band Gap Engineering of GaN Nanowires by Surface Functionalization*, Appl. Phys. Lett. **94**, 073116 (2009).
- [119] R. Didchenko and F. P. Gortsema, *Some Electric and Magnetic Properties of Rare Earth Monosulfides and Nitrides*, Journal of Physics and Chemistry of Solids **24**, 863 (1963).
- [120] G. Busch, E. Kaldis, E. Schaufelberg-Teker, and P. Wachter, *SYNTHESIS, CRYSTAL GROWTH, AND PHYSICAL PROPERTIES OF RARE-EARTH NITRIDE PHASES.*, Pp 359-73 of Les Elements Des Terres Rares. Vol. I. Paris Centre National de La Recherche Scientifique (1970). (1970).
- [121] J. P. Dismukes, Yim, W M, Tietjen J J, and Novak R E, *Vapor Deposition of Semiconducting Mononitrides of Scandium, Yttrium, and the Rare -Earth Elements*, RCA Review **31**, 680 (1970).
- [122] M. J. Winiarski and D. Kowalska, *Electronic Structure of REN (RE = Sc, Y, La, and Lu) Semiconductors by MBJLDA Calculations*, Mater. Res. Express **6**, 095910 (2019).
- [123] D. C. Gupta and I. H. Bhat, *Electronic, Ductile, Phase Transition and Mechanical Properties of Lu-Monopnictides under High Pressures*, J Mol Model **19**, 5343 (2013).
- [124] S. S. Chouhan, G. Pagare, P. Soni, and S. P. Sanyal, *High Pressure Phase Transition and Elastic Properties of Lutetium Monopnictides*, AIP Conference Proceedings **1349**, 97 (2011).
- [125] S. K. Singh and U. P. Verma, *Investigation of High Pressure Phase Transition and Electronic Properties of Lutetium Nitride*, J. Phys.: Conf. Ser. **640**, 012029 (2015).
- [126] S. H. Mir, P. C. Jha, M. S. Islam, A. Banerjee, W. Luo, S. D. Dabhi, P. K. Jha, and R. Ahuja, *Static and Dynamical Properties of Heavy Actinide Monopnictides of Lutetium*, Sci Rep **6**, 29309 (2016).
- [127] A. Oualdine, A. Bentouaf, A. Chebli, B. Nouamane, A. Z. Bouyakoub, and B. Aïssa, *Structural, Elastic, and Electronic Properties of CeN and LuN Using: Ab Initio Study*, J Supercond Nov Magn **31**, 3323 (2018).

- [128] W. Klemm and G. Winkelmann, *Zur Kenntnis der Nitride der Seltenen Erdmetalle*, Zeitschrift für anorganische und allgemeine Chemie **288**, 87 (1956).
- [129] S. Granville, C. Meyer, A. R. H. Preston, B. M. Ludbrook, B. J. Ruck, H. J. Trodahl, T. R. Paudel, and W. R. L. Lambrecht, *Vibrational Properties of Rare-Earth Nitrides: Raman Spectra and Theory*, Phys. Rev. B **79**, 054301 (2009).
- [130] K. Niwa, M. Hasegawa, and T. Yagi, *Synthesis of Ln Nitrides (Ln=Ce, Pr, Gd, Lu) in High Pressure and Temperature*, Journal of Alloys and Compounds **477**, 493 (2009).
- [131] T. Suehiro, N. Hiroaki, Y. Yamamoto, T. Nishimura, M. Mitomo, J. Takahashi, and H. Yamane, *Preparation of Lutetium Nitride by Direct Nitridation*, Journal of Materials Research **19**, 959 (2004).
- [132] J. F. McNulty, E.-M. Anton, B. J. Ruck, M. Suzuki, M. Mizumaki, and H. J. Trodahl, *Tunable Magnetic Exchange Springs in Semiconductor GdN/NdN Superlattices*, Phys. Rev. B **100**, 094441 (2019).
- [133] E.-M. Anton, J. F. McNulty, B. J. Ruck, M. Suzuki, M. Mizumaki, V. N. Antonov, J. W. Quilty, N. Strickland, and H. J. Trodahl, *NdN: An Intrinsic Ferromagnetic Semiconductor*, Phys. Rev. B **93**, 064431 (2016).
- [134] B. D. Sahoo, D. Mukherjee, K. D. Joshi, T. C. Kaushik, and S. C. Gupta, *Prediction of B1 to B10 Phase Transition in LuN under Pressure: An Ab-Initio Investigation*, AIP Conference Proceedings **1731**, 030018 (2016).
- [135] P. Scherrer, *Bestimmung der Größe und der inneren Struktur von Kolloidteilchen mittels Röntgenstrahlen*, Nachrichten von der Gesellschaft der Wissenschaften zu Göttingen, Mathematisch-Physikalische Klasse **1918**, 98 (1918).
- [136] P. Larson and W. R. L. Lambrecht, *Electronic Structure of Gd Pnictides Calculated within the LSDA+U Approach*, Phys. Rev. B **74**, 085108 (2006).
- [137] T. S. Moss, *The Interpretation of the Properties of Indium Antimonide*, Proc. Phys. Soc. B **67**, 775 (1954).
- [138] S. Arajs and R. V. Colvin, *Electrical Resistivity Due to Electron-Phonon Scattering in Yttrium and Lutetium*, Journal of the Less Common Metals **4**, 572 (1962).
- [139] A. Punya, T. Cheiwchanamangij, A. Thiess, and W. R. L. Lambrecht, *First-Principles Study of Nitrogen Vacancies in GdN*, MRS Online Proceedings Library **1290**, 404 (2011).
- [140] V. I. Anisimov, J. Zaanen, and O. K. Andersen, *Band Theory and Mott Insulators: Hubbard U Instead of Stoner I*, Phys. Rev. B **44**, 943 (1991).
- [141] V. I. Anisimov, I. V. Solov'yev, M. A. Korotin, M. T. Czyżyk, and G. A. Sawatzky, *Density-Functional Theory and NiO Photoemission Spectra*, Phys. Rev. B **48**, 16929 (1993).
- [142] A. I. Liechtenstein, V. I. Anisimov, and J. Zaanen, *Density-Functional Theory and Strong Interactions: Orbital Ordering in Mott-Hubbard Insulators*, Phys. Rev. B **52**, R5467 (1995).
- [143] M. Cococcioni and S. de Gironcoli, *Linear Response Approach to the Calculation of the Effective Interaction Parameters in the LDA+U Method*, Phys. Rev. B **71**, 035105 (2005).
- [144] F. Leuenberger, A. Parge, W. Felsch, K. Fauth, and M. Hessler, *GdN Thin Films: Bulk and Local Electronic and Magnetic Properties*, Phys. Rev. B **72**, 014427 (2005).
- [145] M. Topsakal and R. M. Wentzcovitch, *Accurate Projected Augmented Wave (PAW) Datasets for Rare-Earth Elements (RE=La-Lu)*, ArXiv:1408.0863 [Cond-Mat] (2014).
- [146] V. Popescu and A. Zunger, *Extracting E versus Pk Effective Band Structure from Supercell Calculations on Alloys and Impurities*, Phys. Rev. B **85**, 085201 (2012).
- [147] F. Balestra and G. Ghibaudo, *Physics and Performance of Nanoscale Semiconductor Devices at Cryogenic Temperatures*, Semicond. Sci. Technol. **32**, 023002 (2017).
- [148] S. Devese, C. Pot, F. Natali, S. Granville, N. Plank, B. J. Ruck, H. J. Trodahl, and W. Holmes-Hewett, *Non-Volatile Memory Storage in Tri-Layer Structures Using the Intrinsically Ferromagnetic Semiconductors GdN and DyN*, Nano Ex. **3**, 045007 (2023).

- [149] R. E. Camley and J. Barnaś, *Theory of Giant Magnetoresistance Effects in Magnetic Layered Structures with Antiferromagnetic Coupling*, Phys. Rev. Lett. **63**, 664 (1989).
- [150] T. Valet and A. Fert, *Theory of the Perpendicular Magnetoresistance in Magnetic Multilayers*, Phys. Rev. B **48**, 7099 (1993).
- [151] S. Dubois, L. Piraux, J. M. George, K. Ounadjela, J. L. Duvail, and A. Fert, *Evidence for a Short Spin Diffusion Length in Permalloy from the Giant Magnetoresistance of Multilayered Nanowires*, Phys. Rev. B **60**, 477 (1999).
- [152] J. Bass and W. P. Pratt, *Spin-Diffusion Lengths in Metals and Alloys, and Spin-Flipping at Metal/Metal Interfaces: An Experimentalist's Critical Review*, J. Phys.: Condens. Matter **19**, 183201 (2007).
- [153] M. Johnson and R. H. Silsbee, *Interfacial Charge-Spin Coupling: Injection and Detection of Spin Magnetization in Metals*, Phys. Rev. Lett. **55**, 1790 (1985).
- [154] M. Johnson and R. H. Silsbee, *Spin-Injection Experiment*, Phys. Rev. B **37**, 5326 (1988).
- [155] F. J. Jedema, H. B. Heersche, A. T. Filip, J. J. A. Baselmans, and B. J. van Wees, *Electrical Detection of Spin Precession in a Metallic Mesoscopic Spin Valve*, Nature **416**, 713 (2002).
- [156] F. J. Jedema, M. S. Nijboer, Filip A. T., and B. J. van Wees, *Spin Injection and Spin Accumulation in All-Metal Mesoscopic Spin Valves*, Phys. Rev. B **67**, 085319 (2003).
- [157] S. A. Egorov, *Hopping Spin Transport: Interplay of Spin–Orbit Coupling, Hyperfine Interactions, and Exchange*, Physica E: Low-Dimensional Systems and Nanostructures **144**, 115378 (2022).
- [158] Z. Xu, G. D. Hwee Wong, J. Tang, E. Liu, W. Gan, F. Xu, and W. S. Lew, *Giant Spin Hall Effect in Cu–Tb Alloy Thin Films*, ACS Appl. Mater. Interfaces **12**, 32898 (2020).
- [159] W. Fan et al., *Investigation of Magnetization Dynamics Damping in Ni80Fe20/Nd-Cu Bilayer at Room Temperature*, AIP Advances **8**, 056325 (2018).
- [160] K. V. Shanavas, Z. S. Popović, and S. Satpathy, *Theoretical Model for Rashba Spin-Orbit Interaction in d Electrons*, Phys. Rev. B **90**, 165108 (2014).
- [161] F. Hellman et al., *Interface-Induced Phenomena in Magnetism*, Rev. Mod. Phys. **89**, 025006 (2017).
- [162] V. P. Amin and M. D. Stiles, *Spin Transport at Interfaces with Spin-Orbit Coupling: Phenomenology*, Phys. Rev. B **94**, 104420 (2016).
- [163] A. Fert and L. Piraux, *Magnetic Nanowires*, Journal of Magnetism and Magnetic Materials **200**, 338 (1999).
- [164] C. Ahn, K.-H. Shin, R. Loloee, J. Bass, and W. P. Pratt, *Current-Perpendicular-to-Plane Spin Transport Properties of CoFe Alloys: Spin Diffusion Length and Scattering Asymmetry*, Journal of Applied Physics **108**, 023908 (2010).
- [165] Y. V. Nazarov, *Generalized Ohm's Law*, in *Quantum Dynamics of Submicron Structures*, edited by H. A. Cerdeira, B. Kramer, and G. Schön (Springer Netherlands, Dordrecht, 1995), pp. 687–704.
- [166] M. Farooq Khan, H. Kim, G. Nazir, S. Jung, and J. Eom, *Layer Dependent Magnetoresistance of Vertical MoS<sub>2</sub> Magnetic Tunnel Junctions*, Nanoscale **10**, 16703 (2018).
- [167] L. J. van der Pauw, *A Method of Measuring Specific Resistivity and Hall Effect of Discs of Arbitrary Shape*, in *Semiconductor Devices: Pioneering Papers* (WORLD SCIENTIFIC, 1991), pp. 174–182.
- [168] W. L. V. Price, *Extension of van Der Pauw's Theorem for Measuring Specific Resistivity in Discs of Arbitrary Shape to Anisotropic Media*, J. Phys. D: Appl. Phys. **5**, 1127 (1972).
- [169] C. Kasl and M. J. R. Hoch, *Effects of Sample Thickness on the van Der Pauw Technique for Resistivity Measurements*, Review of Scientific Instruments **76**, 033907 (2005).
- [170] M. Liu, W. Du, H. Su, H. Zhang, B. Liu, H. Meng, and X. Tang, *Nonvolatile Voltage-Controlled Magnetization Reversal in a Spin-Valve Multiferroic Heterostructure*, NPG Asia Mater **13**, 1 (2021).
- [171] C. de Buttet, M. Hehn, F. Moutonnet, C. Tiusan, G. Malinowski, A. Schuhl, E. Snoeck, and S. Zoll, *Low-Resistance Magnetic Tunnel Junctions with an MgO-Al<sub>2</sub>O<sub>3</sub> Composite Tunnel Barrier*:



*Asymmetric Transport Characteristics and Free Electron Modeling of a Self-Limited Oxidation Bilayer*, Phys. Rev. B **73**, 104439 (2006).

